

https://dspace.org/

Integration of 3D seismic data analysis techniques and mining-induced seismic data to elucidate the mechanical behaviour of the rock mass in the gold mines of the Witwatersrand Basin

Masethe, Richard Terence

2022

https://hdl.handle.net/10539/37139

Downloaded from a DSpace repository. https://dspace.org/



Integration of 3D seismic data analysis techniques and mining-induced seismic data to elucidate the mechanical behaviour of the rock mass in the gold mines of the Witwatersrand Basin

Richard Terence Masethe

A thesis submitted to the
Faculty of Science, University of the Witwatersrand
in fulfilment of the requirements for the degree of

Doctor of Philosophy

School of Geosciences
University of the Witwatersrand

Johannesburg, 2022

DECLARATION

I declare that this thesis is my own, unaided work. It is being submitted for the Degree of Doctor of Philosophy at the University of the Witwatersrand, Johannesburg. It has not been submitted before for any degree or examination in any other University.



Richard Terence Masethe

21st day of **October** 2022,

at the **University of the Witwatersrand**, Johannesburg.

ABSTRACT

In many hard rock underground mines worldwide, seismicity is observed as stress increases due to increasing mining depth. The rock mass in the hard rock underground mines is generally composed of high strength brittle rock types, so the risk of violent failures increases with increasing mining depth due to increasing stress levels. Seismicity poses a significant geotechnical challenge to the mines as it may damage excavations mining equipment and infrastructure, and cause injuries or even deaths of mining personnel. Mining operations within the Witwatersrand area have mostly taken place at depths of 1.5–3.5 km, but are now migrating to ultra-depth as mines mature. This transition is met with different complexities in the local geology, rock mass conditions, thickness and dip of the reef (ore body). Mining at these greater depths will result in higher mining-induced stresses, induced seismicity and rockbursts. All these complexities affect mining standards and procedures.

This study attempts to mitigate the risk of rockburst by integrating 3D reflection seismic images of geological structures (especially dykes and faults) with the source mechanisms of mining-induced earthquakes to better understand the main drivers of seismicity. The seismicity data covering the Kloof Extension Area (KEA) was investigated in this study. Moderate to large mining-induced seismic events ($M_L \geq 1.5$) within the defined seismic volume were analysed in an area where mining was taking place. The effects that these complexities (high stress, complex structural geology, mining elements, etc.) have on current mining operations was studied to understand the impact on future mine planning and ore reserve evaluation.

High-resolution images of the gold-bearing orebody, the Ventersdorp Contact Reef (VCR), were extracted using seismic attributes. The images are the result of an interpretation of the seismic reflection data. The investigation includes the formulation of a workflow for the computation and interpretation of seismic attributes. The 3D reflection seismic data is under-sampling a series of minor structures (e.g., small faults with a throw less than 5 m and mainly the dykes) that have been identified by the in-stope underground geological mapping. Comparison indicates that the faults determined by the underground mapping generally correlate with those mapped in the 3D reflection seismic data. Mining-induced seismic events frequently occur close to the in-stope identified mapped structures. Numerous faults not detected or visible on the VCR depth structural map and seismic sections were successfully imaged using horizon-based seismic attributes, *viz.* edge detection and dip-azimuth. The dip azimuth attribute provides a better delineation of faults.

The source mechanisms of seventy-five $M_L \geq 1.5$ seismic events were studied in detail. Focal plane solutions were calculated, interpreted, and compared with the geological model derived from underground mine mapping and the interpretation of the 3D seismic reflection data and elements of the mining layout such as abutments, back areas, and pillars. When comparing mining-induced seismic events occurring on mining elements and on geological structures, it was found that they release approximately equal amounts of seismic energy. It was found that moment tensor inversion generally yields fault plane solutions that align with the mining geometry and geological structures. The Es/Ep ratio, routinely used to classify seismic events, was not consistent with the source mechanisms produced by the moment tensor calculations. This study indicated that the parameter is not sufficiently stable to be used for classification.

The data analysis indicates that mining activities may lead to a rockburst (a mining-induced seismic event that causes damages underground) or a slip on pre-existing geological planar structures. However, the geological structures are not the only driving factors of these large seismic events within the 3D reflection seismic volume. Mining elements, such as pillars, remnants and abutments, are sometimes implicated.

All seismic data recorded since the extraction of the Thuthukani shaft pillar commenced in January 2007 has been analysed. We compared seismicity in two five-year periods (1 January 2007 to 30 November 2012 and 1 December 2012 to 31 July 2017) and found an increase in the rate of seismicity and the maximum magnitude (M_{max}) from 2.7 to 3.2. An assessment of seismic hazard using intermediate term probability of occurrence indicates an increase in seismic risk for $M \geq 1.0$ seismic events in period 2 as compared to period 1. Strategies to mitigate the seismic risk during shaft extraction are discussed.

DEDICATION

First, praise and thanks go to my Savior, Jesus Christ, for His favor and the many blessings undeservingly bestowed upon me.

Thank you to my family members, friends, and colleagues for being around in times of need during the research.

Also, thank you to my parents, Lazarus, and my late mother, Martha Masethe, for their unequaled love, support, and Godly example, and my sister and brother for their support and consistent encouragement.

……And thank you to the four most influential people in my life who sacrificed their time to see this research completed: my wife Portia, my son Tshenolo, and my two daughters Omolemo and Lesedi…….

ACKNOWLEDGEMENTS

Professor Ray Durrheim and Professor Musa Manzi for their supervision, guidance, encouragement and motivation throughout this research report, your support have been instrumental throughout this project and throughout my career.

Sibanye-Stillwater is thanked for funding the project and granting permission to publish the findings. I am grateful to the Sibanye-Stillwater Seismology Department staff, particularly the operational team, technical team, and our assistant officer: rock engineering and seismic systems (seismic processors), for their invaluable assistance in completing this project.

The University of the Witwatersrand is acknowledged for granting me the opportunity to do the research project.

Reflection Seismics Research Centre is acknowledged for allowing me the opportunity to use their 3D seismic reflection Software.

Also, I wish to thank the Australian Centre for Geomechanics (ACG), Hamerkop Suite and Institute of Mine Seismology (IMS) for the seismicity interpretations software and, lastly, Schlumberger for providing the Petrel® interpretation software.

However, foremost, sincere thanks to my wife for her unconditional support. This work would not have been completed without your patience and understanding.

Thank you all, so very much.

TABLE OF CONTENTS

DECLARATION ..... **i**
ABSTRACT ..... **ii**
DEDICATION ..... **iv**
ACKNOWLEDGEMENTS ..... **v**
TABLE OF CONTENTS ..... **vi**
LIST OF FIGURES ..... **x**
LIST OF TABLES ..... **xvii**
CHAPTER 1 - INTRODUCTION **1**

1.1 Project Background 1
1.2 Aims and Objectives of the Study 3
1.3 Key Questions 4
1.4 Research Methodology 4
1.5 Challenges 5
1.6 Thesis Structure 5
1.7 Geological and Structural Setting of the 3D reflection seismic cube in the Kloof Gold Mine 6

1.7.1 Introduction 6
1.7.2 Archaean basement (Kaapvaal Craton) 7
1.7.3 Dominion Group 7
1.7.4 Witwatersrand Supergroup 7

1.7.4.1 West Rand Group 8
1.7.4.2 Central Rand Group 8

1.7.5 Ventersdorp Supergroup 8
1.7.6 Transvaal Supergroup 9

1.8 Seismic Interpretation of geological features (faults and dykes) 11

1.8.1 Faults 11
1.8.2 Dykes 11
1.8.3 The impact of dykes and faults on mining activities 12

1.9 Seismic Monitoring 12

1.9.1 Layout of the network 13

1.9.1.1 Type of the Sensors 15
1.9.1.2 Sample rate 17
1.9.1.3 Data acquisition system 18

1.9.2 Hardware components of the seismic network and the data transmission 19

1.9.2.1 Communication 19
1.9.2.2 Generations of data acquisition units (Seismometers) 20
1.9.2.3 Time Synchronisation (Global Position System-GPS) 23

1.9.3 Software 23
1.9.4 Routine data processing procedure 23

1.9.5 Sensitivity and location accuracy 24
1.9.5.1 Seismic system sensitivity 25
1.9.5.2 Location accuracy of the seismic system 26
1.9.6 Problems with the seismic system 28
CHAPTER 2 - MINING, ROCK MASS FAILURE AND SEISMIC EMISSION SOURCES WITHIN THE WITWATERSRAND BASIN 29
2.1 Introduction 29
2.1.1 Rock stress and failure 29
2.2 Empirical Rock Failure Criteria for intact rock 30
2.2.1 Mohr-Coulomb 32
2.2.2 Hoek and Brown 33
2.2.3 Failure mechanism classification 34
2.3 Sources of seismic energy emission 37
2.3.1 Geological structures (dykes and faults) 39
2.3.2 Abutments 41
2.3.3 Stability pillars 41
2.3.4 Stope and mining faces 41
2.3.5 Back areas 41
2.3.6 Development faces 42
2.3.7 Blasting-related events 42
2.3.8 Seismicity at Kloof Gold Mine in terms of emission source and failure mechanism 42
CHAPTER 3 - AN OVERVIEW OF SPATIAL DISTRIBUTION OF SEISMICITY IN SOUTH AFRICA, MAINLY IN THE WITWATERSRAND BASIN 45
3.1 Earthquakes and mining seismicity in South Africa 45
3.1.1 Cape Town Cluster 49
3.1.2 Ceres Cluster 49
3.1.3 Lesotho Cluster 50
3.1.4 Koffiefontein Cluster 50
3.1.5 Witwatersrand (Wits) Cluster 50
CHAPTER 4 - MINING INDUCED SEISMICITY 52
4.1 Introduction 52
4.1.1 Seismological prosessing procedure and location of seismic events 52
4.1.2 Time of the seismic events 54
4.1.3 Seismic energy 55
4.1.4 Seismic moment 55
4.1.5 Source radius 57
4.2 Manipulation of Independent Source Parameters 57
4.2.1 Local Magnitude 57

4.2.2 Frequency magnitude relations 58
4.2.3 Ratio of S- wave to P- wave energy 60
4.3 Source representation 62
4.3.1 Fault plane geometry and focal mechanism 62
4.3.2 Focal mechanism 65
4.3.2.1 Radiation pattern 66
4.3.2.2 First Motion 68
4.3.3 Stress orientation 70
4.3.4 Seismic moment tensor inversion 70
4.3.5 Moment tensor inversion in IMS TRACE software 75
4.4 Data Discussions and Source Parameters Analysis 78
5.1 Introduction 85
5.2. Long-term Seismic Hazard 85
5.3 Medium-term Seismic Hazard 88
5.3.1 Spatially-constrained Seismic Hazard Analysis 88
5.3.2 Numerical modelling 89
5.3.3 Diurnal distribution and the stope blast 89
5.3.4 Seismic Hazard Map and the Grid-based Mapping 90
5.4 Short-term event frequency 92
5.4.1 Large event occurring ($M_L \geq 0.9$), decay analysis, withdrawals procedures and re-entry from the active working place 92
5.5 Peak Particle Velocity related to a seismic event, damage and ground support resistance requirement. 95
5.5.1 Ezulwini - Cooke 4 Case Study: 97
6.1 Background 109
6.2 3D reflection seismic method 109
6.2.1 Survey design and data acquisition 109
6.2.2 Seismic data processing 114
6.2.3 Seismic data interpretation 117
6.3 Seismic attributes 117
6.3.1 Horizon based attributes 117
6.3.1.1 Dip and Dip azimuth 118
6.3.1.2 Edge detection 119
6.3.2 Volumetric seismic attributes 120
6.3.2.1 Edge enhancement 120
6.3.2.2 Ant-tracking 120
6.4 Results 120
6.4.1 Seismic attributes analysis 123

6.5 Discussion 130
7.1 Authorship Statement 132
7.2 Manuscript 1 132
7.3 Summary of publication 133
7.4 Energy Ratio (*Es/Ep*) comparison and the Moment Tensor Inversion 134
7.5 Manuscript 1 135
8.1 Authorship Statement 173
8.2 Manuscript 2 173
8.3 Summary of the publication 173
8.4 Comparison of Seismic Potency release at Kloof, Mponeng and TauTona gold mines 174
8.5 Manuscript 2 177
9.1 Summary and Conclusions 206

REFERENCES 208
APPENDICES 235

Appendix A: *South African National Seismograph Network (SANSN) stations* with their installation date and type of instrumentation.Lastly the brief explanation of seismic parameters 235
Appendix B: Geophones used in the seismic monitoring 238
Appendix C : Software used for the peak particle velocity, location accuracy and seinsitivity analysis. 239
Appendix D : Procedure for the large seismic event. 240
Appendix E : Seismic event locations, Moment Tensor, Fault plane solution and Source Parameters. 241

LIST OF FIGURES

Figure 1.1: *Witwatersrand Basin showing the location of the major goldfields and Kloof Gold Mine (After Dankert and Hein, 2010)* 1
Figure 1.2: *The Kloof-South Deep 2003 3D reflection seismic data survey location map (After Gibson et al., 2000; Manzi et al., 2012a.), where stars represent operational shafts and KEA-Kloof Extension Areas*..... 3
Figure 1.3: *(a) View of the 3D reflection seismic cube in the Kloof Gold Mine area showing the prominent Ventersdorp Contact Reef (VCR) and Black Reef (BR) reflectors. (b) Generalized stratigraphic column showing the various seismic facies. Ages from Krapež (1985), Myers et al. (1989), Armstrong et al. (1991), Kositcin and Krapež (2004) and Dankert and Hein (2010).* 7
Figure 1.4: *Generalised lithostratigraphic columns of the Kloof Gold Mine Operations that is located within the Witwatersrand Basin (Sibanye-Stillwater Geological Department, 2018).*. 10
Figure 1.5: *Amplitude display seismic section showing various types of faults across Kloof operation survey areas. These faults crosscut the Black Reef (BR), Ventersdorp Contact Reef (VCR) and the Kloof Reef (KR) at the base of the Ventersdorp Supergroup. The highly attenuated seismic amplitudes also show near-vertical features (faults and dykes).* 11
Figure 1.6: *Positions of installed geophones in the Kloof Gold Mine (01/01/2017 – 31/12/2018). Green: Operating geophones, Red oval: Geophones that are not functioning due to different reasons (e.g. power cut).* 13
Figure 1.7: *Typical IMS seismic system installed in a hard rock mine (IMS, 2015).* 14
Figure 1.8: *Well-located seismic event within the KEA seismic volume in the mine plan.* 14
Figure 1 9: *IMS sensors: (a). Geophone and (b). Accelerometer .* 15
Figure 1.10: *Seismic moment versus the corner frequency for the different range of stress drops.* 17
Figure 1.11: *Different corner frequencies of seismic events in the KLF database (No evident cut-off corner frequency at 10Hz).* 18
Figure 1.12: *(a) Schematic presentation of the spherically symmetric compressional wavefront (seismic wave) radiating from the source and (b) P-and S-wave triggering different sensors…* 19
Figure 1.13: *A simple sketch of the in-mine seismic recording system*. 20
Figure 1.14: *Changes in a different generation of seismometer technology –underground processors on IMS (ISSI) system, 1989 to 2018.* 22
Figure 1.15: *Sensitivity defining the Kloof seismic system shown by contours. It is assumed that all geophones are operating.* 26

Figure 1.16: *Empirical data and estimations for the Kloof seismic system (01/01/2017 – 31/12/2022).* 26
Figure 1.17: *Location accuracy on XYZ for the period of the data, shown by contours of location errors to adequately cover the Kloof mining working areas. It is assumed that all geophones are operating.* 28
Figure 2.1: *(a) The stress-strain curve resulting from uniaxial compression, (b) Specimen under Uniaxial Compressive Load (c) Brittle behaviour, (d) Ductile behaviour and (e) Hardening behaviour (Yilmaz, 2016)*……29
Figure 2.2: *The Mohr-Coulomb failure criterion in τ: σ plane (extracted from Brady and Brown, 1985).* 32
Figure 2.3: *Mohr-Coulomb failure criterion in terms of the major $\sigma 1$ and $\sigma 3$ minor principal stresses (Wiles, 2006).*..... 32
Figure 2.4: *The diurnal distribution of predominantly crush-type events (M≤2.0) at Kloof Gold Mine, 1/1/2017-30/12/2018. The plot is created in mXrap software (Harris and Wesseloo, 2015).* 35
Figure 2.5: *The diurnal distribution of predominantly shear-type events (M>2.0) at Kloof Gold Mine, 1/1/2017-30/12/2018. The plot is created in mXrap software (Harris and Wesseloo, 2015).* 35
Figure 2.6: *Main seismic emission sources at Kloof Gold Mine.*..... 38
Figure 2.7: *Geological structures and the polygons used to assess hazard (1/6/1999 to 30/12/2018). Purple polygon refers to Figure 2.6.* 40
Figure 2.8: *Gutenberg Richter Plots for the dykes and faults used to assess hazard (1/6/1999 to 30/12/2018) indicating different levels of hazards.* 40
Figure 2.9: *Mine plan with M_L≥1.5 events classified into different types of failure mechanisms based on their Es/Ep ratios, 1/6/1999 to 30/12/2018. Purple polygon refers to Figure 2.6.* ... 43
Figure 2.10: *Sources of M_L≥1.5 seismic events at Kloof Gold Mine, 1/6/1999 to 30/12/2018.* 43
Figure 2.11: *Classification of M_L≥1.5 events at Kloof Gold Mine into different types of failure mechanisms based on their Es/Ep ratios, 1/6/1999 to 30/12/2018*. 44
Figure 3.1: *The location of seismic stations in southern Africa: South African National Seismograph Network (SANSN), Strategic Water Management Project (SWMP), Far West Rand (FWR), Klerksdorp-Orkney-Stilfontein-Haartebeesfontein network (KOSH), AfricaArray-CGS Bushveld Broadband Array, AfricaArray, HARTRAO academic network, and Namibian Geological Survey*……..45

Figure 3.2: *Location of seismic events in South African National Seismological Database (SANSD) indicating the spatial distribution of earthquakes from Pre-1900 to Post 1970. (from Manzunzu et al., 2019).* 47
Figure 3.3: *Location of earthquakes making up the final catalogue (red circles) from 1690-2011 including mining seismic events in Green circles. Sources of data are from SANSN, International Seismological Center (ISC), (after Mulabisana, 2016).* 48
Figure 3.4: *Damaged buildings at in Stilfontein resulting from an M_L5.5 earthquake on 9 March 2005 (Durrheim et.al, 2014).* 48
Figure 3.5: *The aftermath of the worst earthquake to hit South Africa on 29 September 1969, M_L6.3. (Image: Facebook/Tulbagh Aardbewing/Earthquake).* 49
Figure 3.6: *Map of Mining-induced seismicity contained in the MHSC and CGS collaboration Network. The seismic recording stations are represented by the blue colour and seismic events by yellow circles. Red polygons indicate closed mines (extracted from MHSC project).* 50
Figure 3.7: *Spatial plot of seismicity over a 5 year period (2010-2015).Scale bar indicates magnitude.The size of the circles is proportional to moment magnitude Mw. Blue lines represent known surface faults and yellow shades represent previous mine boundaries (after Cichowicz et al., 2016).* 51
Figure 4.1: *Example of 4 tri-axial sites showing components of the seismic sensors (XYZ) including dead components*……53
Figure 4.2: *(a) Location on section view of the scatter of seismic events on depth (b) Spatial plot of seismic events.* 54
Figure 4.3: *Activity rate: Bar graph showing the number of seismic events per week in the mine.* 54
Figure 4.4: *P-wave displacement spectra for earthquakes with two different magnitudes. The solid lines correspond to the real spectra, the dashed lines are the model spectra, and the dotted lines are the low-frequency level of the spectra (modified from Prieto, 2007).* 56
Figure 4.5: *The frequency-magnitude relation is not following an expected power law. Green colour: represent the number of seismic events with given magnitude, blue colour : events with magnitude greater than the given one.* 60
Figure 4.6: *A tri-axial waveform indicating both the P-wave and the S-wave.* 61
Figure 4.7: *Different seismic source mechanisms illustrations based on the energy ratio (E_S:E_P). Blue representing shearing type (E_S:E_P ratio>10), Blue is the Non-Shear (E_S:E_P ratio<7) and Red representing the mix mechanism source type (7< E_S:E_P <10).* 62
Figure 4.8: *Schematic representation of a fault plane, displacement field and spreading rupture front in an elastic medium. Right: Systematic four-lobed distribution of compressional (+) and*

dilatational (-) wavefronts of a P-wave radiation pattern (see section 4.3.2.1): Yellow triangles: geophones (Masethe, 2012) 63
Figure 4.9: *Geometry of a fault plane when studying earthquakes. The Cartesian coordinate system is defined by the axes x_1, x_2 and x_3. The normal vector, slip vector, dip angle, slip angle and strike angle are defined following Stein and Wysession (2003).* 64
Figure 4.10: *Basic types of faulting with strike-slips (the upper row) and dip-slips (the lower row), (after Stein and Wysession, 2003).* 65
Figure 4.11: *(a) Schematic representation for the double couple source body wave radiation pattern, (b) Radiation patterns on x_1-x_3 plane of the P and S waves (after Stein and Wysession, 2003; pp. 221).* 67
Figure 4.12: *First motion of P-waves observed. The two nodal planes (fault plane and auxiliary plane) separate regions of compressional and dilatational first polarity of first arrivals (from Stein and Wysession (2003))* 69
Figure 4.13: *Beachball diagram with defined Tension (T-), Pressure (P-) and B-axes. Dilatational quadrants are shade white and compressional quadrants are in black.* 70
Figure 4.14: *(a) Force Couple and (b) Double Couple (Shearer, 2009).* 71
Figure 4.15: *A set of nine possible force couples of Mkl, the indices k and l denote the directions of the force and arm couple of the moment tensor (after Aki and Richards, 1980).* 71
Figure 4.16: *Moment tensors and their representation as beach-ball diagrams (extracted from Stein and Wysession, 2003)* 73
Figure 4.17: *The two possibilities to decompose a full moment tensor, either into an isotropic and deviatoric tensor or into a residual isotropic component and a general mixed-mode shear crack. The deviatoric component can be further decomposed into different elementary sources (e.g., Double Couple (DC) and compensated linear vector dipole (CLVD)) (modified from Dahm and Krüger, 2014).* 75
Figure 4.18: *Final results (Output) of the Moment tensor Inversion with components Pressure (P-), B orthogonal to the slip vector -, Tension (T-) axes. SWU-South-West Up.* 78
Figure 4.19: *(a) Mine plan view showing the location of seismic events (colored circles). (b) Zoomed-in view showing the spatial distribution of the seismic events, mining layout and the geology in the closer range (1 January 2017 and 30 December 2018). KR:Kloof Reef, VCR:Ventersdorp Contact Reef and MR:Main Reef.* 79
Figure 4.20: *The distribution of seismic events source mechanisms in different mining levels within the VCR orebody at an average depth of 3 000 m. Brown represents the Fault Slip (FS), and Green represents the Non-Shear (NS).* 80

Figure 4.21: *Log Es/Ep ratio with respect to local magnitude for both the fault slip (FS) and seismic events the non-shear (NS)*. 81
Figure 4.22: *The fault slip and non-shear seismic events relationship between the Log seismic energy and the local magnitude.* 82
Figure 4.23: *Log Apparent Volume versus local magnitude for both the fault slip (FS) and non-shear (NS) seismic events.* 82
Figure 4.24: *The fault slip and non-shear seismic events source radius versus their magnitude.* 83
Figure 5.1: *The Gutenberg Richter Plot*……86
Figure 5.2: *Diurnal distribution indicating the background seismic events and the peak (Indicating the blasting time).* 90
Figure 5.3: *Seismic Hazard Map indicating potential unstable geological structures and mining stopes.* 91
Figure 5.4: *(a) Grid-based hazard mapping and the interpretation of b-values within an Australian mine. Red and blue colours highlighted areas represent abutment and stoping areas. (b) Grid-based interpretation of seismicity showing b-value distribution by colour. The size of the grid point markers are scaled by apparent stress (Wesseloo et al., 2014).* 92
Figure 5.5: *An example of the decaying seismicity after large events have occurred in Kloof Gold Mines.* 93
Figure 5.6: *Aftershock decay rate of events $M_L \geq 0$ from the mainshock magnitude of $M_L \geq 1.0$, $M_L \geq 2.0$ and $M_L \geq 3.0$. The estimated background level and the lines representing $0.8 \leq p \leq 1.0$ are also indicated as dash lines on the graph (Kgarume et al., 2010).* 94
Figure 5.7: *The aftershock decay curve indicating the period where event rate has decreased to background levels .* 95
Figure 5.8: *Plan showing shafts (#): Main and the Ventilation (Vent), current mining layout and the infrastructure (development end).* 98
Figure 5.9: *Geological model (faults and a dyke) indicating the infrastructure and the seismic event of $M_L=2.8$ on 21 October 2014 in the south-east of the shaft pillar (red star). Brown coloured tunnel represents the 38A cross-cut south and the green coloured tunnel represent the 38 cross-cut south. Faults (f) and their throws are indicated.* 99
Figure 5.10: *Location of $M_L=2.8$ seismic event on the east of the Cooke 4 shaft pillar near the 38 cross-cut south.* 100
Figure 5.11: *(a). A wave propagation code cartoon is showing seismic energy where the rupture or failure occurs and the radiation pattern attenuating from the source to the recording sites (b). The radiation pattern cartoon of a hanging wall seismic event indicates both the P- and the S- waves from the source and the site's recordings passing through a tunnel.*

Seismograms (blue and red) of the three sites are displayed far-right (IMS-Tunnel source wave propagation code, 2015). 102
Figure 5.12: *Modelled PPV estimation of the M_L=2.8 magnitude seismic event in the vicinity of the 38 cross-cut south.* 103
Figure 5.13: *Magnitude (ML=2.8), corresponding PPV and expected damages at 98m. The colours represent damage observations from the Kloof mines from 2007-2013 (Modified Jager and Ryder, 1999).* 104
Figure 5.14: *Plan of 38 cross-cut south and 38A cross-cut south indicating the radial extent of observed damages.* 105
Figure 5.15: *Damage to 38 cross-cut S showing unravelling of support including sidewall and hanging wall ejection of rock (Tshepo Rabele, 2014).* 106
Figure 5.16: *Footwall heave lifting a 5 ton locomotive above the grade line position (Tshepo Rabele, 2014).* 106
Figure 5.17: *Focal mechanism of M_L =2.8 seismic events indicating the Isotropic (ISO), compensated linear vector dipole (CLVD) and the Deviatoric (DC) components of the Moment Tensor Solution.* 107
Figure 5.18: *The Hudson plot indicating a slip-type implosive seismic source type. It is divided into 3 regions: Upper region (Explosive), Central region (High DC) and Lower region (implosive). Black lines are contours of constant T (measure of deviatoric moment release, running from right to left) and k (measure of the change in volume, running from top to bottom).* 108
Figure 6.1: *Schematic showing reflection of seismic waves from a horizontal interface with contrast in acoustic impedance, Z ($Z_2 > Z_1$) (after Trickett et al., 2004)*……110
Figure 6.2: *Schematic diagram of source-receiver geometry. The diagram shows the reflection wave paths over a horizontal interfaces across which there is an acoustic impedance contrast, where $\nu 1\rho 1 > \nu 2\rho 2$ or $\nu 2\rho 2 > \nu 1\rho 1$ (after Salisbury and Snyder, 2007).* 112
Figure 6.3: *Kloof Gold Mine amplitude-display seismic section showing the imaging of reflective interfaces in the Transvaal Supergroup (Pretoria and Chuniespoort groups) and the base of the Klipriviersberg Group, especially the Black Reef (BR) and Ventersdorp Contact Reef (VCR) horizons. (BSL:Below Surface Level)* 113
Figure 6.4: *The Fresnel zone is the area on a reflector where the incident energy ray is returned within the central ray's half-wavelength (λ) of the central ray. (Kearey and Brooks 1991)...* 114
Figure 6.5: *Processing flow of the reflection seismic data.* 115
Figure 6.6: *A graphic representation of how the dip azimuth (direction) and dip are extracted from a seismic interpreted horizon. Calculation of both the dip azimuth and dip variations along a horizon (after Rijks and Jauffred, 1991).* 118

Figure 6.7: *(a) In-stope mapped geological structures indicating a good correlation with mining-induced seismicity data, (b) Edge attribute map of the VCR overlain with mining-induced seismic events (M_L≥1.5) in Kloof Gold Mine are indicated.*..... 119
Figure 6.8: *(a) The 3D regional model defined from edge detection attribute analysis constructed from regional VCR pick. (b) Edge detection on section view incorporates the major West Rand Fault and Bank Fault (c) Edge detection model indicating the subtle structures and location of mining-induced seismicity (M_L≥1.5).*..... 121
Figure 6.9: *(a) Amplitude display seismic section of the reflection seismic data (Kloof Operations) in the Petrel interpretation package, (b) zoomed-in cross-section for Inline 336 on the top right corner showing the westerly dipping faults and dykes cross-cutting the rock mass with the vertical exaggeration (VE) of 4:1. Owing to the low signal-to-noise of the amplitude display, it is difficult to track faults and dykes up stratigraphy to the Ventersdorp Contact Reef (VCR) and the Black Reef (BR) levels.*..... 122
Figure 6.10: *(a) The VCR depth structure map view, with the colour bar showing depth from 1100 ms to 4200 ms with ±100 ms contour interval (b) Seismic section in amplitude display indicating good depth tie between VCR and a borehole and indicating faults (c) Cross sectional view of the VCR elevation map overlain by mining-induced seismicity data and a borehole (modified from Manzi et al., 2013).*..... 123
Figure 6.11: *The dip-azimuth map, with the colour bar, restricted to 350º, illuminating the general orientation of structures observed on the horizon.*..... 124
Figure 6.12: *The dip-azimuth map, with the colour bar, restricted to 350º, illuminating the general orientation of structures observed on the horizon and the 3D-seismic structure*. ... 125
Figure 6.13: *Edge detection map enlightening an array of lineaments that were below the seismic limit and were seismically 'invisible' to conventional seismic interpretations.*..... 126
Figure 6.14: *VCR edge attribute map overlain with mining-induced seismicity data in Kloof Gold Mine. Structures show good correlation with seismicity data with different magnitude (blue, green and red).*..... 127
Figure 6.15: *Surface stability map with the confidence index of the picked surface. Areas in red and green have a higher confidence index than those in blue. Mining-induced seismic events are indicated with circles that are green, blue and red.*..... 128
Figure 6.16: *Crossline view of the ant-tracking results, run in passive mode, from the structurally – smoothed data with variance attribute applied. The visibility and continuity of structures are considerably enhanced compared to the conventional amplitude display. Steep and gently dipping structures can be clearly seen, and their extent is better resolved. The vertical exaggeration (VE) of the section is 4:1.*..... 129

Figure 6.17: *Crossline view of the ant-tracking results, run twice in passive mode, from the structurally – smoothed data with variance attribute applied. The visibility and continuity of structures are considerably enhanced compared to the conventional amplitude display. Steep and gently dipping structures can be clearly seen, and their extents better resolved. Care should always be taken as such detail can also contain artefacts. The vertical exaggeration (VE) of the section is 4:1* 130

Figure 8.1: *The ratio of potency to production on mining stopes in Mponeng Gold Mine (Rakumakoe, 2019)*……...175

Figure 8.2:*Tautona shaft pillar seismic response compared to the mining rate (Murphy, 2012).* 176

LIST OF TABLES

Table1.1: IMS seismometer and processor specifications (IMS, 2015): 22
Table 2.1: Intact rock failure criteria (Edelbro, 2004)……31
Table 2.2: Rock strength tests from six of each rock type sample from the Kloof Gold Mine (Van der Heever and Ryder, 2007) 34
Table 2.3: Suggested classifications of seismic sources (source mechanism) (Ortlepp and Stacey, 1994, Jager and Ryder, 1999, Ortlepp, 2001). 36
Table 2.4: Main sources of seismic energy emission (Jager and Ryder, 1999) observed at Kloof Gold Mine. 38
Table 2.5: Seismic history of some major geological structures at Kloof Mine (1/6/1999 to 30/12/2018) 39
Table 5.1: Intermediate-term probabilities of seismic event occurrence in a block of ground within the 3D reflection seismic volume for Period 1 (1/7/1999 to 1/7/2009) and Period 2 (2/7/2009 to 31/7/2018)……..87
Table 5.2: Comparison of seismic hazard for both Period 1(1/7/1999 to 1/7/2009) and Period 2 (2/7/2009 to 31/7/2018) 87
Table 5.3: The M_L=2.8 event source parameters summary and comments 100
Table 5.4: Moment tensor for the M_L=2.8 event on 21 October 2014 107
Table 6.1: The summary of parameters used for the 2003 Kloof-South Deep and 1994 Leeudoorn 3D Reflection seismic data sets (Manzi *et al*., 2012b)……116
Table 1A: Source parameters……..……..196
Table 2A: Moment tensor solutions 199
Table 3A: Fault Plane Solutions 202
Table 4A: Moment tensor inversion decomposition (ISO, CLVD and DC) 203

CHAPTER 1 - INTRODUCTION

1.1 Project Background

Since the discovery of gold near present day Johannesburg in 1886, mining in the Witwatersrand Basin has made a significant contribution to the world's stock of gold (Handley, 2004). The basin extends to both west and east of Johannesburg and southwards into the Free State Province, with a long axis of about 350 km (Figure 1.1). Most of the resource lies at depths between 1 and 5 km, presenting significant challenges and risks, such as the occurrence of seismicity and rockbursts that have claimed the lives of many of underground mine workers. After more than a century of mining, operations are currently approaching depths of 4 km. Although production has declined in the last few decades, the basin still makes an enormous contribution to the economy of the country.

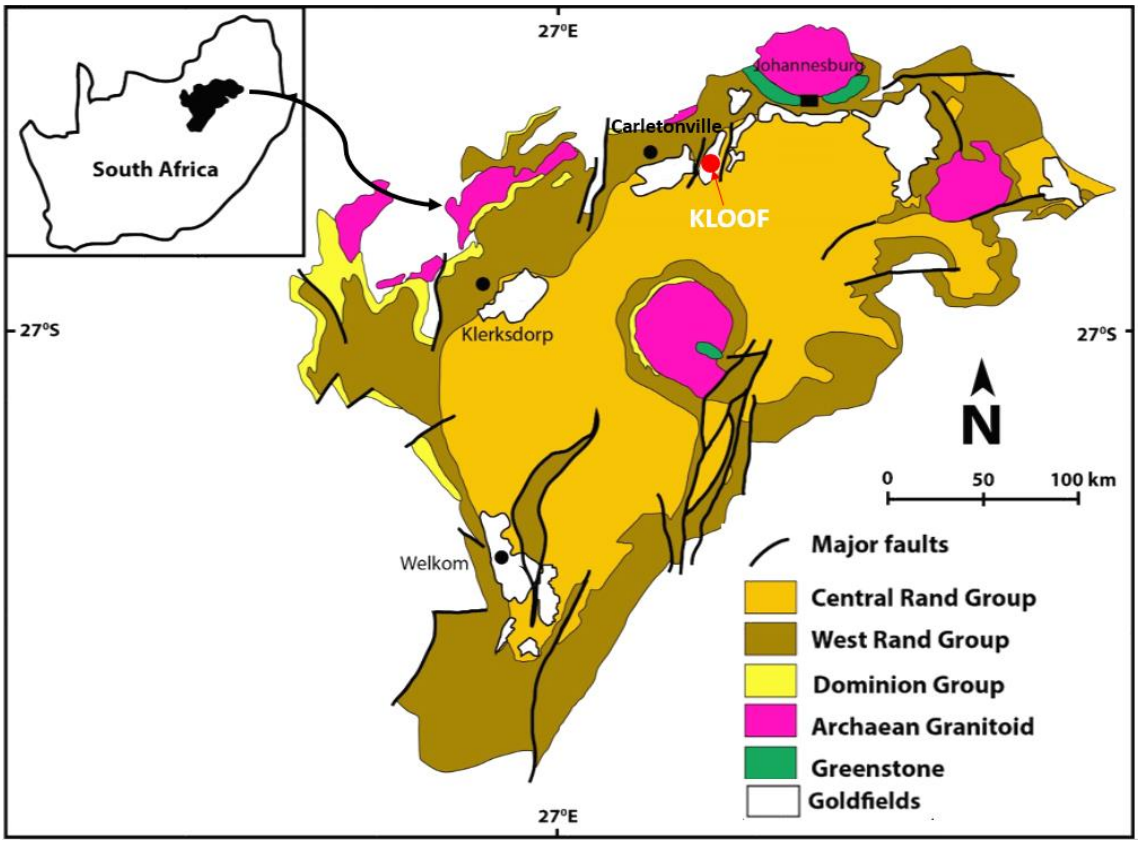

Figure 1.1: *Witwatersrand Basin showing the location of the major goldfields and Kloof Gold Mine (After Dankert and Hein, 2010)*

2D and 3D reflection seismic methods have been used by the oil and gas industry since the 1920s and 1960s, respectively. The use of reflection seismics to explore for minerals and precious metals in the 'hard rock' environment was pioneered in South Africa in the 1980s (Pretorius *et al*., 1994; Salisbury *et al*., 2003). Apart from its use to explore for gold in the Witwatersrand Basin, Stevenson *et al*. (2003) report that the

reflection seismic technique has been used to differentiate areas of “pothole” reef from “normal” platinum-bearing Merensky Reef within the Bushveld Complex of South Africa; explore for base metal deposits related with buried paleokarst features in northern Namibia, and map the downdip extension massive sulfide “shoots” at Otjihase Mine in the Matchless Amphibolite Belt of Namibia.

Reflection seismics has been used for brown- and greenfields exploration in the Witwatersrand Basin and environs, for mine planning, and to image faults that may be conduits of water and methane to mine workings (Campbell and Crotty, 1988; Gibson, 2005; Gibson *et al.,* 2000; Manzi *et al*., 2012b). Although reflection seismic surveys are expensive, their use is justified in the Witwatersrand Basin as they provide far greater resolution than the magnetic and gravity methods, and are cheaper than deep drilling (Manzi *et al.,* 2012b). Recent advances in 3D seismic processing technology make it possible to reprocess legacy data acquired decades ago and produce better stratigraphic and structural images and interpretations. For example, Manzi *et al*. (2012a, 2012b, 2013) used seismic attributes (such as edge detection, azimuth, and dip) to detect fault off-sets that displaced both the Black Reef (BR) and Ventersdorp Contact Reef (VCR) by 10s to 100s of metres in the West Wits Line gold fields.

Mining-induced seismicity has been studied in South Africa for more than a century (Riemer and Durrheim, 2012). A *seismic event* is defined as “a sudden release of strain energy that was stored in a rock mass”, while a *rockburst* is defined as “a seismic event that causes damage to underground workings” (Jager and Ryder, 1999; Ryder and Jager, 2002). Both result from the interaction of complex ambient and mining-induced stresses acting on a rock mass that is inelastic, anisotropic and heterogeneous. The rock mass is intersected by a large variety of geological weaknesses and discontinuities. The weight of the overlying strata results in high stresses at depth and may either cause the pre-existing geological weaknesses to be reactivated or might create new fractures in the previously intact rock. When sudden movement on a pre-existing feature or fracture occurs, stored elastic energy is released as seismic waves.

The larger mining-induced seismic events in the deep gold mines of the Witwatersrand Basin are usually associated with both - major and minor geological structures. These geological structures and their off-shoots can be mapped and understood by using high-resolution 3D reflection seismic survey method (Manzi *et al*., 2012a). Here we integrate the 3D reflection data, geological structures that were mapped underground, and mining-induced seismic data to determine whether large seismic events and their aftershocks are related to the geological structures.

Gold Fields commissioned a high-resolution 3D reflection seismic survey in 2003 (Figure 1.2) to understand the geological character of the down-dip extension of the Ventersdorp Contact Reef (VCR) on the lease areas of South Deep and Kloof Gold Mines, which are situated to the east and west of the West Rand Fault, respectively (Manzi *et al*., 2012a). The specific objectives of the 3D seismic reflection survey were to image

the Black Reef Formation (BR) at depths of 1500–2000 m; the VCR at depths of 3000-4200 m; and the Booysen shales, a marker horizon that lies about 400 m below the VCR (Manzi *et al*., 2014).

The primary objective of this PhD study is to integrate the 3D reflection seismic survey data from the Kloof Extension Area (KEA) seismic data volume with mining-induced seismic data from the same volume. Seismic data volume is a cube (228 km^3) where the 3D reflection seismic data was analysed. The large mining-induced events and their aftershocks are plotted and interpreted using moment tensor solutions and compared with the orientation of faults, abutments and remnants to determine the main controls and drivers of the seismicity.

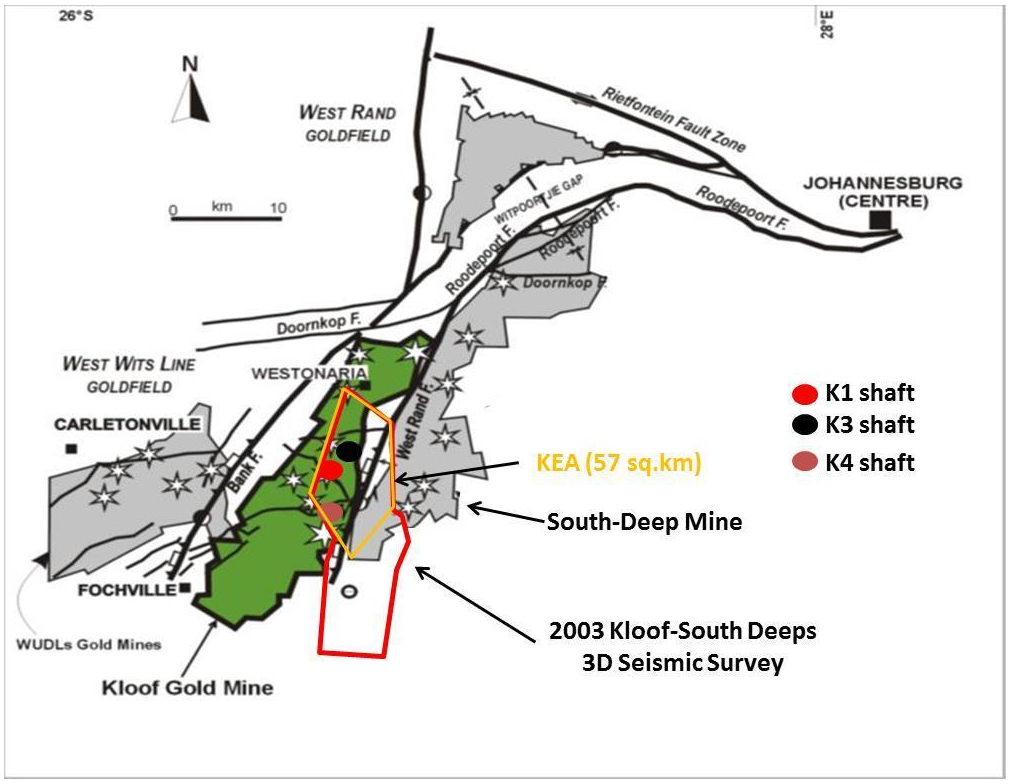

Figure 1.2: *The Kloof-South Deep 2003 3D reflection seismic data survey location map (After Gibson et al., 2000; Manzi et al., 2012a.), where stars represent operational shafts and KEA the Kloof Extension Areas.*

1.2 Aims and Objectives of the Study

The overall aim of this work is to improve the efficiency and reduce the risk of deep level mining by mitigating the risk of rockbursts. The specific aim is to gain a better understanding of the controls and drivers of mining-induced seismicity so that safer mining layouts can be designed.

The objectives of the research are to determine the relationship between large mining-induced seismic events and

1. Geological structures (such as faults and dykes) mapped in mine workings, in boreholes, on the surface, structures obtained using 3D reflection seismic data; and
2. Features of mining layouts, such as pillars, abutments and back-areas.

1.3 Key Questions

The KEA 3D seismic data were reprocessed using modern techniques and the source and seismicity parameters of larger seismic events ($M_L \geq 1.5$) that occurred in the same area were recalculated using advanced techniques in order to address the following important questions:

1. How well can the geological structures (dykes, faults) imaged by 3D seismics be correlated with the structures mapped in mine workings and boreholes?
2. Are these structures associated with the larger seismic events?
3. How do the source mechanisms of the larger seismic events relate to the mapped geological structures?
4. How do the source mechanisms of the larger seismic events relate to the major features of the mining layout, such as pillars, abutments and back areas?
5. How does production data correlate with mining-induced seismic data?
6. How well does seismic hazard compared to different time periods compare?
7. What are the strategies to mitigate the seismic risk during shaft extraction?
8. How does the seismic response to mining change?

1.4 Research Methodology

The geological structure of the area covered by the KEA 3D reflection seismic volume (Figure 1.2) was studied in detail. The author reprocessed the data in the 3D seismic volume (i.e. post-processing using attributes computation) using modern ‘seismic attribute’ methods to enhance subtle features and enhance resolution with the aim of mapping dykes and faults, some of which are capable of emitting seismic events triggered or induced by mining. The seismic interpretation was constrained by geological mapping on the surface, in underground workings and in boreholes; progressing from the ‘known’ to the ‘unknown’ (known mapped structure to unkown unmapped structure).

Seventy-five large mining-induced seismic events ($M_L \geq 1.5$) that occurred within the 3D seismic volume were studied, along with their aftershocks. The events were selected to have a range of magnitudes and source mechanisms. The hypocentre of each event was located, its source parameters (e.g., energy, moment, stress drop) determined, and its moment tensor calculated, which is indicative of the co-seismic slip and deformation. All calculated moment tensor solutions were rotated into the reef plane and compared to the structures in the vicinity. These two data sets were then integrated in an effort to answer the key questions posed above.

1.5 Challenges

1. The seismicity and reflection seismic data sets use different coordinate systems; hence adjustments and corrections had to be made.
2. Discrepancies were found between imaged surface structures and the in-mine geological structures.
3. Some parts of the Kloof operation were out of the KEA 3D seismic volume and hence could not be used for this study.
4. The depth coordinate of the hypocenters was difficult to determine accurately owing to the planar geometry of the in-mine seismic network.
5. Some of the larger seismic events were not surrounded by seismic stations, making it difficult to determine the source mechanism reliably.

1.6 Thesis Structure

The research background, aim and objectives, key questions, research methodology, challenges, geological and structural setting are outlined in **Chapter 1**.

Chapter 2 focuses on mining, rock mass failure highlighting the relationship between rock stress and failure, the empirical rock failure criteria for intact rock. Only two failure mechanisms were looked at, the Mohr-Coulomb and Hoek and Brown rock failure criteria and the different sources of seismic events within the Witwatersrand Basin.

An overview of the spatial distribution of seismicity in South Africa, focusing mainly on the Witwatersrand basin, is given in **Chapter 3**, emphasizing the various spatial clusters of earthquakes scattered around the country. These include the Cape Town, Ceres, Lesotho, Koffiefontein and Witwatersrand.

Chapter 4 introduces a summary of the key concepts in mining seismology, from the location of seismic events, time of seismic events (diurnal distribution), seismic energy, seismic moment, and source radius. Source parameters were further elaborated. The chapter explained the focal mechanism, source representation, and some source parameters.

Chapter 5 deals with the seismic hazard at Kloof that covers long-term, medium-term and short-term seismic hazards. The chapter discusses the different seismic hazard approaches based on the long-, and medium-term. The author further discussed peak particle velocity relating to a seismic event and associated damages within the Witwatersrand Basin. The related case study is also given on the M_L2.8 seismic event that caused damages within the operating tunnel.

Chapter 6 is dedicated to the seismic reflection method, summarizing the acquisition, processing and interpretation of the 3D reflection seismic data previously acquired at Kloof Gold Mine in the KEA area. Seismic sections were processed, the author used auto-tracking and manual picking to pick the horizons. Geological structures were imaged (faults and dykes) and interpreted. Lastly, the seismic reflection attributes were analyzed and discussed.

In **Chapter 7**, the 3D seismic data analysis techniques and mining-induced seismic data were integrated and interpreted. The integration was to understand the sources of seismic energy emissions at Kloof Gold Mine to mitigate the rockburst hazard and understand the mechanical behaviour of rock mass within the Witwatersrand Basin. The focal mechanism and moment tensor solutions were related to the mapped and interpreted seismically active geological structures within the 3D seismic reflection volume. The chapter highlighted the energy ratio (E_S:E_P) comparison and the Moment Tensor Inversion. It is intended to submit this paper to Geophysics as it is a sequel to a paper that received the 2012 "Best paper in Geophysics" Award that the supervisors of this thesis authored.

In **Chapters 8**, A summary of the manuscript is provided, highlighting its primary objectives, methods, results and conclusions. A description of the candidate's contribution and the contribution of each author is summarized. The manuscript covers the seismic response to mining during the extraction of the Thuthukani shaft pillar at Kloof Mine. The manuscript focused on mining seismology methods and the rock mass response to mining. Comparison of Seismic Potency release at Kloof, Mponeng and TauTona gold mines are highlighted.

Chapter 9 summarises and concludes the discussions of the previous chapters, including the specific contributions of this research.

1.7 Geological and Structural Setting of the 3D reflection seismic cube in the Kloof Gold Mine

1.7.1 Introduction

The 2.8 Ga Witwatersrand Basin (Figure 1.1), situated on the Archaean Kaapvaal Craton, hosts one of the world's largest gold deposits (Robb and Meyer, 1995; James *et al*., 2003). Knowledge of the type of strata that fill the basin and the major geological structures (syn- and anticlines, faults, intrusions) is important when interpreting the 3D seismic data (Figure 1.3). This study focuses on the Witwatersrand, Ventersdorp and Transvaal supergroups, as they host the most important orebodies. The Witwatersrand Basin is structurally complex. Numerous faults and dykes cross-cut the orebodies and may cause loss of ground, affecting ore reserve estimates. They may also pose difficulties to the ore extraction process as they are often associated with stress instabilities, are prone to failure, and may cause seismicity (Dankert and Hein, 2010; Durrheim *et al*., 2012; Ogasawara *et al*., 2009a, b). The generalized lithostratigraphic column for Kloof Operations is indicated in Figure 1.4.

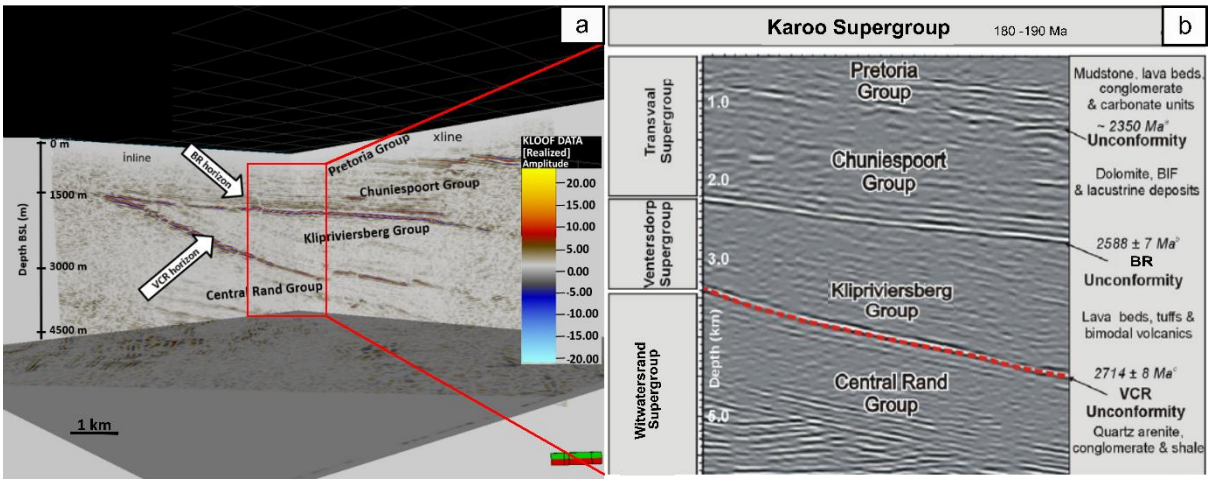

Figure 1.3: *(a) View of the 3D reflection seismic cube in the Kloof Gold Mine area showing the prominent Ventersdorp Contact Reef (VCR) and Black Reef (BR) reflectors. (b) Generalized stratigraphic column showing the various seismic facies. Ages from Krapež (1985), Myers et al. (1989), Armstrong et al. (1991), Kositcin and Krapež (2004) and Dankert and Hein (2010).*

1.7.2 Archaean basement (Kaapvaal Craton)

The Archaean basement formed between 3.7 and 2.6 Ga and is the most ancient remnant of continental crust (Nguuri *et al*., 2001). Accretion and stabilisation of the Kaapaal Craton occurred between 3.7 and 2.5 Ga (Robb *et al.,* 2006). The basement comprises tonalitic gneisses (3.6 – 3.2 Ga) and greenstone belts, intruded by various granitic bodies (3.3 – 3.0 Ga) (Robb *et al*., 2006). Four significant meta-sedimentary and volcanic sequences were deposited on the Craton: firstly, the Dominion Group, followed by the Witwatersrand, Ventersdorp and Transvaal Supergroups (De Wit *et al.,* 1992; Robb *et al*., 2006). Terranes accreted along the flanks of the Craton in the late Archaean and early Proterozoic.

1.7.3 Dominion Group

The volcano-sedimentary strata of the Dominion Group were deposited on the granite-greenstone basement terrane (Jackson, 1992). Fluvial sediments were deposited first, followed by the extrusion of the felsic and the mafic volcanics. The felsic volcanic rocks are welded pyroclastics with interbedded volcaniclastic sediments, while the amygdaloidal lavas (mafic volcanic) were deposited in shallow subaqueous or subaerial conditions (Jackson, 1992). The tectonic setting of the Dominion Group has been interpreted as an incipient foreland basin adjacent to a continental margin arc system (Crow and Condie, 1987; Armstrong *et al*., 1991; Marsh, 2006).

1.7.4 Witwatersrand Supergroup

The geology of the Witwatersrand Supergroup (Figure 1.1) has been documented by many authors, including Beach and Smith (2007), Fletcher (2009), Viljoen (2009) and Dankert and Hein (2010). The basin was formed when the Zimbabwean and Kaapvaal cratons collided between 3.07 and 2.71 Ga (Armstrong

et al., 1991; Robb and Meyer, 1995). The Witwatersrand Supergroup, which overlies the Dominion Group, is subdivided into the (lower) West Rand Group, mostly quartzite and ferruginous shale; and the (upper) Central Rand Group, mostly quartzite with conglomerate bands (McCarthy, 2006; Dankert and Hein, 2010).

1.7.4.1 West Rand Group

The ca. 5 km thick West Rand Group is divided into three subgroups, *viz.* the Hospital Hill, Government and Jeppestown (SACS, 1980). It is mostly composed of quartzite and shale units, which are the metamorphosed products of sand, silt and mud deposited in shoreface and fluvio-deltaic to offshore environments; while the basalt-andesite Crown Formation provides evidence of a period of volcanism (Stanistreet and McCarthy, 1991; Coward *et al.,* 1995; McCarthy, 2006; Dankert and Hein, 2010). The Hospital Hill Subgroup sediments unconformably overlie the Dominion Group volcanic rocks and mark a period of significant transgression in the Witwatersrand Basin. In both the shoreface and foreshore sedimentary environments, the depositional sequence comprises siltstones, orthoquartzites, and iron formations (Robb and Meyer, 1995; McCarthy, 2006). The Government and the Jeppestown subgroup rocks were deposited in a range of depositional settings, and represent the transition from volatile and to steady tectonic settings in the craton (McCarthy, 2006).

1.7.4.2 Central Rand Group

The ca. 2.8 km thick Central Rand Group was deposited between 2.89 and 2.71 Ga (Robb and Meyer, 1995). The stratigraphy of the Central Rand Group is characterized by two palaeo-sedimentary environments, *viz.* braid-plains and alluvial fans. It is divided into the Johannesburg and Turffontein subgroups. The Johannesburg Subgroup is characterised by alternating quartzite and conglomerate units. The subgroup is marked by numerous erosional surfaces associated with periods of placer development and non-deposition. It hosts the major auriferous conglomerate mined at Kloof operations, *viz.* the Elsburg, Libanon, Kimberley, and Kloof reefs. The Turffontein Subgroup hosts the auriferous Middelvlei and Carbon Leader reefs.

1.7.5 Ventersdorp Supergroup

The Ventersdorp Supergroup, largely composed of basalt, lies unconformably above the Witwatersrand Supergroup. The meta-volcanic sequence has been dated approximately between 2.71 and 2.60 Ga (Armstrong *et al*., 1991; van der Westhuizen *et al.,* 1991). The Venterspost Formation, which lies at its base, is largely composed of the erosional products of the Witwatersrand Supergroup, includes the gold-bearing conglomerate beds known as the Ventersdorp Contact Reef (VCR). The Klipriviersberg Group comprises komatiites and flood basalts that erupted over a short period of time and preserved the mineralized VCR. The overlying Pniel and Platberg groups are not found in the study area.

The VCR dips between 20° and 25° to the southeast. It is a prominent seismic reflector within the 3D

reflection seismic data due to the significant contrast in acoustic impedance between the Central Rand quartzites and Klipriviersberg volcanic rocks (Figure 1.3).

1.7.6 Transvaal Supergroup

A thick sequence of clastic and carbonate rocks was deposited in the Transvaal Basin between 2.6 and 2.4 Ga (Frimmel and Gartz, 1997; Eriksson and Altermann, 1998). The Black Reef Formation (BR), at the base of the Transvaal Supergroup, unconformably overlies the Ventersdorp Supergroup rocks. It is an upward-fining conglomerate to sandstone sequence followed by inter-bedded shale and dolomite beds (Els *et al*., 1995; Eriksson and Altermann, 1998). The Black Reef Formation has a maximum thickness of about 30 m. It is a prominent seismic reflector as it is situated between the underlying Ventersdorp basalts and the overlying dolostones of the Chuniespoort Group (Figure 1.3).

The Chuniespoort Group consists of dolomites, ironstones and shales that were deposited in shallow to deep marine settings. The carbonates (Malmani Subgroup, Chuniespoort Group) form the largest karstic aquifer in South Africa and have been dewatered in the mining areas as they posed a flooding risk (Eriksson and Altermann, 1998; Ngcobo, 2006).

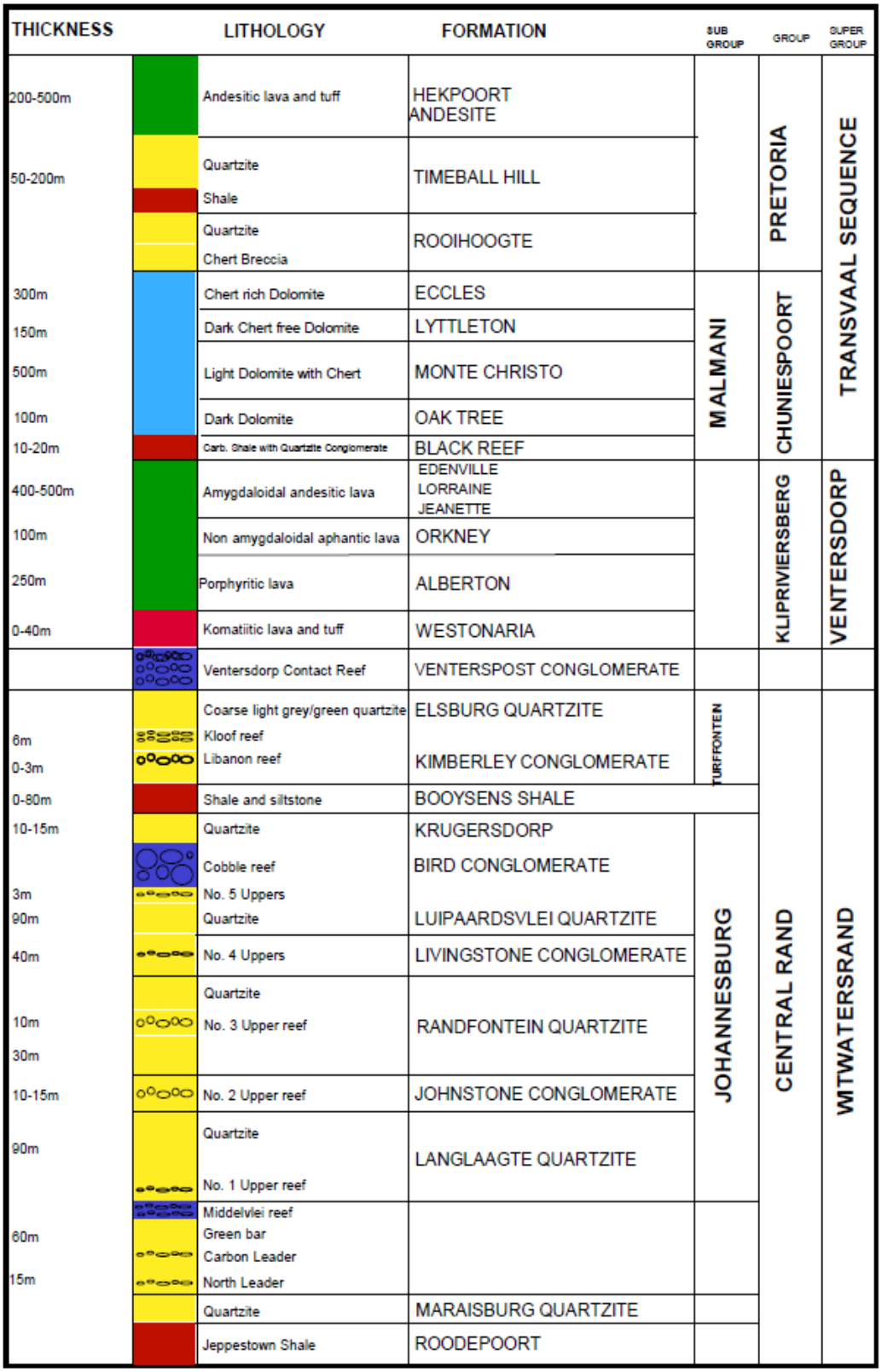

Figure 1.4: *Generalised lithostratigraphic columns of the Kloof Gold Mine Operations that is located within the Witwatersrand Basin (Sibanye-Stillwater Geological Department, 2018).*

1.8 Seismic Interpretation of geological features (faults and dykes)

1.8.1 Faults

Geological structures (e.g., faults) can be mapped on the seismic section. According to Davis and Reynolds (1996), a fault can be seen as a discontinuity within a rock mass volume. The rock masses would move parallel to the discontinuity but relative to one another on either side. The different fault types are identified and distinguished based on their movement between the footwall and the hanging wall of the block of ground (Figure 1.5).

Normal faults, where the footwall rocks move down relative to the hanging wall rocks, occur when the crust is extended. It may result in gaps in the ore body, known as 'loss of ground' (Figure 1.5). Based on various geometries, several types of normal faults, reverse fault and structures (e.g., listric normal fault, grabens and horsts) were observed.

1.8.2 Dykes

Dykes are geological structures formed when igneous rock intrudes an existing rock mass through existing or new fractures (Figure 1.5). The rock mass quality close to dykes is often poor and prone to falls of ground. Dykes sometimes fail when they are exposed to mining-induced stresses, generating large and hazardous seismic events. Two types of dykes are encountered in the Kloof Gold Mine *viz.* syenite and dolerite dykes and are mainly post-Black Reef in age (e.g., cross-cutting both the BR and VCR). Some dykes also pre-date Black Reef (e.g., they are Ventersdorp in age).

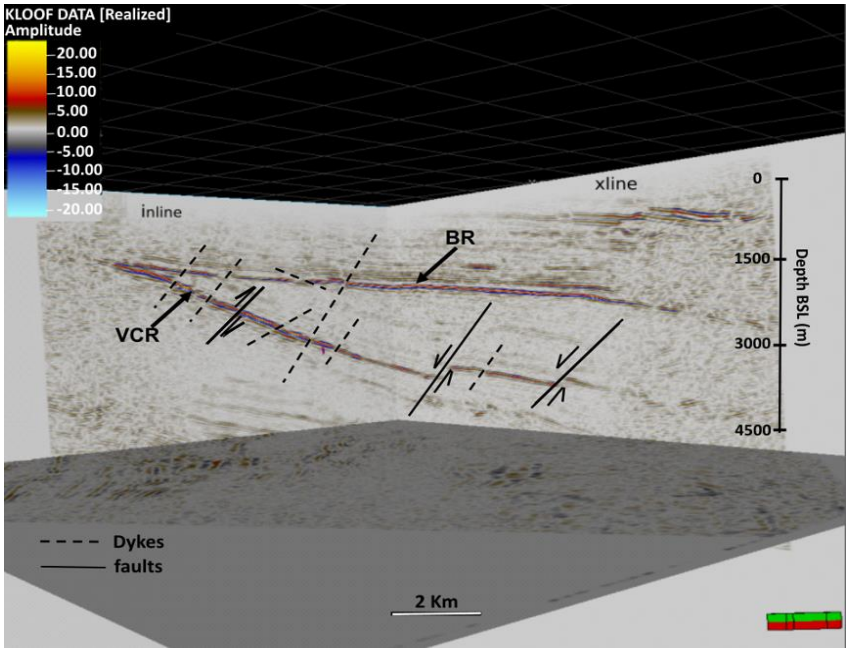

Figure 1.5: *Amplitude display seismic section showing various types of faults across Kloof operation survey areas. These faults crosscut the Black Reef (BR), Ventersdorp Contact Reef (VCR) and the Kloof Reef*

(KR) at the base of the Ventersdorp Supergroup. The highly attenuated seismic amplitudes also show near-vertical features (faults and dykes).

1.8.3 The impact of dykes and faults on mining activities

Geological structures significantly influence the mine infrastructures (e.g., development, shafts barrel, active stopes). The geometry of these geological structures (faults and dyke) can be mapped on the seismic section using the 3D reflections seismic and the underground geological mapping data. Several faults and dykes cross-cut the orebody and influence orebody behaviour. Dykes can also transport methane gas to different underground levels that could cause explosions, and they may also act as water pockets that could cause flooding in mines (Nkosi, 2016). Faults also have numerous impacts on underground mining (Manzi *et al*., 2012a), and these include:

- Physical displacement of the gold-bearing reefs (orebody), which may result in the loss of ground,
- Both the hanging wall stability and rigidity can be compromised resulting in extensive falls of ground,
- They may act as methane gas and water conduits to the mining levels.

Failure to recognize these geological features poses a risk to the mine infrastructure and safety. The data set from the underground geological mapping allowed the definition of minor dykes and faults below specific seismic resolution (Manzi, 2013). According to Manzi *et al*. (2012a), integration of the underground geological mapping data and the 3D reflections seismic allowed (1) assessment of 3D reflection seismic under-sampled structures; (2) the definition of possible zones of difficult mining ground conditions and faults geometry, especially around the seismically imaged faults and dykes (3) better prediction of spacing and number of faults that off-set the Venterspost Contact Reef (VCR) band in the minable section.

1.9 Seismic Monitoring

Seismic networks play a significant role in managing safety in deep mining operations worldwide. In South Africa, the seismic systems are operated in the deep gold and platinum mines. Due to seismicity and rockburst, ground motions are monitored continuously (including non-working days)

The section describes the components of a typical IMS seismic system being used in South African mines. Apart from various sensors that fulfil different purposes, there are at least three fundamentally different ways to record seismic data from a spatially limited rock mass volume for a given period. These are:

1. Stand-alone units that can record and store data underground until manually retrieved,
2. Store-and-forward systems that sample the recorded signal declare trigger and store until a central site requests the data for further processing, and
3. A sensor delivers an uninterrupted stream of signals to the central site where data are sampled, triggers are declared, and non-trigger data discarded.

The Institute of Mine Seismology seismic networks installed in the mines are divided into three major parts: sensors, digital acquisition, and data communication (hardware and software). These components include sensors (geophone, accelerometers, etc.), cabling (fibre, copper, etc.), data acquisition units (e.g., GS, GS+, NetSP, and NetADC), time-based synchronization (GPS timing), and the central computers (server and the client machines). Various forms of communication systems link these components.

1.9.1 Layout of the network

The seismic network for Kloof operations comprises 40 tri-axial sensors arranged in an array to monitor all operating shafts. Figure 1.6 and Figure 1.7 gives a plan and section views of the IMS system installed at Kloof mine. The array of tri-axial sensors is typical for a South African gold mine, which is planar due to the sub-horizontal, narrow, tabular orebodies and footwall access development. The result is that the location accuracy in the plan is generally good, but the elevation is not well constrained. The tri-axial sensors comprise three SM6B 4.5 Hz geophones oriented along the co-ordinate axes of the mine survey system. This enables three-dimensional calculations of energy and moment. The guidelines (Jager and Ryder, 1999; Chapter 9) suggest that the "sensors should be able to determine a maximum frequency of at least five times the corner frequency of the smallest seismic event to be recorded". The SM6B geophones are not rated for high frequencies. They record very high frequencies but may also record spurious responses, which influence the calculation of energy and moment.

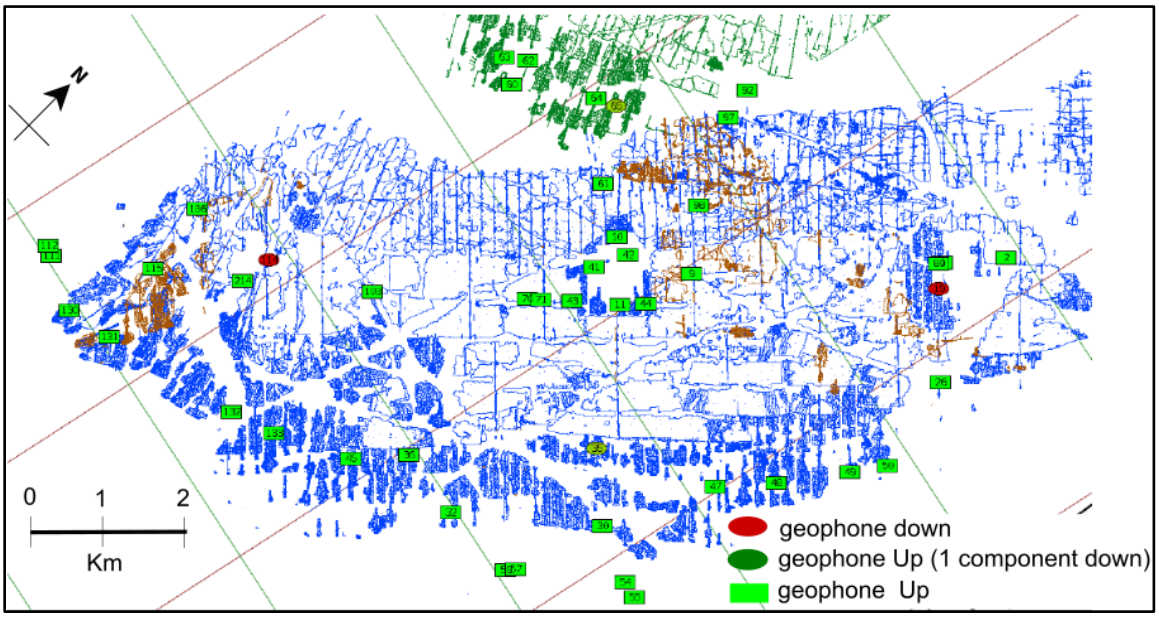

Figure 1.6: *Positions of installed geophones in the Kloof Gold Mine (01/01/2017 – 31/12/2018). Green: Operating geophones, Red oval: Geophones that are not functioning due to different reasons (e.g. power cut).*

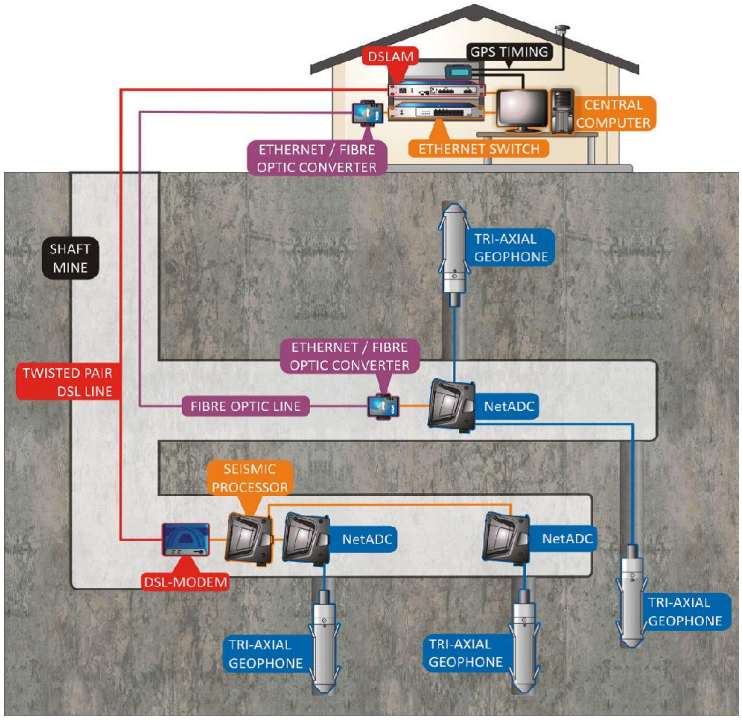

Figure 1.7: *Typical IMS seismic system installed in a hard rock mine (IMS, 2015).*

A view of a well-located seismic event within the KEA seismic volume cube is shown in Figure 1.8.

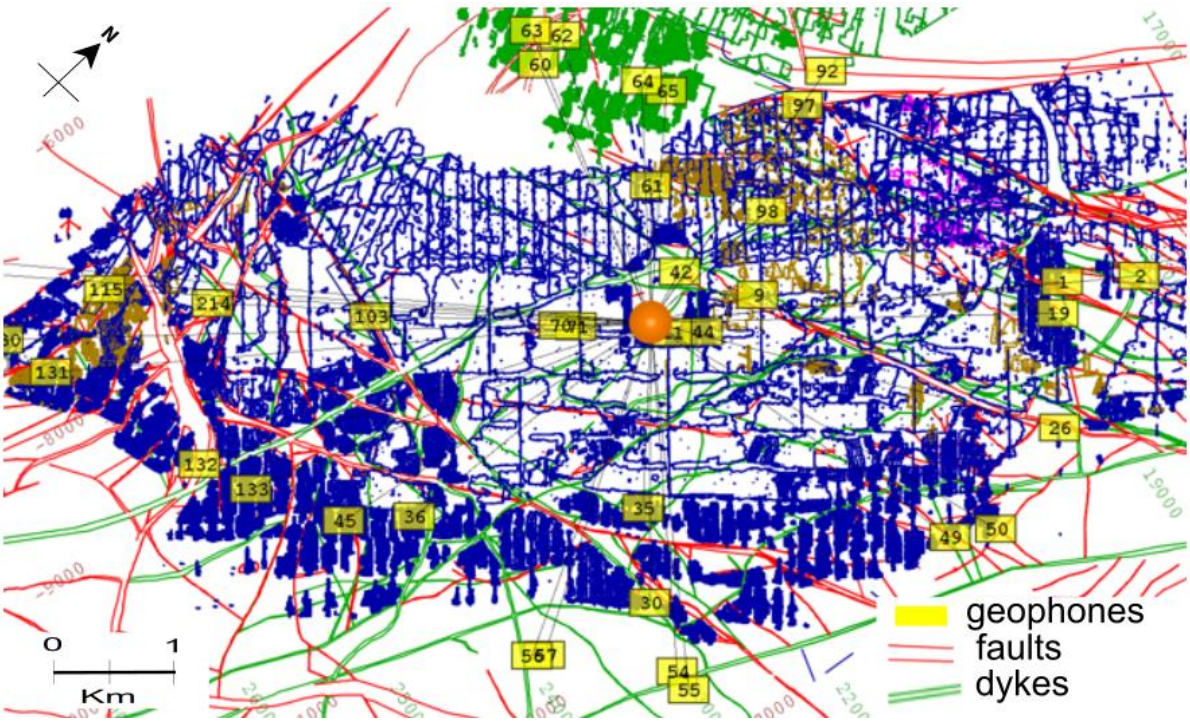

Figure 1.8: *Well-located seismic event within the KEA seismic volume in the mine plan.*

1.9.1.1 Type of the Sensors

These are the electronic devices used in measuring ground motion and converting them into a quantifiable electronic signal. Classifications of these devices are according to the type of ground motion they measure, ground acceleration (accelerometer), or ground velocity (geophones) (Figure 1.9 (a) and (b)). The sensors are usually installed in 10 m deep holes of diameter 76 mm. Electronic signals from these sensors have less distortion and is less noisy compared to the surface-mounted geophones.

Geophones and accelerometers are generally employed as seismic sensors in the seismic network. Ideally, seismic sensors should surround the volume of the minable ore body. If this is impossible, it becomes vital to have an array of sensors spread geometrically in 3D within the mine. For the deep mining applications, the 4.5 Hz geophones are usually used, with a frequency bandwidth of 3 Hz minimum to 2 kHz maximum. The sensor must be installed in a borehole to within five degrees of its pre-set orientation concerning the vertical or horizontal (Jager and Ryder, 1999). The knowledge of the known orientation provides vital information about the location and the known moment tensor calculations. “For a small array, four triaxial sensors are typically adequate to get consistent and stable seismic source parameters” (Hudyma and Brummer, 2007).

A dynamic range (DR) and frequency range can generally characterize the performance of sensor. It is defined as the ratio of the amplitudes of the maximum measurable signal. The maximum measurable (A_{max}) and the noise level (A_{noise}), within a sensor are represented in Equation (1.1).

$$DR = 20 \log (A_{max}/A_{noise}) \quad [1.1]$$

The IMS seismic system dynamic range is 132 dB, larger than the dynamic range of any of the sensors used. The sensors, therefore, control the dynamic range of the system (Appendix B). The dynamic range is calculated per sensor. This is because the seismic network comprises several types of sensors, some sensitive to weak ground motion and others to strong ground motion.

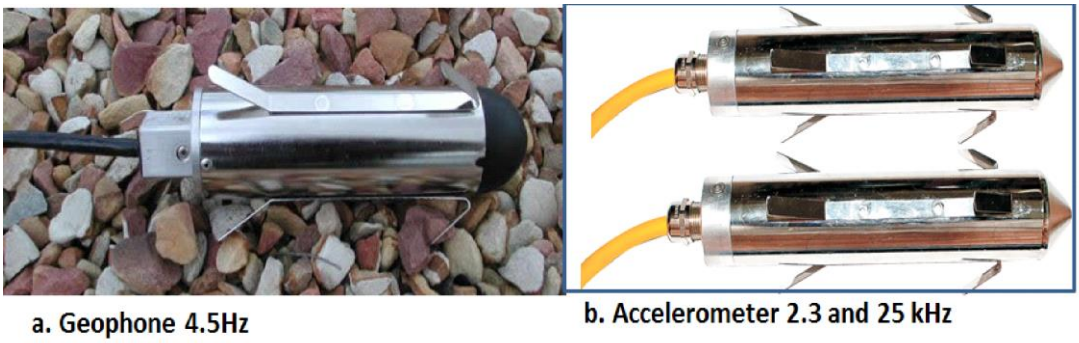

Figure 1 9: *IMS sensors: (a). Geophone and (b). Accelerometer .*

The frequency range is determined through the Fast Fourier Transform of the instrument-corrected time-domain signal. Measurements of corner frequency and spectral plateau are used by applying Brune's source model to determine seismic source characteristics. Radiated seismic energy and seismic moment are calculated directly from the spectra, and the accuracy of this information depends on how accurately the model represents the recorded information. When applying this model, specific requirements are imposed for recording ground motions that will enable the radiated seismic energy to be estimated accurately and consistently.

For a seismic moment, the sensor must record low frequencies such that the spectrum must have at least five spectral points below the corner frequency and at least half the corner frequency (f_0) of the recorded large seismic event. Jager and Ryder (1999) recommend that frequencies of at least five times the corner frequency of the smallest seismic event must be recorded to represent the full spectrum accurately. These criteria were summarised by equation 1.2:

$$\frac{f_0(L)}{2} < f < 5f_0(S) \qquad [1.2]$$

where $f_0(L)$ and $f_0(S)$ are the corner frequencies of the largest and smallest events to be recorded.

The moment *vs* corner frequency graph can provide an estimate of the expected corner frequencies for given magnitudes for a range of static stress drops (Figure 1.10). The Kloof seismic data was processed using an unbounded upper cutoff frequency (~2520 Hz) for spectral fitting and an automatic Q value. Few seismic events exhibited a corner frequency greater than 1000 Hz. The lower frequency is associated with the de-attenuation model, particularly the quality factor (Q value) and appeared to be closer to 10 Hz. The auto values are being used by the software provider (IMS) for both the Quality factor and frequency**.** The software used is applying the low-frequency correction, and all events are included in spectra calculation. This means that the corner frequencies for your large events are being corrected, so they are not being underestimated (Figure 1.11).

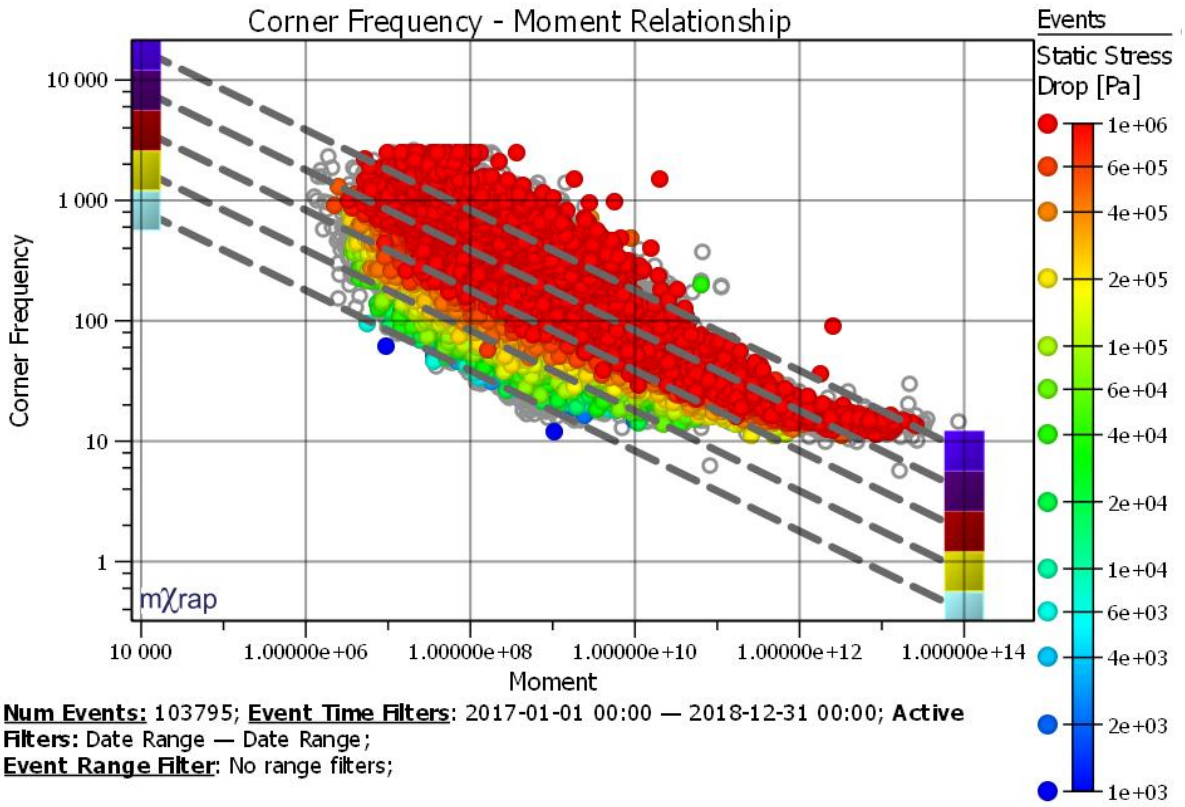

Figure 1.10: *Seismic moment versus the corner frequency for the different range of stress drops.*

1.9.1.2 Sample rate

The sampling rate is the number of data points acquired per second. The Kloof seismic system samples at 6 kHz, meaning there are 6000 samples in a second converted from an analogue to a digital signal to form a seismogram. The data analyzed in this study were collected during Jan 2017- Dec 2018, particularly in 57.6 km^2 area covered by the 3D reflection seismic survey. The following selection criteria were used: (i) at least 20 sites (geophones) triggered around the seismic event, (ii) seismic events with location falling within the central part of the in-mine seismic network and the 3D reflection seismic volume, and (iii) a final seismic event selection was made after sorting the seismic events by recording stations with verified sensor orientations (misfit angle <20^0) in descending order.

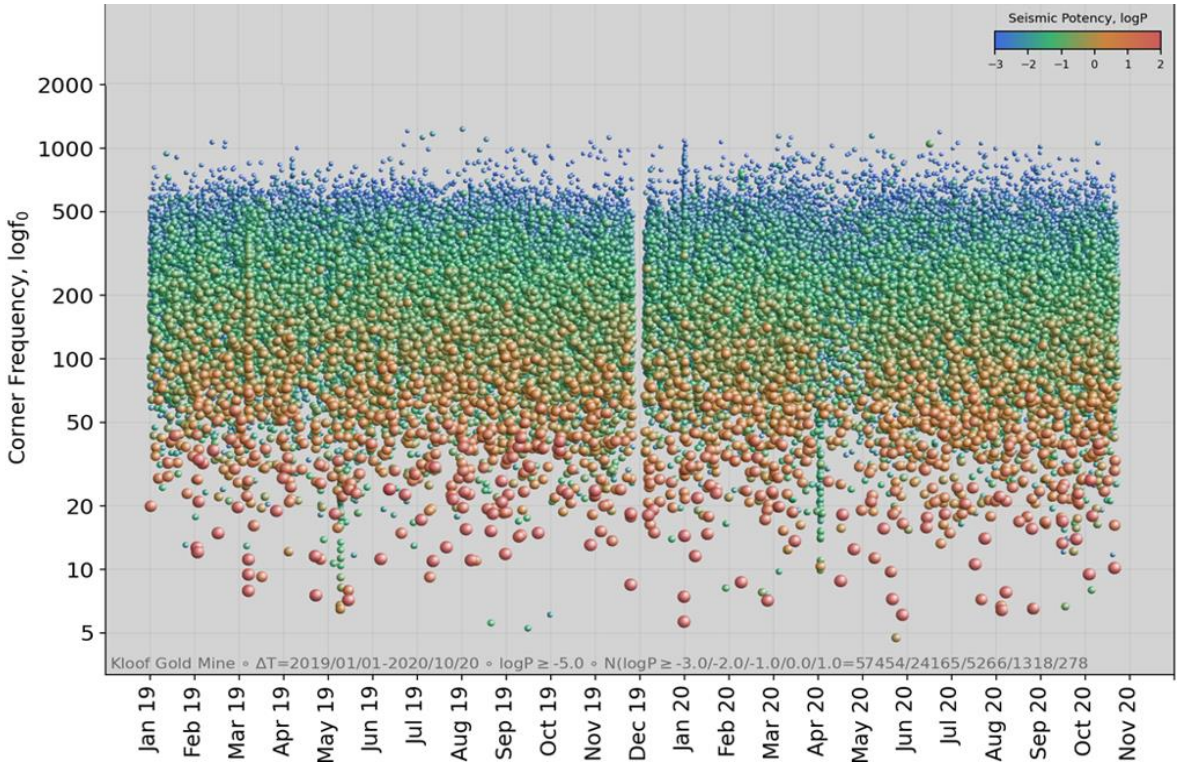

Figure 1.11: *Different corner frequencies of seismic events in the KLF database (No evident cut-off corner frequency at 10Hz).*

1.9.1.3 Data acquisition system

The in-mine seismic monitoring systems use the seismic data recorded and processed from numerous underground sites and dispersed across - different mining layouts. A seismic system consists of both hardware and a data acquisition system. These include seismic sensors, digital acquisition units for acquisition and transmission of data, software for seismogram processing and other analyses, for example, the quantification of the seismic response to mining and the identification of potential instabilities.

“Rockburst-prone mines have seismic networks useful for locating events, initiating rescue efforts, evaluating mining methods, and assessing seismic hazard” (Durrheim *et al*., 2006). The seismic system is designed to monitor the mine continuously and records seismic events as they happen underground. Seismic waves are recorded at each seismic station underground and sent via the fibre to the synapse server on the surface. When the power trips during strong ground vibration, the data is recorded and stored in the Geophysical Seismometer (GS) unit, powered by a backup battery in the GS box. The functionality allows the data to be retrieved when the server or power is restored. The seismic triggers are packaged into seismic events and sent to the Synapse Server. The IMS provided both the hardware and software for the seismic system. Similar IMS systems are installed on all seismically active gold mines in South Africa.

1.9.2 Hardware components of the seismic network and the data transmission.

Mining activities disturb the rock mass stress condition, which may lead to an increase or decrease in stress level. Seismicity occurs when the rock mass responds to both deformation and failure. The energy that is released radiates as a seismic wave (Figure 1.12a). Since most rock fracturing around mining excavations is shear related, the S-wave forms the dominant phases of the resulting radiation pattern. The magnitude of the fracturing and proximity to the source determines the amplitude and signal-to-noise ratio triggers for the individual underground site. As long as the triggering and association processes are working correctly, a seismic event will generally produce a well grouped or associated recording of the brittle fracture process as a seismogram. This dynamic waveform contains a record of the individual Primary and Secondary waves radiating out from the source volume that subsequently trigger the different geophone sites on the network (Figure 1.12 b).

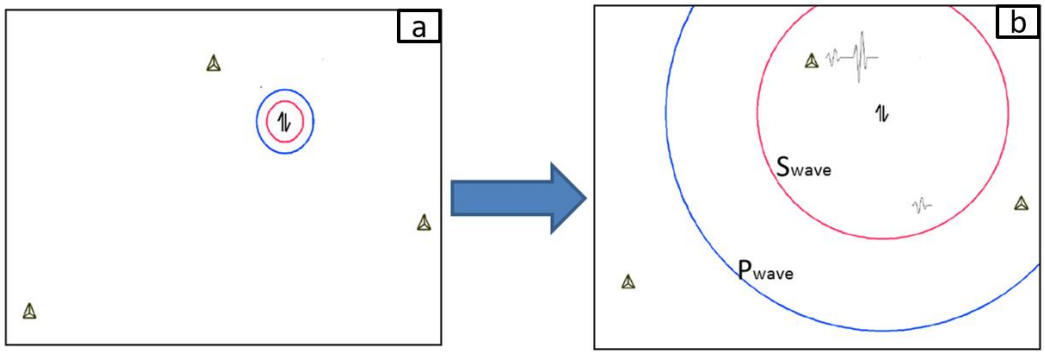

Figure 1.12: *(a) Schematic presentation of the spherically symmetric compressional wavefront (seismic wave) radiating from the source and (b) P-and S-wave triggering different sensors.*

The seismograms of every seismic event that triggers four or more stations are transmitted from underground through the local area network to the seismic server on the surface. These seismograms are manually processed by operators who pick the P and S arrivals on every triggered geophone. The hypocentre and other source parameters are automatically calculated, e.g., the corner frequency, radiated, seismic energy magnitude, static and dynamic stress drop, and the seismic moment. The calculated parameters and the hypocentre are then saved in the database. Quality control is routinely applied for certain seismic events.

1.9.2.1 Communication

A combined surface and underground monitoring system were deployed at Kloof Gold Mine. The data is transmitted from the sensor underground to the processing machine on the surface. This is done via the horizontal cabling in the cross-cuts, tunnels between sensors and shaft, and the vertical cabling in the shaft up to the central computer room.

In the case of a seismic event occurring, the sensor outputs an analogue signal, which is transformed into a digital signal using the analogue-to-digital-converter (ADC). The recording system then records it. When the output that is recorded from the sensor, it is sent to the Analog Signal Preparation (ASP), where a correction is made for the impedance of the recording system. The recorded signal is filtered and then digitized or either directly sent to an ADC. Some recorders have a high pass filter, which removes potential DC-offsets and long term drift from the signal (Asch, 2009). A simple low-pass filter is used for anti-aliasing purposes. The signal is converted from the analogue to digital time series in the NetADC and is saved in the arbitrary network called the “Cloud” (Figure 1.13). The word “Cloud” indicates that the system does not dictate over which infrastructure the data travels.

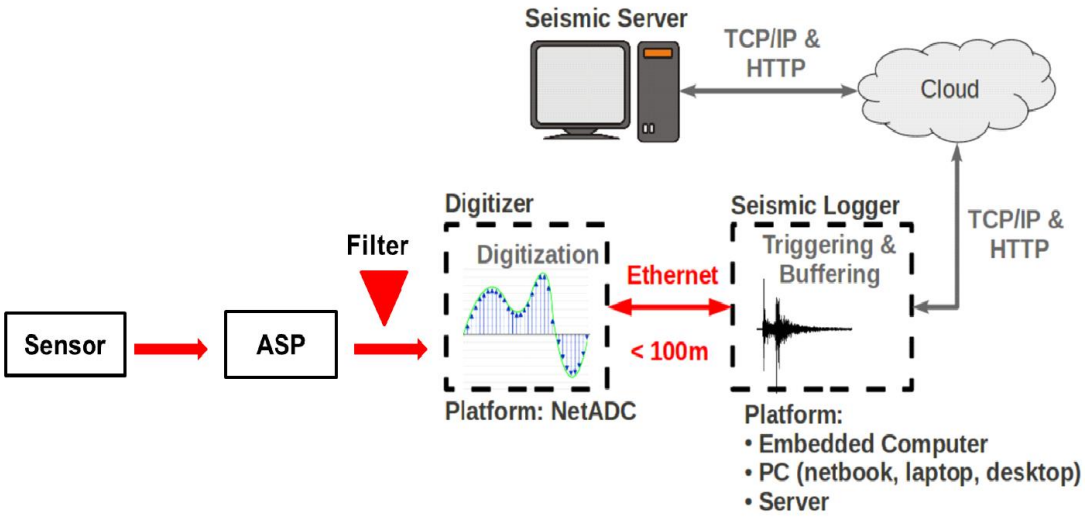

Figure 1.13: *A simple sketch of the in-mine seismic recording system*.

The TCP/IP and HTTP are communications protocols widely used today (most internet traffic uses these protocols). The significance of this in a seismic system is that communications and data transfer can happen over any industry-standard network in most mines today. No unique infrastructure or proprietary hardware is required for the data transfer. TCP/IP and HTTP, which are end-to-end protocols, enable the data to go through any standard network equipment (the "Cloud") without affecting the system's operation.

1.9.2.2 Generations of data acquisition units (Seismometers)

A *seismometer* is a sensor that enables the transformation of transient ground motion into an electrical voltage (signal) as a function of time. The electronics within the seismometer exhibits computational abilities and data storage, but it also shapes and amplifies the signal. The IMS system has evolved with time owing to advances in data storage, processing power, communication, and digital processing technology (Figure 1.13). The red arrow in Figure 1.14 indicates the increase in memory with time. The blue arrow indicates how power consumption has reduced from the intelligent seismometer to the Network Seismological

Processor (NetSp) technology. The speed was as well directly proportional to the memory of the instrument. Table 1.1 highlights the specs of different generation seismometers:

- Integrated Seismometer (IS) -1989 to 1992

  It is the oldest technology seismology box that was used initially and contained only four buffers to store waveforms. This seismometer could only interface with only one tri-axial sensor. The seismometers tended to hang occasionally. The boxes were installed very close to the sensor to keep the analogue transmission distance as small as possible.
- Processing Seismometer (PS) -1992 to 1994/5

  These are the second generation of seismometers and were introduced with more advanced hardware and 250 buffers to store waveforms. The design allowed the box to carry out automatic seismic events and record a large number of microseismic events. The PSs effectively operates as highly efficient ISs with additional capacity storage.
- Multi-Seismometer (MS) - 1994/5 to 2000

  Improvements in technology led to the manufacturing of the Multi-Seismometer, which could be connected 150 m away from the sensor. The recorded analogue signal can be influenced by noise when it is transmitted to the box. The analogue signal amplitude attenuates with an increase in distance. The seismometer cables are supposed to be connected 1 m from the power cable to reduce the signal interference and distortions.
- Quake Seismometer (QS) - 2000 to 2007

  These seismometers were upgraded to the multi-seismometer with advanced features and were made small and lighter than the MS box. The seismometer can connect the sensor to 250m away.
- Geophysical Seismometer (GS and GS+) 2007 to 2012

  It is a technology-enabled sensor with an increased sampling rate and storage memory. The power consumption is down to 3 W. The integrated uninterrupted power supplier powered the GS for 6 hours. In this way, seismograms of the largest events are preserved should the power and communication be disrupted.
- Network Seismological Processor (NetSP) and Network Analogue-to-Digital Converter (NetADC) – 2012 to 2018

  The netADC digitizes the analogue signals produced by the seismic sensors and transmits the digitized data to a netSP. The netSP runs the seismological triggering algorithms on the data from the netADC, buffering any triggered data identified by the algorithm. The triggered data is then prioritized and queued for sending to the Synapse Seismic Server for processing.

The seismic system currently installed at Kloof Gold Mine has a data acquisition network that consists of the low noise analogue-to-digital convertor (netADC) of a 24-bit. The network seismological processor (netSP) runs the data acquisition software capturing the data from the netADC, triggering, pre-trigger filtering, buffering, and transferring it to the seismic server.

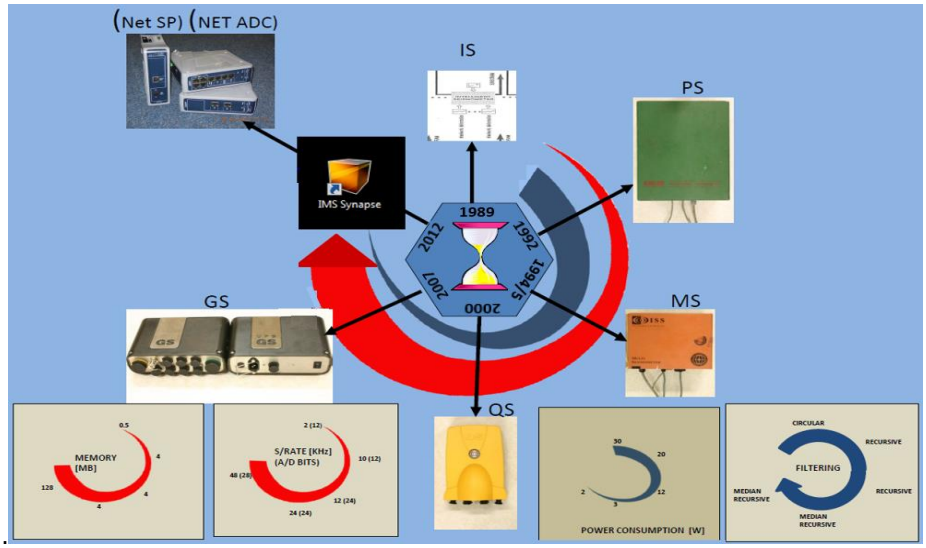

Figure 1.14: *Changes in a different generation of seismometer technology –underground processors on IMS (ISSI) system, 1989 to 2018.*

Table1.1: IMS seismometer and processor specifications (IMS, 2015):

Device	Year	Platform	A2D	Channels	Memory (Volatile/ non-Volatile)	Sampling Rate	Communications
IS (Integrated Seismometer)	1989	AT		3		198Hz	150/1200
PS (Processing Seismometer)	1992	T805	Gain Ranging	3		10KHz	FSK
MS (Multi- Seismometer)	1994/5	T425		3/6/9		2K, 10K,	RS232 FSK
QS (Quake Seismometer)	2000	ARM	Gain Ranging 24bit	6	4MB 1MB		RS232 FSK RS485
GS (Geophysical Seismometer)	2007	ARM (Embedded Linux)	24bit	6	128MB/16MB	48kHz	RS232 RS485 LAN
NetSP	2012	ARM	24bit	4 x 4/8	128MB/4MB	192kHz	LAN
NetSP+	2012	X86	24bit	4 x 4/8	256MB/ 32GB	192kHz	LAN

1.9.2.3 Time Synchronisation (Global Position System-GPS)

Each data acquisition system underground records a common timing signal derived from GPS satellites; the system receives this timing signal via fibre/copper cables. GPS ensures common time with the central computer and thus the seismic system underground.

1.9.3 Software

The IMS software products (Synapse, Trace and Vantage) used in the gold and platinum mines serves the purposes of recording, processing, visualisation and analysing the mine microseismic data collected by the IMS seismic system.

(i) ***Synapse*** is the new generation seismic server software used to control the seismic network and record the seismic data. The software is written in Java, and according to IMS (2015), its functions include:

- Coordination of the seismic network, hardware
- Transmission of the seismic data,
- Association of triggers into seismic events,
- Auto-processing of a seismic event,
- Configuration of seismic network and devices,
- Control of seismic network devices and monitoring.

(ii) ***Trace*** is the software that was used for recorded seismograms processing and visualisation. Data processing was done by picking both the P- and S- wave arrivals. This is performed to estimate the seismic source parameters (e.g., magnitude, location, seismic radiated energy, and inelastic co-seismic deformation) as well as focal mechanism solutions (time and frequency domain). Visualisation of the data can be displayed as acceleration, velocity or displacement.

(iii) ***Vantage*** is the software package utilized for seismic data visualization and analysis to understand and explore micro-seismicity.

The HAMERKOP software suites are also used to visualise and analyse the data collected from the IMS seismic system. The software includes Korhaan, which contains the same functionality as the Vantage program from the IMS software suite.

1.9.4 Routine data processing procedure

In real-time network control, the data is collected and auto processed by the algorithm in the Synapse software. This is followed by manual processing with regular quality control, including re-processing of outliers (seismic events locating on the edge of the network) and events showing abnormal seismic parameters (e.g., large magnitudes and high location error seismic events). Quality control includes the random selection of either rejected or accepted large seismic events (inaccurate location due to the P- and

S- picks). Both the mislocated and rejected seismic events would be scrutinised and reprocessed again by looking at the different seismic parameters that could have led to the seismic events being rejected or mislocated (e.g., events that are located at the edge of the network or outside the mine's boundary). A decision would be made whether to keep the seismic event in the database or not.

Only seismograms with a good signal-to-noise ratio of both P- and S-wave arrivals were used to ensure accurate picks of arrival times. The processing procedure included the manual picking of the P-and S-wave arrival times. Three component seismograms were rotated into the P-SV-SH local co-ordinate system to help pick the S-wave accurately. The location of the seismic event was then calculated, and the theoretical arrival time at each location was determined and compared with the initial pick. The picks were checked and refined until the location residual was less than 100 m, or 3% of the average distance between the event and the sites. For each seismic event, three orthogonal components at each seismic station produce complete seismograms (X, Y, and Z). The hypocenters and other source parameters such as seismic energy, seismic moment, and corner frequency are obtained for each seismic event and stored in a database. On average, about 300 seismic events of magnitude ML≥-3 are recorded daily by the mine seismic network.

1.9.5 Sensitivity and location accuracy

The location and distribution of the geophones were modelled for the optimum coverage of seismicity in all mining areas. The local density of geophones determines the variability of the minimum recorded magnitudes of events. Depth resolution optimization of seismic event locations depends on some geophones' positioning at a reasonable distance from the orebody mined as the mine's infrastructure allowed.

The EGRET software program from the HAMERKOP suite was used to calculate the location accuracy and the sensitivity of the seismic network for any geophones configuration (Appendix C, Table C).
The following were assumed in the software when calculating both the location accuracy and sensitivity of the seismic system:

- The average velocity of waves is constant from any source to a given station,
- Velocities can be different for different stations, but their relative variance is the same,
- All stations have the same errors in arrival times,
- Level of sensitivity is the same for all stations, and
- Isotropic relations valid for all events

The location errors and sensitivity in the XYZ plane were contoured on a flat plane at a representative point of the mining. Most of the location errors normally occur in the plane's direction defined by the positions of the geophones. Due to the installation of geophones close to the (reef /orebody) the most significant errors occur in determining seismic event elevations (depths).

1.9.5.1 Seismic system sensitivity

Equation 1.3 and 1.4 represent the sensitivity of the seismic network. System sensitivity can be easily calculated using the empirical relationship between magnitude (or energy (J)), peak particle velocity (PPV) of a seismic event and the hypocentral distance (m) as follows:

$$log_{10}(PPV) = A * Magnitude - B * log_{10}(Distance) + C \quad [1.3]$$

and

$$log_{10}(PPV) = A_1 * log_{10}(Energy) - B_1 * log_{10}(Distance) + C_1 \quad [1.4]$$

A, A_1, B, B_1, C and C_1 represent the constant values.

Values currently used in Kloof Seismic system and the current study as inputs for the constants are:

A = 0.981, *B* = 1.363 and *C* = - 0.83,

A_1 = 0.469, B_1 = 1.363 and C_1 = - 1.99,

Other assumptions include:

(i) The station can be used for location if the amplitude of the waveform exceeds some threshold level,

(ii) Seismic event with some magnitude occurred in a given place.

The plane was selected to coincide with the plane of the reef plane striking 225˚ and dipping 25˚. Contouring on sensitivity was carried out on that plane (Figure 1.15). The seismic system sensitivity is directly relational to the number and proximity of installed and operating geophones. The Kloof Gold operation sensitivity is depicted in Figure 1.15 and Figure 1.16 indicates a minimum sensitivity of magnitude M_L= -1.6 that is achievable towards the centre of the network

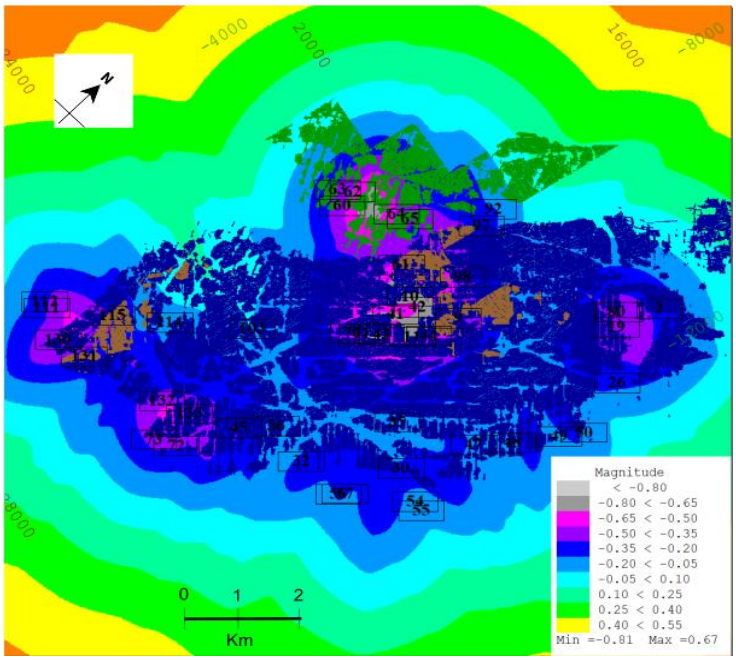

Figure 1.15: *Sensitivity defining the Kloof seismic system shown by contours. It is assumed that all geophones are operating.*

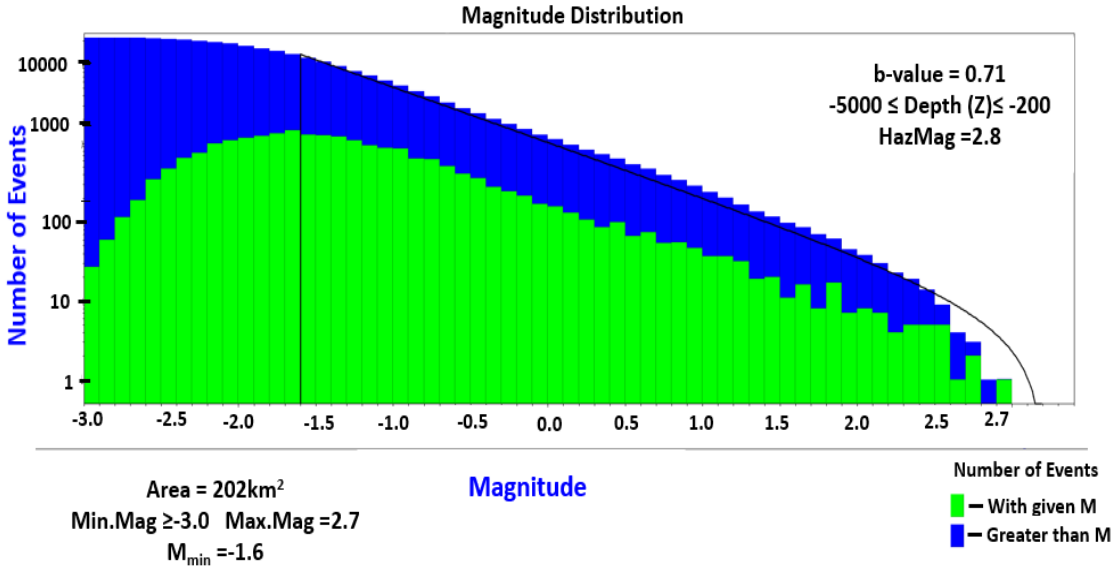

Figure 1.16: *Empirical data and estimations for the Kloof seismic system (01/01/2017 – 31/12/2022).*

1.9.5.2 Location accuracy of the seismic system

Calculation of the accuracy of the seismic network is slightly more complicated. Firstly one has to check whether a specific magnitude is within a certain range of sensitivity. If so, then the covariance matrix can be constructed from the equations for arrival times used for location. The covariance matrix of unknowns (t_0 , x_o, y_o, z_o) corresponds to 4-dimensional confidence ellipsoid, where the matrix's eigenvalues form the

lengths of the principal axes. The covariance matrix C is a 4x4 matrix. The formula gives the covariance matrix in Equation 1.5 (Buland, 1976 and Kijko et. al, 1986):

$$C_a = (A^T\, WA)^{-1} \qquad [1.5]$$

where:

A - the matrix of partial derivatives of arrival times against parameters (t_o, x_o, y_o, z_o, v) (**t_0** - origin time, x_o, y_o, z_o, hypocentre, v - velocities from source to stations)

W - the matrix of parameters' variances.

The matrix **A** has the form of

$$\begin{matrix} 1 & \frac{\partial(T_1+\Delta T_1)}{\partial x_o} & \frac{\partial(T_1+\Delta T_1)}{\partial y_o} & \frac{\partial(T_1+\Delta T_1)}{\partial z_o} \\ \vdots & \vdots & \vdots & \vdots \\ 1 & \frac{\partial(T_n+\Delta T_n)}{\partial x_o} & \frac{\partial(T_n+\Delta T_n)}{\partial y_o} & \frac{\partial(T_n+\Delta T_n)}{\partial z_o} \end{matrix}$$

where:

T - Arrival time;

$$\Delta T = 0.5 * \sigma_v^2\, Tr(\tfrac{\partial^2 T}{\partial v^2})$$

The matrix **W** is diagonal, and its elements are represented in Equation 1.6:

$$W_i = \sigma_t^2 + (\sigma_v * \tfrac{\partial T_i}{\partial v})^2 \qquad [1.6]$$

where:

σ_t^2 a variance of arrival time;

σ_v^2 variance of velocity

The errors of location can be found easily from the covariance matrix C_a where C_{11} is one element row 1 column 1 and $C_{12,12}$ is a two dimensional matrix with rows and columns 1 and 2:

Error X = $(C_{11})^{1/2}$ Error Y = $(C_{22})^{1/2}$ Error Z = $(C_{33})^{1/2}$

Error XY = $(\det(C_{12,12}))^{1/4}$ Error XYZ = $(\det(C_{123,123}))^{1/6}$

The seismic systems criterion is set to four to five minimum stations for recording a seismic event. Seismic network sensitivity is indicated in terms of the minimum magnitude seismic event that the geophone array can record.

The current modelled system location accuracy on XYZ is represented in Figure 1.17. At best, the location could go down to 10 m depending on the geometry of the spread sensors. Figure 1.17 indicates the location errors varying from 10 m at the centre of the network where the sensors are dense to 200 m on the network's edge. The accuracy in depth (~90 m) has always been a challenge unless additional sensors are installed on the upper level of the reef/orebody if accessible.

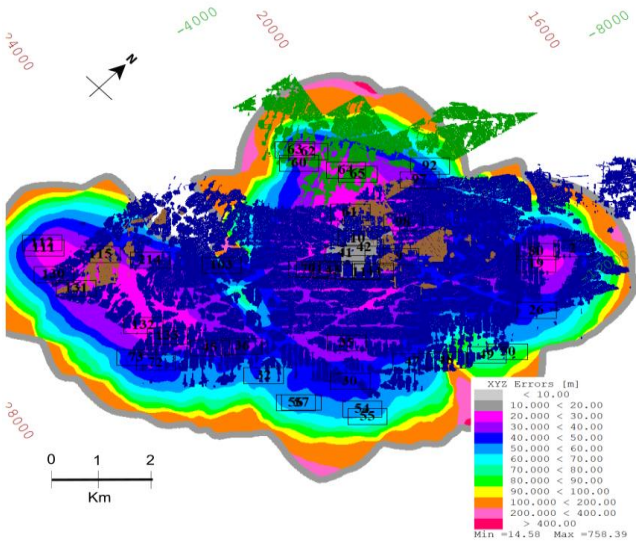

Figure 1.17: *Location accuracy on XYZ for the period of the data, shown by contours of location errors to adequately cover the Kloof mining working areas. It is assumed that all geophones are operating.*

Durrheim *et al*. (2006) identified several seismic network shortcomings in some mines, and this may include:

- High-frequency (4.5Hz) geophones are used, which underestimate the lower frequency ground motion of large magnitude events.
- Poor quality of seismograms due to negligence of seismic system maintenance
- No consistency in the historical data due to failure in calculating source parameters when new software is introduced, and
- When mines are closed or personnel change, it is difficult to assess hazard and trends (e.g., loss of data).

1.9.6 Problems with the seismic system

The operational efficiencies and computation of the event source characteristics are being negatively impacted by the decaying geophones to such an extent that the poor quality of the sites. Due to power outages, some underground geophones go offline, while others have noisy or defective signals that obscure the genuine nature of the recorded underground ground motions. The coverage of geophone sites has often lagged behind the development of mining faces, which has caused errors in the estimates of the position and source parameters. Some problems include:

- Outlier seismic events, false seismic events and blasts.
- Some seismic events might occur at the edge of the network.
- Under-recording of seismic events' magnitude.
- Change in the seismic monitoring hardware and software systems (inconsistency of database) with the database showing an abrupt change in source parameters.

CHAPTER 2 - MINING, ROCK MASS FAILURE AND SEISMIC EMISSION SOURCES WITHIN THE WITWATERSRAND BASIN

2.1 Introduction

The gold mines of the Witwatersrand Basin are the deepest globally, with depths approaching 4 km. As the depth increases, so do the stress levels, with concomitant increases in stress fracturing and mining-induced seismicity (Jager and Ryder, 1999). Rock mass failure processes in mines are complex and result into complex signature of seismicity. Understanding the factors that affect rock behaviour (rock stress, rock mass strength, failure processes, etc.) is vital to design stable and safe excavations. This chapter gives an overview of selected failure criteria and factors controlling the rock mass mechanical behaviour.

2.1.1 Rock stress and failure

The rock mass properties and mechanical behaviour around an excavation can be assessed by field observations, laboratory testing or the use of numerical modelling. A rock failure criterion is a description of the stress state at which the ultimate rock strength is reached, given the stress conditions (Figure 2.1 (a)). They are expressed in terms of the major (σ_1), intermediate (σ_2), and minor (σ_3) principal stresses. Numerous rock failure criteria are described in the rock engineering literature (e.g. Fairhurst, 1964; Franklin, 1971; Jaeger and Cook, 1979; Hoek and Brown, 1980; Johnston, 1985; Yoshida *et al.*, 1990). In this research, only two failure criteria are used, *viz.* the Hoek-Brown (non-linear), and the Mohr-Coulomb (linear) failure criteria. These criteria are preferred due to the large amount of experimental data that are available and the simplicity in their formulation (Melkoumian *et al*., 2009).

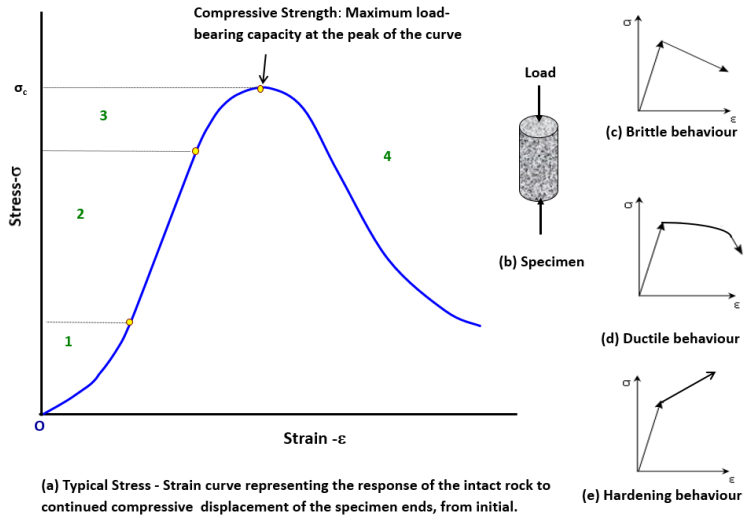

Figure 2.1: *(a) The stress-strain curve resulting from uniaxial compression, (b) Specimen under Uniaxial Compressive Load (c) Brittle behaviour, (d) Ductile behaviour and (e) Hardening behaviour (Yilmaz, 2016).*

Figure 2.1 shows a rock specimen's stress (load) - strain (displacement) behaviour during uniaxial compressive strength (UCS) testing in the laboratory. A specimen subjected to applied stress will experience deformation to the point where the yielding stress is reached. The loading is initially non-linear as voids are slowly closed; most of the loading increases occur in the linear elastic stage (Stage 2 in Figure 2.1a). Deformation becomes non-linear as damage accumulates until the maximum strength is reached and failure occurs. The post-failure behaviour (Stage 4) depends on many factors, but especially on the confinement of the specimen.

Failure can be categorized into either brittle or ductile behaviour in solid mechanics, depending on the failure characteristics (Figure 2.1). Brittle failure occurs when the rock loses all its resistance to stress when the maximum (peak) stress has been reached (Figure 2.1 (c)). In a ductile failure, the loss of strength is gradual (Figure 2.1 (d)). When the rock fails, the stress will decrease with an increase in strain. The residual strength (stage 4) is the post-break maximum stress level (stage 4) that the rock mass can withstand after considerable deformation has occurred (Brady and Brown, 1993).

2.2 Empirical Rock Failure Criteria for intact rock

Empirical rock failure criteria methods are the common ways to determine the rock mass strength (Table 2.1). These stress-dependent criteria usually include one of the various parameters describing the properties of the rock mass.

Table 2.1: Intact rock failure criteria (Edelbro, 2004)

Failure equations:	Development / Comments	Author, criterion first published
$(\sigma_1 - \sigma_3)^2 = a + b(\sigma_1 - \sigma_3)$	An empirical generalisation of Griffith theory of intact rock	Fairhurst (1964)
$\sigma_1 = \sigma_c + \sigma_3 + F\sigma_3^f$	Empirical test data fitting for intact rock	Hobbs (1964)
$\sigma_1 = \sigma_c + a\sigma_3^b$	Studied using practical cases of rock structures in coal and coal measure strata	Murrel (1963)
$\frac{\tau_m - \tau_0}{\sigma_c} = D\left\|\frac{\sigma_m}{\sigma_c}\right\|^C$	Empirical curve fitting for intact rock	Hoek (1968)
$\sigma_1 = \sigma_c + a\sigma_3$	Triaxial test of soft rocks	Bodonyi (1970)
$\sigma_1 = \sigma_3 + \sigma_c^{1-B}(\sigma_1 + \sigma_3)^B$	Empirical curve fitting for 500 rock specimens	Franklin (1971)
$\|\tau\| = S_0 + \sigma tan\emptyset$	investigations of retaining walls by Coulomb	Heyman (1972)
$\sigma_1 = \sigma_3 + (m\sigma_c\sigma_3 + s\sigma_c^2)^{1/2}$	Application of Griffith theory and empirical curve fitting. Both for intact and heavily jointed rock masses	Hoek and Brown (1980)
$\frac{\sigma_1}{\sigma_c} = a + b(\frac{\sigma_3}{\sigma_c})^{\alpha}$	Empirical curve fitting for 700 rock specimens. Both for intact and heavily jointed rock masses	Bieniawski (1974), modified by Yudhbir *et al*. (1983)
$\sigma_1 = \sigma_1 + a\sigma_3(\frac{\sigma_c}{\sigma_3})^b$	Applied to 80 rock samples	Ramamurthy *et al*. (1985)
$\sigma'_{1n} = (\frac{M}{B}\sigma'_{3n} + 1)^B$	Empirical curve fitting for both soil and rock specimens	Johnston (1985)
$\sigma_1 = \sigma_c(1 + \frac{\sigma_3}{\sigma_c})^b$	Both for intact and heavily jointed rock masses	Balmer (1952), Sheorey *et al*., (1989)
$\sigma_1 = \sigma_3 + A\sigma_c(\frac{\sigma_3}{\sigma_c} - S)^{1/B}$	*A, B* and *S* are strength parameters	Yoshida (1990)

Where: $\tau_m = \frac{(\sigma_1 - \sigma_3)}{2}$ and $\sigma_m = \frac{(\sigma_1 - \sigma_3)}{2}$

$\tau = shear\ stress,$ $\sigma_1 = Major\ principal\ stress$

$\sigma = Normal\ stress,$ $\sigma_3 = Minor\ principal\ stress$

$\sigma_c = Uniaxial\ compressive\ strength$ $\sigma'_{1n} = Major\ normalized\ effective\ principal\ stress,$

$\sigma_t = Uniaxial\ tensile\ strength$ $\sigma'_{3n} = Minor\ normalized\ effective\ principal\ stress,$

$S_0 = Apparent\ cohesion$ $\emptyset = the\ angle\ of\ internal\ friction$

$and\ a, b, F, f, C, D, B, M\ and\ \alpha\ are\ constants.$

2.2.1 Mohr-Coulomb

The Mohr-Coulomb failure criterion is a function of the apparent cohesion (S_0) and the angle of internal friction (∅) (Equation 2.1). It is the most used criterion. It can be written as a function of both the (σ_1) and (σ_3) or normal stress σ and the shear stress τ on the plane of failure (Jaeger and Cook, 1979). The criterion assumes that rock failure occurs along a plane of weakness without dilation, due to the shear stress acting along that plane. The failure criterion is represented by equation (2.1):

$$|\tau| = S_0 + \sigma tan\emptyset \qquad [2.1]$$

where $|\tau|$ is the shear stress along the shear plane at failure, S_0 is apparent cohesion or shear strength, σ is the normal stress acting on the shear plane, ∅ is the shear plane's angle of internal friction and co-efficient of internal friction $\mu = tan\emptyset$. The criterion contains two material constants, ∅ and So. The representation of Equation (2.1) in the Mohr diagram is a straight line inclined to the σ-axis by the angle ∅ (Figure 2.2). In Figure 2.3 C_0 and q represent, respectively, the rock mass unconfined compressive strength and slope of the best fit-line. Representation of Equation (2.1) in the τ: σ and in σ_1: σ_3 planes is shown in Figures 2.2 and 2.3, respectively.

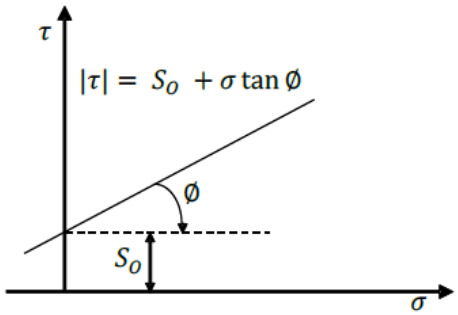

Figure 2.2: *The Mohr-Coulomb failure criterion in* $\boldsymbol{\tau}$*:* $\boldsymbol{\sigma}$ *plane (extracted from Brady and Brown, 1985).*

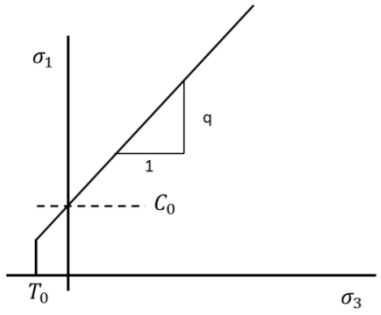

Figure 2.3: *Mohr-Coulomb failure criterion in terms of the major* $\boldsymbol{\sigma_1}$ *and* $\boldsymbol{\sigma_3}$ *minor principal stresses (Wiles, 2006).*

Rock deformation and the strength characteristics are typically determined by rock laboratory experiments done on a rock specimen both under uniaxial ($\sigma_3 = 0$) and tri-axial conditions ($\sigma_3 > 0$). Mathematically the failure criterion can be represented by a linear relationship (σ_1: σ_3 plane) as in the Equation (2.2) according to Wiles (2006):

$$\sigma_1 = q\sigma_3 + C_0 \qquad [2.2]$$

where σ_1 is the major principal stress and σ_3 is the minor principal stress respectively

and $$q = tan^2(45^o + \frac{\emptyset}{2}) \qquad [2.3]$$

which is the slope of the best fit (referred to as strengthening parameter where 3 ≤ q ≤ 5 for strong rock types; Jager and Ryder, 1999), $\emptyset$ is the friction angle and C_0 is the unconfined compressive strength (UCS) of the rock mass.

Other failure criteria, such as the Hoek-Brown, should be considered if experimental tests show a non-linear shear and normal stress relationship, rather than the linear relationship predicted by the Mohr-Coulomb.

2.2.2 Hoek and Brown

The Hoek and Brown failure criterion differs from the Mohr-Coulomb failure criterion since the criterion is represented in the parabolic form, i.e., non-linear. It is expressed in terms of both major and minor principal stress and does not take σ_2 (intermediate principal stress) into account. The strength of the rock mass is estimated by the failure criterion developed from underground observations and actual laboratory test values (Ulusay and Hudson, 2007). The Hoek-Brown criterion for the intact rock can be represented by equation (2.4) according to Hoek and Brown (1980):

$$\sigma_1 = \sigma_3 + \sqrt{sC_{UCS}{}^2 + m\, C_{UCS}\, \sigma_3} \qquad [2.4]$$

where m and s are empirical constants, C_{UCS} is the rock mass UCS in MPa, m indicates the rock's frictional strength and s relates to cohesion and fracturing of the rock mass (Ulusay and Hudson, 2007). The intermediate principal stress (σ_2) does not appear in the equations except. It is assumed that rock failure is controlled by σ_1 and σ_3 as illustrated in Equation (2.4) (Ulusay and Hudson, 2007).

The Hoek-Brown failure criterion has been updated several times since the original formulation was presented in the early 1980s. The updates were to cater to certain practical limitations of the criterion in improving the estimate of the rock mass strength (Hoek and Brown, 1980; Hoek *et al*., 1992, 2002).

Strength properties and elastic constants of some rock types in the Kloof Gold Mine are represented in Table 2.2, where E is Young's modulus, UCS – Uniaxial Compressive Strength, and the v – Poisson's ratio. The UCS is the most important property for rock engineering design. About 28 samples of rock strength tests from Kloof Operations indicates that the UCS can vary significantly of each rock type (Chen, 2007).

Table 2.2 : Rock strength tests from six of each rock type sample from the Kloof Gold Mine (Van der Heever and Ryder, 2007)

Formation	**Rock Type**	**E (GPa)**	**UCS (MPa) Low - High**	v
Alberton	Basalt	80 – 80	220 - 300	0.14 - 0.33
Westonaria	Komatiitic Basalt	65 – 80	6 - 120	0.2 - 0.4
Mondeor	Quartzite	70	220 - 300	0.14 - 0.33

2.2.3 Failure mechanism classification

The rock mass properties have a substantial effect on its strength, especially the number of joints, joint orientation, joint condition, uniaxial compressive strength (UCS), and the presence of water. Rock mass failure may occur in intact rock or by dilation and shear along pre-existing planes of weakness. The factors that control the initiation and failure mechanisms include the stress field, rock strength and friction properties. In hard rock mining, two end-member failure mechanisms are observed *viz.*: namely crush- and shear-type (Figures 2.4 and 2.5; Jager and Ryder, 1999).

- Crush-type failure (e.g., buckling, spalling, strain-, pillar- or face bursts) accounts for most small magnitude seismic events ($M_L < 2$). They tend to locate close to mining faces and the reef horizon (Figure 2.4; Table 2.3). Their source mechanisms involve a high degree of volumetric closure and a minor degree of pure shear. Damage is usually limited to a single mining panel.

- Shear- or slip-type failure (e.g. shear rupture or fault-slip) accounts for most of the larger seismic events ($M_L \geq 2$). They tend to occur on geological features such as dyke contacts, faults and joints (Figure 2.4; Table 2.3). Underground observations indicated that large seismic events tend to occur on steeply dipping faults (dip angle more than 60^0) with large throws (more than 40 m) and especially where the faults are planar, clean and tightly closed.

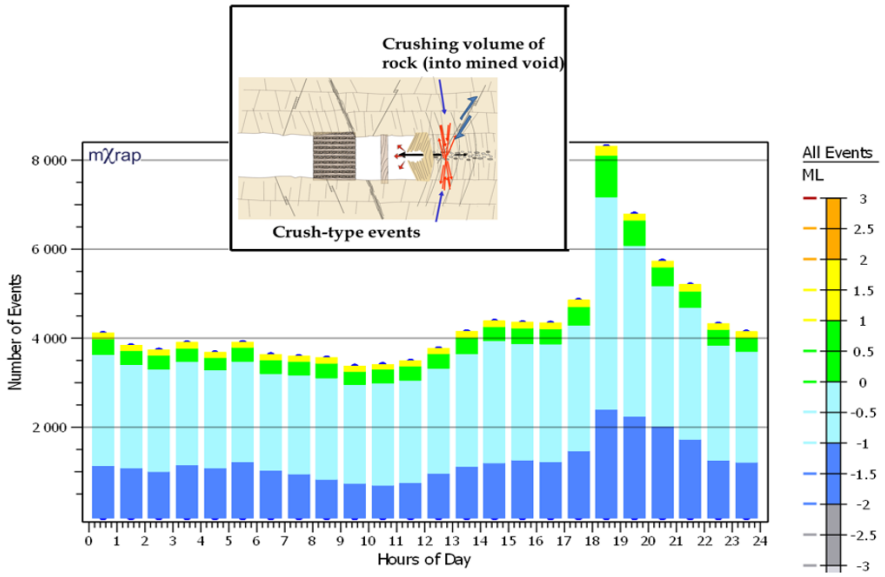

Figure 2.4: *The diurnal distribution of predominantly crush-type events (M≤2.0) at Kloof Gold Mine, 1/1/2017-30/12/2018. The plot is created in mXrap software (Harris and Wesseloo, 2015).*

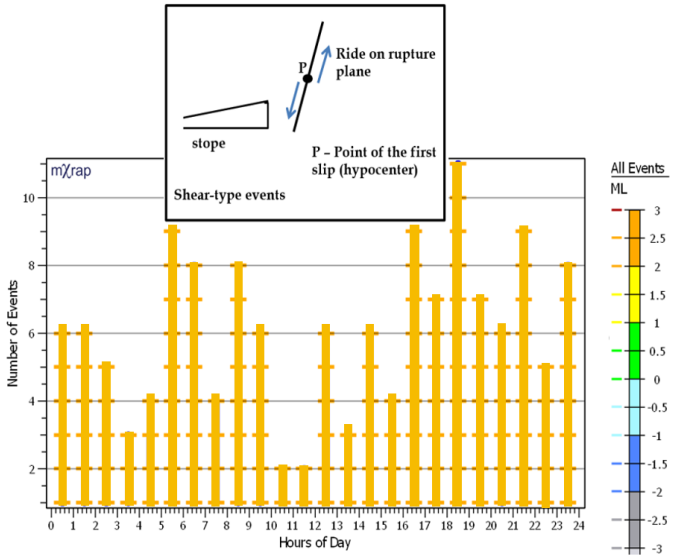

Figure 2.5: *The diurnal distribution of predominantly shear-type events (M>2.0) at Kloof Gold Mine, 1/1/2017-30/12/2018. The plot is created in mXrap software (Harris and Wesseloo, 2015).*

Ortlepp (2001), Jager and Ryder (1999) and Ortlepp and Stacey (1994) define five different source mechanisms that occur in shallow to deep underground mines (Table 2.3). The table lists rock mass movement, the direction of the first motion recorded by the sensor, maximum magnitude for each mechanism.

Table 2.3: Suggested classifications of seismic sources (source mechanism) (Ortlepp and Stacey, 1994, Jager and Ryder, 1999, Ortlepp, 2001).

Rockburst Type	Postulated Source Mechanism	First Motion from Seismic Records	Local Magnitude (M_L)
Strain-bursting	Superficial spalling with violent ejection of fragments	Usually undetected, could be implosive	-0.2 to 0
Buckling	Outward expulsion of larger slabs pre-existing parallel to surface of opening	Probably implosive	0 to 1.5
Pillar or face crush	Sudden collapse of stope pillar, or violent expulsion of large volume of rock from tabular stope face or tunnel face	Possibly complex, implosive and shear	1.0 to 2.5
Shear rupture	Violent propagation of shear fracture through intact rock mass	Double – couple shear	2.0 to 3.5
Fault-slip	Sudden movement along existing fault	Double – couple shear	2.5 to 5.0

Description of all rockburst type is given in Ortlepp and Stacey (1994), Jager and Ryder (1999) and Ortlepp, 2001):

- **Strain bursting**

  Occurs when the rock mass strength in the excavation wall is exceeded by the stress redistribution and the stored strain energy of the rock mass is released. Violent failure of the intact rock of the excavation characterizes the source mechanisms.

- **Buckling**

  It is more likely to occur in laminated or the transversely anisotropic rock mass. The energy source is strain energy stored in large rock slabs prone to buckling. The damage may occur anywhere around the periphery of the excavation.

- **Pillar bursts or face crush**

  The violent failure of a specific dimension pillar that was over-loaded characterizes the pillar burst, whether it is total collapse or partial collapse. Damage of this kind occurs close to the pillar. The rock fragments can either be ejected in the existing gully or in a panel.

- **Shear rupture**

  It is a shear failure through the intact rock mass, which usually occurs suddenly and causes a seismic wave to be radiated and causes damages to the nearby excavations. Shear rupture

requires confinement, otherwise the rock will fail in tension as tensile strength is usually far lower than compressive or shear strength. A stress vector can be decomposed into a normal and tangential (i.e., shear) component on any plane. Shear rupture occurs when the strength stress exceeds the shear strength. The shear strength of any potential rupture surface depends on cohesion and friction. Cohesion depends on the rock strength, while friction depends on the normal stress and the properties of the surface.

- **Fault slip**
  Occurs when mining triggers a slip along an existing dyke or a fault due to the redistribution of stress. The failure will occur due to the clamping force on the geological feature that has been exceeded.

Other mechanisms may include the class of dynamic brittle shears known as Ortlepp shear, formed in the deep mines. They are large shear fractures linked to considerable sizes seismic events. Ortlepp shear is a known result of interaction between stress fields due to mining, fault properties and the tectonic stress field. This occurs when the high-stress condition drives the failure of homogeneous, intact rock. The Ortlepp shear is geometrically defined by combining breakthrough shear ruptures and extension fractures (van Aswegen, 2008).

In very deep mines where large areas of massive hard rock exist without significant faulting or dykes, rockburst occurs, which are more localized in extent but often more violent than those associated with geological faults. The local magnitude of these events usually ranges between M_L 1.5 and M_L 3.0, and they are believed to have significantly higher stress drops (Ortlepp, 2000)

2.3 Sources of seismic energy emission

In the gold mines of the Witwatersrand Basin, seismicity is triggered by changes in the stress state in the rock mass due to shaft and tunnel development and stoping. Stoping operations induce the most significant changes to the stress state due to the far larger volume of extracted rock. This chapter reviews the situations that most commonly give rise to seismic events.

All mining fracturing processes are accompanied by seismic energy emissions, although these are often not detected by the seismic monitoring systems. In the underground mining environment, the more important processes are the formation of shear-fractures, slip along geological discontinuities or the violent failure of a volume of rock (Jager and Ryder, 1999). The sources of seismic emissions experienced in the Witwatersrand Basin gold mines are shown in Figure 2.6. Medium to large magnitude events (say $M_L \geq 1.5$) occur in remnant areas, geological structures such as dykes and faults, abutments, stability pillars, and the back areas. Adverse mining geometry can cause seismic events close to the active mining faces that cannot

be associated with any known geological structure, such as poor face shapes due to leads and lags that deviate from standards. These damaging events, commonly referred to as face bursts, generally have $M_L \leq 2$.

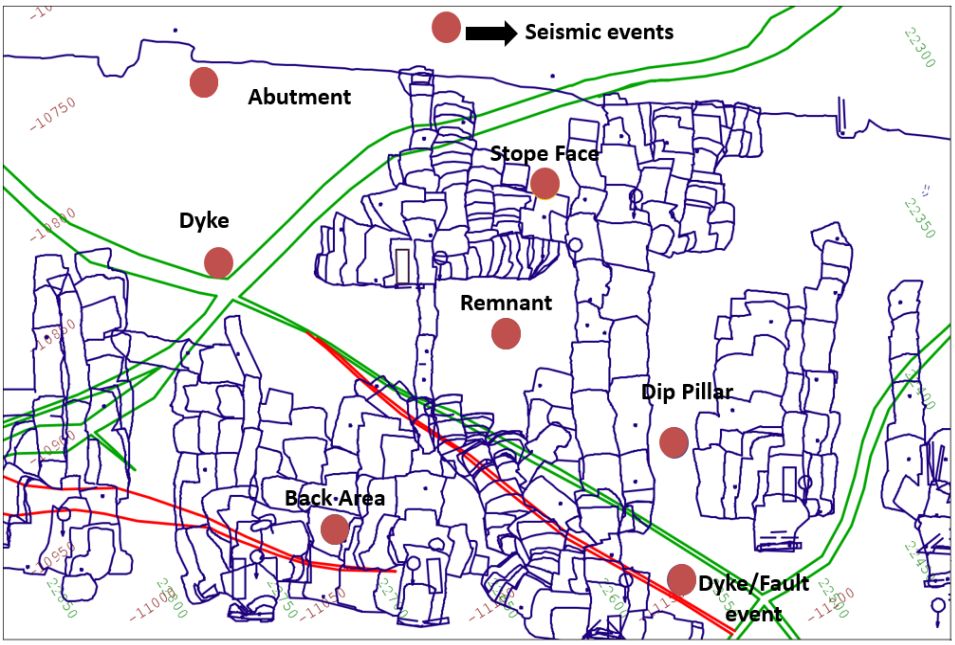

Figure 2.6: *Main seismic emission sources at Kloof Gold Mine.*

The main sources of seismic energy emissions observed at Kloof Gold Mine have been analyzed using the following categories (Table 2.4):

Table 2.4: Main sources of seismic energy emission (Jager and Ryder, 1999) observed at Kloof Gold Mine.

Emission sources	Features
Geological structures	Dykes, faults, and especially intersections of these structural elements.
Abutments	Edge of mining areas, not in the direction of mining, usually on the downdip side of mining, probably due to fracturing and higher stresses.
Stability pillars	Possibly foundation failure; stress increases on stabilising pillars as mining advances.
Stope / Mining faces	Shear failure in hanging- and footwall, minor discontinuities (joints, in the stope faults/dykes), shear failure between different rock types, and facebursting due to high local stress concentrations.
Back areas	Slow regional loading; little or no damage is observed in working faces.

2.3.1 Geological structures (dykes and faults)

The sources of largest seismic events experienced in the Kloof Gold Mine are the major geological structures. In the analysis of seismic energy emission sources, faults and doleritic dykes were grouped since some of the geological structures are zones that consist of both faults and dykes. When events are located near the intersection of geological structures, determining which structure was associated with a seismic event is often difficult. Fault slip, dyke bursting, or a combination could be the potential mechanisms of some large seismic events. Table 2.5 lists some of the major geological structures in the Kloof Gold Mine 3D reflection seismic cube. Various seismic parameters can describe seismic hazards on geological structures within the drawn polygons in the Mine (Figure 2.7). Seismic hazard parameters were determined for each structure in terms of the observed maximum magnitude (M_{max}) and the number of potentially seismic damaging events recorded. Where the seismic data are sufficient for statistical analysis, number of seismic events ($M_L \geq 1.5$), the theoretical M_{max}, *b*-value, and Hazard Magnitude (HazMag) were calculated for the geological structure (Figure 2.8), where the expected maximum magnitude (expected M_{max}) is the magnitude for which the mean return period is equal to the specified time span (1, 2, or 5 years), while the Hazard magnitude (HazMag) is the magnitude calculated from total moment and total energy (normalized for one year).

Table 2.5: Seismic history of some major geological structures at Kloof Mine (1/6/1999 to 30/12/2018)

Geological Structures	No. Events $M_L \geq 1.5$	Recorded M_{max}	*b*-value	Expected M_{max}	HazMag
Dyke 1	39	3.2	0.92	3.4	2.8
Fault 1	22	2.7	0.68	2.9	2.8
Dyke 2	37	3.0	0.83	3.2	2.6
Fault 2	19	3.0	0.65	3.2	2.3

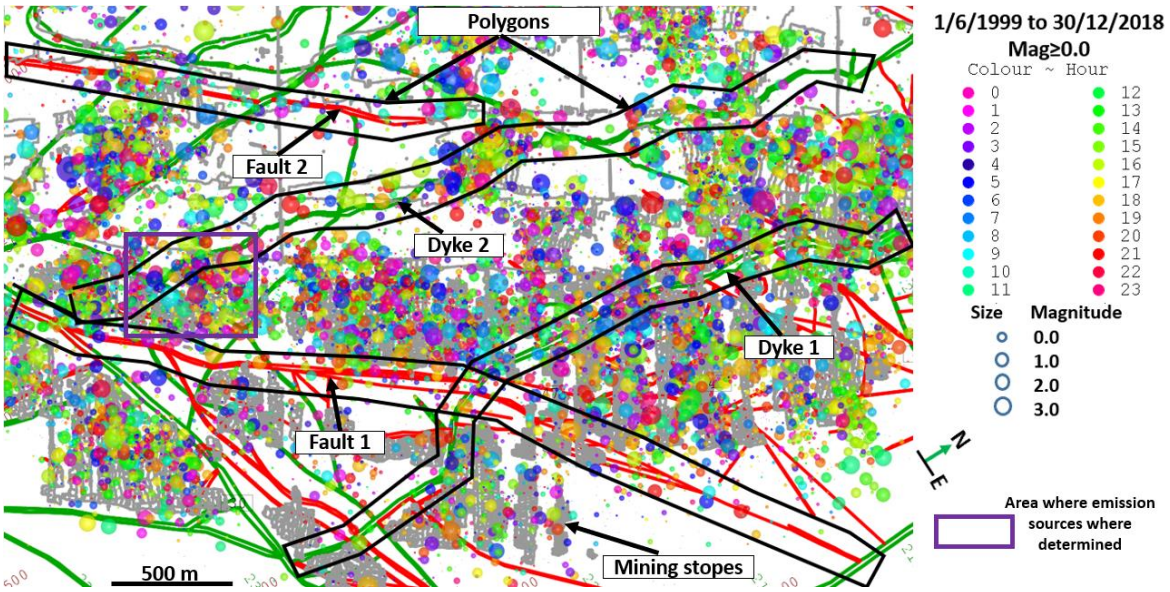

Figure 2.7: *Geological structures and the polygons used to assess hazard (1/6/1999 to 30/12/2018). Purple polygon refers to Figure 2.6.*

More M≥1.5 seismic events were recorded on the dykes compared to the faults, with high b-values and high recorded Maximum magnitudes. The analysis indicated that dykes are, generally speaking, more hazardous than the faults.

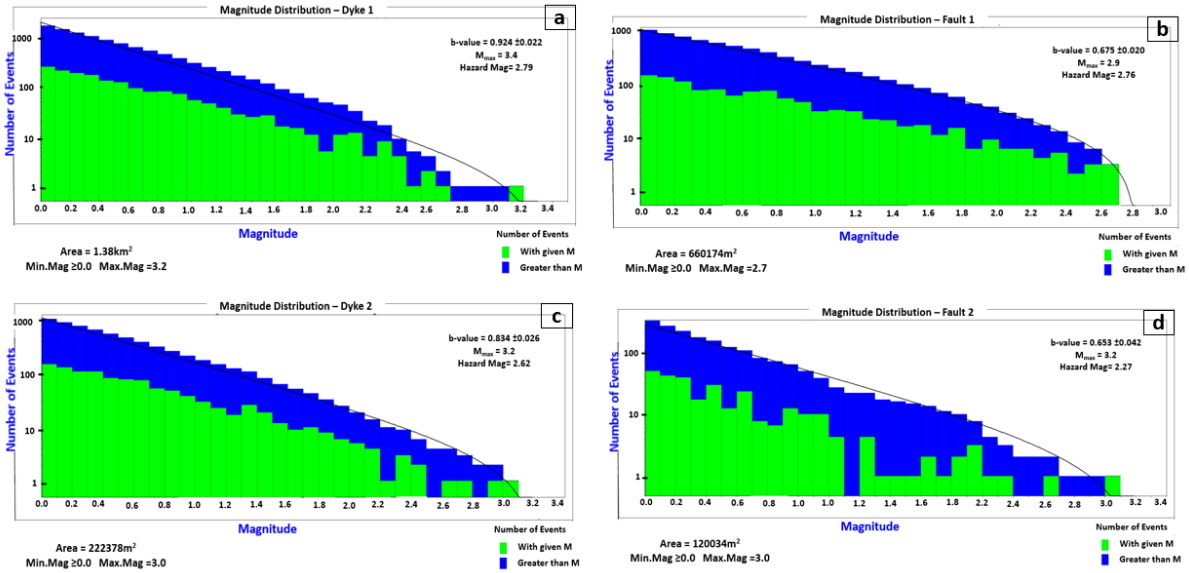

Figure 2.8: *Gutenberg Richter Plots for the dykes and faults used to assess hazard (1/6/1999 to 30/12/2018) indicating different levels of hazards.*

2.3.2 Abutments

Abutment seismic events are categorised as seismicity located along the static edges of the mined-out areas excluding those ahead of the direction of mining (Figure 2.6). These seismic events are due to abutment fracturing, as abutment stresses are elevated due to mine span increases. Some shear-type events can be associated with abutments, probably relating to fracturing occurring in the vicinity of abutments or pillars.

2.3.3 Stability pillars

Several mechanisms can cause seismic events that are recorded in, above, or below regional stability pillars. One possible mechanism for these seismic events is the failure of the foundation of the stabilizing pillars. The seismic events can also be associated with geological structures, often incorporated into the regional pillars. A regional stability system that includes stabilizing pillars is generally implemented in the gold mines. The sequential grid layout is implemented at Kloof Mines. The system limits the mining spans, controls convergence, and controls face stresses, thus mitigating the incidence and effects of massive damaging failures.

2.3.4 Stope and mining faces

Advancing mining faces tend to be associated with the small to medium magnitude seismic events that usually occur immediately after blasting. These recorded seismic events represent the majority of seismic activity in the mine. They occur close to the active mining faces and cannot be associated with any known major geological structure. The mechanism for these seismic events could be a shear failure in the hanging- or footwall, failure on minor geological discontinuities (joints or small faults and dykes), shear failure on the contact between different rock types, or face bursting due to high local stress concentrations (crush-type events). Poor face shapes can also result in localized strain bursting.

2.3.5 Back areas

Seismic events can occur on unmined blocks of ground (pillars) left behind in the old mining environment. These pillars are sufficiently far away to assume that no direct influence from active mining has taken place. Owing to slow regional loading, foundation or pillar failure are likely seismic source mechanisms. The resultant damage is usually not problematic, owing to the distance from active mining faces. Smaller pillars in the back areas are known to have deformed aseismically or associated with seismicity, producing crush-type seismic events. Other emission sources in the back areas include events related to blasting and development ends. These seismic events are generally small, say $M_L \leq 2.0$, but does not exclude a very large magnitude seismic events, say $M_L \geq 4.0$ can occur in the back areas.

2.3.6 Development faces

Micro-seismic events (M_L~-3.0) induced by the advancing tunnel are recorded in the vicinity of some of the deeper development ends on the mine. When these events are plotted versus time, these events track the advancing tunnel faces and localized rock mass response to the development blast.

2.3.7 Blasting-related events

Blasting perturbs the rock mass equilibrium and redistributes the stress state daily (Figure 5.2, section 5.3.3). Kloof Mine practices centrally-controlled blasting, which causes a peak in the diurnal distribution of events, at 18:00. The number of events quickly decays within a few hours after the blast to the background levels (Figure 5.2 from 21:00).

2.3.8 Seismicity at Kloof Gold Mine in terms of emission source and failure mechanism

Figure 2.9 provides an overview of a mine plan with seismic events characterised by different failure mechanisms according to energy ratios. Seismic events occur when stress exceeds the rock strength (or the cohesion and the friction on a fault plane), sudden failure occurs accompanied by the release of strain energy. There are more burst-type seismic events (Es/Ep≤7) than slip (Es/Ep ≥10) or mixed source events (7< Es/Ep <10). Figure 2.10 shows the number of M_L≥1.5 events that occurred from 1 June 1999 to 30 December 2018 related to faults, dykes, pillars/remnants, abutments, and back areas. Pillars/remnants hosted most M_L≥1.5 seismic events, followed by faults, and then dykes. Large seismic events of M_L≥2.5 were observed in the back areas (Figure 2.10). These seismic events were classified into different mechanisms based on their S-wave to P-wave energy ratios (Es/Ep). The results (Figure 2.11) show that slip-type events (high Es/Ep) dominated on faults. In contrast, dykes, pillars/remnants, and abutments hosted mostly burst-type events (low Es/Ep). The events in the back areas did not show a predominant overall mechanism and had mostly mixed-type solutions.

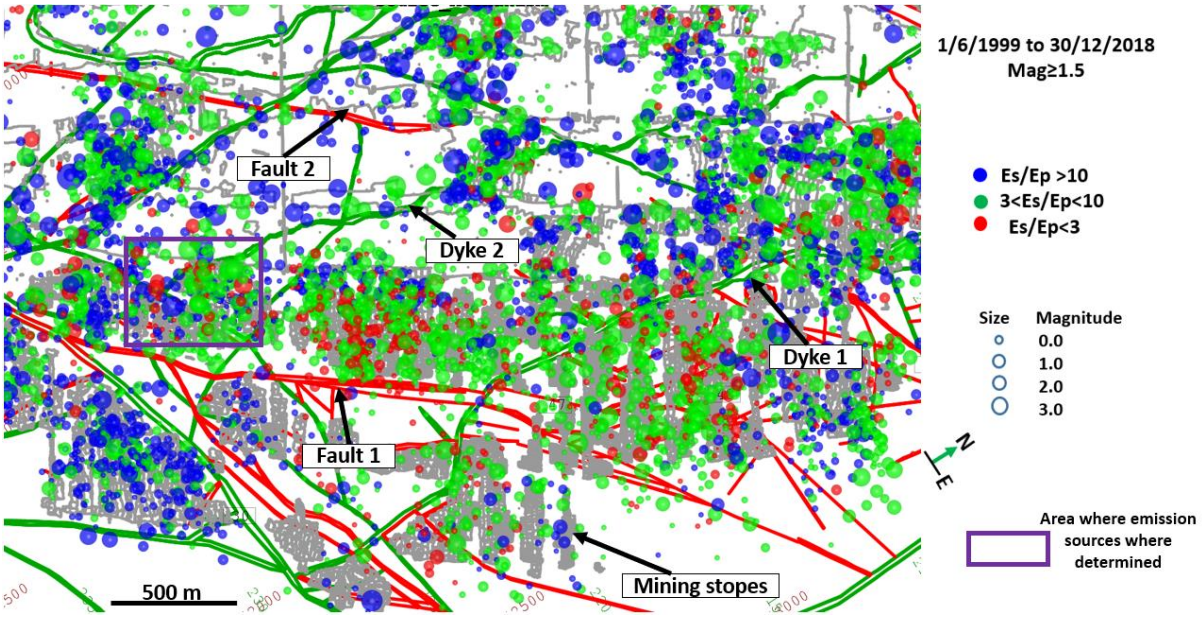

Figure 2.9: *Mine plan with M_L≥1.5 events classified into different types of failure mechanisms based on their Es/Ep ratios, 1/6/1999 to 30/12/2018. Purple polygon refers to Figure 2.6.*

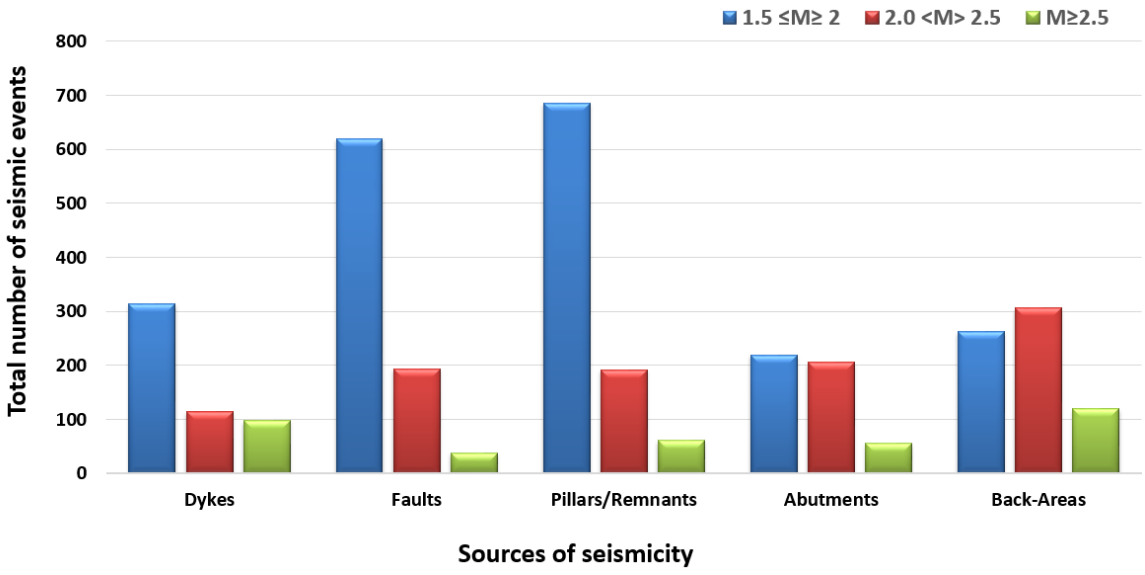

Figure 2.10: *Sources of M_L≥1.5 seismic events at Kloof Gold Mine, 1/6/1999 to 30/12/2018.*

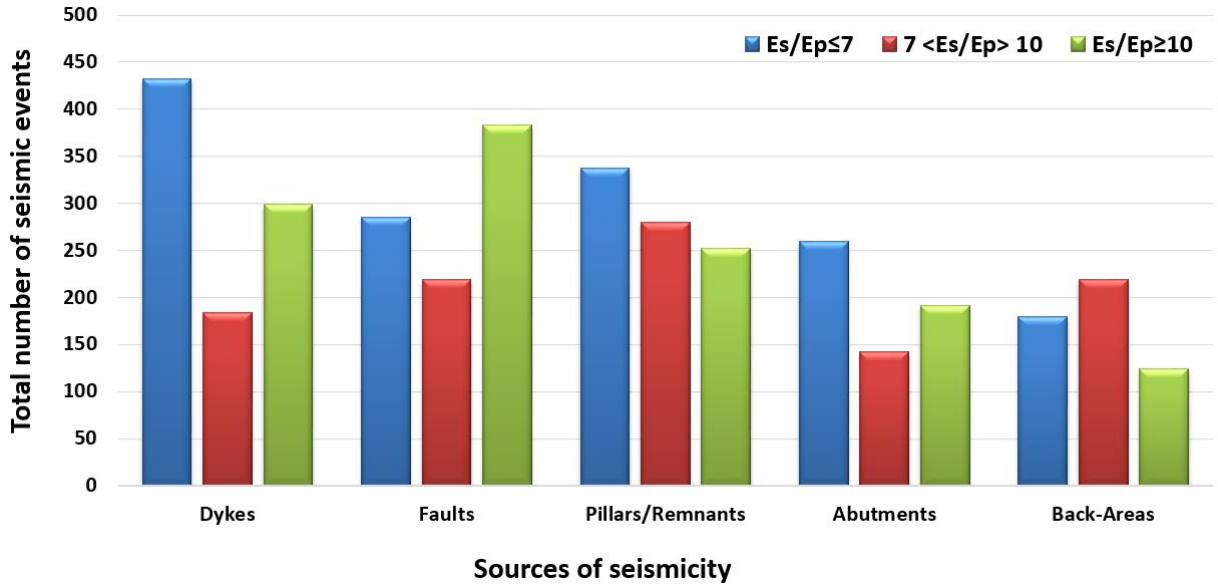

Figure 2.11: *Classification of M_L≥1.5 events at Kloof Gold Mine into different types of failure mechanisms based on their Es/Ep ratios, 1/6/1999 to 30/12/2018*.

CHAPTER 3 - AN OVERVIEW OF SPATIAL DISTRIBUTION OF SEISMICITY IN SOUTH AFRICA, MAINLY IN THE WITWATERSRAND BASIN

3.1 Earthquakes and mining seismicity in South Africa

South Africa is situated in the southern part of the African plate, far from plate tectonic boundaries, and is thus classified as a 'stable continental region'. The earthquake activity is far lower than in seismically active regions such as Haiti, Sumatra and Japan. Tectonic earthquakes are comparatively rare but still do happen from time to time.

The South African National Seismograph Network (SANSN), established in 1971 and operated by the Council of Geoscience (CGS), is responsible for local and regional earthquake monitoring in South Africa. The SANSN operates 37 seismic stations distributed over South Africa (Figure 3.1). The seismic stations were initially analogue but were upgraded to digital in 1988 (Mulabisana, 2016). In addition, the CGS also operates three clusters of seismic stations in gold mining districts on the rim of - Witwatersrand Basin. The seismic stations are located several hundreds of kilometres away from each other and used for - earthquake location determination in South Africa. The denser network (station clusters) allows for - more sensitive and accurate location of events in the gold mining regions. The locations of some seismic stations are given in Table A1 in Appendix A.

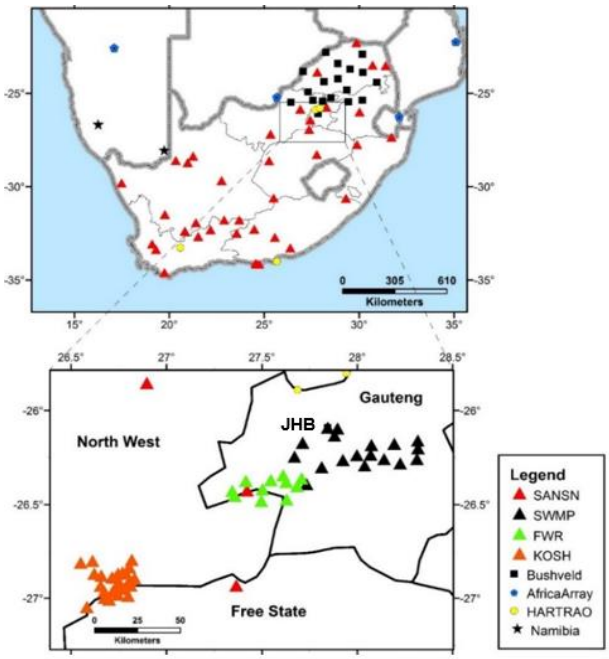

Figure 3.1: *The location of seismic stations in southern Africa: South African National Seismograph Network (SANSN), Strategic Water Management Project (SWMP), Far West Rand (FWR), Klerksdorp-Orkney-Stilfontein-Haartebeesfontein network (KOSH), AfricaArray-CGS Bushveld Broadband Array, AfricaArray, HARTRAO academic network, and Namibian Geological Survey.*

The regional coverage is essential to monitor natural seismicity and allows comparison with mining-induced seismicity when required. The SANSN only records reliably seismic events with magnitudes greater than three, and it is often challenging to locate the hypocentres with accuracy better than 5 km. Thus, the regional network coverage can only indicate the mining area where the seismic events occurred. However, it is often difficult to identify the actual mine and impossible to pinpoint the part of the mine where the event occurred.

The SANSN has used several local magnitude relations from 1970 to the present days. According to Fernández (1973), the first relation, used from 1971 to 1997, is given by equation 3.1:

$$M_L = Log_{10}(A) - Log_{10}(A_0) + S \qquad [3.1]$$

where:

(A) : Maximum amplitude, and

(A_0) : Distance correction factor

$-Log_{10}(A_0)$: Distance correction term (0.84 $Log_{10}\Delta$) where $\Delta\ (in\ degrees)$ is epicentral distance

S : Station correction term

This distance-magnitude relation was based on the data from southern California (Richter, 1935). After the Seisan computer software was introduced for routine data analysis by the Council of Geoscience (South Africa) in 1997, an equivalent local Magnitude relation (M_L) was developed and applied. It is based on the Hutton and Boore (1987) equation (3.2):

$$M_L = 0.010\,(Log_{10}(A) - Log_{10}(A_0) + S) + 0.0118 \qquad [3.2]$$

It compared well with the local magnitude relation of Equation (3.1) that was first used to define the magnitude relation (M_L) in South Africa. In 2012 the magnitude relation scale was calibrated using a minimum of five high-quality recording stations (Saunders *et al.*, 2013), resulting in Equation (3.3) :

$$M_L = 1.1149\,Log_{10}(R) + 0.00063R + Log_{10}(A_0) - 2.04 + S \qquad [3.3]$$

where (A_0) is a distance correction factor, R (km) is the hypocentral distance and S is the station correction term.

The three magnitude relations are largely equivalent. Other magnitude equations that are used are presented in Appendix A.

Numerous authors have documented and described - patterns in seismicity in South Africa, including Gane, 1939; Fernandez and Guzman, 1979; Singh et al., 2009; Brandt et al., 2005. These studies have traced seismicity back to the 1620s with no instrumental monitoring and dating back to 1899 when instrumental monitoring started. The studies also highlighted that seismicity had been dominated by mining seismic events in the gold and platinum regions. The existence of several clusters of tectonic events and mining seismic activities are observed throughout the country (Figure 3.2). Different clusters of these seismic events with various tectonic and mining regions were clearly identified by Singh et al. (2009). Figure 3.2 indicates the distributions of earthquakes above magnitudes of 1 in the SANSN database kept by the CGS.

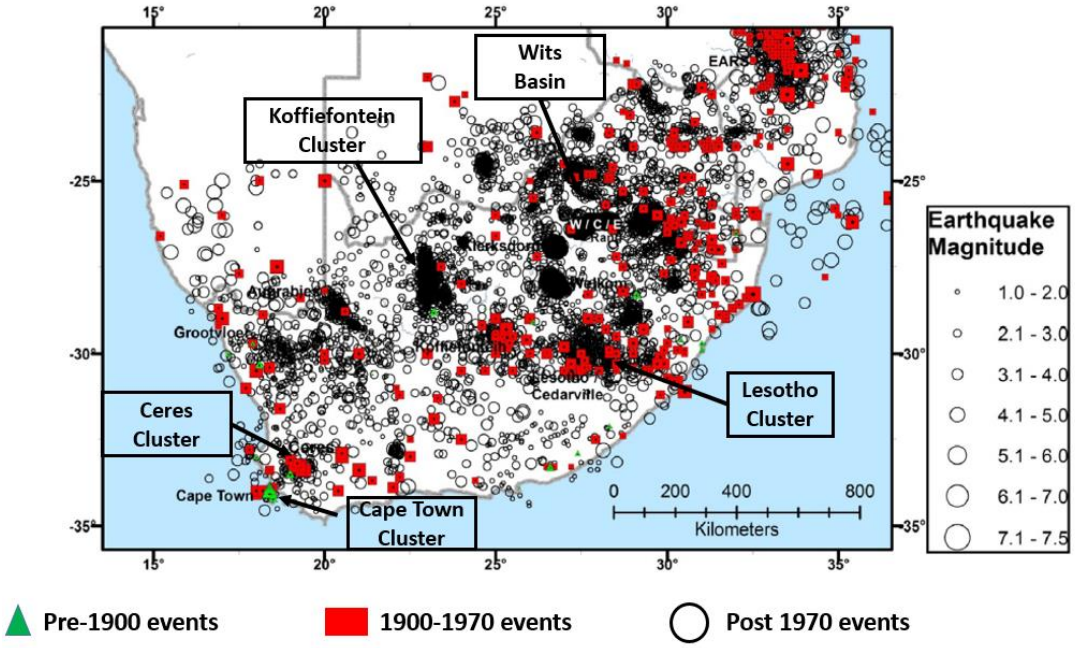

Figure 3.2: *Location of seismic events in South African National Seismological Database (SANSD) indicating the spatial distribution of earthquakes from Pre-1900 to Post 1970. (from Manzunzu et al., 2019).*

Mulabisana (2016) identified 65 370 earthquakes, including mining-related events, in Southern Africa (Figure 3.3). The largest earthquake, having a magnitude of M_w6.7, occurred on 11 October 1952 in the Okavango Delta (Western Botswana). The largest mining-related seismic event occurred on 5 August 2014 near Orkney, with a magnitude of M_L5.5. The next largest was a M_L5.3 earthquake that occurred on 9 March 2005 in Stilfontein within the Klerksdorp region. The M_L5.3 event caused damage to several buildings (Figure 3.4), including two fatalities (in a mine), 58 injuries (public), and trapped 3200 miners.

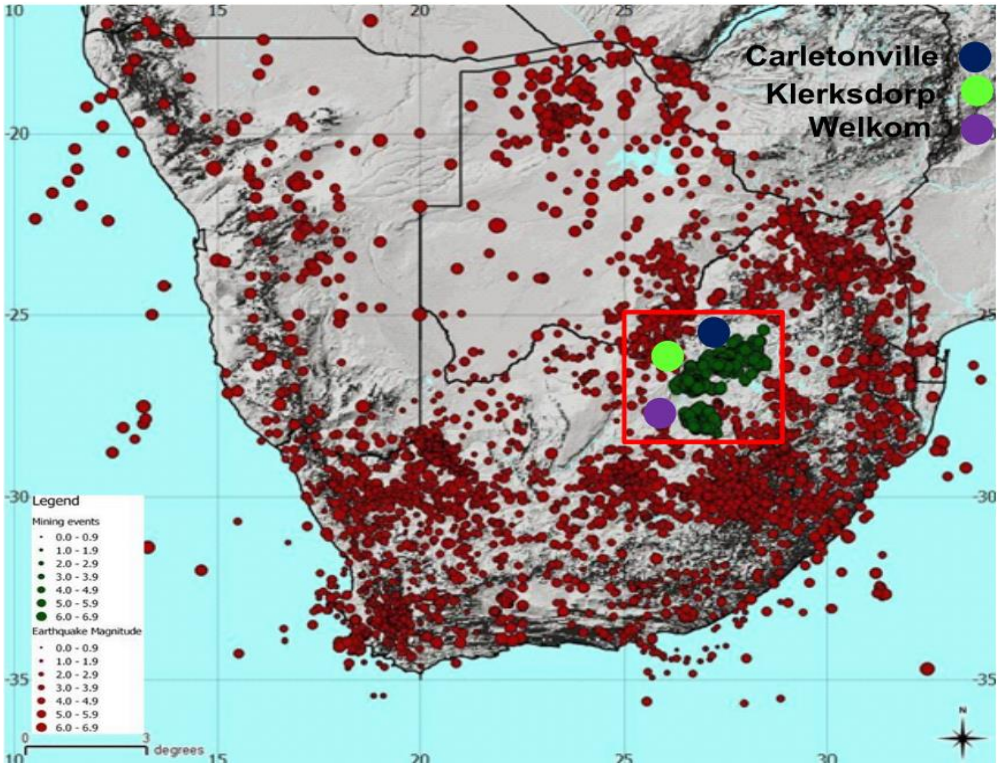

Figure 3.3: *Location of earthquakes making up the final catalogue (red circles) from 1690- 2011 including mining seismic events in green circles. Sources of data are from SANSN, International Seismological Center (ISC), (after Mulabisana, 2016).*



Figure 3.4: *Damaged buildings at in Stilfontein resulting from an M_L5.5 earthquake on 9 March 2005 (Durrheim et.al, 2014).*

The identification of zones of higher density highlighted some prominent seismic clusters (hotspots) in South Africa, namely: Cape Town, Ceres, Lesotho, Koffiefontein, and Witwatersrand clusters (Singh *et al*., 2009):

3.1.1 Cape Town Cluster

The actual epicenters of the earthquakes that make up the Cape Town cluster could be 100 km away or more, according to Brandt *et al.* (2005). The events' location was based on macroseismic data (e.g., newspapers, journals and diaries) and thus they were influenced by the population distribution. Therefore, it is possible that the events in this cluster could be located away from Cape Town, especially given that no major events have been recorded and located in the Cape Town area since the deployment of the national seismic station network in 1971.

3.1.2 Ceres Cluster

The largest known earthquake recorded in South Africa was located in the Ceres region. It had a magnitude value of M_L6.3. The event occurred on 29 September 1969 at 10:03 (local time) in the Ceres-Tulbagh region and claimed 12 lives (Figure 3.5). After this earthquake, a five-station temporary network was deployed in the epicentral region to monitor the occurrence of aftershocks in the vicinity (Green and Bloch, 1971).



Figure 3.5: *The aftermath of the worst earthquake to hit South Africa on 29 September 1969, M_L6.3. (Image: Facebook/Tulbagh Aardbewing/Earthquake).*

3.1.3 Lesotho Cluster

Seismicity towards the south and west of Lesotho is of natural origin. Brandt (2000) highlighted that the rate of seismicity towards the north of Lesotho increased significantly after the impoundment of the Katse dam.

3.1.4 Koffiefontein Cluster

Paleoseismic studies indicate that an earthquake of M_w8.0 occurred some 50 000 years ago near Koffiefontein (Visser and Joubert 1990; Joubert *et al.* 1991). In 1912 an earthquake of M_L6.2 occurred. within the Koffiefontein cluster, thermal springs are found, confirming the presence of seismically capable faults.

3.1.5 Witwatersrand (Wits) Cluster

The current mining within the Witwatersrand Basin is reaching depths approaching 4 km. At this depth, the rock mass is subjected to high stresses and prone to seismicity and rockburst (Ortlepp, 1994). Although most gold mines are in the last stages of their operations, seismicity related to deep gold mining accounts for most seismicity within South Africa, (Singh and Pule 2007; Gay *et al.,* 1995). Clusters within the basin can be classified into the Evander, East, Central, West, Far West Rand, KOSH and Welkom goldfields. The addition of seismic cluster networks in the Witwatersrand basin has helped to improve the depth and location of seismic events in the region compared to the SANSN records (Figure 3.6).

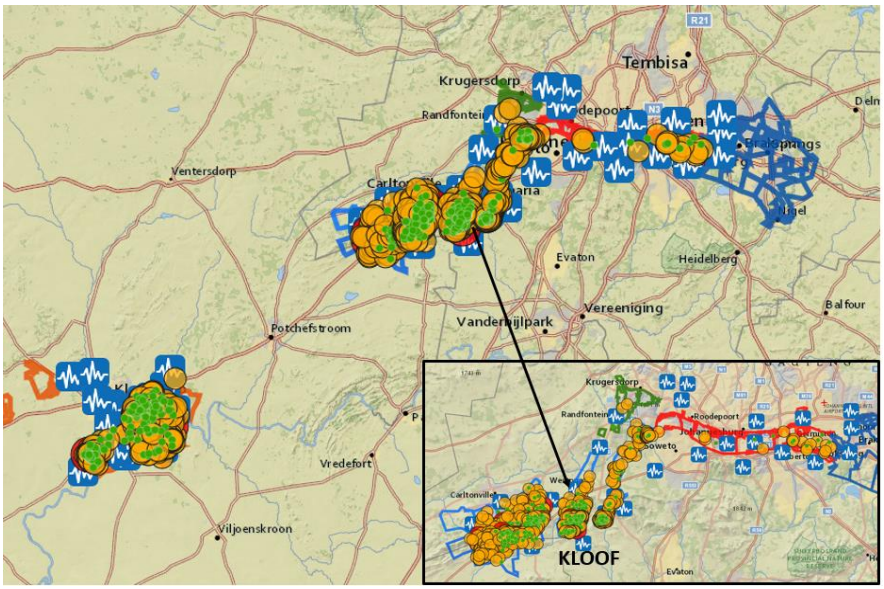

Figure 3.6: *Map of Mining-induced seismicity contained in the MHSC and CGS collaboration Network. The seismic recording stations are represented by the blue colour and seismic events by yellow circles. Red polygons indicate closed mines (extracted from MHSC project).*

Literature has highlighted that an increased pore pressure within the rock mass reduces the amount of friction on a fault (Shapiro et.al. 2005; Shapiro et al. 2002; Sibson 1986) and may trigger induced seismicity.

Owing to the closures of mines within the Witwatersrand Basin, groundwater will gradually fill the mining voids. When re-watering occurs in these mines, it will generate an increased level of fluid-induced seismicity (Figure 3.7). The level and location of seismic activity in the closed mines might coincide with some structures in those regions, which might prove to be most likely to fail under conditions related to flooding in the closed mines. The observed high level of seismicity patterns is strongly related to the presence of old mining voids. The seismic patterns from the mining flooding indicate that these are still seismically-active closed mines within the Witwatersrand Basin. Some events plot outside the mine historical boundaries and might be either mislocated or related to unknown or unmapped reactive structures in the vicinity. These can have a detrimental impact on both the communities (surface) and the neighbouring mines should structures be re-activated outside the historical mining boundaries.

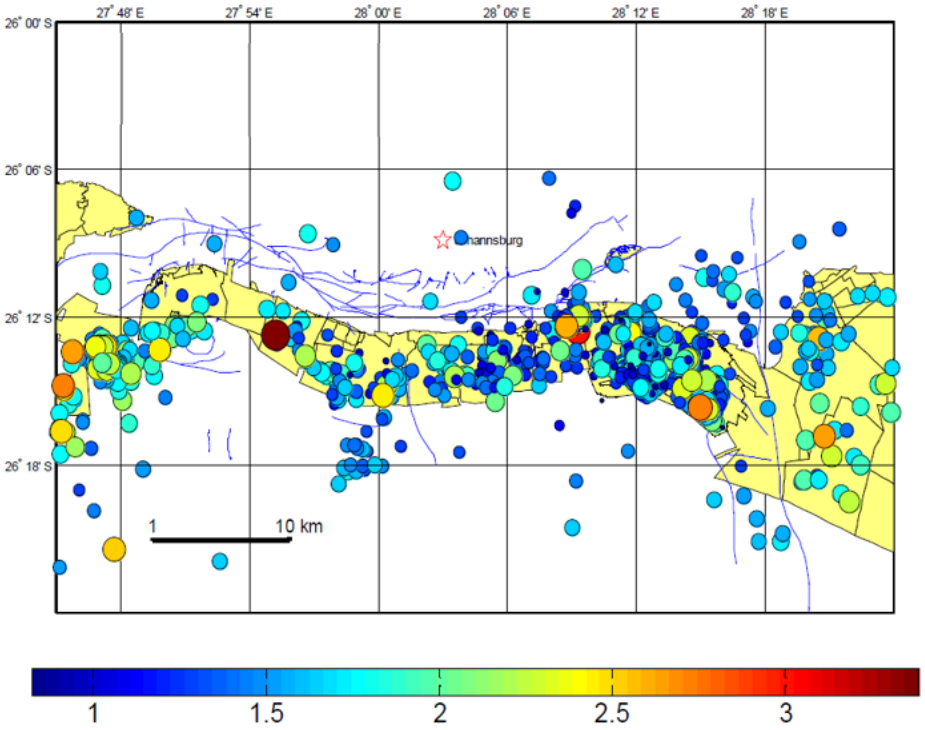

Figure 3.7: *Spatial plot of seismicity over a 5-year period (2010-2015). Scale bar indicates magnitude.The size of the circles is proportional to moment magnitude Mw. Blue lines represent known surface faults and yellow shades represent previous mine boundaries (after Cichowicz et al., 2016).*

CHAPTER 4 - MINING INDUCED SEISMICITY

4.1 Introduction

This chapter gives an overview of the seismic source parameters, manipulation of seismic source parameters, seismic monitoring system at Kloof Gold Mine, the seismic network's layout, sensitivity and location accuracy, data acquisition, data processing, seismic event location, and moment tensor calculation. The evolution of the Institute of Mine Seismology (IMS) seismic system is also discussed.

Quantitatively, the information required to describe a seismic event includes the location of a seismic event, its time, and at least two seismic source parameters (e.g seismic energy, source size and seismic moment) (Mendecki et al., 1999). The source parameters can be able to describe a seismic event. These parameters are explained in the following section.

4.1.1 Seismological prosessing procedure and location of seismic events

The seismograms of every seismic event that triggers four or more stations are transmitted from underground to the seismic server on the surface. Seismic events are manually processed by operators who pick the P and S arrivals on every triggered and usable seismogram, this will be within a certain picking error level and overall location error. Five or more tri-axial geophones surrounding the source should record a seismic event to obtain reliable source parameters. Seismic source parameters, e.g., the corner frequency, seismic energy radiated, magnitude, static and dynamic stress drop and lastly, the seismic moment is automatically calculated. Quality control is routinely applied on certain seismic events.

The location of seismic events is of fundamental importance since all subsequent seismological processing depends on the event position and the distances to the station. Finding the location of the seismic event includes solving an inverse problem that consists of the location and original time vector, $\mathbf{x} = (\mathbf{h}, t_0)^T = (x_0, y_0, z_0, t_0)^T$ (Mendecki, 1997). This is the first major step in seismic data analysis. From the seismic data, we can retrieve the four unknowns in the equation. The input data should consist of:

- P- and S- waves arrival times (derived from waveforms),
- P- wave polarization direction (derived from waveforms),
- Seismic velocity model,
- Station coordinates.

The locations of seismic events are affected first of all by the arrival times of the P- and S- waves. The accurate location of seismic events can be challenging due to factors that affect the velocity model and ray path. Such factors include fracturing in the rock mass due to high-stress conditions, and scattering and reflection of the waves due to random heterogeneities within the rock mass.

There are generally two main factors affecting the quality of waveforms. The first factor is the loss of any of the three geophone components (Figure 4.1). The second is associated with the introduction of any noise that effects the signals recorded by the system. Seismic events can often be located when a component is missing or the seismograms are noisy, but source parameter calculations are severely compromised.

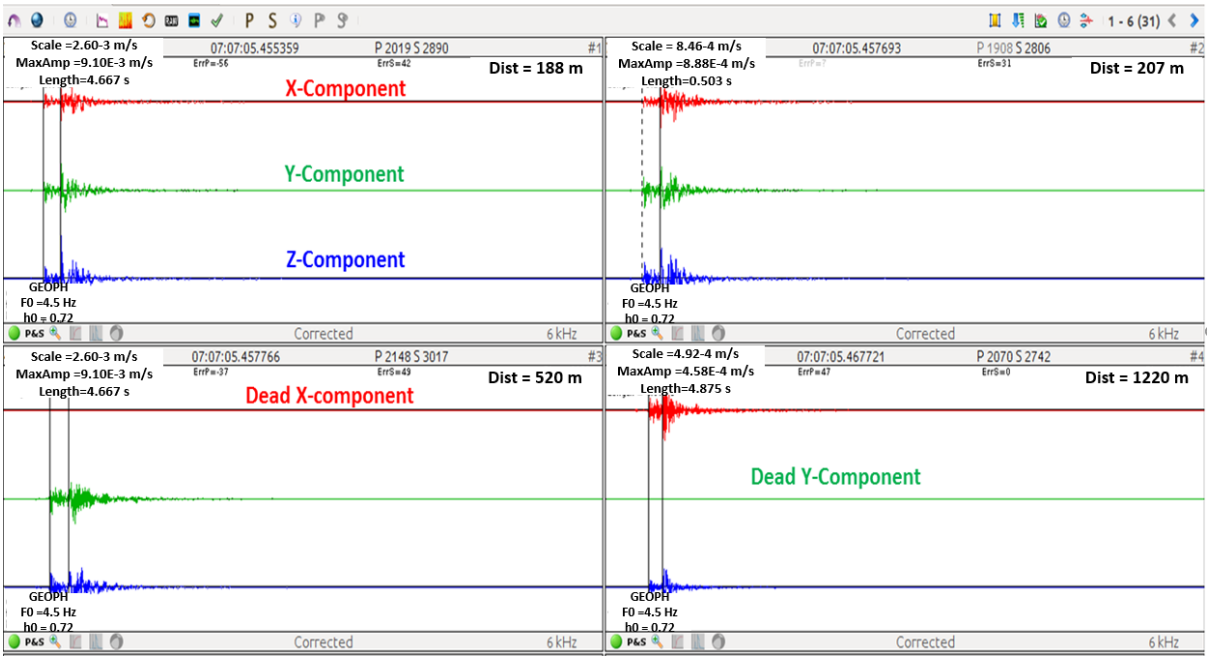

Figure 4.1: *Example of 4 tri-axial sites showing components of the seismic sensors (XYZ) including dead components.*

Accurate seismic events locations are the most critical parameters for the mine personnel. Accurate source location is possible when the seismic sensors are sufficient within the mine (Figure 1.6, section 1.9). Seismic data interpretation becomes problematic due to poor location. Location of seismic events in the mine are indicated with elevation errors up to hundred metres, but most within the marked range (Figure 4.2a). The wrong picking of both the P- and S- wave arrival incorrectly determines seismic event location. Figure 4.2b shows a degree of seismic event location scatter; only a few areas highlight a cluster of events on some of the active mining stopes.

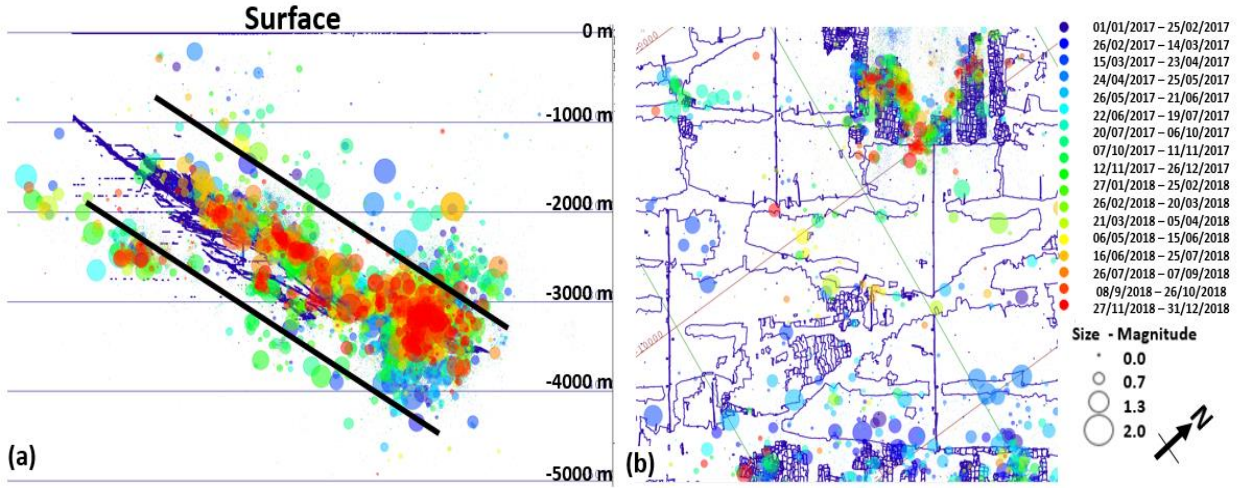

Figure 4.2: *(a) Location on section view of the scatter of seismic events on depth (b) Spatial plot of seismic events.*

4.1.2 Time of the seismic events

Seismic event time relates to the beginning of rock mass failure process due to a seismic event or when the blasting occurs. In mining, the occurrence time of most seismic events relates to blasting activities in the mine. Stress changes induce seismicity due to blasting the stope geometry. The activity rate is indicated in Figure 4.3, and the peak within the histogram indicates the area in the mine when blasting is taking place (e.g., stopes or developments).

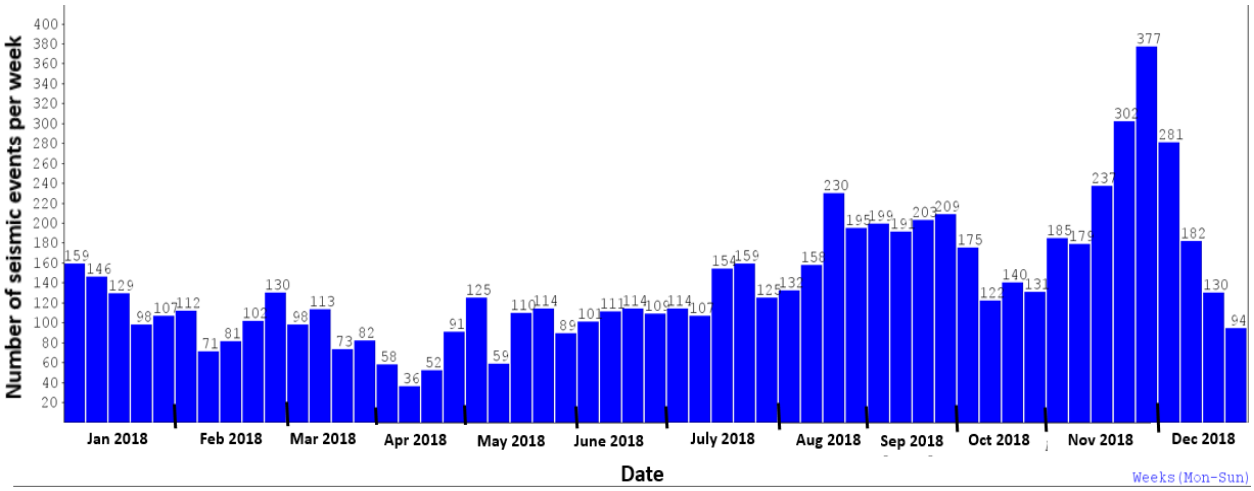

Figure 4.3: *Activity rate: Bar graph showing the number of seismic events per week in the mine.*

Many small events are observed after the mining stope blast, and large seismic events may be triggered. This means that large seismic events are driven by factors different from those driving small ones (e.g., geological structure, extraction rate, stress migration, etc.). Brummer (1999) reports that “the larger the seismic event, the more random the pattern of its occurrence”.

4.1.3 Seismic energy

At the source of a seismic event or an earthquake, the portion of the total elastic energy radiated as seismic waves are represented by seismic energy. In deep-level mines, seismic energy is used to measure the size of the recorded seismic event. Haskell (1964) defined *radiated energy* as "the wave energy that would be transmitted to infinity if an earthquake occurred in an infinite, lossless medium". The radiated seismic energy, represented by E can be determined for P-wave or S-wave by Equation 4.1 (Gibowicz and Kijko, 1994):

$$E = 4\pi\rho_0 c_0 R^2 \frac{Jc}{Fc^2} \qquad [4.1]$$

Where:

E - Radiated seismic energy (Joules)

ρ_0 - The density of the source material (kg/m^3)

c_0 - The velocity of the wave at the source (either the velocity of P- or S- wave) (m/s)

R - Receiver's distance from the source (m)

Jc - The sum of the squared ground velocity in the recorded waveform (m/s)

Fc - Empirical radiation pattern co-efficient for a specific seismic wave

4.1.4 Seismic moment

Seismic moment is another measure of earthquake size. It is widely accepted as the best means of estimating the slip size of the related seismic event. It is an inelastic deformation within the rupture area and is defined as:

$$M_o = \mu DA \qquad [4.2]$$

where the shear modulus is represented by μ (N/m^2) at the source of the event, average displacement D (m) and A (m^2) represents the fault slip area.

The seismic moment can be obtained by moment tensor inversion or spectral analysis (Havskov and Ottemöller, 2010). The seismic moment for a seismic event can be determined from the spectral analysis of P- or S-wave using the equation (4.3) as defined by Gibowicz and Kijko (1994):

$$M_0 = \frac{4\pi\ c_o^3 \rho_o R\, \Omega_o}{F_c R_c S_c} \qquad [4.3]$$

Where:

M_0 – Seismic moment (Nm)

ρ_0 - The density of the source material (rock density (kg/m^3))

c_0 - The velocity of the wave at the source (either the velocity of P- or S- wave) (m/s)

R - Receiver's distance from the source (m)

Ω_0 - Low-frequency level of the displacement spectrum (Figure 4.4)

F_c - Empirical radiation pattern coefficient for a specific seismic wave

R_c - Free surface amplification, and

S_c - Correction for the site

Figure 4.4 represents the source displacement spectrum from the P-wave displacement of earthquakes of two different magnitudes, namely the M_L=1.1 and M_L=3.5.

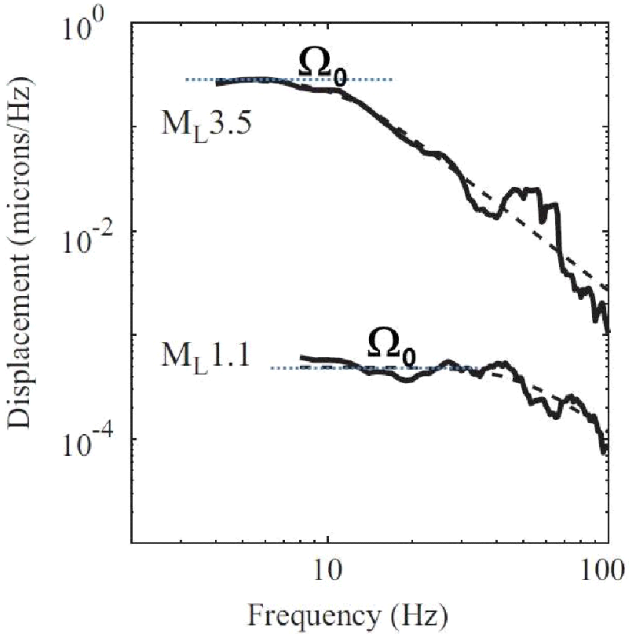

Figure 4.4: *P-wave displacement spectra for earthquakes with two different magnitudes. The solid lines correspond to the real spectra, the dashed lines are the model spectra, and the dotted lines are the low-frequency level of the spectra (modified from Prieto, 2007).*

The Brune model (Brune, 1970), which primarily corresponds to the circular-shear dislocation model, is a semi-empirical and semi-theoretical model that describes the mechanisms of rupture based on stress. This model is based on two key assumptions: (1) at the time of rupture, the entire dislocation circle experiences

a stress of the same magnitude as the released stress but in the opposite direction; and (2) S-waves account for 80% of seismic wave energy.

4.1.5 Source radius

Equation 4.4 indicates that the source radius of a seismic event r_0 in Brune's model depends on the shear wave velocity v_β and the corner frequency f_o (Gibowicz, 1990). Brune's model relies on several assumptions, including an instantaneous stress drop: penny-shaped cracks, etc. The source radius is a measure of the seismic failure surface dimension. The source radius increases with the decrease in corner frequency of the shear wave velocity and can be represented as:

$$r_o = \frac{2.34\, V_\beta}{2\pi f_o} \qquad [4.4]$$

4.2 Manipulation of Independent Source Parameters

Combinations of the seismic source parameters are used to investigate populations of seismic events.

4.2.1 Local Magnitude

Magnitude is a parameter that describes the 'size' or 'strength' of an earthquake. Charles Richter (1935) introduced a magnitude scale to measure the earthquake strength in southern California, which was adopted worldwide and is known as the local magnitude M_L. The method was based on the amplitude of the ground displacement within a specific frequency range (Gibowicz and Kijko, 1994). It is a logarithmic scale and is defined in Equation 4.5:

$$M_L = Log\ A\ (\Delta) - Log\ A_o\ (\Delta) \qquad [4.5]$$

Where:

A_o is the maximum amplitude of the displacement, measured in micrometres, on a Wood-Anderson seismograph at the distance of 100 km.

$Log\ A_0\ (\Delta)$ is the calibration function for earthquakes is recorded at distances different from 100 km.

A - maximum amplitude measure at the distance Δ

Mines have adopted a local magnitude scale that uses defined constants. The local magnitude (M_L) is consistent with the magnitude of seismic events determined by the Council of Geoscience (CGS). The mines' local magnitude scale uses Energy and Moment as parameters calculated by the IMS seismic system derived from the Fourier spectra. This type of local magnitude is currently used by most of the mines that installed the IMS systems (Equation 4.6):

$$M_L = a\ Log\ E + b\ Log\ M_O + c \qquad [4.6]$$

Where:

M_L - Local Magnitude

E - Seismic Energy (J)

M_O - Seismic Moment (Nm)

a, b and **c** - constants that are set for different mining regions.

- Carletonville: **a** = 0.272, **b** =0.393, **c** = - 4.630
- Klerksdorp: **a** = 0.263, **b** =0.333, **c** = - 3.612 and
- Welkom: **a** = 0.275, **b** =0.433, **c** = - 5.124.

The Sibanye-Stillwater Gold mines use the following standardised magnitude calibrating parameters for all operations: M_L = 0.326 log (E) + 0.467 log (Mo) – 6.167.

4.2.2 Frequency magnitude relations

The frequency-magnitude relation quantifies the statistical relationship between the number and size of earthquakes. This distribution is best known as the Gutenberg Richter relation (Gutenberg and Richter,1944):

$$N = a - bM \qquad [4.7]$$

where a,b represent parameters and N is the number of events with magnitude *M* and above. The b value represents the ratio of small to large seismic events. It can be used as a stress indicator within a rock mass. The introduction of the upper limit for magnitudes modified the formula (equation 4.7 to equation 4.8). A truncated Gutenberg-Richter relation was proposed to account for the upper limit of the frequency magnitude relation (Gibowicz and Kijko, 1994). The number of seismic events exhibiting magnitude greater than M which occur in time T is given by:

$$N(M,T) = \lambda T[1 - F(M)] \qquad [4.8]$$

where λ represents the seismic activity rate (i.e number of seismic events with $M > M_{min}$) per unit time.

The modified frequency-magnitude relation is represented by equation 4.8. It describes the cumulative frequency magnitude distribution of a seismic data cataloque. This relation has cumulative distribution function $F(M)$ where M is a magnitude variable and considered to be continuous in the form (Stankiewicz, 2006):

$$F(M) = \frac{1 - exp\,[-\beta(m - M_{min})]}{1 - exp\,[-\beta(M_{max} - M_{min})]}$$

where:

M_{min} Threshold of completeness, the magnitude above which all events are reliably recorded.

M_{max} Maximum possible magnitude

β Distribution parameter, $\beta = b\,In(10)$ where b is a frequency-magnitude relation slope.

Thus the distribution of magnitudes is described by only four parameters: λ, β, M_{min} and M_{max}.

Often the Gutenberg-Richter relation does not fit the observed distribution, which is more complex than the theoretical one. One of the reasons for this behaviour might be the bimodal (polymodal) distribution of events. Seismic hazard is usually calculated with the assumption that there is one mechanism responsible for the seismic events, so their magnitude distribution can be described by some simple model (e.g., Gutenberg-Richter relation). In many mines, more than one type of seismic event can be observed. For example, in Kloof Gold Mines, three types of seismic events can be identified (Figure 4.5):

I Small events, usually due to fracturing after blast (usually M_L<0.0),

II Medium to large events related directly to mining and to localized geological structure, and

III Very large events, related to regional geological structures, possibly release of residual tectonic stress.

- Small seismic events (Type I) can be ignored, when doing the static seismic hazard analysis, by selecting threshold for data slightly higher than their magnitude.
- Type II events can be correlated with mining; the frequency-magnitude distribution of these events fit the Gutenberg Richter relation if the whole mine area over a long time period is analysed, but does not fit this relation if only small area or short time are considered.
- Large events of Type III occur on regional faults and dykes within the Kloof Mining operations and are difficult to correlate with mining.

The observed frequency magnitude relation is not a linear function for the whole magnitude range. For certain range is linear and it can be used to check the data integrity. The deviation at low magnitudes is due to the sensitivity of the network, as small events are not detected. Deviations at high magnitudes may be due to the size of time or space window, not being large or long enough to capture the less frequent large events, or due to physical limitations on the source size e.g., stope spans. Lastly, several linear segments may be observed that might indicate different source mechanisms e.g., a high b-value at small magitudes indicative of fracturing of intact rock caused by stress redistribution following the production blast, and a lower b-value at higher magnitudes indicative of mining-induced seismicity on faults and dykes. Over a relatively large magnitude range, the analysis of a catalogue of events would generally produce a linear relation. In the case of tectonic events, the slope is often close to b=-1.0 (Figure 4.5). The relation can be used to check the minimum recordable event and the stiffness (b-value) of the seismic system. One commonly used method to assess long-term seismic - hazard within the area of interest can be the calculation of the *a- and b*-values to determine the seismic recurrence rate (Jager and Ryder, 1999). Events

related to blasting frequently have a b-value of greater than 1.0 (small seismic events), while events related to fault slip generally have a b-value of 0.8 or less. For any selected subset of data, the b-value may vary depending on the nature of seismicity.

The seismic event population data in Figure 4.5 does not follow the expected power law. The slope of the frequency-magnitude relation is - 0.8. It is linear over a significant range. The increase of a b-value above M2.7 is due to the different subsets of events with varying source mechanisms.

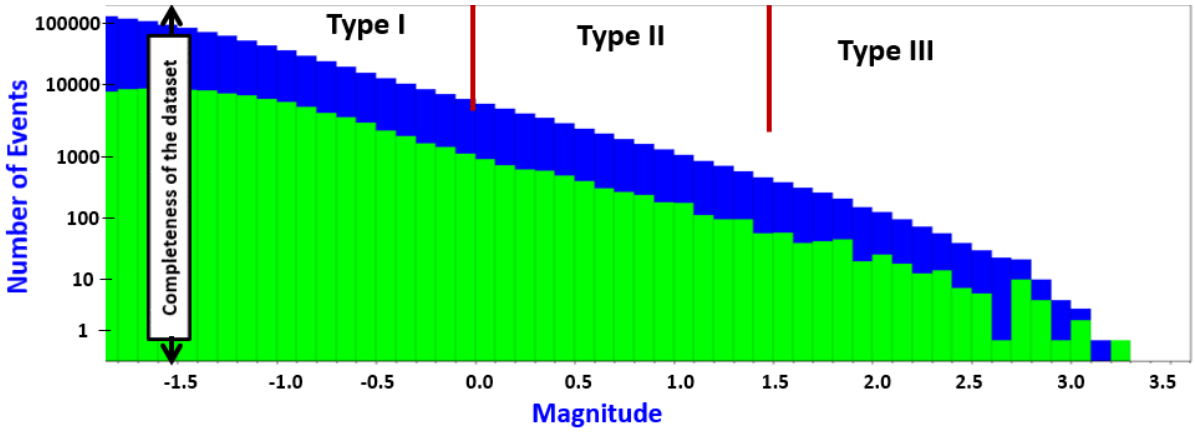

Figure 4.5: *The frequency-magnitude relation is not following an expected power law. Green colour: represent the number of seismic events with given magnitude, blue colour: events with magnitude greater than the given one.*

The b-value (slope) parameter describes large event frequency as compared to that of the small seismic events within the database. It is a seismic hazard indicator parameter. The database with b=0.6 has more occurrence of large events than a database of b=1.3 with the same a-value. When analyzing an individual, localized group of seismic events, the b-value may show too much variation depending upon the mechanisms of seismicity in the database. The b-value frequently ranges from 1.2 to1.5 for events caused by stress change due to mining (Legge and Spottiswoode, 1987; Hudyma *et al.*, 1995) and less than 0.7 due to a geological feature (e.g fault-slip).

4.2.3 Ratio of S- wave to P- wave energy

Seismic events comprise a compressional wave (P- wave) and a shear wave (S-wave). The P-wave velocity in a hard rock range from 5500 – 6500 m/s and S-wave from 3000 – 3500 m/s. P-waves are usually faster and arrive before the S-wave to the sensor. Equation 4.1 can be used to calculate the amount of energy in the S- wave and P- wave. For a fault-slip, S- wave exhibits significantly more seismic energy than P- wave (Boatwright and Fletcher, 1984). Figure 4.6 indicates a typical waveform and the S- wave and P- wave arrival time.

The S- wave (E_S) to P- wave (E_P) energy ratio (E_S: E_P ratio) can be used as an indicator in providing information about the likely source mechanism of a seismic event (Gibowicz and Kijko, 1994) but according to Morkel et al. (2019) the parameter is not reliable. In this section, the reliability of the energy ratio parameter (E_S: E_P ratio) was assessed.

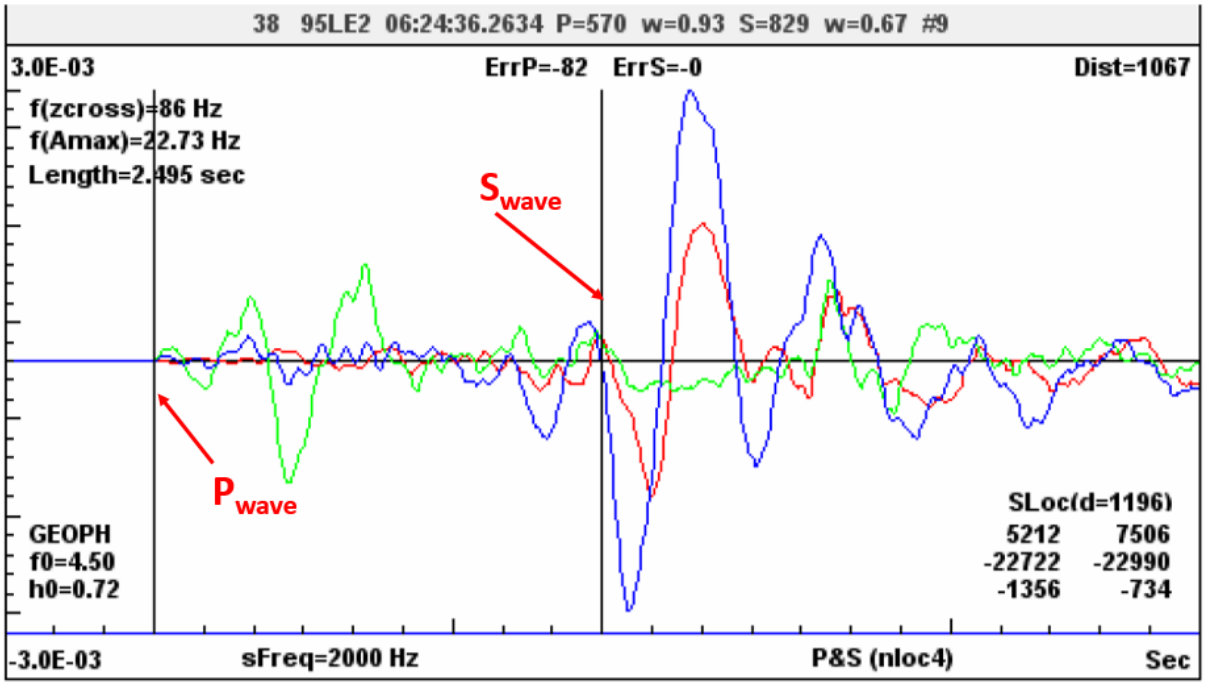

Figure 4.6: *A tri-axial waveform indicating both the P-wave and the S-wave.*

In previous studies, seismic events with a ratio of E_S:E_P <10 were regarded as indicative of a non-shear (tensile) failure mechanism, while a shear failure mechanism was indicated by a larger energy ratio (E_S:E_P >10) (e.g Gibowicz *et al*., 1991; Gibowicz and Kijko, 1994). Events with energy ratios 1< E_S:E_P <7 are associated with tensile seismic source mechanisms (Hudyma and Potvin, 2008; Gibowicz, 1992). The literature also indicated that 7< E_S:E_P <10 indicates a mix of seismic source mechanisms. McGarr (1984) and Gibowicz and Kijko (1994) determined that seismic events with large moment magnitudes exhibit a high E_S:E_P ratio, while Boatwright and Fletcher (1984) found that natural shear seismic events had E_S:E_P in the order of 20–30. Figure 4.7 below indicates the locations of seismic events with different seismic source mechanisms at Kloof Gold Mine based on their E_S:E_P ratios.

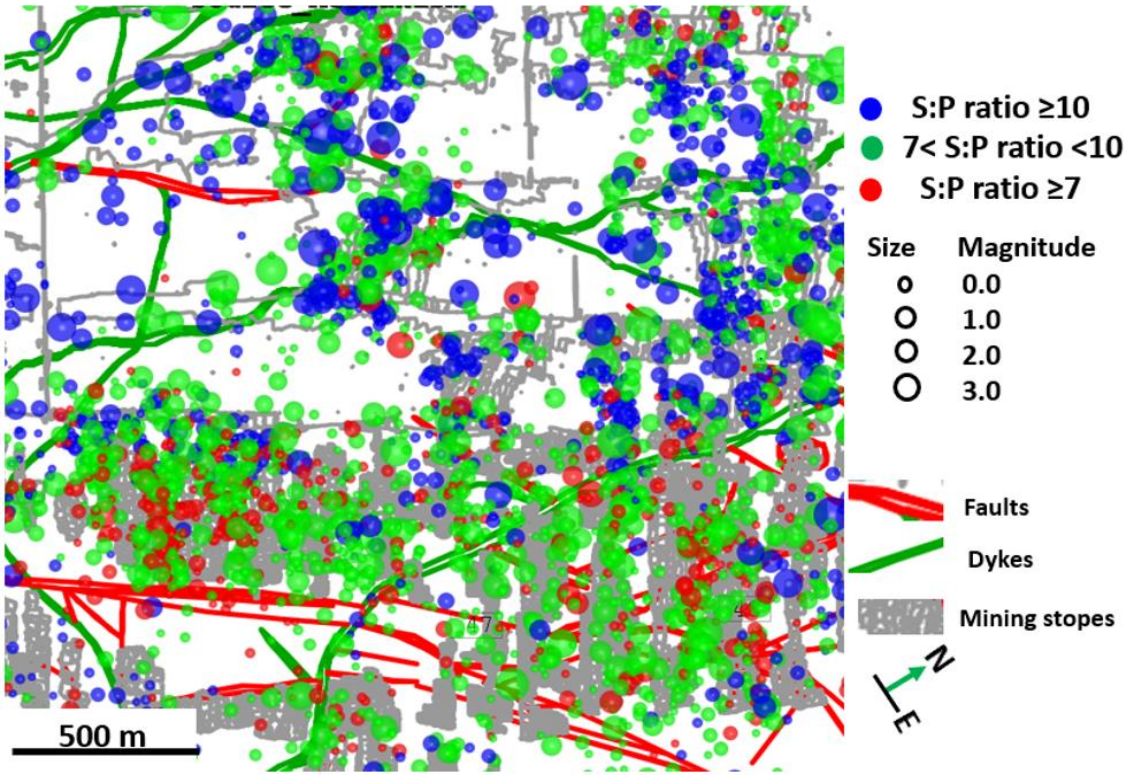

Figure 4.7: *Different seismic source mechanisms illustrations based on the energy ratio (E_S:E_P). Blue representing shearing type (E_S:E_P ratio>10), Blue is the Non-Shear (E_S:E_P ratio<7) and Red representing the mix mechanism source type (7< E_S:E_P <10).*

The source parameter used to classify specifically mining-induced seismic events was the Es/Ep ratio in the past years, some recent example includes Wesseloo and Sweby (2008), Disley (2014), Abolfazlzadeh et al (2019).

4.3 Source representation

Summarised conditions to be met for the occurrence of a seismic event (Jager and Ryder, 1999) including those occurring in mining-induced shear fracture are:

- A zone of overstressed rock must first exist in a state of unstable equilibrium,
- Sufficient stress change should occur to trigger a seismic event, and
- The rupture of intact rock or slip along a pre-existing geological weakness such a fault should produce a significant and rapid stress drop.

4.3.1 Fault plane geometry and focal mechanism

The fault plane geometry is well represented when a failure occurs along a plane of weakness within the rock mass. The shear stress drives failure along that plane (Figure 4.8). The seismic event severity and the amount of the slip depend on the shear-strength properties of a plane (Ryder and Jager, 2002). In

examining a fault plane, the assumptions are that the seismic energy is radiated from a planar surface. The wavefront is circular in an isotropic medium. The lobes show variations in the amplitude and polarity of the particle motion experienced in the 'far-field,' i.e., a distance away from the source that is several times greater than the rupture size. The ground motion recorded by a particular sensor depends on the position of the hypocenter and sensor, the orientation of the rupture plane, and the direction of the slip vector. Some sensors will experience a first motion that is 'push' away from the source, others a 'pull' towards the source, while those along the projections of the fault and auxiliary nodal plane will experience minimal ground motion.

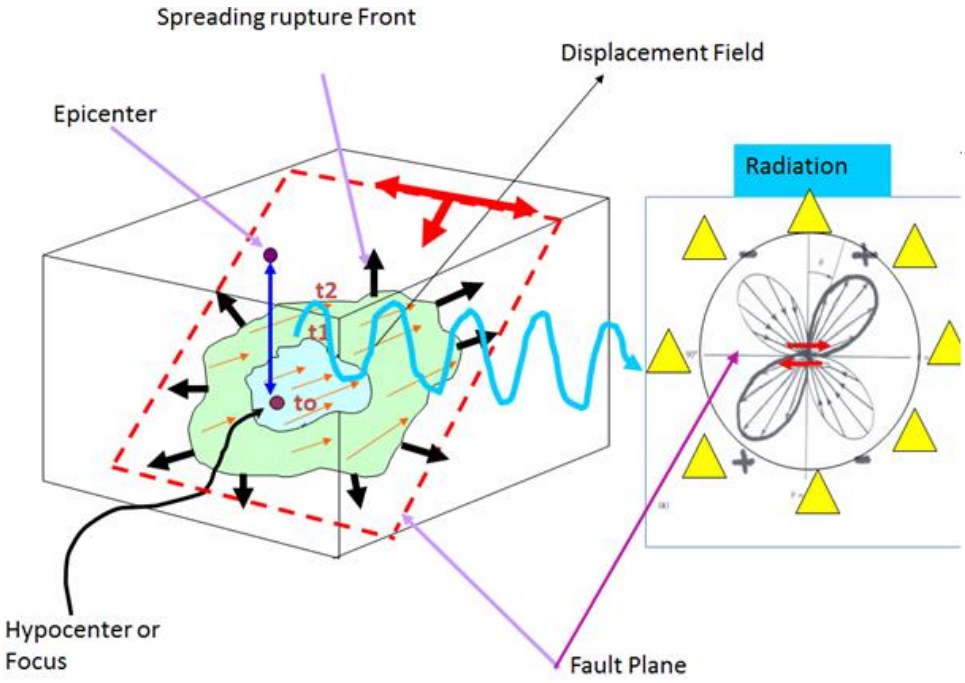

Figure 4.8: *Schematic representation of a fault plane, displacement field and spreading rupture front in an elastic medium. Right: Systematic four-lobed distribution of compressional (+) and dilatational (-) wavefronts of a P-wave radiation pattern (see section 4.3.2.1): Yellow triangles: geophones (Masethe, 2012)*

Fault geometry is represented by either three angles (parameters): strike, dip, and slip or two orthogonal vectors, fault normal and slip vector. Figure 4.9 illustrates the fault plane where the strike is denoted as (ϕ_f), the intersection of the earth's surface and the fault define it. The strike angle is measured from the north in a clockwise direction from 0° to 360° angle in a horizontal plane. The dip angle of the fault plane, denoted as (δ), gives the fault plane orientation with respect to the earth's surface and it ranges from 0° to 90°. The slip (rake) angle (λ) represent the direction of the rock movement on either side of the fault and is measured from x_1-axis (Stein and Wysession, 2003).

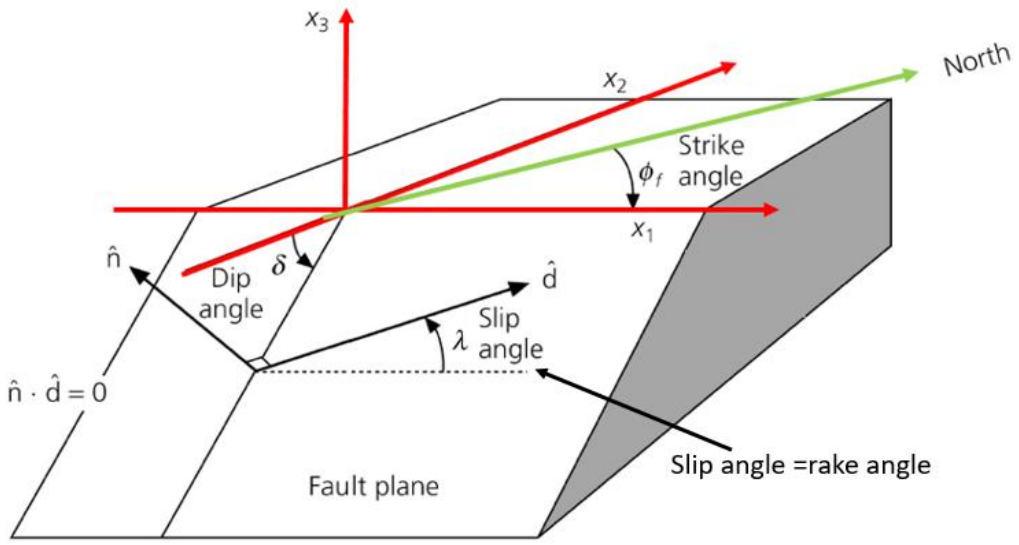

Figure 4.9: *Geometry of a fault plane when studying earthquakes. The Cartesian coordinate system is defined by the axes x_1, x_2 and x_3. The normal vector, slip vector, dip angle, slip angle and strike angle are defined following Stein and Wysession (2003).*

The fault plane is characterised by both the normal vector $\underline{n}$ and the slip vector $\underline{d}$. The normal and slip vector to the plane in the Cartesian coordinate system are given by:

$$\bar{n} = \begin{bmatrix} -\sin\delta \sin\phi_f \\ -\sin\delta \cos\phi_f \\ \cos\delta \end{bmatrix} \quad \text{and} \quad \bar{d} = \begin{bmatrix} \cos\lambda \cos\phi_f + \sin\lambda \cos\delta \sin\phi_f \\ -\cos\lambda \sin\phi_f + \sin\lambda \cos\delta \cos\phi_f \\ \sin\lambda \sin\delta \end{bmatrix}$$

The slip vector ($\underline{d}$) is an indication of the direction in which the foot wall (lower side) will move with respect to the hanging wall (upper side). The normal vector $\underline{n}$ represents the vector perpendicular to the slip vector $\underline{d}$ and the null vector- $\underline{b}$. Both $\underline{n}$ and $\underline{d}$ vectors are normal to the null vector $\underline{b}$ (Stein and Wysession, 2003). The vectors $\underline{n}$ and $\underline{d}$ can be described in a geographic coordinate system with x pointing North, y pointing West and z pointing up.

Several basic fault geometries depending on the slip angle are represented below (Figure 4.10). One type of the basic fault geometries describes the dip-slip motion and the other type of strike-slip motion (e.g when slipping on the hanging wall occurs parallel to the x_1 – axis and is called *strike-slip fault* and when a slip occurs parallel to the x_3 – axis is known as a *dip-slip fault*).

According to Stein and Wysession (2003), geometries of fault planes can be characterised by the hanging wall movement and the slip angle (λ) (Figure 4.10):

- When the slip angle of λ=0° (equal to the x_1 – axis), then the hanging wall will move to the right and the movement would be called a *left-lateral strike-slip fault.*
- When the hanging wall moves instead in the opposite direction of λ=0°, i.e., λ=180° the movement is then known as a *right-lateral strike-slip fault.*
- When the movement of the hanging wall is at λ=90°, the movement would be known as the *reverse dip-slip fault* and lastly;
- For a movement in the opposite direction λ=90°, i.e., λ=270°, the movement is known as a *normal dip-slip fault.*

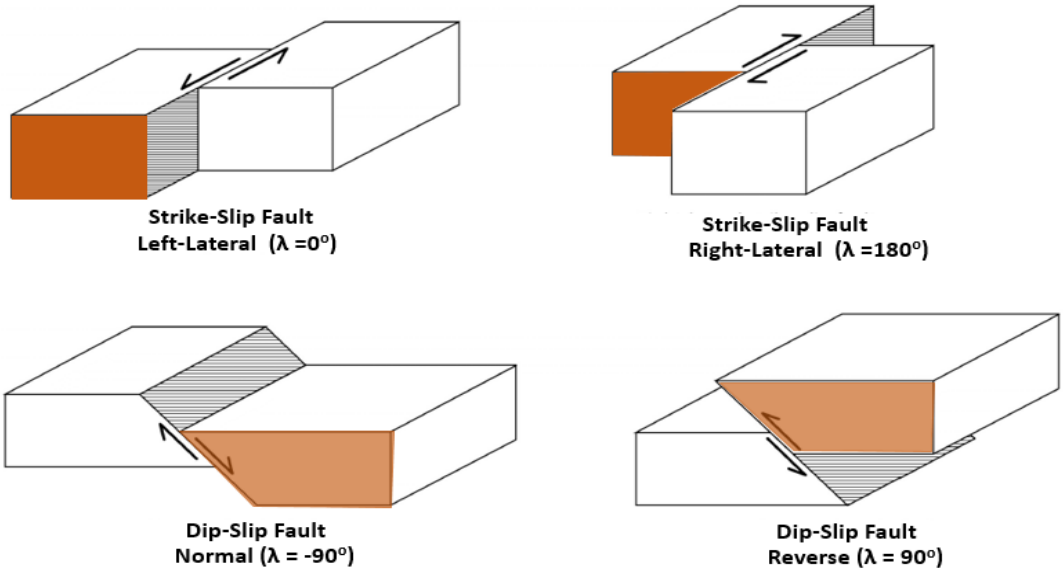

Figure 4.10: *Basic types of faulting with strike-slips (the upper row) and dip-slips (the lower row), (after Stein and Wysession, 2003).*

4.3.2 Focal mechanism

A mathematical or geometric representation of the faulting (double-couple source representation) during the earthquake/seismic event is called a focal mechanism. It simply represents a mechanism of a seismic source and explains the source region's inelastic deformation that generates the seismic wave. The aim of focal mechanism studies is to determine the seismic fault model by finding the nodal planes of the observed polarity of P-waves radiated from a hypocenter. Once the orientation of the nodal planes has been determined, the solution is referred to as the fault-plane solution. A focal mechanism is a geometrical representation known as a "beach ball" that describes the faulting geometry during a seismic event using seismograms recorded at various distances and azimuths. It indicates the radiation pattern of the seismic waves, which depends on fault geometry (Stein and Wysession, 2003). A focal mechanism can be obtained using seismic source theory and the source radiation pattern.

4.3.2.1 Radiation pattern

The radiation pattern is generated by a set of forces with a corresponding geometry. P- and S-waves radiation pattern can be obtained using the theory of seismic sources. The radiation pattern due to motion on a fault plane is what would occur for a pair of double couple, pair of forces with opposite direction, a small distance apart (Stein and Wysession, 2003).

To see how the radiation pattern vary with the direction of the receiver, consider the radiation field in spherical coordinates, where (θ) is measured from the x_3 axis and ($\emptyset$) is measured in the x_1-x_2 plane.
First motion (polarity) of P-wave arrival picks vary depending on the direction to the seismic station (receiver) relative to the source, and the motion or polarity (compression or dilatation) of P-wave first arrivals. In spherical coordinate system this position is defined by two angles θ and $\emptyset$ (Figure 4.11). In the cartesian coordinate system on this figure the fault plane lies in $x_1 – x_2$ plane and is normal to x_3 axis. The slip vector is in the fault plane, parallel to x_1 axis. The angle is measured from the x_3 – axis - the normal vector to the fault plane, and is the angle measured from x_1-axis in the $x_1 – x_2$ plane as shown in Figure 4.11.

The amplitude and polarity of P- and S-waves are affected by the receiver's (geophone's) position relative to the source (so-called P- and S-wave radiation patterns). For a shear source (slip on a fault), the radiation pattern will be equivalent to the pattern created by a set of force couples (double couple), the equivalent body forces. The geometry of the wavefront radiated by the shear source is illustrated below (Figure 4.11). Around the source, there are quadrants where the initial motion of the P-arrival would be either dilatation (down) or compressional (up).

In the spherical coordinate system, the orientation of the receiver is described by θ (measured from the x_3-axis) and the angle ϕ in x_1-x_2 plane measurement (Figure 4.11).

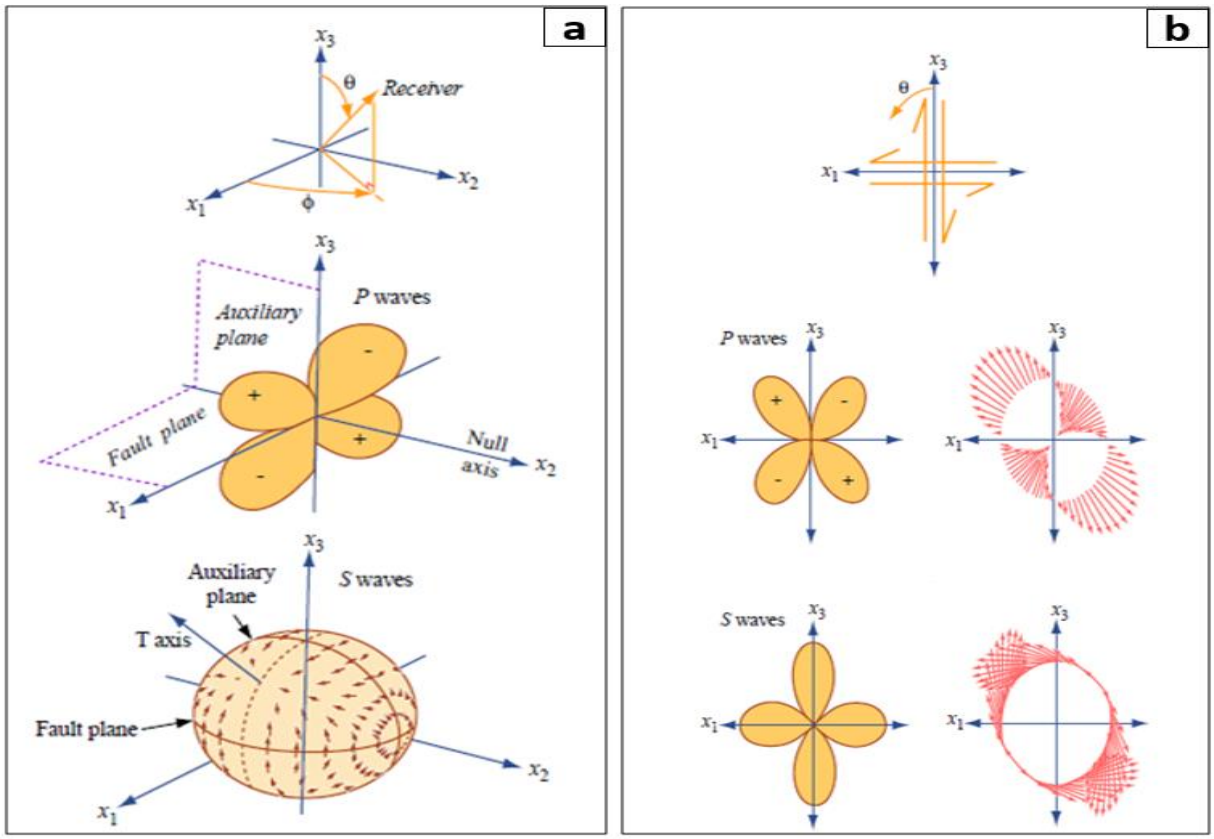

Figure 4.11: *(a) Schematic representation for the double couple source body wave radiation pattern, (b) Radiation patterns on x_1-x_3 plane of the P and S waves (after Stein and Wysession, 2003; pp. 221).*

The seismic source theory states that radial components will be present in the displacement caused by compressional waves far from the source, because their motion is along the propagation. This is represented by (Stein and Wysession, 2003):

$$u_r = \frac{1}{4\pi\rho\alpha^3 r}\dot{M}\left(t-\frac{r}{\alpha}\right) sin\ sin\ 2\theta\ \ cos\ cos\ \emptyset \qquad [4.9]$$

Where: $\frac{1}{4\pi\rho\alpha^3 r}$ represents the amplitude that decays $\frac{1}{r}$

$\dot{M}\left(t-\frac{r}{\alpha}\right)$ is the source time function representing pulse radiated away from the source with the P-wave velocity α, and arriving at distance r at time $t - r/\alpha$

$sin\ sin\ 2\theta\ \ cos\ cos\ \emptyset$ describes the P-wave radiation pattern

For shear waves the displacement has two components, u_θ and $u_\emptyset$ where:

$$u_\theta = \frac{1}{4\pi\rho\beta^3 r}\dot{M}\left(t-\frac{r}{\beta}\right) sin\ sin\ 2\theta\ \ cos\ cos\ \emptyset \quad [4.10]$$

$$u_\emptyset = \frac{1}{4\pi\rho\beta^3 r}\dot{M}\left(t-\frac{r}{\beta}\right)(-\ cos\ cos\ \theta\ \ cos\ cos\ \emptyset\ ) \quad [4.11]$$

Where: the term $\dot{M}\left(t-\frac{r}{\alpha}\right)$ represents the source time function and corresponds to a wave propagating at the S-wave velocity β.

Since the radiated seismic waves vary as a function of θ and $\emptyset$, seismograms recorded at different direction from the seismic event can be used to determine the fault geometry.

$\dot{M}\ (t)$ is called source time function or seismic moment rate function. It is the time derivative of the seismic moment

$$M(t) = \mu D(t)S(t), \quad [4.12]$$

describing the faulting process in terms of the rigidity (μ), slip on the fault $D(t)$ and the fault area $S(t)$.

4.3.2.2 First Motion

The first motion (polarity) of body waves serves as the foundation for the most straightforward way for calculating the focal mechanism of the seismic source. There are more advanced methods that make use of body wave waveforms. All methods make use of the fact that the pattern of the energy radiated depends on the fault geometry (focal mechanism) and first polarity of the body waves, and their amplitudes fluctuate depending on where the seismic station (sensor) is in relation to the seismic source (Stein and Wysession, 2003).

The projection of upward and downward motions on the focal sphere located at the hypocenter location defines four quadrants for a double-couple source (two compressional and two dilatational) (Stein and Wysession, 2003). Division between the quadrants occurs along the so called "nodal planes" (Figure 4.12). However, both nodal planes present the same first motion slips so first motions alone cannot resolve which of these planes describes the real fault plane

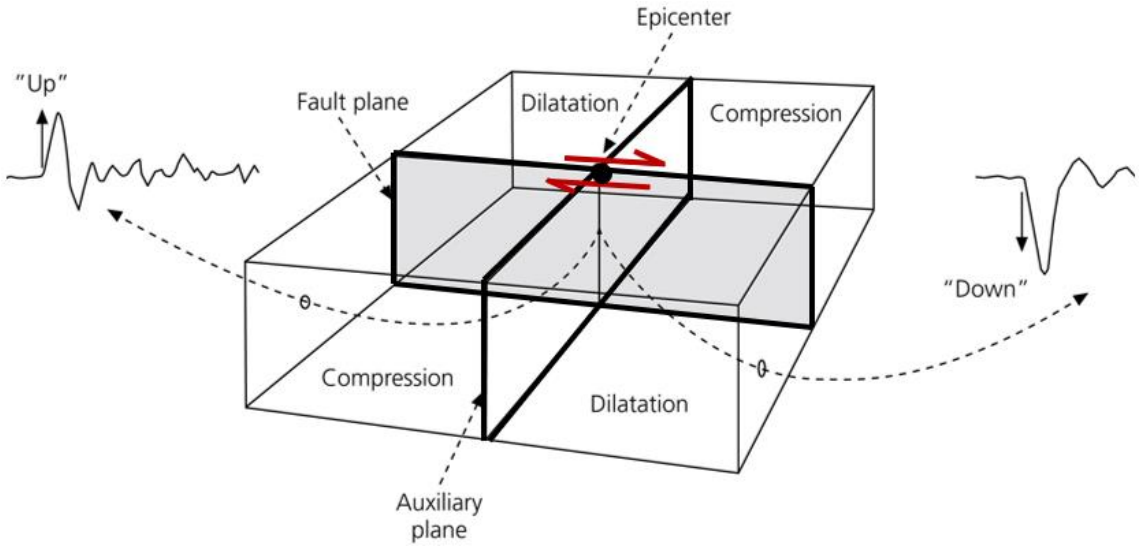

Figure 4.12: *First motion of P-waves observed. The two nodal planes (fault plane and auxiliary plane) separate regions of compressional and dilatational first polarity of first arrivals (from Stein and Wysession (2003))*

Calculation of the focal mechanism is determined using the polarity of P-wave first motion. The procedures in the IMS software were developed to follow the method of Hardebeck and Shearer (2002). Description of some necessary steps in the process of focal mechanism includes:

- Pre-processing of data
    - Source location
    - Station locations
    - P-wave polarities
    - Seismic velocity model
    - Computed ray azimuths
    - Computed take-off angles
- Acceptable solution calculations
    - The grid search is being applied to find acceptable solutions
    - All solutions which do not fulfil the set criteria are re-calculated with new input parameters.
- Re-calculating using the seismic velocity model
    - Another seismic velocity model is chosen from other possible models
    - Findings of all acceptable solutions
- Compilation of results.
    - Compiling of all acceptable solutions sets.
    - The outliers are removed.
    - A solution is compiled as an average of all acceptable (possible) solutions

4.3.3 Stress orientation

Information about the stress orientation in the seismic source area can be obtained using the focal mechanism. The stress tensor can be represented by three mutually perpendicular vectors: - P, T, and B. The P-axis represent the “pressure” direction and is oriented in the centre of the dilatation quadrant; the T-axis represent the “tension” direction and is oriented in the centre of the compressional quadrant, while the B (or null) -axis is orthogonal to the slip vector (Figure 4.13). This classification (B-, T- and P- axes) does not map the stress axes perfectly.

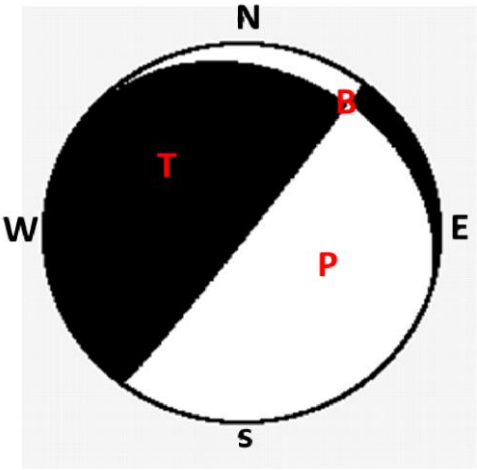

Figure 4.13: *Beachball diagram with defined Tension (T-), Pressure (P-) and B-axes. Dilatational quadrants are shade white and compressional quadrants are in black.*

4.3.4 Seismic moment tensor inversion

“Moment tensor inversion is often deemed to be the best method or approach to studying failure mode of a mining-induced seismic event” (Gibowicz and Kijko, 1994). A mining-induced seismic event's seismic moment tensor serves as a generic description of the seismic source, which may consist of several force pairs of different directions. A distribution of forces for a fault model can be created that results in precisely the same displacement as a slip on an internal fault. For the fault model, the forces are referred to as equivalent body forces (Shearer, 2009).

Force representations must conserve momentum within the elastic medium and can be made by two types of equivalent body forces, which are force couples and double couples. Force couples are made up of two opposing forces separated by a distance d (Figure 4.14a). Double couples are made up of two perpendicular pairs of force couples (Figure 4.14b). The two force couples form a balance with zero angular momentum.

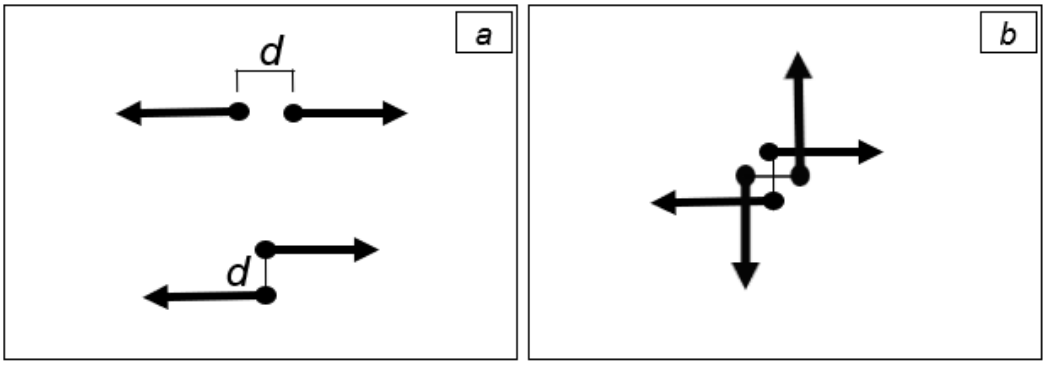

Figure 4.14: *(a) Force Couple and (b) Double Couple (Shearer, 2009).*

Components or force couples are used to represent the fault geometry. There are nine representations of the force couple, and their combinations can be used to describe different seismic sources (Figure 4.15). The moment tensor M_{kl} combines the force couples of a different orientation (Figure 4.14) and its moments thereby provide a general description of various seismic sources.

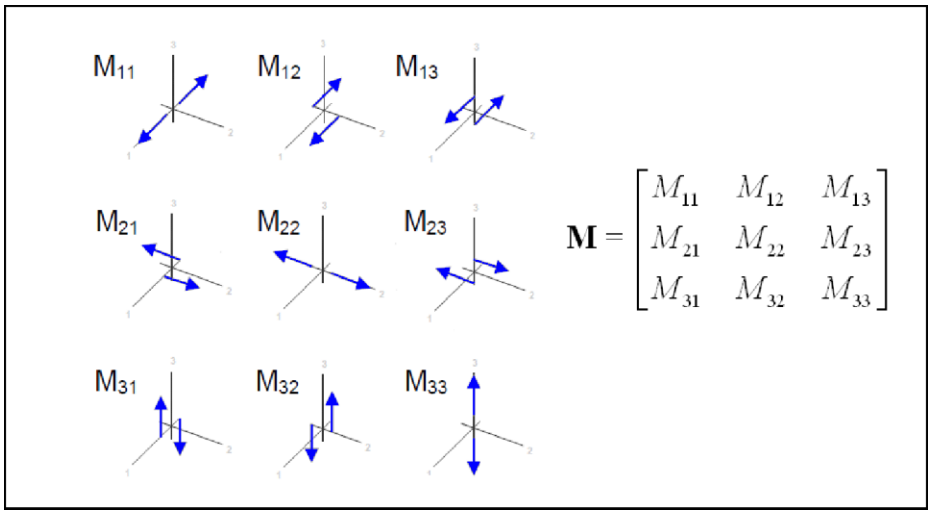

Figure 4.15: *A set of nine possible force couples of $\boldsymbol{M_{kl}}$, the indices k and l denote the directions of the force and arm couple of the moment tensor (after Aki and Richards, 1980).*

Equivalent forces acting on the source point can be expressed mathematically by means of the representative theorem (Aki and Richards, 2002, Eq. 2.41), assuming infinite homogeneous medium (Equation 4:13):

$$U_i(\boldsymbol{x}, t) = f_n * G_{ik} = \int_{-\infty}^{\infty} \iiint_V f_k(\boldsymbol{\xi}, \tau)\, G_{ik}(\boldsymbol{x}, t, \boldsymbol{\xi}, \tau)\, d\tau\, dV(\boldsymbol{\xi}) \qquad [4.13]$$

where $U_i = U_i(x,t)$ is the displacement field along the fault, observer's position vector is **x**, t represents time, and $G_{ik} = G_{ik}(x,t,\xi,\tau)$ is the Green's tensor. The Green's function gives the equation of motion

solutions for a point single force with time dependence of the Dirac delta function. It is defined as the ith force produced displacement component in the direction of x_k. The propagation effect on the seismic waves from a source to a receiver along a straight path is described by a vector $G_k(x, t, \xi, \tau)$ and is a function of the time τ and position vector ξ at the source. Integration of the function is on the focal volume V and the time τ.

The equivalent forces along the fault (ϑ) are described by $m_{kl} = m_{kl}(\xi, \tau)$ which is the moment tensor density. Equation 4.13 is an example of dipole forces replacing single force and leading to modified equation (4.14) to (4.15) as explained in Burridge and Knopoff (1964) and Eq. 3.20, in Aki and Richards (2002).

$$U_i(\boldsymbol{x}, t) = \int_{-\infty}^{\infty} \iint_{\vartheta} m_{kl}(\boldsymbol{\xi}, \tau) \frac{\partial}{\partial_{\xi_l}} G_{ik}(\boldsymbol{x}, t, \boldsymbol{\xi}, \tau)\, d\tau\, d\vartheta(\boldsymbol{\xi}) \qquad [4.14]$$

A simpler point source approximation can be used in cases where the fault size is less than the distance of the source to the receiver, then the equation could be represented as Equation 4.15 below:

$$U_i(\boldsymbol{x}, t) = \int_{-\infty}^{\infty} M_{kl}(\tau) \frac{\partial}{\partial_{\xi_l}} G_{ik}(\boldsymbol{x}, t, \boldsymbol{\xi}, \tau)\, d\tau, \qquad [4.15]$$

This simply means $U_i = M_{kl} * G_{ik,l,}$ where the symbol " $*$ " represents convolution and $M_{kl} = M_{kl}(t)$ is the seismic moment tensor. Equation 4.16 represents the integration over the fault ϑ and results in seismic moment tensor **M** with nine force couples.

$$M_{kl} = \iint_{\vartheta} m_{kl} d\vartheta \qquad [4.16]$$

The moment tensor M_{kl} represents a seismic source; it is decomposed and diagonalised into elementary parts. The deviatoric can be decomposed into three double couples (Jost and Herrman, 1989):

- Minor and major double couples (Kanamori and Given, 1981, Wallace 1985),
- Double couple with the same T axis (Wallace, 1985) or a
- Compensated Linear Vector Dipole (CLVD) and Double Couple(DC) component (Knopoff and Randall, 1970).

Both the CLVD and DC decomposition components are widely accepted and proven beneficial in Moment Tensor physical interpretation. (Vavryčuk, 2014).

Figure 4:16 indicates various selected seismic source moment tensors and their beach-ball graphical representations (Stein and Wysession (2003)). In the table

- Isotropic sources are shown in the top row (left (explosive source) and right (implosive source)).
- Double couple sources are shown in rows 2 to 4.
- Compensated linear vector dipole (CLVD) sources are equivalent to tensile failure, and these corresponds to rows 5 to 6.

Moment tensor	Beachball	Moment tensor	Beachball
$\frac{1}{\sqrt{3}}\begin{pmatrix}1&0&0\\0&1&0\\0&0&1\end{pmatrix}$		$-\frac{1}{\sqrt{3}}\begin{pmatrix}1&0&0\\0&1&0\\0&0&1\end{pmatrix}$	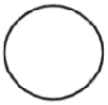
$-\frac{1}{\sqrt{2}}\begin{pmatrix}0&1&0\\1&0&0\\0&0&0\end{pmatrix}$		$\frac{1}{\sqrt{2}}\begin{pmatrix}1&0&0\\0&-1&0\\0&0&0\end{pmatrix}$	
$\frac{1}{\sqrt{2}}\begin{pmatrix}0&0&-1\\0&0&0\\-1&0&0\end{pmatrix}$		$\frac{1}{\sqrt{2}}\begin{pmatrix}0&0&0\\0&0&-1\\0&-1&0\end{pmatrix}$	
$\frac{1}{\sqrt{2}}\begin{pmatrix}-1&0&0\\0&0&0\\0&0&1\end{pmatrix}$		$\frac{1}{\sqrt{2}}\begin{pmatrix}0&0&0\\0&-1&0\\0&0&1\end{pmatrix}$	
$\frac{1}{\sqrt{6}}\begin{pmatrix}1&0&0\\0&-2&0\\0&0&1\end{pmatrix}$		$\frac{1}{\sqrt{6}}\begin{pmatrix}-2&0&0\\0&1&0\\0&0&1\end{pmatrix}$	
$\frac{1}{\sqrt{6}}\begin{pmatrix}1&0&0\\0&1&0\\0&0&-2\end{pmatrix}$		$-\frac{1}{\sqrt{6}}\begin{pmatrix}1&0&0\\0&1&0\\0&0&-2\end{pmatrix}$	

Figure 4.16: *Moment tensors and their representation as beach-ball diagrams (extracted from Stein and Wysession, 2003)*

The source description is conveniently represented by M_{kl} which is the seismic moment tensor. It explains the theoretical relation at the source between the ground motions at the geophone (station) and the moment released. The seismic moment tensor is a second-order three-by-three symmetric tensor describing the seismic source varieties. It consists of nine couples of equivalent body forces expressed mathematically (Aki and Richards, 1980). The nine possible couples of a moment tensor M_{kl} are indicated in Figure 4.15; the subscripts k and l denote force directions and the couple's arm. Since *k* and *l* can either be 1, 2, or 3, a local geographic coordinates system is often used to define a Cartesian system tensor. Force couples where both the arm and the force are in the same direction represent either a vector dipole or vector couples without a moment. The remaining vector dipoles have a non-zero moment.

Aki and Richards (1980) described a *moment tensor inversion* as "the equivalent forces of a general seismic point source and can be used to describe the seismic radiation pattern and the strength of a seismic point source." The moment tensor M may be expressed in matrix notation, as in Figure 4.15. For a location of a seismic source at (ξ_1, ξ_2, ξ_3) and sensor (receiver) at (x_1, x_2, x_3), the far-field expression in the kth direction for the displacement (μ_k) would be expressed as Equation 4.17 (Pujol and Herrmann ,1990) below:

$$\mu_k = \frac{1}{4\pi\rho\alpha^3}\gamma_k\gamma_i\gamma_j\frac{1}{r}.\dot{M}_{IJ}\left(t-\frac{r}{\alpha}\right) - \frac{1}{4\pi\rho\beta^3}(\gamma_k\gamma_i - \delta_{ki})\frac{1}{r}.\dot{M}_{IJ}\left(t-\frac{r}{\beta}\right) \quad [4.17]$$

where:

ρ indicates density,

α is the P- wave velocity and β is the S-wave velocity,

$r = |x - \xi|$ is the distance between the source and receiver,

$\gamma_i = \frac{(x_i - \xi_i)}{r}$ are the direction cosines between source and receiver,

δ_{ij} is the Kronecker delta (δ_{ij} = *1* for *i = j,* and δ_{ij} = *0* for *i ≠ j*).

$\dot{M}_{IJ}$ Indicates the derivative with respect to time.

The moment tensor inversion problem can be described by a system of linear equations and can be represented in matrix-vector form [for full details, see Pujol and Hermann (1990)]:

$$\begin{bmatrix} u_1 \\ u_2 \\ \vdots \\ u_6 \end{bmatrix} = \begin{bmatrix} G_{11} & G_{12} & \cdots & G_{16} \\ G_{21} & G_{22} & \cdots & G_{26} \\ \vdots & \vdots & \ddots & \vdots \\ G_{n1} & \cdots & \ldots & G_{n6} \end{bmatrix} \begin{bmatrix} m_1 \\ m_2 \\ \vdots \\ m_6 \end{bmatrix}$$

where u is the ground displacement observed; n represent seismograms numbers, in most cases $n \gg 6$; while G are the Green's functions and

$$m_1 = M_{11}, m_2 = M_{12}, m_3 = M_{13}, m_4 = M_{22}, m_5 = M_{23}, m_6 = M_{33}$$

A seismic moment tensor can be fully decomposed into isotropic (M_{iso}) and deviatoric (M_{dev}) tensors (Figure 4.17). The deviatoric component can be decomposed further into compensated linear vector dipole (M_{CLVD}) and double couple (M_{DC}). Their proportions add up to 100% (i.e., M_{DC}% + M_{ISO}% + M_{CLVD}% = 100%). The decomposition of the moment tensors into isotropic tensor (M_{iso}) and the deviatoric tensor (M_{dev}) is unique. The M_{iso} tensor radiates only P waves, Rayleigh waves, and spheroidal normal modes with no directional preference (Dahm and Krüger, 2014). The M_{dev} often has no direct geological meaning and is therefore further decomposed into different geologically reasonable sources. Several decompositions have been suggested for the deviatoric tensor, for instance (e.g., Jost and Herrmann, 1989 and Figure 4.17):

- a best double-couple (DC) and a CLVD,
- a strike slip, a pure dip slip, and a vertical compensated linear vector dipole (vs CLVD),

- an isotropic source and a mixed mode double couple and tensile crack on the same crack (general dislocation source).

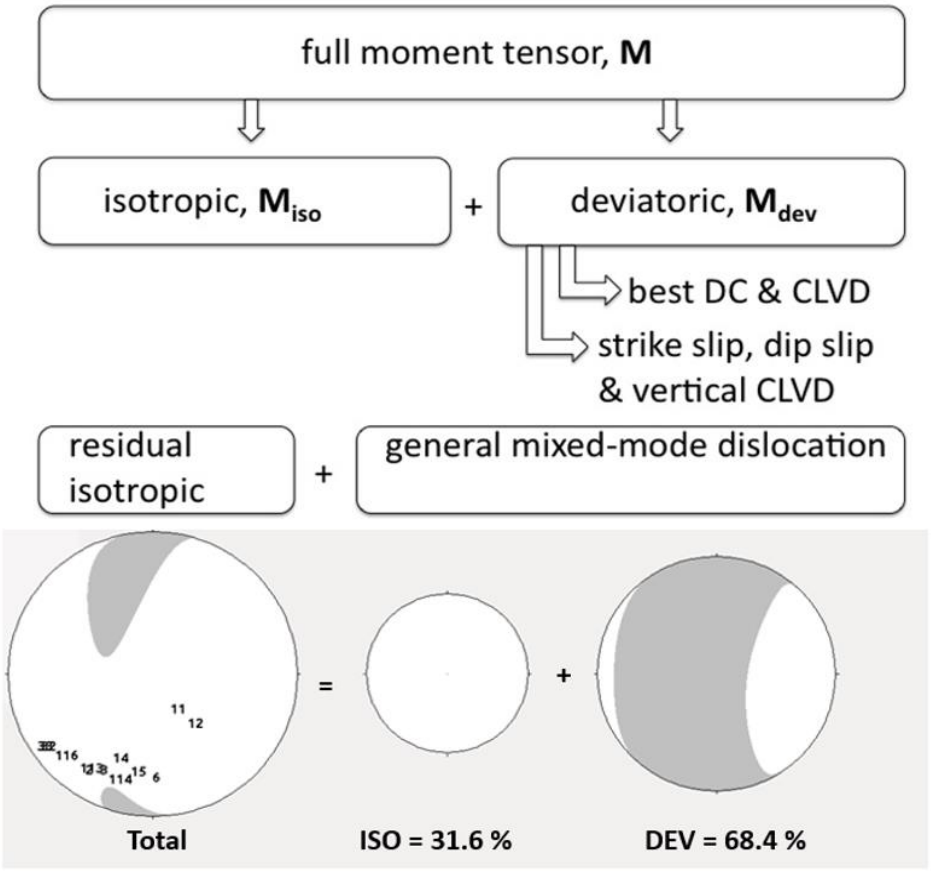

Figure 4.17: *The two possibilities to decompose a full moment tensor, either into an isotropic and deviatoric tensor or into a residual isotropic component and a general mixed-mode shear crack. The deviatoric component can be further decomposed into different elementary sources (e.g., Double Couple (DC) and compensated linear vector dipole (CLVD)) (modified from Dahm and Krüger, 2014).*

4.3.5 Moment tensor inversion in IMS TRACE software

The moment tensor inversion has been performed routinely by different authors (e.g., Aki and Richards, 2002; Ben-Menahem and Singh, 1981; Jost and Herrmann, 1989; McGarr, 1992b and Andersen, 2001).
It is the best approach when studying mining-induced seismic events modes of failure (Gibowicz, 1993). It provides a general framework to describe the seismic point source equivalent forces. The observed sources in mines can be compared to these equivalent forces (Jost and Herrman, 1989), which are (i) sudden

volume increase due to explosion failure, (ii) sudden volume decreases associated with implosion failure, and (iii) displacement on a fault.

The moment tensor inversion software IMS uses are based on an algorithm published by Vavryčuk and Kuhn (2012). The seismic moment tensor inversion is based on the amplitude and polarities of waveforms only and information is recorded at the seismic sensor site. It first inverts for the source-time function in the frequency domain. Using this source-time function, it inverts for the moment tensor in the time domain. This keeps the system of equations linear.

The following selection criteria were used by the author for quality control purposes: (i) at least 20 closest geophones were triggered around the seismic event; (ii) seismic events with locations in the central part of the in-mine seismic network and the 3D reflection seismic volume; (iii) a final seismic event selection was made after sorting the seismic events by recording stations with verified sensor orientations (misfit angle $<20^0$), (iv) correct picks of first arrival were performed, (v) high signal to noise ratio and (vi) accurate velocity model was used.

The moment tensor inversion method procedures consist of the following (Malovichko and Lotter, 2016):

- Input parameters for the inversion includes the
    - Seismograms
    - P- and S- waves arrival times (P- and S- picks)
    - Sensor parameters (co-ordinates, sensor type, natural frequency, sensitivity, spectral response and orientation)
    - Rock mass parameters (density (ρ), P- (α) and S-wave (β) velocities)
    - Seismic source parameters (origin time, location)
- The seismic data from pre-processing, automatic used by Trace software.
    - Estimation of the dominant period of every trace
    - P- and S-wave signal-to-noise ratio estimation
    - P-wave polarization estimation (direction of P-wave)
    - Waveform transformation into P-SV-SH wave co-ordinate system.
    - Selection of events with very good and clear P- and S- wave arrival with good signal-to-ratio
    - P- and S-wave polarity estimation
    - Manual re-location of selected seismic events with accurately picked arrival times.
    - P- and S-waves normalised spectra calculation
    - P- and S-waves normalised spectra fitting with Brune model
    - Normalised noise spectrum calculation
    - Spectral model fitting of normalized P, SV and SH spectra

- Calculation of Moment tensor parameters
    - Are based on a system of N linear equations that is composed as (Equation 4.18) (Malovichko and Lotter, 2016):

$$B.M = A \qquad [4.18]$$

or written out as

$$\begin{bmatrix} b_{11}\, b_{12}\, b_{13}\, b_{14}\, b_{15}\, b_{16} \\ b_{21}\, b_{22}\, b_{23}\, b_{24}\, b_{25}\, b_{26} \\ \vdots \quad \vdots \quad \vdots \quad \vdots \quad \vdots \quad \vdots \\ b_{N1} b_{N2} b_{N3} b_{N4} b_{N5} b_{N6} \end{bmatrix} \begin{bmatrix} m_{11} \\ m_{22} \\ m_{33} \\ m_{12} \\ m_{13} \\ m_{23} \end{bmatrix} = \begin{bmatrix} U^1.sign\,(U^{i(1)}) \\ U^2.sign\,(U^{i(2)}) \\ \vdots \\ U^N.sign\,(U^{i(N)}) \end{bmatrix}$$

Where:

B - Matrix containing directional angles between every station and the hypocentre,

M - Vector containing components of seismic moment tensor,

A - Contains information about the spectra and polarities of P-and S- waves on tri-axial sensors.

    - Triaxial, rotated to P, SV, SH
    - Normalization of the system
- Solution of the System

The solution of the system of N linear equations use Singular Value Decomposition and obtains

- Moment tensor components $m_{11}, m_{22}, m_{33}, m_{12}, m_{13}, m_{23}$

Figure 4.18 indicates the results (output) of the moment tensor. The moment tensor solution showed an ISO (of 23.7% indicating some burst), a CVLD (of 1.1 % indicating less stope closure), and a DC component of (75.2%) indicating more of a slip. The moment tensor (FPS) suggests that the seismic event was due to either NS (strike = 184^0, dip = 75^0 and Rake = 100^0) or NNE (strike = 38^0, dip = 18^0 and rake = 57^0) trending geological structures. The result of the moment tensor solution obtained for this seismic event is: M_{11} = - 0.22 x 10^{11} Nm; M_{12} = - 0.15 x 10^{11} Nm; M_{13} = + 0.01 x 10^{11} Nm; M_{22} = + 0.12 x 10^{11} Nm; M_{23} = - 0.65 x 10^{11} Nm; and M_{33} = - 0.61 x 10^{11} Nm. The misfit between the observed and synthetic data is 0.308 (this indicates 31% disagreement between the observed and synthetic data of the seismic waves and 69% agreement).

Reliable moment tensor results are dependent on (i) sensors' installation and polarity aligned with survey axes, (ii) correct good picks of the first arrivals, (iii) high signal to noise ratio, (iv) accurate velocity model, and good network coverage, among other things. Interpretation of the moment tensor gives insight into

whether the rockmass failed in tension, compression or shear and indicates the direction of movement and the failure plane.

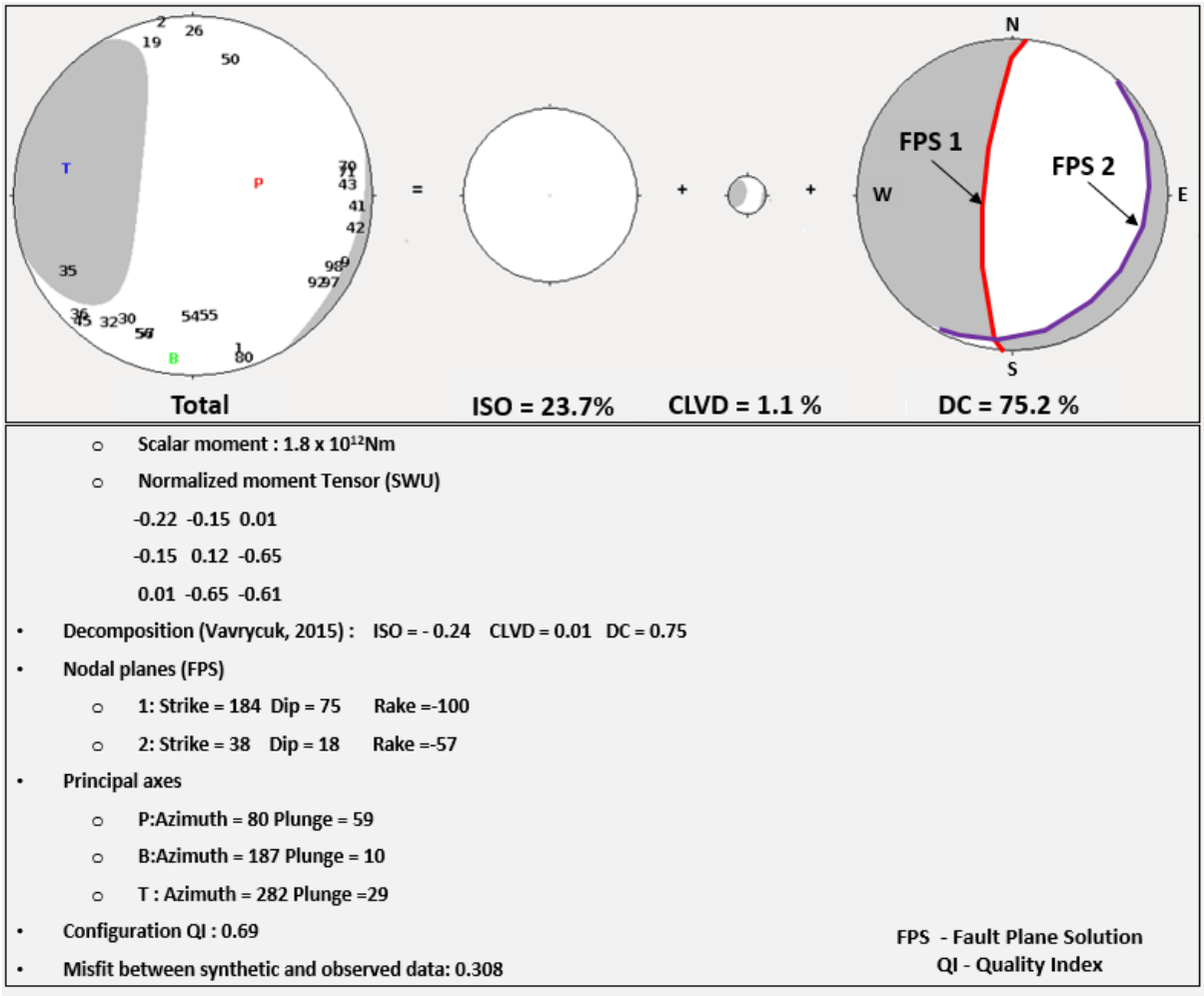

Figure 4.18: *Final results (Output) of the Moment tensor Inversion with components Pressure (P-), B orthogonal to the slip vector -, Tension (T-) axes. SWU-South-West Up.*

In mining seismology, moment tensor analyses have the potential to provide valuable insight into the physical mechanisms of large seismic events and associated fore- and aftershocks. It provides an improved determination of the orientation of the geological structures responsible for the seismic events (see Figure 4.10, section 4.3.1).

4.4 Data Discussions and Source Parameters Analysis

The seismic events data for this study was recorded by the mine-wide seismic system operating at Kloof Gold Mine. A set of 103,753 mining related seismic events ($-3 \leq M_L \leq 3$) was used for this study within the KEA seismic volume. The mining depth of these seismic events ranges from 1700 – 4000 m. The main criteria used to select a subset of events for detailed analysis were the number of stations that recorded the event and the azimuthal distribution of the sensors. The same combinations of sensors were used for

the Es:Ep and moment tensor inversion analyses. The author did the data analysis and the information is presented in Figures 4.17 to 4.23.

The study focused on 75 large (1.5≤ M_L ≤2.7) seismic events recorded at 20 or more sites and located within the central part of the in-mine seismic network and the 3D reflection seismic volume. The seismic events occurred between 1 January 2017 and 30 December 2018 near the reef elevation between - 2082 m and -3558 m (Figure 4.19). After sorting the seismic events by the number of recording stations with verified sensor orientations (misfit angle <20°) in descending order, a final selection was made. The selection criteria is likely to have excluded events occurring in virgin ground ahead of mining (as they would not have been surrounded by sensors or triggered by many sensors). For the seismic events classification study within the area of interest, the data used only two classification types, *viz.* Es/Ep<10 as non-shear (Gibowicz and Kijko, 1994) and Es/Ep>10 as shear (Boatwright and Fletcher,1984). The locations were determined manually using the IMS Trace software using the body wave arrival times (Mendecki, 1993, 1997). The source parameters for 75 selected events were calculated using the spectral method developed by Andrews (1986) within the IMS software, and later adapted by Richardson and Jordan (2002).

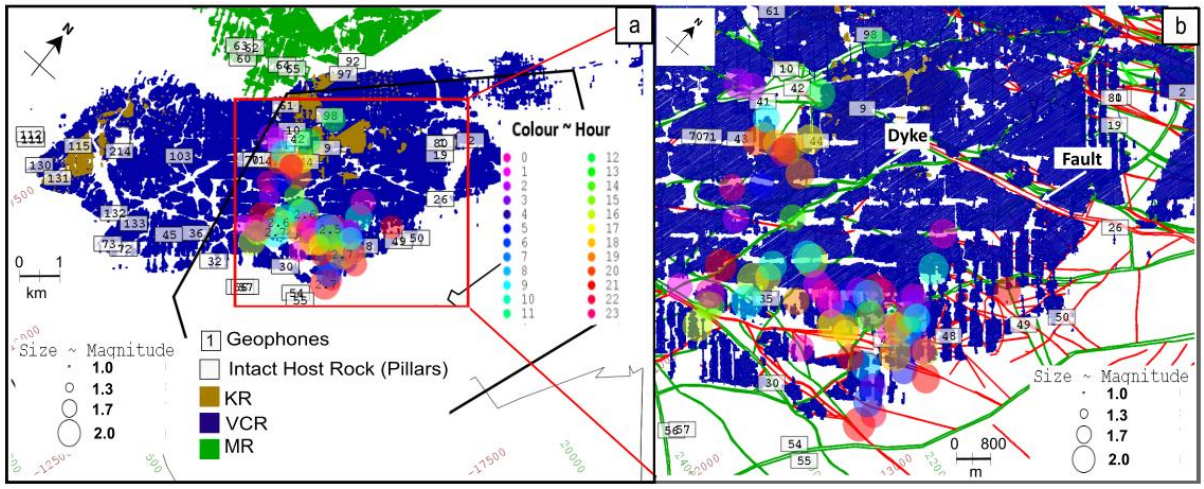

Figure 4.19: *(a) Mine plan view showing the location of seismic events (colored circles). (b) Zoomed-in view showing the spatial distribution of the seismic events, mining layout and the geology in the closer range (1 January 2017 and 30 December 2018). KR:Kloof Reef, VCR:Ventersdorp Contact Reef and MR:Main Reef.*

Seismic events were divided into two distinct failure modes (a mechanism) depending on their *Es/Ep* ratio: non-shear type events (NS, *Es/Ep* <10, 62 events) and shear-type events (FS, *Es/Ep* >10, 13 events). The fault slip events occur between 1600-4000 m (Figure 4.20) with a mean depth of 2500 m. In contrast, most non-shear events occurred between 2800-3200 m, with a mean depth of 2900 m. Figures 4.20 indicates that the distribution is more- or less symmetrical about the mean, and the mean is roughly similar to the reef elevation.

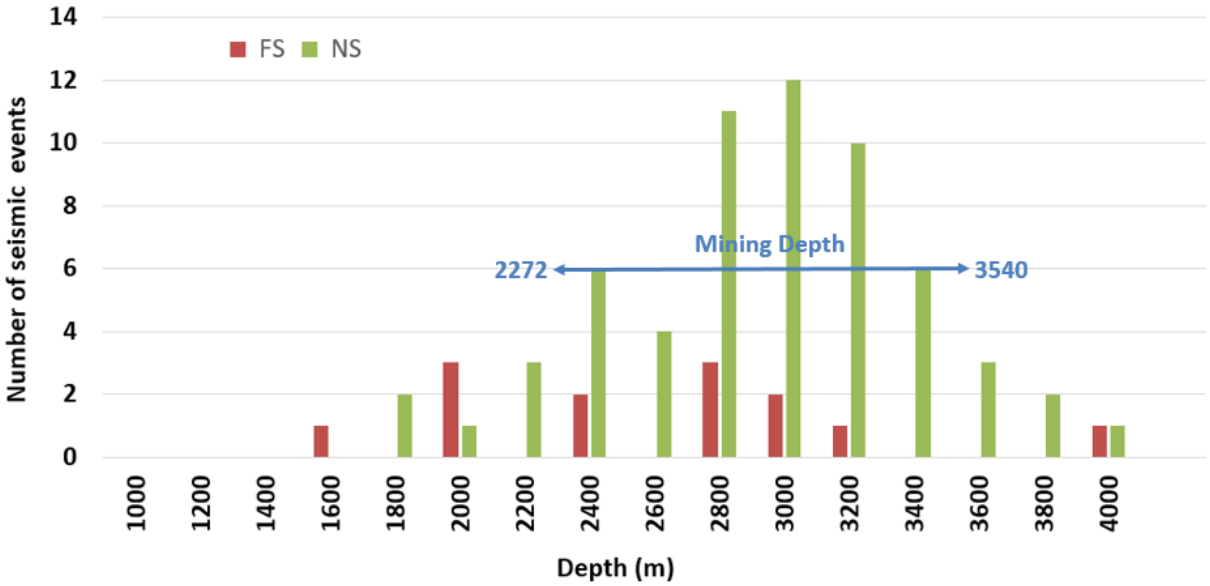

Figure 4.20: *The distribution of seismic events source mechanisms in different mining levels within the VCR orebody at an average depth of 3 000 m. Brown represents the Fault Slip (FS), and Green represents the Non-Shear (NS).*

The study indicates that 48% of recorded and selected seismic events occurred in the footwall of the VCR horizon within the quartzite formation. Several factors could have resulted in the location and mechanisms of these seismic events, including geological structures, mining methods, high-stress concentration, remnant and abutment.

In greater depths, less non-shear is observed within the VCR. The results indicate that the studied seismic events, both FS and NS, occurred mostly in the hanging wall (52%). Their spatial distribution on the section follows the dip of the reefs. When one looks at the dip of the ore body as the regression line within the ± 100m hypocentre location error (Figure 4.2a, section 4.1), most events will plot along with the dip of the ore body (VCR).

In general, FS seismic events have larger magnitudes than NS seismic events. The results agree with the widely accepted Ortlepp source mechanism classification (see Table 2.3 in Section 2.2.3) (Ortlepp and Stacey, 1994). In the current study, both the NS and FS mechanisms were obtained for local magnitudes up to 2.7. The energy ratio (*Es/Ep*) for NS events ranged from 1.1 to 9.4 and from 10.0 to 19.9 for FS events, respectively (Figure 4.21). The energy ratio (*Es/Ep*) for the FS seismic events is negatively related to the local magnitudes. The NS seismic events (*Es/Ep*) ratio increases slightly with the local magnitude (Figure 4.21). The NS and FS seismic events indicated a weak correlation coefficient on (*Es/Ep*) ratio versus the local magnitude. Hence, a conclusion can be made that there is no trend in the energy ratio depending on the local magnitude.

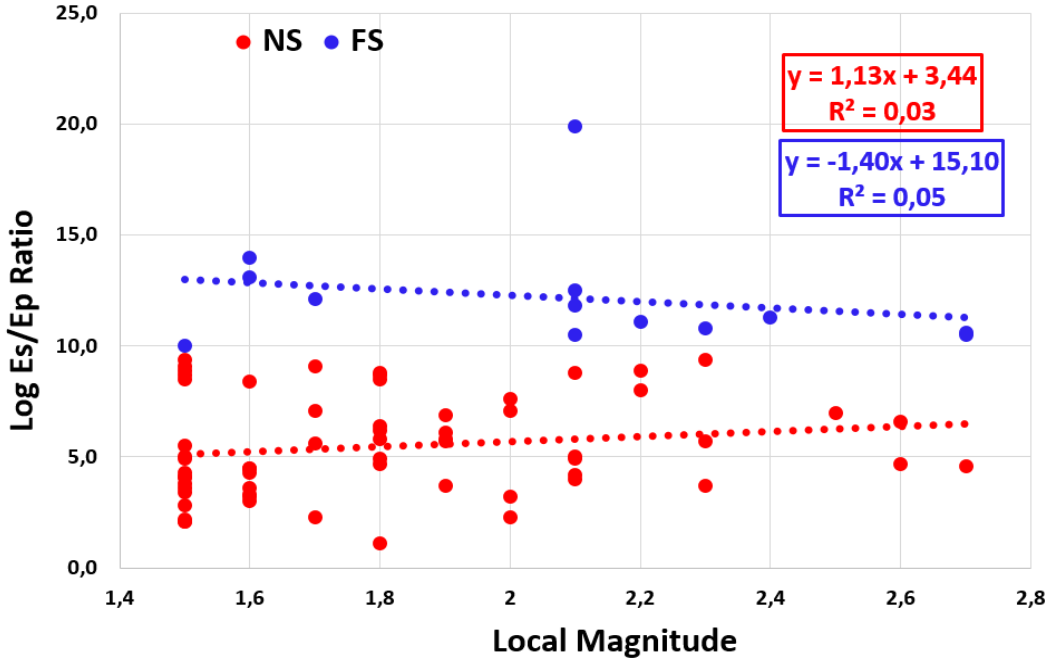

Figure 4.21: *Log Es/Ep ratio with respect to local magnitude for both the fault slip (FS) and seismic events the non-shear (NS).*

A strong correlation is observed between the seismic energy and the local magnitude for NS and FS events. The correlation coefficients for the NS and FS events are 0.96 and 0.93, respectively. This good correlation is because the seismic magnitudes are a weighted sum of the moment and energy. FS seismic events were, on average, slightly more energetic than the NS seismic events for the equivalent seismic moment (Figure 4.22).

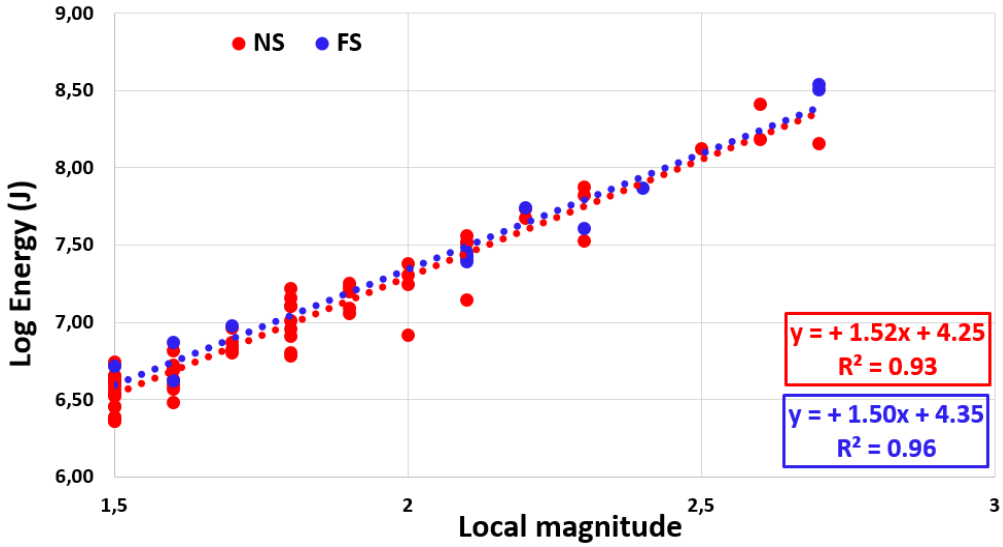

Figure 4.22: *The fault slip and non-shear seismic events relationship between the Log seismic energy and the local magnitude.*

A relative increase in log apparent volume is observed with local magnitude for NS and FS seismic events. Log apparent volume varied between 5.93 and 7.75 m^3. The correlation coefficient between the apparent volume and local magnitude is strong (R^2=0.64) for FS compared to NS with a R^2=0.20 correlation coefficient (Figure 4.23). There was a variation between the corner frequencies from 13 to 27 Hz for these seismic sources. The anticipated corner frequency increase with decreasing in magnitude was evident (see Table E1, Appendix E).

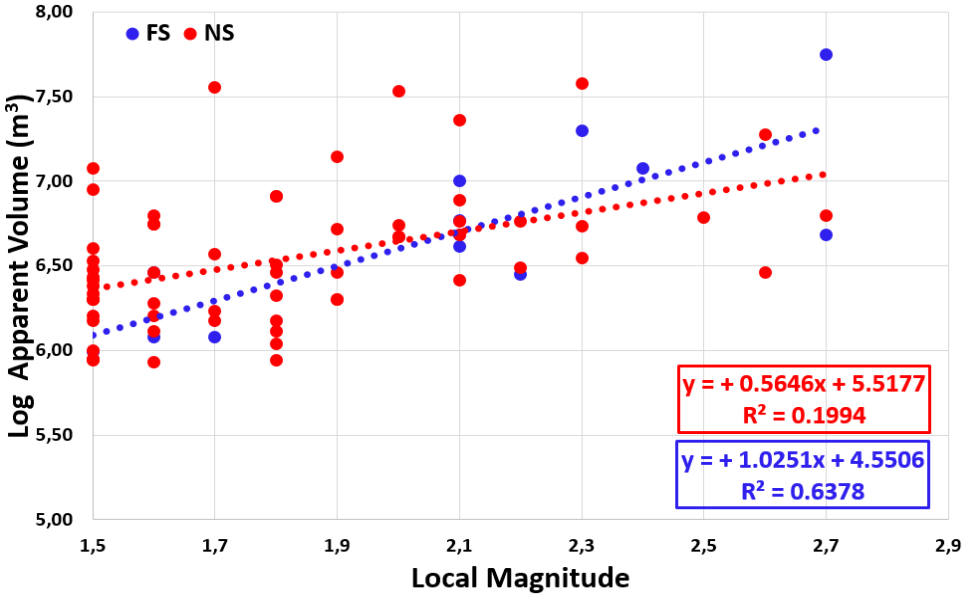

Figure 4.23: *Log Apparent Volume versus local magnitude for both the fault slip (FS) and non-shear (NS) seismic events.*

A low positive correlation is observed between the local magnitude and the source radius for the NS and FS seismic events. An increase with source radius is observed with an increase in magnitude through there is no much difference between the NS and FS seismic events (Figure 4.24). Averagely, NS seismic events exhibited lower corner frequencies, resulting in a significant source radius compared to the same magnitude FS seismic events. The comparison indicates that NS seismic events will have more stress drop than FS seismic events.

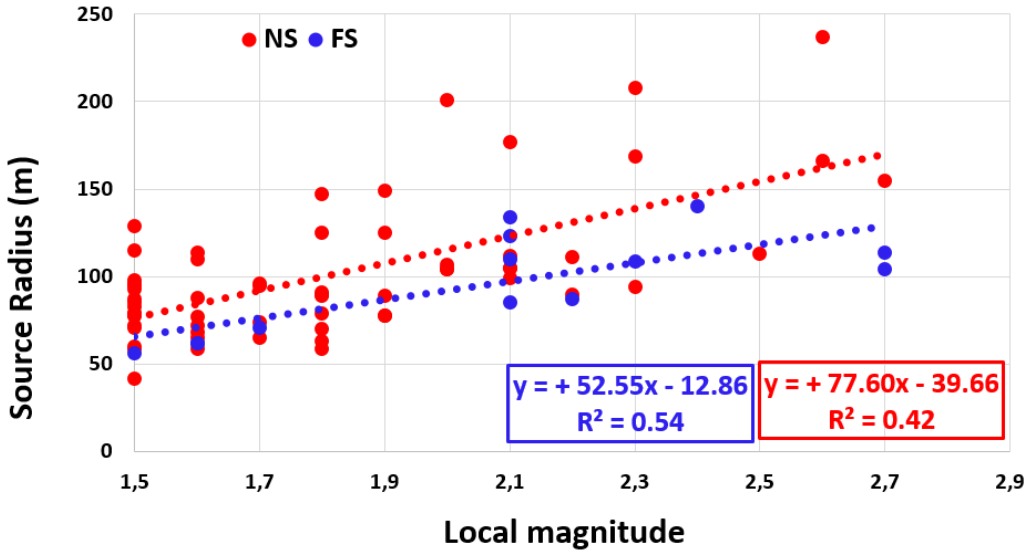

Figure 4.24: *The fault slip and non-shear seismic events source radius versus their magnitude.*

During the study, no clear difference was derived between the FS and NS seismic events. The source radius increases with a local magnitude between FS and NS events with no significant difference. Comparisons of some source parameters and magnitude were explored, and observations that transpired included:

- NS seismic events generally had larger source radii than the FS seismic events of the same magnitude (Figure 4.24),
- On average, more seismic energy was released by fault-slip (FS) events compared to the same magnitude for non-shear events (NS). As a result, the FS events could be more damaging, depending on the distance from the vulnerable excavations.

Nordström *et al*. (2017) investigated the parameter Es/Ep for the forty-six mining-induced seismic events with a moment magnitude of between 1.2 and 2.1 at mining depths ranging from 850–1350 m in the Kiirunavaara Mine (Sweden). The results were comparable to the Kloof Gold mine operations; similarity in Es/Ep classification system indicated that (i) energy showed a good correlation with the seismic moment for both types of seismic events (NS and FS), (ii) energy of FS events was found to be higher than energy

of NS events for the same seismic moment, (iii) source radius and moment magnitude showed a moderate correlation for FS and NS events, and (iv) NS seismic events exhibited lower corner frequencies, resulting in a significant source radius compared to the same magnitude FS seismic events. The comparison also indicates that NS seismic events will have more stress drop than FS seismic events.

CHAPTER 5 - SEISMIC HAZARD AT KLOOF GOLD MINE

5.1 Introduction

A seismic hazard assessment is generally defined as the likelihood of a potentially damaging seismic event occurring of a certain magnitude. Risk assessment takes the consequences of a damaging event into account, which is governed by the fragility of structures and the exposure of people and other assets. In mine seismology, seismic hazard is defined as the probability of occurrence within time ΔT for a potentially damaging seismic event. The application of this seismic hazard definition commonly depends upon the time interval. It generally attempts to evaluate the recurrence times, or probabilities of occurrence, of seismic events above certain magnitudes. It is convenient to consider seismic hazard assessment in three different periods: long-, medium-, and short-term (van Aswegen, 2005). Durrheim *et al*. (2007) and van Aswegen (2005) suggested that:

- **Long-term seismic hazard assessment** should refer to the order of years as the duration allows the global change in the mining parameters (e.g., trends of seismic response to mining, year planning, and future mining).
- **Medium-term seismic hazard assessment** should refer to a week or month, which would fit with the monthly planning cycles in the mine (diurnal distribution trends or the mine planning inputs, numerical modelling). Monthly seismic hazard ranking allows the assessment of mining strategies to minimize the seismic hazard.
- **Short-term seismic hazard assessment** should be evaluated for either period of hours or days (e.g., daily workplace instability assessment daily seismic rating). These allow special procedures to minimize the exposure to be implemented, e.g., rock engineering audits.

The analysis techniques are different for these three assessment methods since they could indicate relative hazard over time and space. However, only the first two first assessments would be explained.

5.2. Long-term Seismic Hazard

Long-term seismic hazard relates to the planning of future mining and its hazard estimates in the mines. It involves determining recurrence times or probabilities of seismicity occurrence above certain magnitudes (Mendecki *et al*., 1999). The seismic hazard magnitude parameter considers the area under the Gutenberg-Richter relation and is applied as a comparative measure for geotechnical areas. The Gutenberg-Richter frequency magnitude relation shown in Figure 5.1 is utilized to determine the average number of mining-induced seismic events that would be likely to happen in a given time (McGarr, 1984). The relative exposure to both the seismic risk and seismicity may thus be measured.

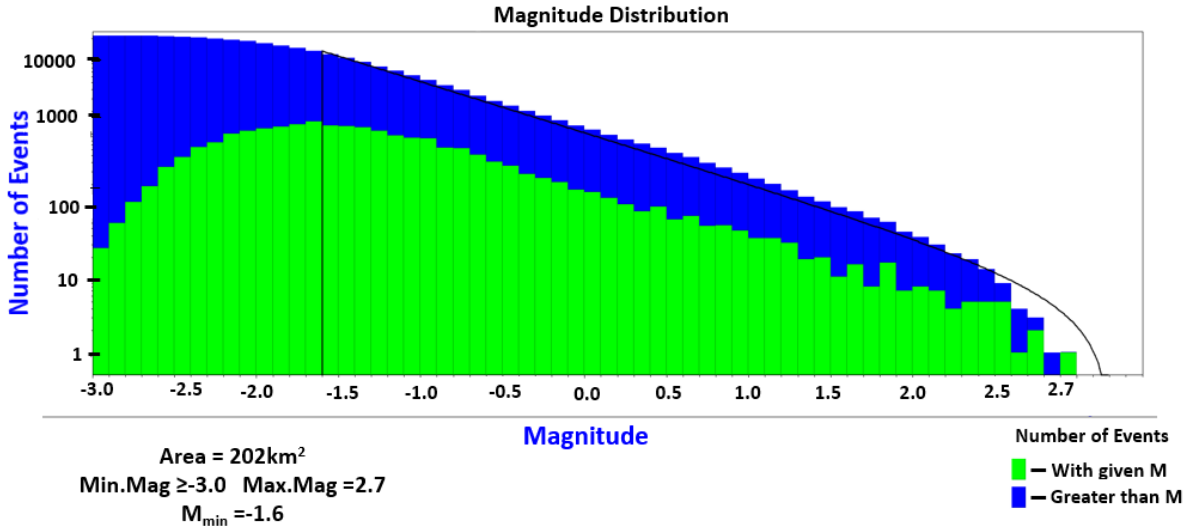

Figure 5.1: *The Gutenberg Richter Plot*.

Hazard assessments in the mining areas are of great assistance in evaluating both the frequency and intensity of seismic events. This allows the adoption and implementation of measures to be taken in reducing both the risks and associated damages to seismicity. The probabilities of occurrence in the area of interest are estimated by assuming a stationary Poisson process (Mendecki, 2016):

$$Pr(\geq P, \Delta T) = 1 - exp\left[-\frac{\Delta T}{T} N(\geq P)\right] \quad [5.1]$$

where the time observed is represented by T and $N(\geq P)$ is the seismic events number during the time (T). Table 5.1 summarises the intermediate and long-term probabilities of occurrence in time domain comparing both Period 1 and Period 2, respectively in a block of ground within the 3D reflection seismic volume. While the durations of P1 and P2 are different (10 and 9 years 1 month, respectively), probabilities are normalised for standard time periods of 1 month and one-quarter, one-half, one, two and five years. The probability of the occurrence of a seismic event of any given magnitude obviously increases as the period increases.

Table 5.1: Intermediate-term probabilities of seismic event occurrence in a block of ground within the 3D reflection seismic volume for Period 1 (1/7/1999 to 1/7/2009) and Period 2 (2/7/2009 to 31/7/2018)

Probabilities (Period 1/Period 2)					
	M_L= 1.0	**M_L= 1.5**	**M_L= 2.0**	**M_L= 2.5**	**M_L= 3.0**
ΔT = 30 days	1.000/1.000	0.995/0.985	0.845/0.783	0.468/0.318	0.175/0.064
ΔT = 90 days	1.000/1.000	1.000/1.000	0.996/0.990	0.849/0.763	0.438/0.179
ΔT = 180 days	1.000/1.000	1.000/1.000	1.000/1.000	0.977/0.944	0.684/0.326
ΔT = 365 days	1.000/1.000	1.000/1.000	1.000/1.000	0.999/0.997	0.900/0.546
ΔT = 2 years	1.000/1.000	1.000/1.000	1.000/1.000	1.000/1.000	0.990/0.794
ΔT = 5 years	1.000/1.000	1.000/1.000	1.000/1.000	1.000/1.000	1.000/0.981

In Period 1, the probability that a seismic event with $M_L \geq 1.5$ occurs somewhere in the 3D reflection seismic cube for one month period is $Pr\ [\geq P, \Delta T]\ = 0.995$; while the corresponding probability for Period 2 is lower, 0.985. The probability that a seismic event of $M_L \geq 2.5$ occurs within six months in Period 1 is 0.977; while it is 0.944 in Period 2.

Parameters used to calculate both Period 1 and Period 2 seismic hazard are summarised in Table 5.2. Period 1 shows a higher probability of $M_L \geq 1.5$ events (hence a shorter recurrence time) with a seismic event of expected $M_L \geq 1.5$ to occur in the 3D seismic volume every 5 days on average. The maximum credible magnitude (M_{max}) is greater in P1 than P2. This indicates a decrease in seismic hazards. This might be due to amount of mining (Chapter 8, section 8.4), improved working conditions, change in behaviour of workers in the mining stopes, on the job coaching, improvement in mining technology, strata control coaching, etc. A decrease in the amount of mining would decrease the seismic risk in a given scenario, and the increase in depth increases stresses that will result in seismicity.

Table 5.2: Comparison of seismic hazard for both Period 1(1/7/1999 to 1/7/2009) and Period 2 (2/7/2009 to 31/7/2018)

Seismic Parameter	**Period 1 (P1)**	**Period 2 (P2)**
M_{max} Recorded (Date of Occurrence)	3.6 (6/7/2002)	3.0 (4/3/2018)
M_{max} Expected	3.80	3.20
b-value	1.327	0.90
Recurrence Time M ≥ 1.5 (months)	0.152	1.586
Probability M ≥ 1.5 (per month)	≈ 99.9%	≈ 82.9%
No. of Events M ≥ 1.5	1354	634
On-shift occurring seismic events	87%	70%

The majority of $M_L \geq 1.5$ events occur on-shift in both periods; the second period indicates a 17% improvement of events occurring on-shift, limiting the exposure of mine workers to injury.

5.3 Medium-term Seismic Hazard

This seismic hazard assessment enables the development of mining strategies to minimize seismic hazard and exposure. This assessment is an input parameter in monthly planning meetings (Durrheim *et al*., 2007). The monthly assessment analyses allow relations between the seismic hazard and local geological structure, mining layouts, and mining rates to be established and monitored. (Durrheim *et al*., 2007). Van Aswegen (2005) suggested that the method should be used for the recognition of potentially unstable geological structures (e.g., dykes and faults), or human-made structures (e.g., abutments and pillars). The medium-term seismic assessment can be categorized into numerous steps (Durrheim *et al*., 2007; Hudyma, 2008 and van Aswegen, 2005):

- Space-time delimitation of datasets (Identifying spatial population).
- Seismic parameters selections to be analyzed/ statistical and quantitatively analyses (trends in seismic population, time history analysis).
- Non-seismic parameters selections to be analyzed (e.g., numerical modelling outputs).
- Change in seismic hazard signal identification (spatial analysis, clustering, stiffness diagrams, seismic response parameters, diurnal distributions, etc.

Owing to the scope of the thesis only three issues will be considered in depth, *viz.* spatially constrained seismic hazard analysis, numerical modelling and diurnal distribution.

5.3.1 Spatially constrained Seismic Hazard Analysis

A simple study of the Kloof operation was undertaken, where the operation was divided into five different polygons drawn around shafts. The study was an internal study conducted by the author to investigate the frequency of events in different parts of the mine. The analysis highlighted that some shafts were prone to a large number of small seismic events with few big events (e.g., active mine working stopes); while other shafts had comparatively few small events with many large ones (e.g., extensive mined-out areas within a shaft or seismically active geological structure). The finding was that in the back areas and along the abutment more large seismic events were observed as compared to the current mining blocks with no geological structures and pillars. Observations indicate the different nature of seismic events in different parts of the Kloof operation.

Hudyma (2005) conducted a similar analysis in 50 mining blocks in 11 Australian mines and found that within the mining blocks, the largest seismic event was generally less than the expected largest event. This was by investigating the frequency magnitude relation. His conclusion was valid for relatively small events ($M_L=0$). The analyses indicated that local mining, geological and geomechanical influences within the

mining block controls the largest expected seismic event. Morrison *et al*. (1993) made a similar finding when studying the nature of seismic events of the Creighton Nickel Mine in the city of Great Sudbury in Canada.

5.3.2 Numerical modelling

A well-maintained (accurate, reliable and consistent) seismic database allows both hazardous geological structures and mining layouts to be recognized and can also be used to calibrate numerical models so that standard rock engineering design tools can be applied appropriately (Durrheim *et al*., 2007). Numerical modelling techniques are commonly used to investigate long-term seismic hazard assessments (van Aswegen, 2005). Both the Energy Release Rate (ERR) and the Excess Shear Stress (ESS) are used by Rock Engineers in South African mines as methodologies to simulate future mining and identify conducive conditions for generation of a seismic event. The two have been used to back analyse failure and compare different mining layouts. Regular updating and recalibration of numerical models as mining progresses is essential for routine long-term seismic hazard assessment (van Aswegen, 2005). As mining progress, the faces are updated to form part of the master model used to compute the face stress and average pillar stress.

ERR has been in use to investigate the elastic energy stored and release associated with different mining sequences. ESS is used to determine whether a fault is prone to slip that might endanger the mining personnel or damage mining infrastructure. There is a good correlation between modelled slip using an ESS criterion and large seismic events within the gold mines (Ozbay *et al*., 1993).

5.3.3 Diurnal distribution and the stope blast

The variation of event frequency about the time of day describes the nature of the mining-induced seismic event distributions. The rate of mining in development ends has a strong influence on the number of smaller magnitude events ($M_L \leq 0$) generated. While $M_L \geq 0$ events are possible in development ends they are mostly caused by stoping. Viewing the hourly seismic event rate on a horizontal time axis shows a distribution that rises from a background level to a peak at or around the blasting time (17:00-19:00). The increase in an activity does not rise sharply to a peak as would be expected but shows a gradual increase (Figure 5.2). Following the peak, there is a typical decline or drop off in activity rate.

The monthly back analyses of seismicity have value where the mining environment insignificantly changes in the medium-term period (van Aswegen, 2005). The weekly diurnal distribution is an additional method used by the operations (Sibanyestillwater Gold Operations) to assess the workforce's exposure to seismic activity. Exposure of the workforce to such events can be limited by concentrating blasting in a short time window characterized by centralized blasting (Figure 5.2). Maintaining blast information accurately is important for, removing blast information from seismic data information database, studying the effects of

blasting on seismicity, calculating decay period after the blast and calculating both the P- and S- wave velocities.

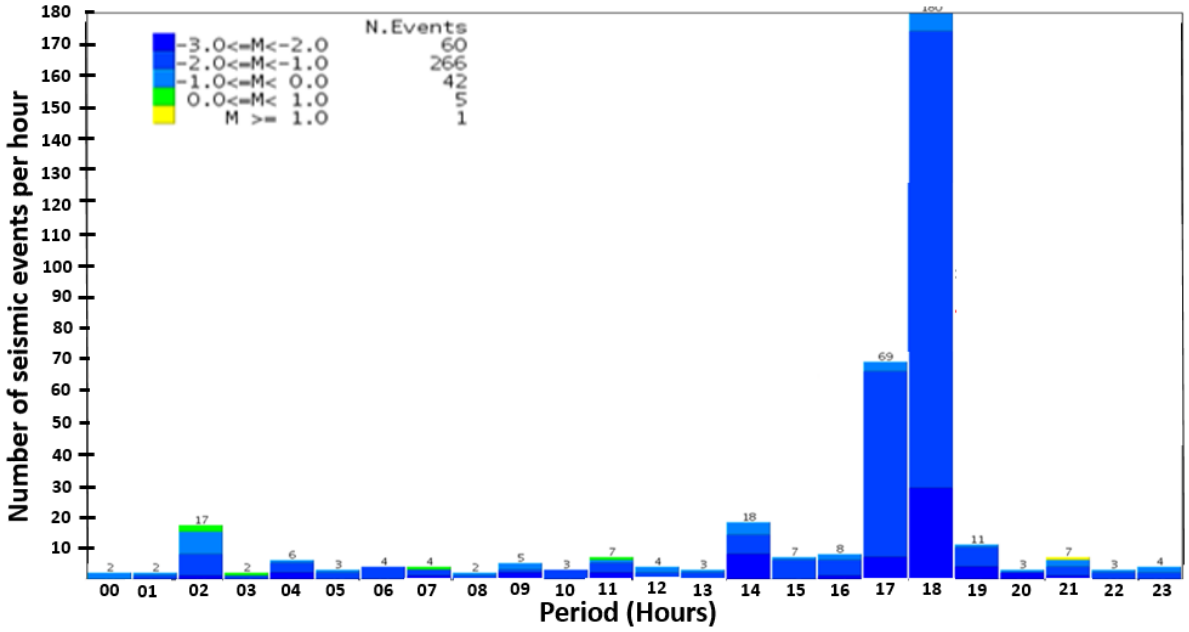

Figure 5.2: *Diurnal distribution indicating the background seismic events and the peak (Indicating the blasting time).*

5.3.4 Seismic Hazard Map and the Grid-based Mapping

A Seismic Hazard Map (Instability analyses) can be classified as the locations where there is a high possibility of a seismic event of $M_L \geq 1$ occurring in 30 days in the vicinity of an actively working stope, and can be used for medium-term assessment (Figure 5.3). Seismic Hazard Maps" are easily generated and particularly useful to direct priority attention to working areas that have a higher probability of damaging seismic event. The method uses the pre-defined population group of seismic events (spatial filter). This introduces an interpretation bias due to the defined user population (polygon) selected events.

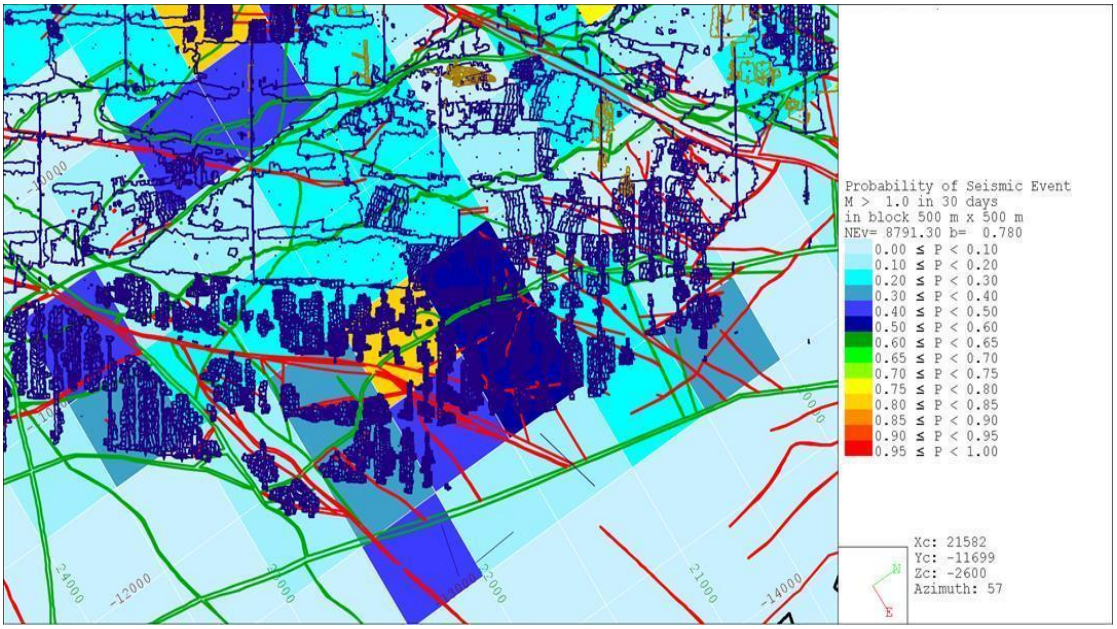

Figure 5.3: *Seismic Hazard Map indicating potential unstable geological structures and mining stopes.*

The common approach to creating a hazard map would be Grid-based hazard mapping. The approach has the ability to identify irregular activity without using a pre-defined polygon (spatial filter). It eliminates the potential bias that can be introduced by the user-defined polygon. According to Wesseloo et al. (2014).," based on the purpose of the analysis the grid spacing and search radius must be defined and will vary based on the density and quality of seismic data".

The method relies on the concepts of data neighbourhood. Before a seismic parameter (b-value, Energy index (EI), Apparent stress, etc.) is assigned, the grid point events around the grid point must be dense and close enough. This prevents the idea of seismic parameters values to be transferred to further areas. A simple sensitivity analysis test performs the sensitivity of the chosen seismic parameter. Figure 5.4 (a) and (b) shows an example of a grid-based spatial variation of b-values and seismicity showing the distribution of b-values, for an Australian mine (Wesseloo et al., 2014).

The results indicated that high b-values mechanism seismic event observed in the local stoping activity and while the abutments failure mechanism exhibits low b-values (Figure 5.4a). The difference can be related to stress fracturing seismicity (high b-value) or shear failure mechanism (low b-value). Figure 5.4b indicate high b-values corresponds to low apparent stress and low b-value to high apparent stress. Hazard maps to aid in identifying areas within a rock mass of higher seismic risk.

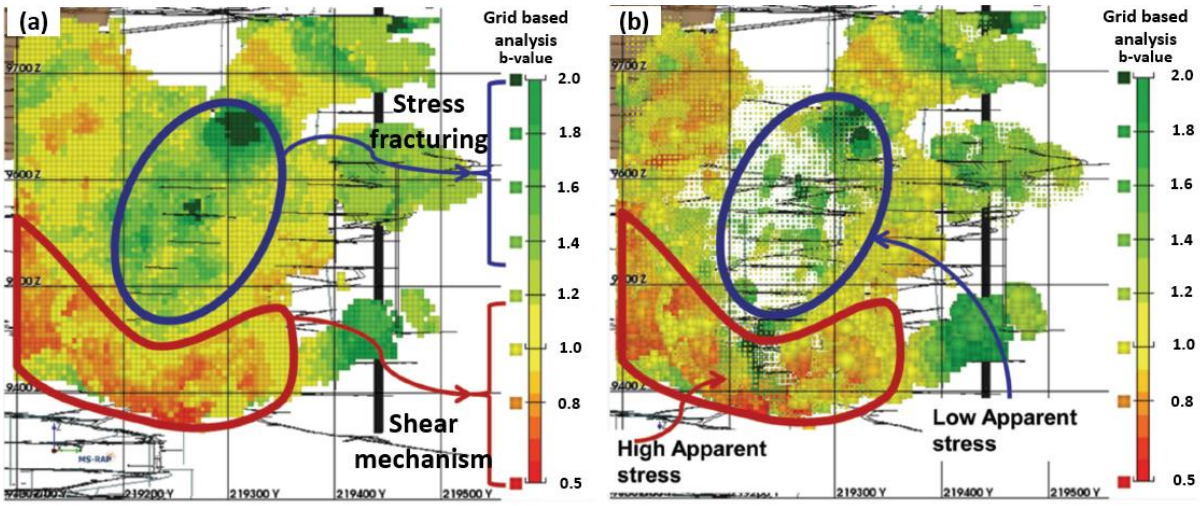

Figure 5.4: *(a) Grid-based hazard mapping and the interpretation of b-values within an Australian mine. Red and blue colours highlighted areas represent abutment and stoping areas. (b) Grid-based interpretation of seismicity showing b-value distribution by colour. The size of the grid point markers are scaled by apparent stress (Wesseloo et al., 2014).*

5.4 Short-term event frequency

Seismic hazards can also be associated with the aftershock after the largest seismic event and the stope blast. Warning measures associated with microseismic monitoring in mines include the seismic event rate over the last few hours to several hours (short term event frequency). These are when the seismic events recorded are compared to the typical event rate or the background event rate (Figure 5.5). When the number of seismic events is deemed high in an active workplace, the workplace would be considered unstable, and the workforce would be evacuated or not allowed in the workplace. The workforce would only be permitted to reenter the workplace when the seismic event rate is reduced to acceptable levels and a risk assessment has been done.

5.4.1 Large event occurring ($M_L \geq 0.9$), decay analysis, withdrawals procedures and re-entry from the active working place

A seismic event of $M_L \geq 0.9$ is classified and considered a large seismic event, usually associated with damage within the Witwatersrand Basin, especially within the Kloof operations. Large event procedures and the radius of influence are tabulated in Table D1. Action to be taken includes the shift going down the shaft when the seismic rating is acceptable and has decreased.

There might be increased seismicity (aftershocks) after a large seismic event when the rock mass reaches the new stress conditions. The Omori power law can be applied to estimate the decay in activity rate after the large seismic event (Figure 5.5). In 1894, Omori studied the decay of aftershocks occurrence with time

and found that the aftershocks increase with time following the main shock. (i.e. activity rate ~ 1/t). Utsu (1961), and Vallejos and McKinnon (2010) later modified the Omori's simple relation where constants c and p were added (Equation 5.2).

$$n(t) = \frac{K}{(t+c)^p} \qquad [5.2]$$

where: $n(t)$ is the events rate at time t, t represents the time after mainshock occurred, c and K are parameters that are constant and relate to the time offset and productivity. Lastly, p is the aftershock decay constant (Nanjo *et al*., 1998) has a value close to one. Other functions were found to fit the aftershock decay rates in the widely accepted modified Omori's model (e.g., Gross and Kisslinger, 1994). The analysis considered all seismic events within a defined radius from their centroid within the specified period after recording them.

Figure 5.5 indicates a sample of the rate of occurrence of aftershocks after the different ranges of seismic event magnitudes have occurred. The larger the main shock magnitude, the greater the seismic activity afterwards. Consider the period 06h00-06H30 there were two events of M>2.5 recorded and these produced 16 M>0 aftershocks in 2-hour window. This translates into a rate of 192 events/day. Considering a single event, the number of aftershocks would likely to be giving a rate of 96 events per day in 2-hour window.

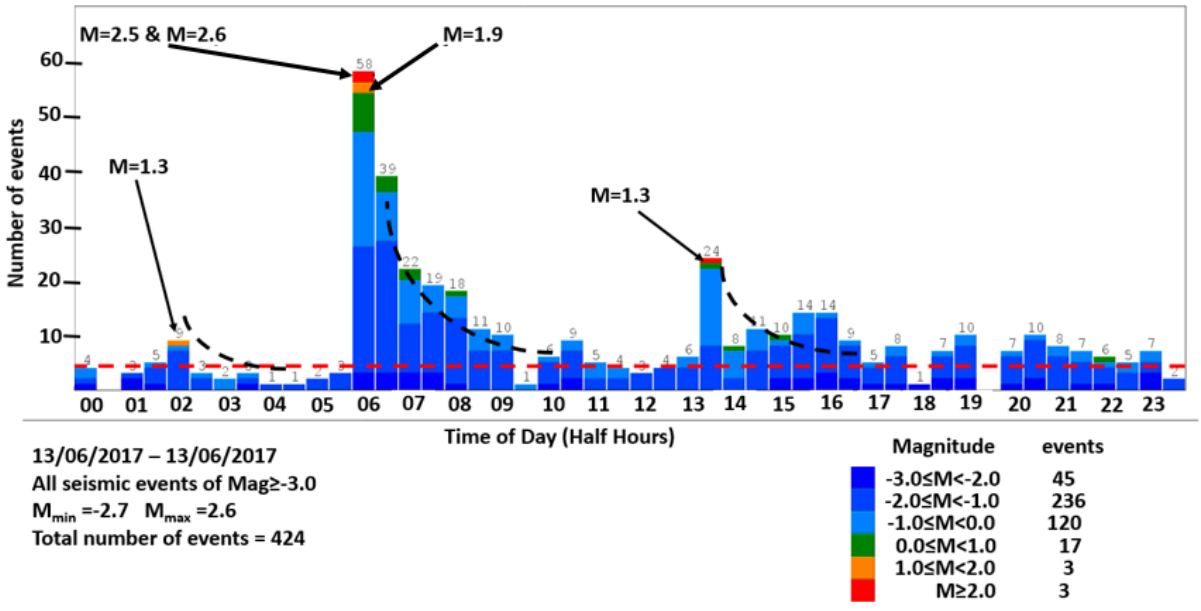

Figure 5.5: *An example of the decaying seismicity after large events have occurred in Kloof Gold Mines.*

The re-entry time was determined by estimating the time it would take for aftershock activity to decrease to the background level. Polygons were assessed using the five instability analysis parameters and the rock engineering checklist (Table D4). Kgarume *et al*. (2010) investigated the statistical properties of aftershocks at the two gold mines in the Carletonville district, one mining the Ventersdorp Contact Reef and the other the Carbon Leader Reef. They estimated the period after the occurrence of the mainshock when the seismic hazard would have decreased to the background level (Figure 5.6). Since the study was done in the mining depth of greater than 2 500 m within the VCR, it is comparable to the Kloof working stopes. In the Kloof Gold Mines analysis, a large seismic event was defined as a seismic event with $M_L \geq 0.9$ (approx. 1.0). The aftershock decay rate estimated background level and the lines representing p = 1 and p = 0.8 are shown in Figure 5.6. Kgarume et al. (2010) found that the mainshock magnitude does not affect the aftershock decay constant (the p-value) significantly. However, larger mainshocks are more productive (i.e., have higher K values), and thus it takes longer for the activity rate to decrease to background levels.

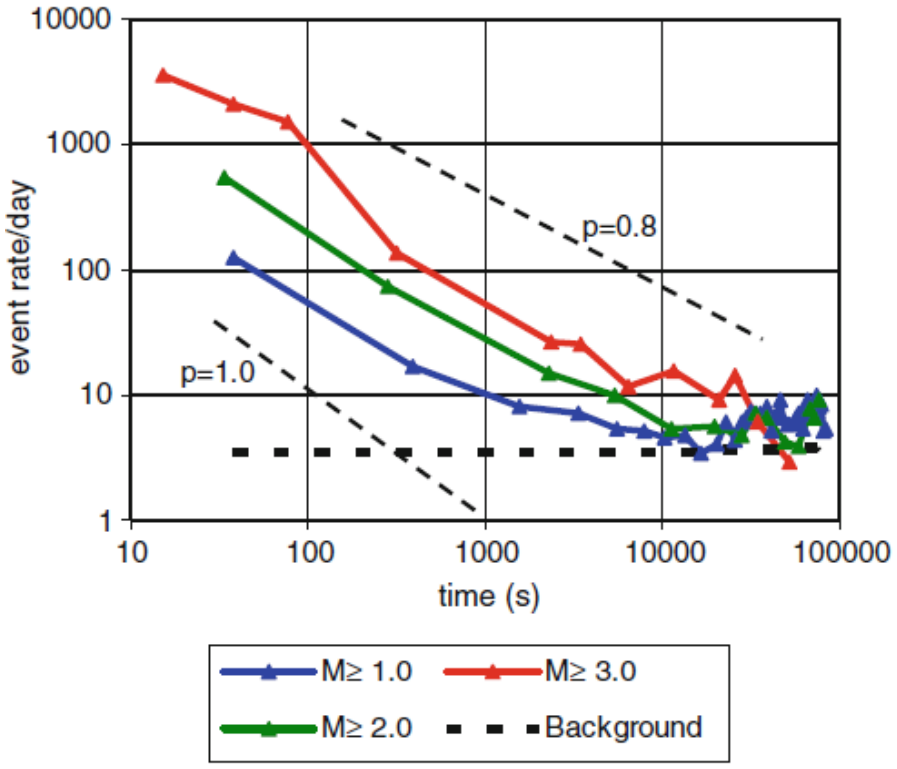

Figure 5.6: *Aftershock decay rate of events $M_L \geq 0$ from the mainshock magnitude of $M_L \geq 1.0$, $M_L \geq 2.0$ and $M_L \geq 3.0$. The estimated background level and the lines representing $0.8 \leq p \leq 1.0$ are also indicated as dash lines on the graph (Kgarume et al., 2010).*

An increase in seismic rate follows instantly after the mainshocks, usually more than 100 events per day for $M_L \geq 1.0$ mainshocks. For a magnitude $M_L \geq 3.0$, the aftershocks are close to a thousand with the $0.8 \leq p$

≤1.0 (Kgarume *et al*., 2010). The modified Omori's law can determine guidelines for the re-entry times and the background levels into a stope area following the large seismic event occurring (Kgarume *et al*., 2010).

The aftershock decay curve of seismic events of $M_L \geq -2.4$ is represented in Figure 5.7, indicating the periods determined where seismicity has declined to the background levels. It is used to assess the aftershock hazard just after the main seismic event occurred. The Omori decay curve was used to the time taken for a seismic hazard to a decreased acceptable level.

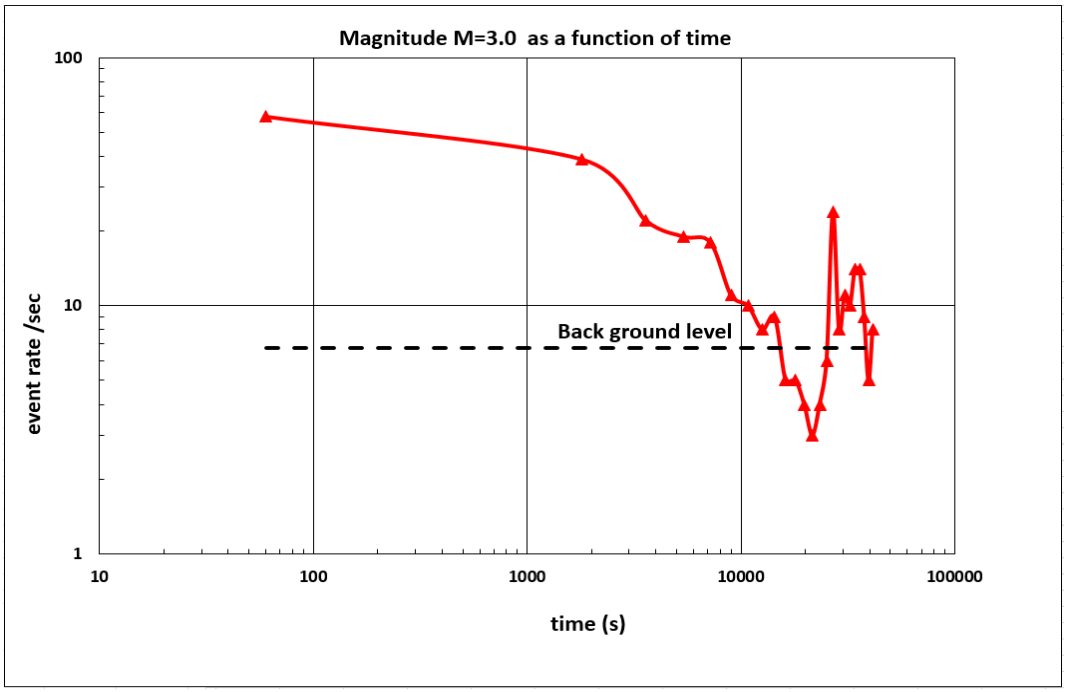

Figure 5.7: *The aftershock decay curve indicating the period where event rate has decreased to background levels.*

The probability of a seismic event with the potential to cause injury to mining personnel increases significantly immediately after a moderate-sized event (M=3.0) (Figure 5.7).

5.5 Peak Particle Velocity related to a seismic event, damage and ground support resistance requirement.

The primary source of dynamic loading in deep level stopes is mining-induced seismicity. The surrounding rock mass is subjected to deformation. A sufficiently large dynamic loading can result in damage to infrastructure and injuries. The Peak Particle Velocity (PPV) is generally used to estimate the likelihood of damage to the rock mass and structures. It is not an accurate measure of the PPV generated by a seismic event (particularly in the near field). Still, it represents a scaled-distance relationship, which can be correlated to the rockburst damage.

The passage of a seismic wave through the rock mass causes ground vibration. These vibrations occur in radial, vertical and transverse directions. The ground vibrations are usually recorded and measured using a seismograph, and the maximum velocities of all three directions are given. The measurement of the ground vibration can provide us with seismic source parameters that could be used to calculate the PPV and can be classified into three main categories (Mutke *et al*., 2016):

1. Measurement of ground motion in underground workings in deep mines, especially in the near field (Butler and van Aswegen, 1993; McGarr *et al*., 1991; Dubiński and Mutke, 1996; Kaiser *et al*., 2005; Mutke, 2002, 2008)
2. Measurement of load on the support during natural dynamic phenomena (Szweda, 2003; Masny and Prusek, 2012; Jarufe and Vasquez, 2014; Kaiser and Cai, 2013).
3. Load on the roof support and measurement of PPV during blast experiments (Kidybiński, 1986; Tannant *et al*., 1992; Stjern and Myrvang, 1998; Hagan *et al*., 2001; Ansell, 2004; Malmgren and Nordlund, 2006; Masny, 2006; Hadjigeorgiou and Potvin, 2007; Heal, 2010).

These ground vibrations can cause damage within the rock mass and the source radius and at a considerable distance away from the source of a seismic event. The PPV is closely linked to the potential to damage structures of the rock mass. The measurement is vital in the design of support systems used underground. It occurs in response to the *S*-wave since it carries most of the seismic energy. Studies have indicated that the near field PPV can surpass the value of 10 m/s in the gold mines of South Africa (Butler and van Aswegen, 1993). PPV very close or near the source (near field PPV) cannot be directly or accurately measured but can be estimated. Ground motion has two components, namely the near-field and the far-field. The generic form of the peak particle velocity was used by McGarr et al. (1991) and is shown in Equation (5.3):

$$Log_{10}(R.v_{max}) = A.M + Log_{10}(C) \qquad [5.3]$$

Where:

v_{max}	Peak particle velocity
$A\ and\ C$	Mine-specific scaling parameters.
R	Distance to source (m)
M	Seismic event magnitude

Kaiser *et al*. (1996) highlighted that A and C are site-specific empirical constants that need calibration. If no data is available for calibration, the constants can use A=0.5 and C=0.25. The two-site empirical constants were determined from the regression line calculated from the seismic data population and McGarr (1984)

data. The ground motion relationship was further developed by Durrheim *et al*. (2005) from work done by McGarr (1991) and is presented in Equation (5.4):

$$v_{max} = \begin{cases} \frac{v_s.\Delta\sigma}{G} & for \quad R \leq r_0 \\ \frac{v_s.\Delta\sigma}{G}.\frac{r_o}{R} & for \quad R > r_0 \end{cases} \qquad [5.4]$$

Where:

v_{max}	peak particle velocity
v_s	shear wave velocity
$\Delta\sigma$	static stress drop
G	rock mass shear stiffness
r_o	radius in the near field
R	hypo central distance

In a 250 rockburst incidents study conducted by Heal et al. (2006), they found that the intensity of rock mass damages with seismic events depends on a series of many factors related to :

- Source mechanism of a seismic event,
- Travel time of seismic energy,
- Local rock mass conditions (e.g presense of geology, ground support, level of stress in the rock mass and etc.). The extend of damages depend on the vulnerability and the distance of the excavation from the seismic source (Figure 5.17).

A classical case study is represented below correlating the PPV and the associated degree of rock mass damages. In most cases, the Peak Particle Velocity is linked to damage potential rather than the rock mass displacement/acceleration.

5.5.1 Ezulwini - Cooke 4 Case Study:

M_L=2.8 event, corresponding PPV and damage at Cooke 4 Operation within the shaft pillar.

Cooke 4 is part of the Sibanye-Stillwater conglomerate situated a few kilometres from the Kloof operation. The shaft consists of quartzites, pebbly quartzites, argillaceous quartzites, conglomerate (VCR), medium-strong lava, and weak lava Klipriviersberg group. The Cooke 4 operation consists of a 400 m x 450 m circular shaft pillar situated 1038 m below the surface. The rest of the mine has effectively been mined out along its circular abutment perimeter (Figure 5.8). Before mining, the virgin principal stress state was in the order of 26 MPa. The Rock Engineering Department performed numerical modelling before mining the shaft pillar, which showed induced stress levels ranging from 40 to 50 MPa. With the current extraction of the northern section of the shaft, the principal stress can be expected to be considerably higher. These would increase the potential for large seismic events that may cause casualties and infrastructural damages. The dip planes of the normal faults are also steeply inclined and therefore maybe be more prone to fault slip type seismic events.

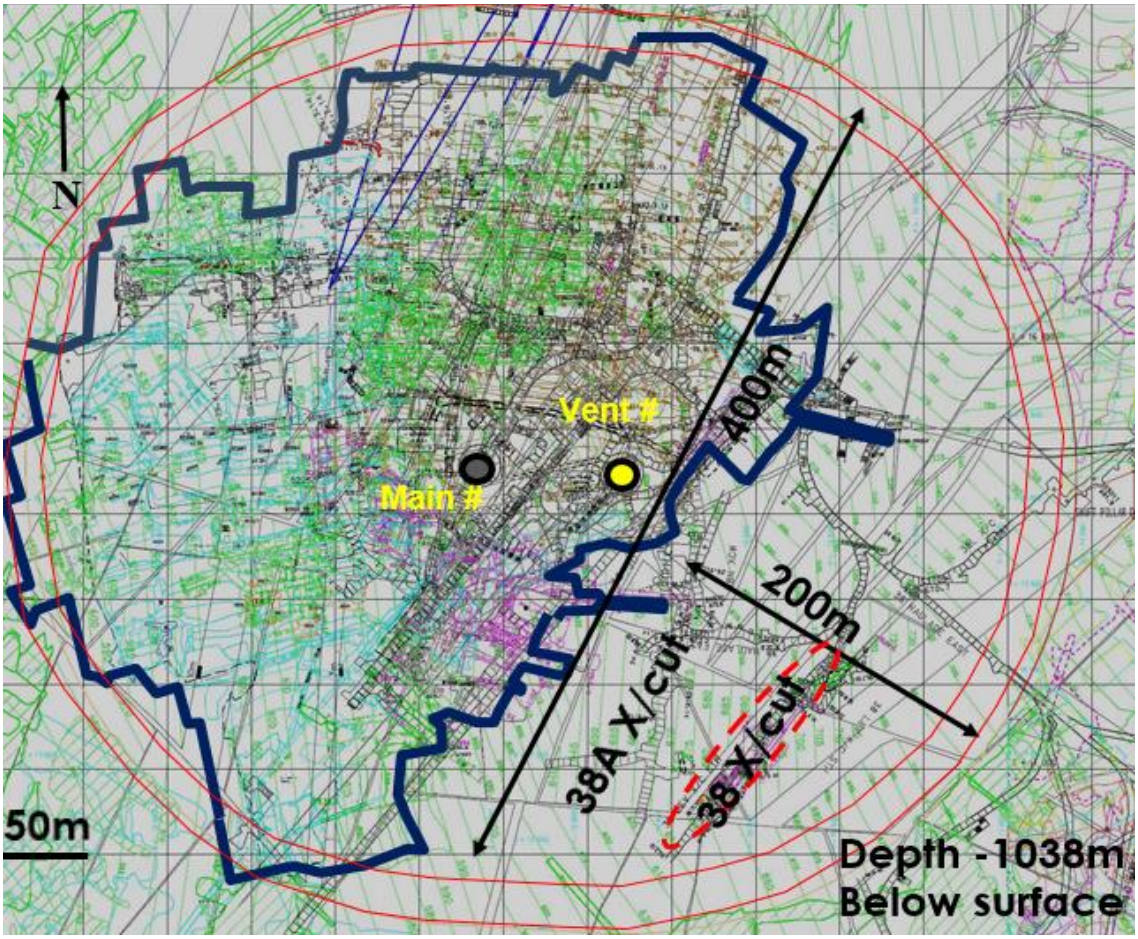

Figure 5.8: *Plan showing shafts (#): Main and the Ventilation (Vent), current mining layout and the infrastructure (development end).*

The southeast portion of the shaft pillar indicated below has several NNE trending faults and an E-W trending dyke (Figure 5.9). The faults all comprise normal fault systems and have throws ranging from 5 m to 20 m. The overall strike direction in the shaft pillar is N – NW. The shaft pillar seismic array of sensors comprises eight tri-axial geophones with network sensitivity capable of recording minimum events to a magnitude M_L=-1.8 thresholds with a location accuracy of 20 - 30 m.

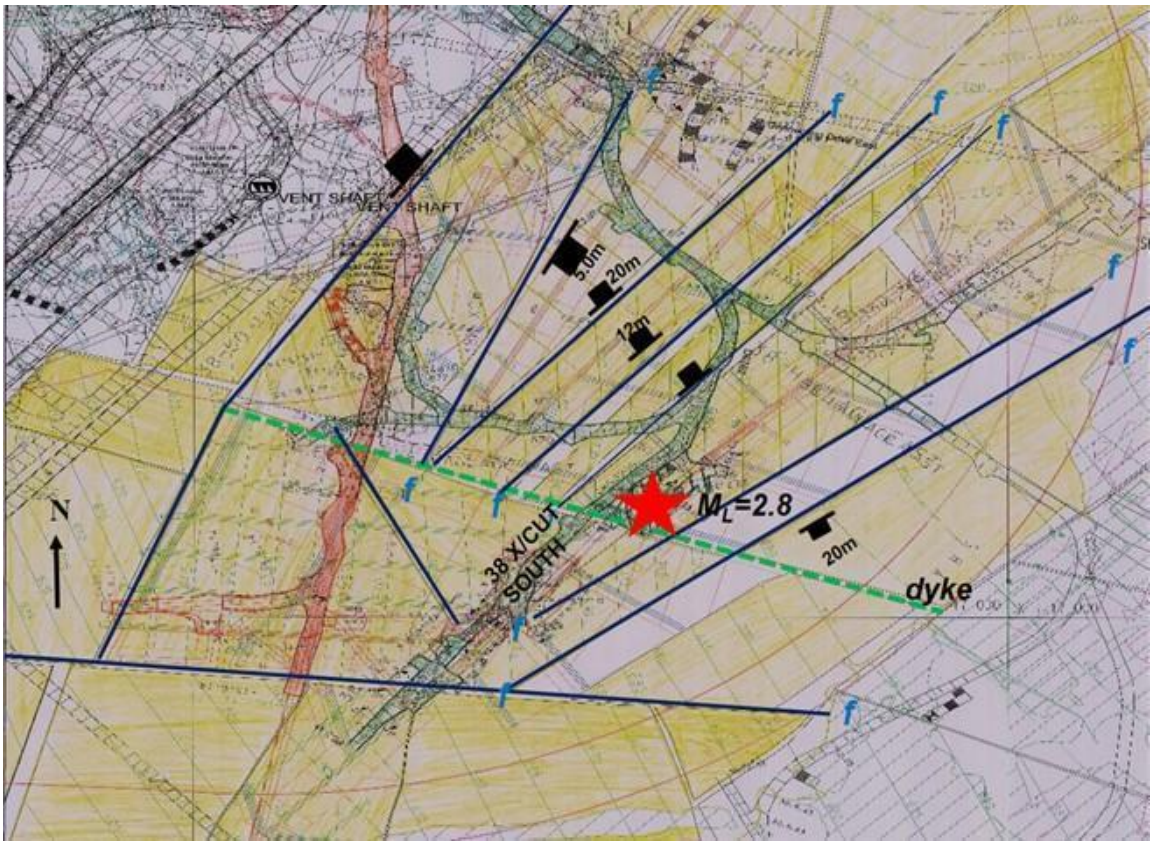

Figure 5.9: *Geological model (faults and a dyke) indicating the infrastructure and the seismic event of M_L=2.8 on 21 October 2014 in the south-east of the shaft pillar (red star). Brown coloured tunnel represents the 38A cross-cut south and the green coloured tunnel represent the 38 cross-cut south. Faults (f) and their throws are indicated.*

Mining within the shaft pillar started in April 2009 (Figure 5.10). The north and the northwestern side of the shaft pillar has mainly been extracted. The original design layout from the master plan required a more symmetrical sequence of extraction, with mining moving outwards from the shaft barrels. However, due to complex geology, the mining to the east of the shaft barrels was limited. New development access drives have been routed through in the southeast of the shaft pillar. During the developmental phase in the east part of the shaft pillar, the mine undertook a comprehensive diamond drilling program (prospecting holes). This has enabled a greater knowledge of the geological features and the expected reef elevations ahead of mining. Several new faults with large throws were identified, which further complicate access to the south-eastern mining block. The hypocenter is located near the 38 cross-cut south (Figure 5.10) within the block where the developments were occurring.

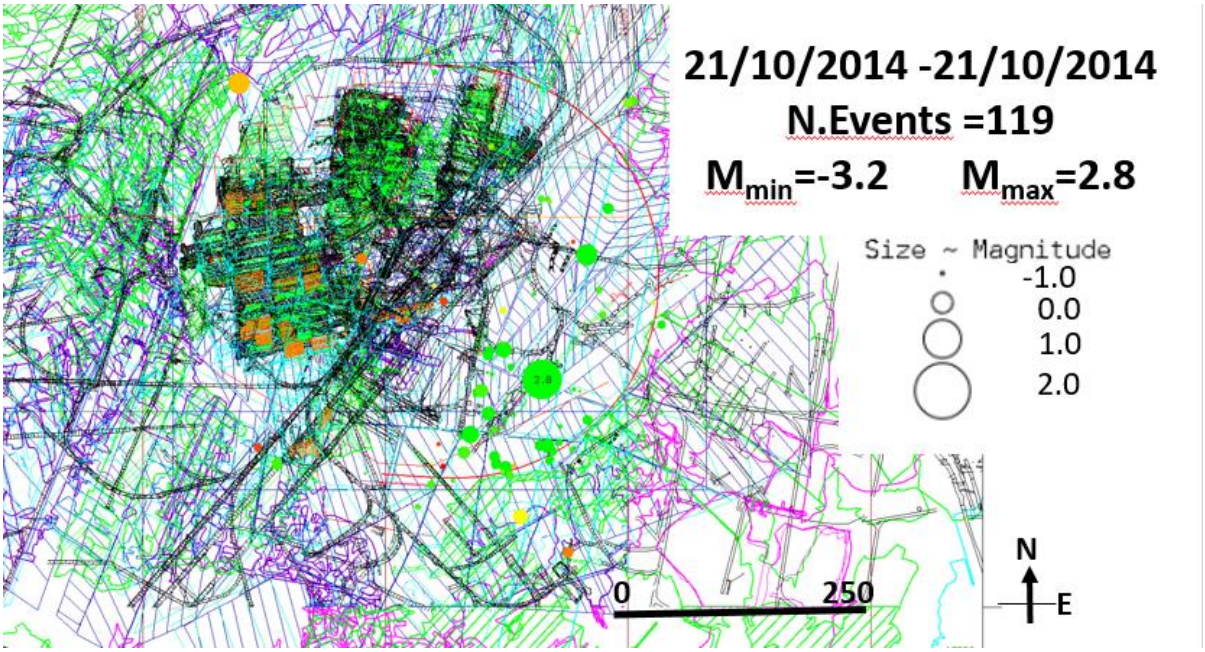

Figure 5.10: *Location of M_L=2.8 seismic event on the east of the Cooke 4 shaft pillar near the 38 cross-cut south.*

Seismic parameters and seismic source quantification

Seismic source parameters calculated from the accepted and processed waveforms for the M_L2.8 event are described in Table 5.3.:

Table 5.3: The M_L=2.8 event source parameters summary and comments

Seismic Parameter	Values	Comments
Max slip velocity at source	4.2 x 10^{-1} ms^{-1}	
Source size	76.3 -140.5 m	Correlates to the observed underground damages
Radiated energy	1.2 x 10^{8} Joules	
Energy S /energy P	34.7	Indicating a fault slip
Corner frequency	19.8 Hz	-
Static stress drop	7.8 MPa	-
Seismic Moment	3.1 x 10^{12} Nm	-

The seismic event mechanism that is suggested by Ortlepp and Stacey (1994) for the M_L2.8 seismic event that occurred and caused damages in the south-east of the shaft pillar can be classified as a “fault slip” type event mechanism (see Table 2.3 in section 2.2.3).

An estimation of the strong ground motions experienced on the rock mass in the vicinity of the seismic event.

In a rockburst situation, the seismic energy attenuates radially through the rock mass in the form of vibrations. Vibrations travel outward from the source (hypocenter) at speeds of approximately 5900 m/s for the P wave and 3600 m/s for the S wave (Figure 5.11). The S wave produces ground motion that is perpendicular to the direction of energy propagation. The P wave generally has a smaller amplitude (less energy) than the S-wave (more energy) and introduces volume change in the material. This energy excites the rock on the excavation surface. It results in disintegration and ejection of the loose key block (friable) material on the excavation free surfaces (e.g., side-, foot-, and hanging wall). These key blocks may be large or small. They are defined by pre-existing discontinuities, which comprise bounding edges of either stress fractures, blast fractures, joints, bedding planes, or fault surfaces. The main energy (high amplitude) is carried in the S wave (depending on the Es/Ep ratio), which might be responsible for most damage. The seismic energy travelling radially out from the source decays exponentially as a function of distance ($E(r) = \frac{E_0}{r}$, where E_0 is the seismic energy at the source and r representing the distance from the source). We have studied the position of the source radius with respect to the face of the excavation to characterize the level of ground motion. McGarr (2001) indicated that the strong ground motion is controlled by the strength of the rock mass that ruptures during a tectonic-type seismic event in the source region. This implies that in a weak rock mass, a seismic dislocation would have a low-rupture velocity that will generate only low levels of PPVs. The tunnel we studied was developed in a strong quartzite rock mass in the footwall of the Ventersdorp Contact Reef (VCR). The seismic dislocation in this geotechnical area will rupture with high velocity and generates high-level PPVs, which associates with the most damaging seismic events in this mining region on the skin of the excavation.

The damage to the rock mass is localized to the source area of the rockburst. For a M=2.8 large seismic event, the velocity at which these key blocks are ejected correlates to the modelled estimated peak particle velocity (PPV) in Figures 5.12 and 5.13. Many other factors influence the PPV on the skin of the excavation (e.g., doubling of the wave due to constructive interference, the resonance of blocks, etc.). Several previous studies (Cichowicz and Durrheim, 1997; Milev et al., 1999) on peak particle velocities and site response have “indicated that the PPV on the skin of the excavations may be larger by four to ten times the PPV at a point in solid rock at a similar distance from the source”. Milev and Spottiswoode (2005) highlighted that the higher PPVs have a minor influence on the site response. Milev and Spottiswoode (2005) found that the site response obtained at the excavation surface attenuates with the hypocentral distance. Severe damages were observed within the source radius of 35 m, which is within the source dimension of an M=2.8 event (110m -240m).

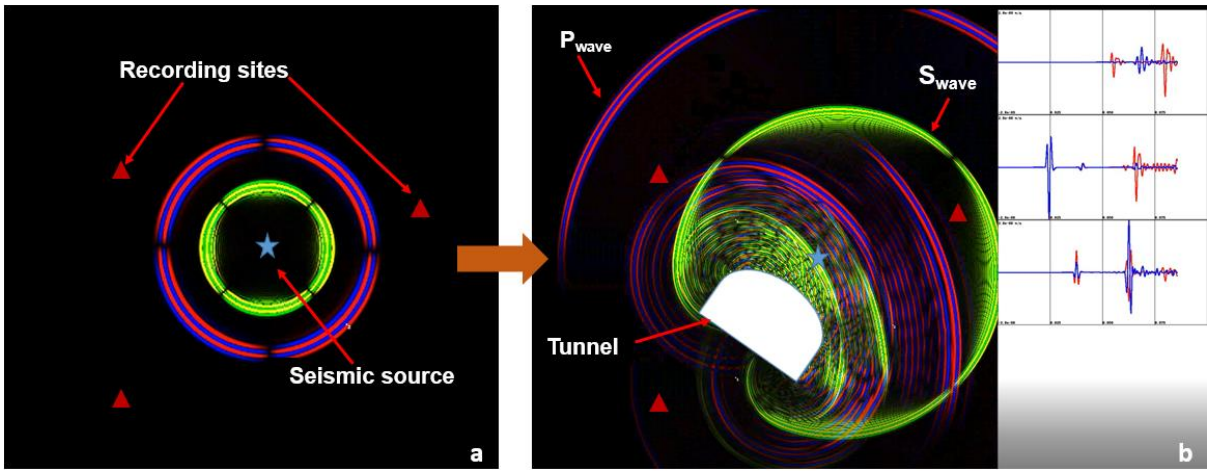

Figure 5.11: *(a). A wave propagation code cartoon is showing seismic energy where the rupture or failure occurs and the radiation pattern attenuating from the source to the recording sites (b). The radiation pattern cartoon of a hanging wall seismic event indicates both the P- and the S- waves from the source and the site's recordings passing through a tunnel. Seismograms (blue and red) of the three sites are displayed far-right (IMS-Tunnel source wave propagation code, 2015).*

This generic attenuation equation for the Cooke 4 Operation was used in the software, (Equation 5.5):

$$Log\ PPV = 0.761(M_L) - 1.620\ LogD\ + 4.096 \qquad [5.5]$$

where the PPV is peak particle velocity (mm/s), M_L is local magnitude and D represent a distance (m). The reduction of the amplitude due to attenuation of the rock mass was modelled using equation 5.9 in a radius of 407 m away from the seismic event centroid. The contouring indicates the decrease in PPV with distance (Figure 5.12).

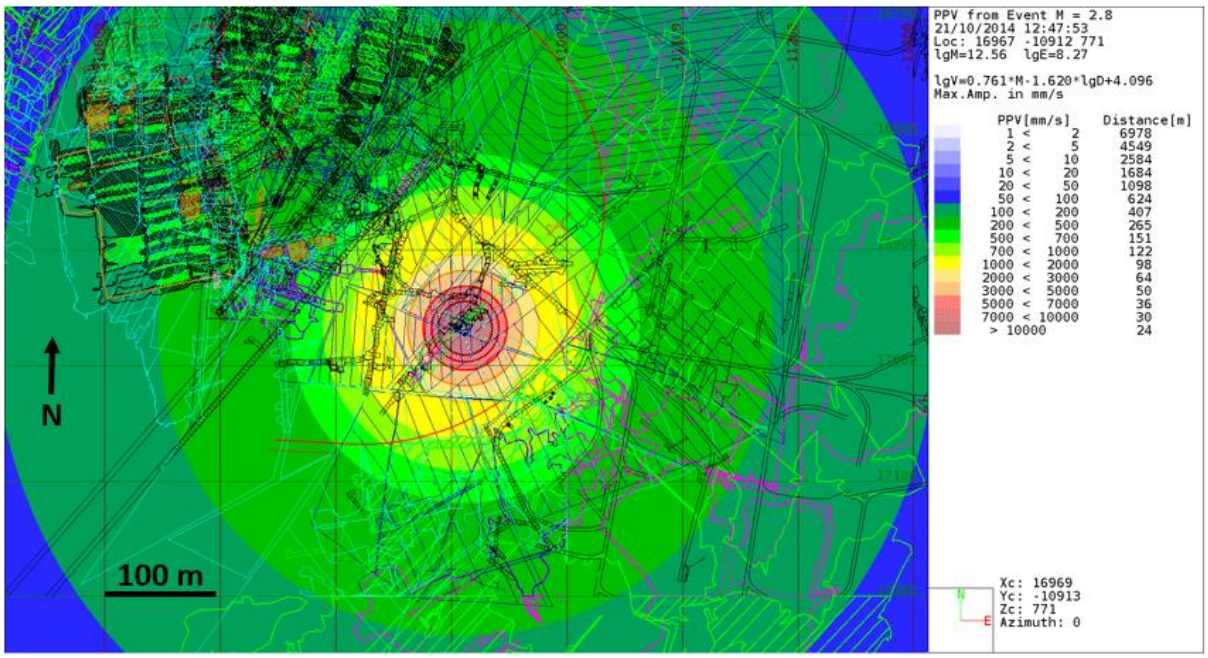

Figure 5.12: *Modelled PPV estimation of the M_L=2.8 magnitude seismic event in the vicinity of the 38 cross-cut south.*

The modelled PPV for the M_L2.8 seismic event indicates values in the source area in the order of 2000 mm.s^{-1}, which decreases as the wave attenuates to tolerable levels of less than 50 mm.s^{-1} within 1098 m distance from the centroid of the seismic source (Figure 5.13). The equivalent maximum expected PPV for such an event is predicted by the attenuation equation as 2200 mm.s^{-1}. Figure 5.13 indicates a relationship between PPV and distance from the source for magnitudes ranging from 0.0 – 5.0. The relationship between equation [5.9], Figure 5.12 and Figure 5.13 do not correspond because Figure 5.13 underestimates the PPV (0.65 m/s compared to 1.0 m/s at 98 m). The graphs colouring was due to the underground observation that was subjective.

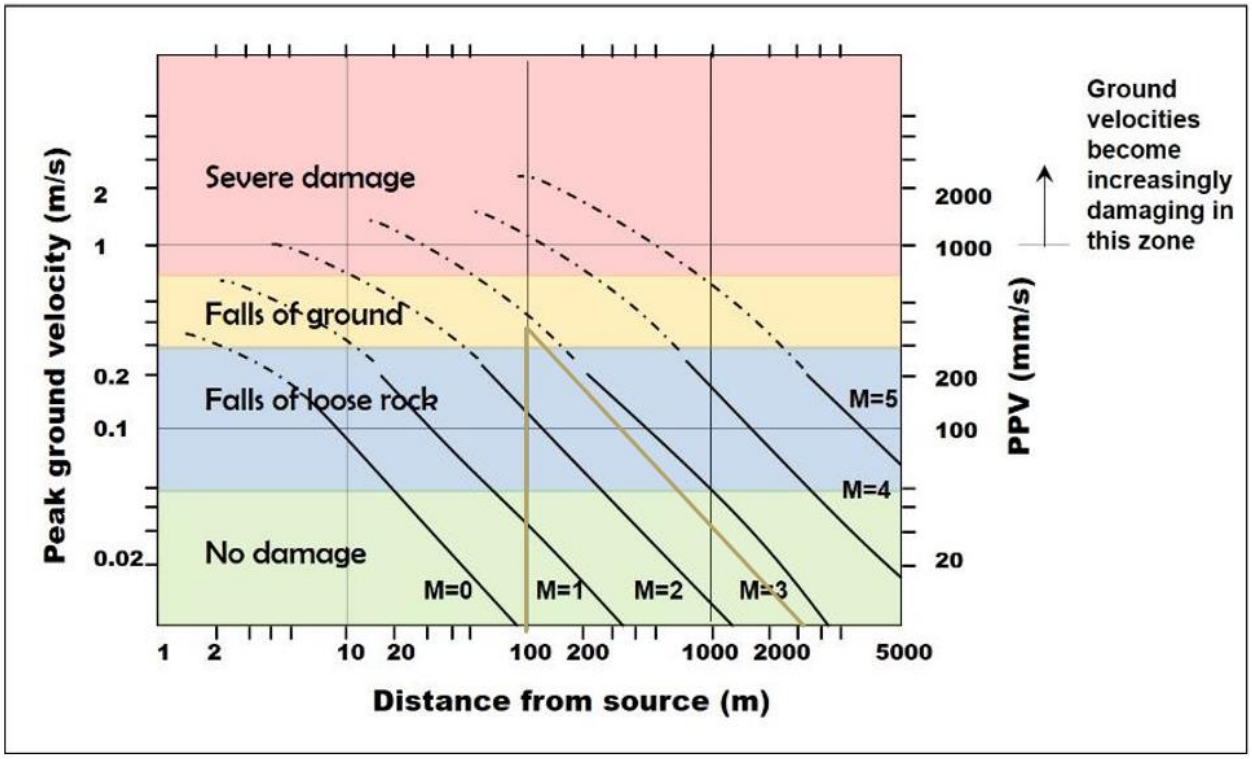

Figure 5.13: *Magnitude (ML=2.8), corresponding PPV and expected damages at 98m. The colours represent damage observations from the Kloof mines from 2007-2013 (Modified Jager and Ryder, 1999).*

Underground observations at the rockburst site and the damage assessment

The M_L2.8 seismic event with a source length of between 110-240 m affected two primary working levels at a depth of 1808 m (38 and 38A level; see Figure 5.14). One injury was reported from the 38A level, and 11 injuries were reported from 38 level cross-cut south. The vertical elevation difference between these levels is 35 m. The most severe rockburst damages were encountered on 38 level cross-cut south, consisting mainly of sidewall and hanging wall ejection of rock and footwall heave (Figure 5.15 and Figure 5.16). The damage extended over a 70 m length of the 38 cross-cut south. From the underground observations, it is estimated that the seismic event's hypocenter is located near the 38 cross-cut south, and resulting in this excavation experiencing strong ground motion. Scattered falls of ground were experienced up to 70 m radially out from the hypocenter location. Figure 5.14 below describes the radial extent of observed damage experienced by the block of ground. Within 35 m radius, there was severe rock ejection.

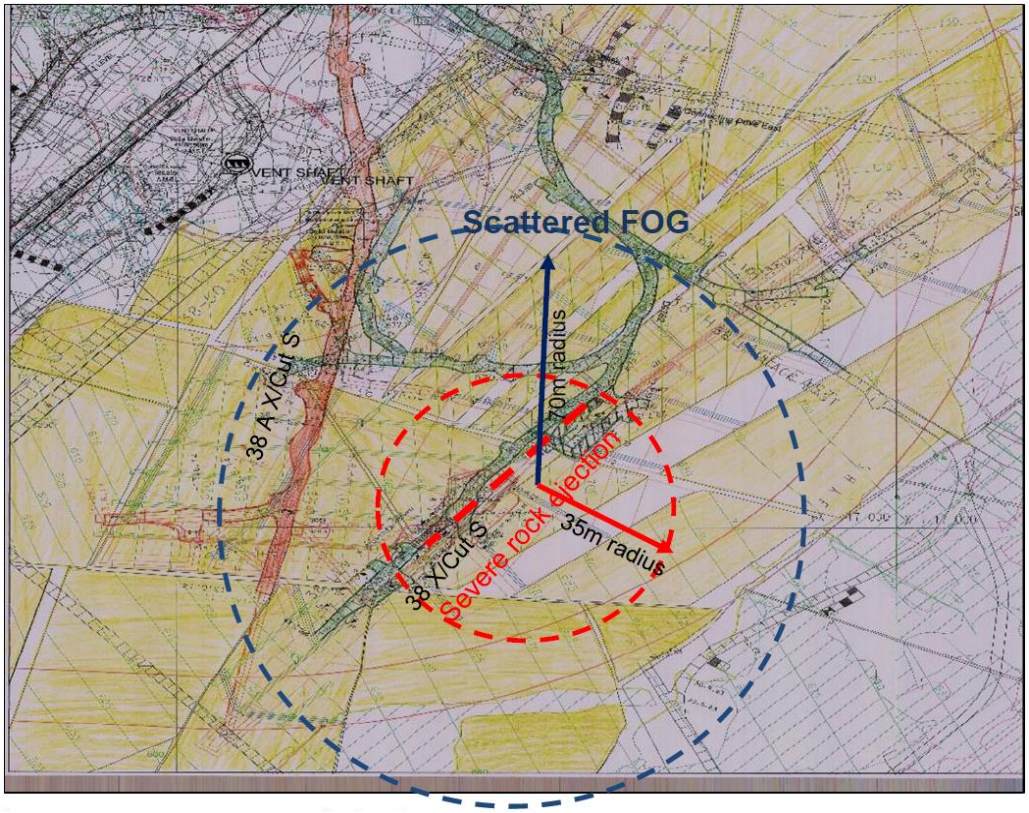

Figure 5.14: *Plan of 38 cross-cut south and 38A cross-cut south indicating the radial extent of observed damages.*

However, in the 38 cross-cut south, sections of both the sidewall and hanging wall were damaged, and the mild steel wire mesh failed in tension and allowed the unravelling of friable rock through the mesh pockets. Also, several long anchor plates were loosened during the seismic event, which led to unravelling and loss of the linkage between the tunnel secondary support (mesh and lacing). Figures 5.15 and 5.16 below indicate conditions observed at the site after the M_L2.8 seismic event.



Figure 5.15: *Damage to 38 cross-cut S showing unravelling of support including sidewall and hanging wall ejection of rock (Tshepo Rabele, 2014).*



Figure 5.16: *Footwall heave lifting a 5 ton locomotive above the grade line position (Tshepo Rabele, 2014).*

The M_L2.8 seismic event is located ±15 m from the West trending dyke and the NNE trending fault intersections (Figure 5.10 and Table 5.3). The Fault Plane Solution (FPS) indicates the induced seismic event was likely to be associated with the geological feature in the vicinity of its source location, trending North-North East (NNE). It is likely to be the slip fault, according to the energy ratio (Es/Ep =34.7). The moment tensor solution showed an isotropic component of 14.3%. One of the FPS had a dip of 45° and strike of NNE (197°), which aligns with the fault in the vicinity of the seismic event (Figure 5.17 and Table 5.4). Lower isotropic components indicate fewer volume changes and low stope closure in the affected rock mass. The higher double couple (62%) suggests a slip (shear) mechanism seismic event, possibly related to a structure. The PPV plot for the M_L=2.8 seismic event would be between 700 - 1000 mm/s at the 38 and 38A cross-cut south, which correlates well with the damage within the source radius of the seismic event. The expected damage for these PPV values will range from severe damage to fall of ground within 50 -100 m from the centroid of the seismic event. The intense damages in 38 cross-cut south are much easier to explain in terms of a seismic source that is very close (probably less than 20 m) to the tunnel, which is within the source radius. The Hudson diagram indicates the source as a double couple and more of an implosive source positive linear dipole (Figure 5.18).

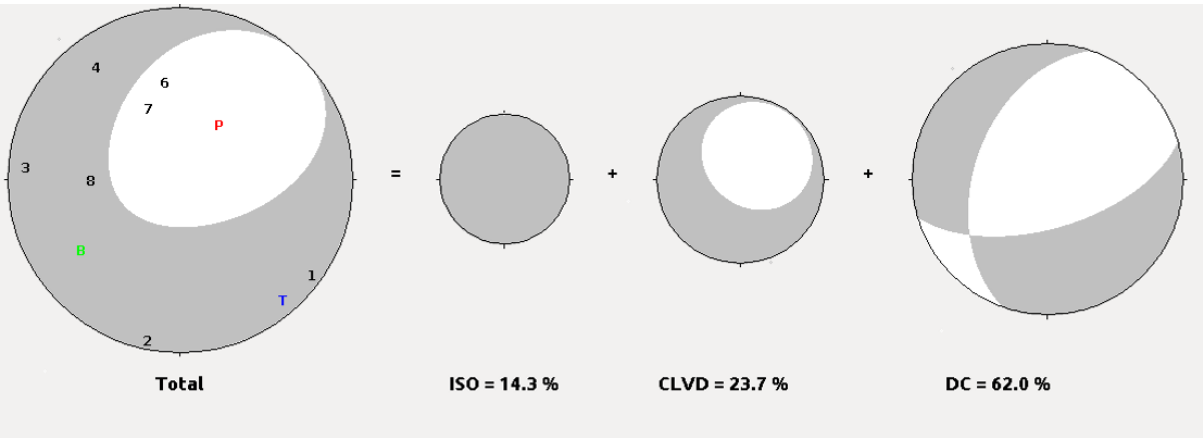

Figure 5.17: *Focal mechanism of M_L =2.8 seismic events indicating the Isotropic (ISO), compensated linear vector dipole (CLVD) and the Deviatoric (DC) components of the Moment Tensor Solution.*

Table 5.4: Moment tensor for the M_L=2.8 event on 21 October 2014

Event	Mag	Date	Time	Depth (m)	ISO [%]	CLVD [%]	DC [%]
1	2.8	2014/10/21	12:47:53	1808	14.3	23.7	62.0%

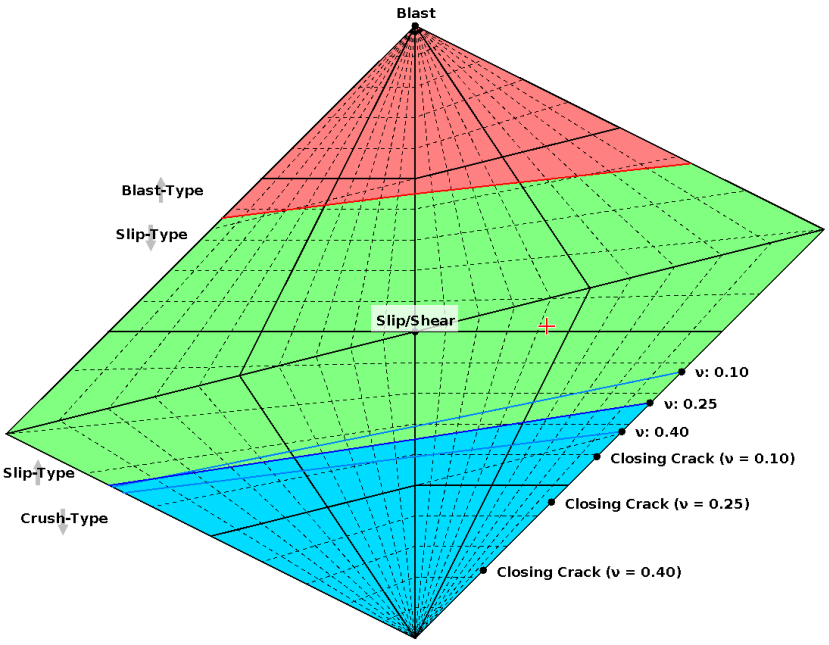

Figure 5.18: *The Hudson plot indicating a slip-type implosive seismic source type. It is divided into 3 regions: Upper region (Explosive), Central region (High DC) and Lower region (implosive). Black lines are contours of constant T (measure of deviatoric moment release, running from right to left) and k (measure of the change in volume, running from top to bottom).*

Conclusions

In summary, the following conclusions were reached by the author:

1. The seismic event appeared to be within the mining excavations and was most likely associated with movement on one or more faults in the area. This seismic event was likely due to a rock mass failure (instability) directly below the 38 south cross-cut south and 38A south.
2. The stress state change due to mining in the shaft pillar area was probably responsible for the instability on the geological features in the vicinity (e.g., faults).
3. The damage in the access development was controlled partially by the friable conditions of the rock mass and largely the quality of the initially installed secondary support that was planned to be re-installed by the time the seismic event occurred.
4. The hanging wall (above the fall out) displayed a complex structure, including the west-dipping fractures, which were activated during the rockburst and the planar discontinuities of different ages, with slickenside, some old and some reflecting dynamic deformation during the rockburst.
5. The moment tensor solution showed a DC component of (62.0%) indicating more of a slip, CVLD (of 23.7% indicating some stope closure), and ISO (of 14.3% indicating some burst). One of the fault plane solutions had a dip of 45^0 and a strike of NNE. Moment Tensor (FPS) suggests that the seismic event was due to the NNE trending geological structure.

CHAPTER 6 - THE 3D REFLECTION SEISMIC METHOD

6.1 Background

The reflection seismic method is a geophysical technique that generates seismic waves at a source and records the time it takes for components of that seismic energy to return to the surface and be recorded by receivers (Musset and Khan, 2000). It was originally developed to map the earth's crust along 2D profiles. Advances in technology, especially in computing power, have made it possible to produce 3D data in 'cubes' the crust in 3D. The method has been used widely by petroleum companies to map geological structures, determine rock mass properties, and locate exploration and appraisal boreholes. The first 3D reflection seismic surveys were shot in the 1970s, and it has since become popular in crustal and mineral exploration in the continental basins (Davies *et al*., 2004; Trickett *et al*., 2005).

The technique is advantageous for deep mineral exploration and exploitation as it provides high-resolution imaging of the subsurface (e.g., Malehmir *et al*., 2012; Pretorius *et al*., 1994; Pretorius *et al*., 2000; Trickett *et al*., 2004). Compared to other geophysical methods (e.g., gravity, magnetic and 2-D reflection seismic), the 3D reflection seismic proved to be a mineral exploration tool that provides a more complete and detailed image of the subsurface (Pretorius *et al*., 1994; Milkereit *et al*., 1996; Trickett *et al*., 2004; Salisbury and Snyder, 2007; Malehmir *et al*., 2012, 2013). The deep South African gold mines adopted the technique in the 1980s to image the structurally complex Witwatersrand basin at great depths hosting the world-class gold-bearing conglomerate (Gibson *et al*., 2000; Salisbury *et al*., 2003).

6.2 3D reflection seismic method

6.2.1 Survey design and data acquisition

The 3D reflection seismic method is a geophysical method that is used to study the earth's crust. The method generates seismic waves in the earth's crust using energy sources (e.g., vibroseis). Snell's law governs this technique by describing the incident rays' behaviour at the boundary of two media exhibiting different refractive indices (Kearey *et al.*, 2002).

As with any other geophysical method, the seismic reflection method is only sensitive to specific physical properties (e.g., seismic velocity and density) and contrasts. These may include lithological and structural boundaries such as conformities and unconformities, faults and dykes (Peters, 2005). The injected seismic waves are reflected back to the surface at discontinuities that have a strong acoustic impedance. The acoustic impedance (Z) is dependent of rock density (ρ) and seismic velocity (υ) as defined in Equation (6.1):

$$Z = \rho * \upsilon \qquad [6.1]$$

A geological structure (interface) reflection may be observed when an acoustic impedance contrast between the surrounding rock units and the interface is sufficient. In this case a geological structure (interface) reflection may be observed. The reflected seismic waves are recorded on the surface of the earth by arrays of receivers called geophones. The reflected seismic waves can map subsurface structure and acoustic impedance anomalies by analyzing the seismic wave's time to reflect from subsurface interfaces and return to the surface (*viz.* two-way travel time) and the amplitude of the reflected pulse (Figure 6.1).

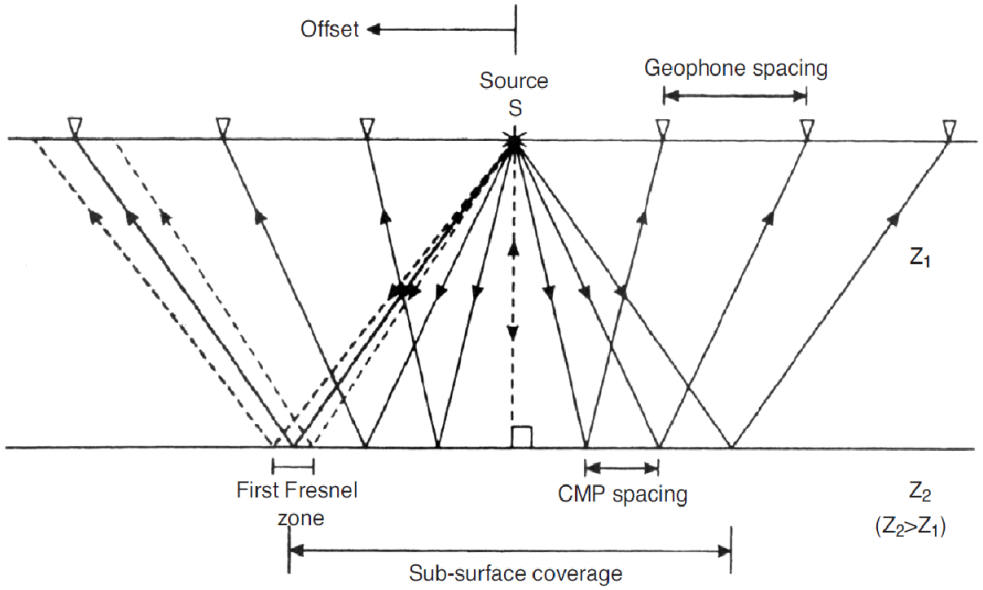

Figure 6.1: *Schematic showing reflection of seismic waves from a horizontal interface with contrast in acoustic impedance, Z ($Z_2 > Z_1$) (after Trickett et al., 2004).*

Sharp changes in the acoustic impedance contrast (Z) within the rock mass usually produce continuous and strong reflections that will allow the interpretation of the subsurface geology (Salisbury *et al*., 2003). So, when an acoustic impedance contrast is high between rock units, strong reflections will result in interpretation of the subsurface geology (Bacon *et al*., 2003). Typically, an impedance contrast of at least 2.5×10^5 g/cm^{2}s is required to produce a sufficient seismic reflection (Milkereit *et al*., 1996; Salisbury and Snyder, 2007; Chopra *et al*., 2006). Poor seismic reflections will result from a lower acoustic impedance contrast, increasing the difficulty of interpreting the geology.

The strength of the reflection at rock layer interfaces - depends on a parameter referred to as the reflection coefficient (R). The parameter (R) is defined in terms of the contrast in acoustic impedance (Z) at a rock layer interface. The reflection coefficient (R) describes how much of a wave an impedance boundary can reflect (Kearey and Brooks, 1991; Salisbury *et al*., 2000; Kearey *et al*., 2002). Sheriff (2002) describes it as'

the ratio of the amplitude of a reflected wave to that of the incident wave'. For a P-wave that hits the interface at normal incidence (head-on), the reflection coefficient is defined by Equation (6.2)

$$R = \frac{\rho_2\ v_2 - \rho_1\ v_1}{\rho_2\ v_2 + \rho_1\ v_1} \qquad [6.2]$$

which can be represented as

$$R = \frac{Z_2 - Z_1}{Z_2 + Z_1}$$

where Z_1, v_1, ρ_1, represent the first layer's acoustic impedance, the P-wave velocity, and the density of the first layer and the Z_2, v_2, ρ_2 the acoustic impedance, the P-wave velocity and density of the second layer (Figure 6.2).

The reflection coefficient can be positive or negative depending on the acoustic impedance difference in the first and second layers. When the reflective coefficient is either negative or positive there will be reflection, but the polarity of the seismic wave will change if the reflection coefficient is negative. Besides the reflection coefficient and the acoustic impedance contrast, the depth and geometry of the deposit are other parameters that can determine a horizon's reflectivity.

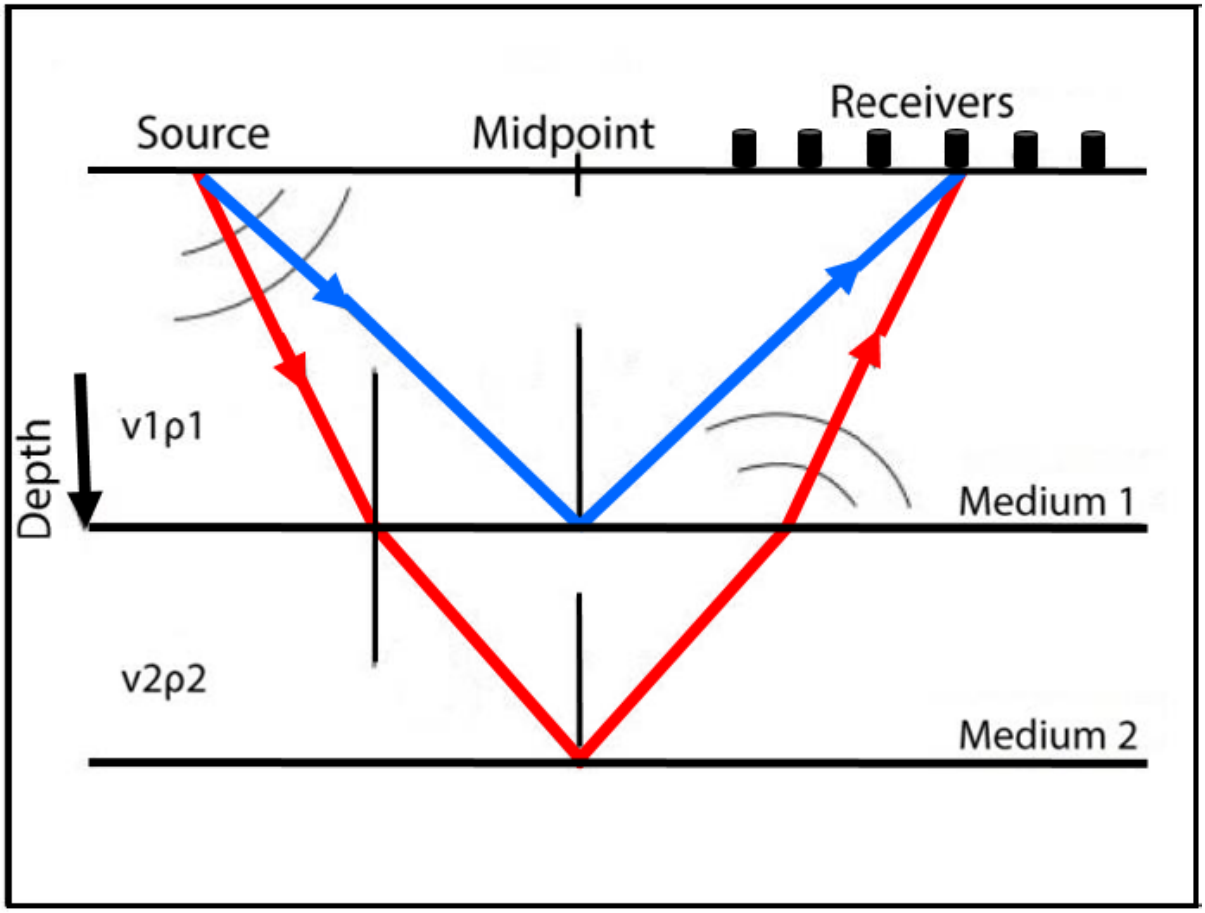

Figure 6.2: *Schematic diagram of source-receiver geometry. The diagram shows the reflection wave paths over a horizontal interface across which there is an acoustic impedance contrast, where* $\boldsymbol{v_1\rho_1} > \boldsymbol{v_2\rho_2}$ *or* $\boldsymbol{v_2\rho_2} > \boldsymbol{v_1\rho_1}$ *(after Salisbury and Snyder, 2007).*

Within the Witwatersrand Basin, Kloof Gold Mine provides perfect cases of continuous and strong seismic reflectors well defined by the 3D seismic reflection method (i.e., Black-Reef (BR) and Ventersdorp Contact Reef (VCR)) (Figure 6.3). The BR is imaged between the overlying dolostones of the Chuniespoort Group of the Transvaal Supergroup (density ~2.84 g.cm^{-3} and velocity ~5000 m.s^{-1}) and the underlying basic-ultrabasic volcanic rocks of Klipriviersberg Group (density ~2.90 g.cm^{-3} and velocity ~6400 m.s^{-1}). The VCR is imaged as a strong reflector, and it locates between basic to ultrabasic volcanic rocks of the Klipriviersberg Group and the quartzites of the Central Rand Group (density ~2.67 g.cm^{-3} and velocity ~5700 m.s^{-1}).

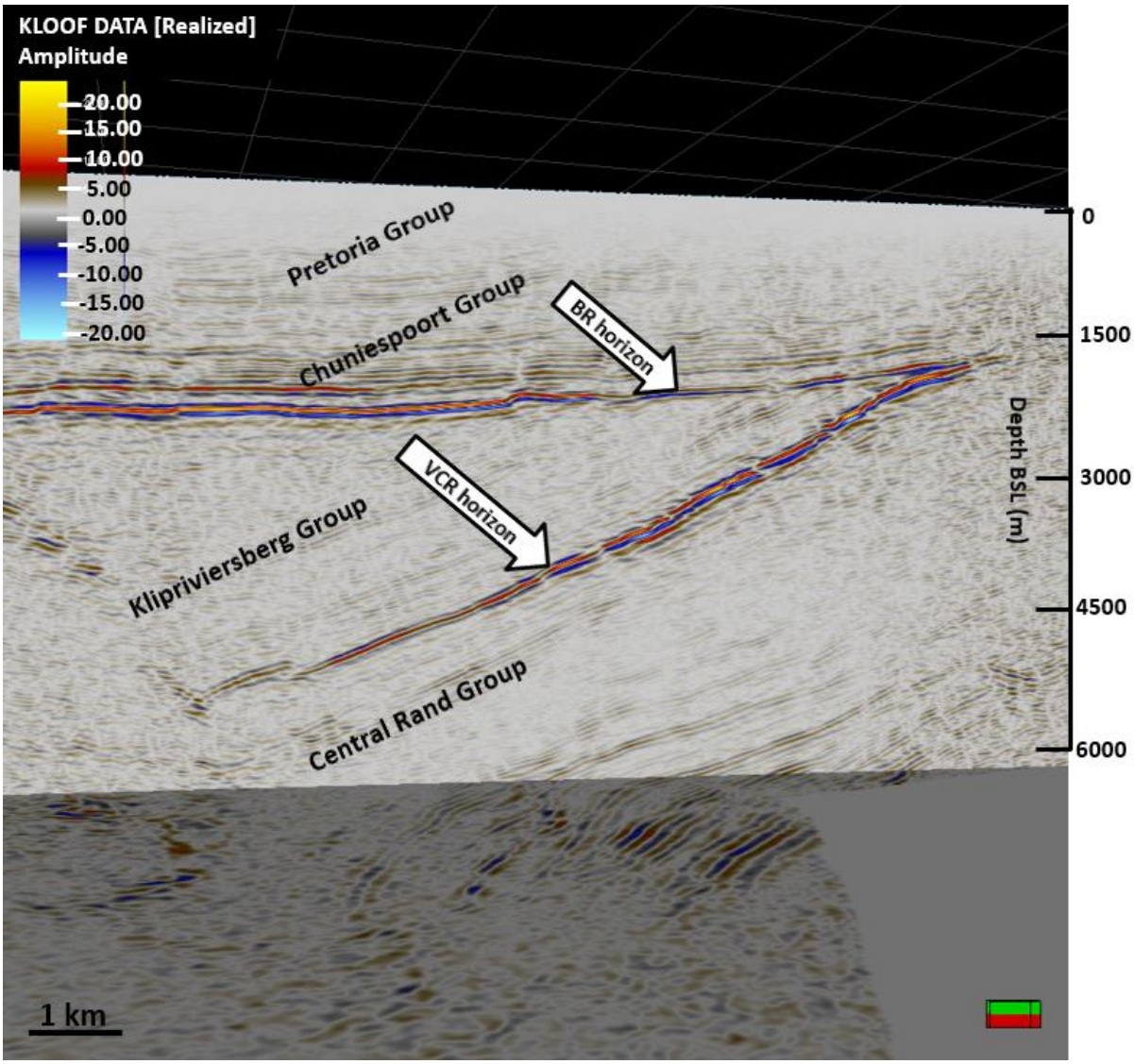

Figure 6.3: *Kloof Gold Mine amplitude-display seismic section showing the imaging of reflective interfaces in the Transvaal Supergroup (Pretoria and Chuniespoort groups) and the base of the Klipriviersberg Group, especially the Black Reef (BR) and Ventersdorp Contact Reef (VCR) horizons. (BSL:Below Surface Level)*

The 3D reflection seismic surveys are designed to give details about the subsurface at a specific degree of resolution and a particular depth of penetration in the vertical dimensions and horizontal resolution (Kearey and Brooks, 1991). “The horizontal dimension gives the capability to recognize and distinguish two laterally displaced features as two distinct adjacent events while the vertical dimension provides the ability to differentiate at different depth levels the closely spaced reflectors” (Chopra *et al*., 2006). The horizontal resolution depends on the Fresnal Zone, which in the portion of the reflector from which reflected energy can reach a detector within one-half wavelength of the first reflected energy. The Fresnel zone size depends on the interface's depth and the dominant seismic wavelength (Figure 6.4). In interpreting the small features within the seismic data, attention is focused on the vertical resolution (Chopra et al., 2006). According to

Gibson (2004), this is known as the 'Fresnel zone' sampling, and the seismic wavelength defines it. Yilmaz (2001) described the horizontal resolution by the first Fresnel zone dimension, the area of subsurface where the reflected waves interfere constructively, and they're of paths travel differ by less than a half wavelength ($\lambda/2$). Seismic resolution is measured in wavelengths (λ). The vertical resolution in seismic data with a high ratio of signal-to-noise that will be defined by $\lambda/8$ (λ represents the data's dominant wavelength), while $\lambda/4$ resolution may be achieved with a lower signal-to-noise ratio.

As the transmitted seismic wave travels through the earth's crust, location uncertainties of the imaged structure will be unavoidable (Kearey and Brooks, 1991).

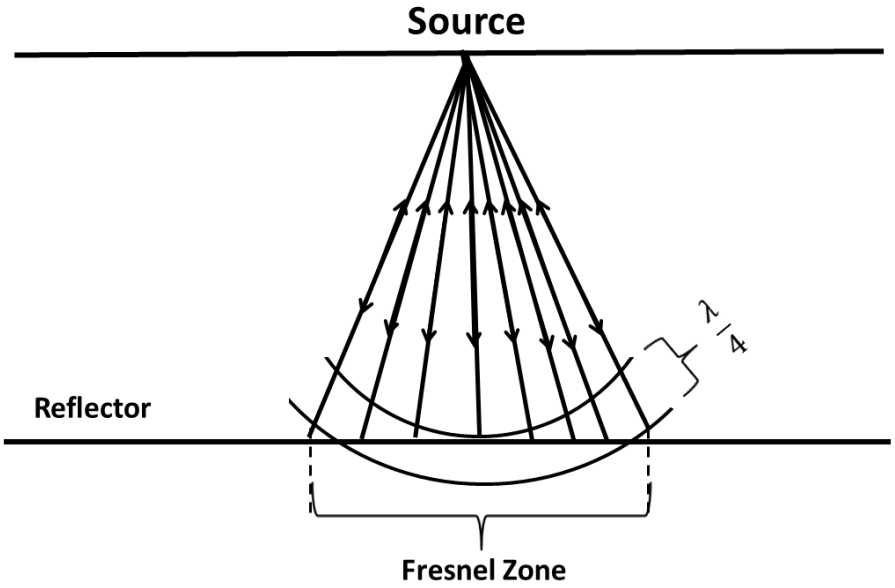

Figure 6.4: *The Fresnel zone is the area on a reflector where the incident energy ray is returned within the central ray's half-wavelength (λ) of the central ray. (Kearey and Brooks 1991).*

6.2.2 Seismic data processing

Removing the noise and keeping the reflected signal is the primary goal of seismic data processing. These provide reflectivity images of the correct reflector geometry. When processed, the digital signal gets converted into an image that will best represent the geological subsurface. Typically, on the raw seismic record the following waves can be identified: head waves - refractions, reflections, airwaves, surface waves. Figure 6.5 indicates the processing workflow of the reflection seismic data.

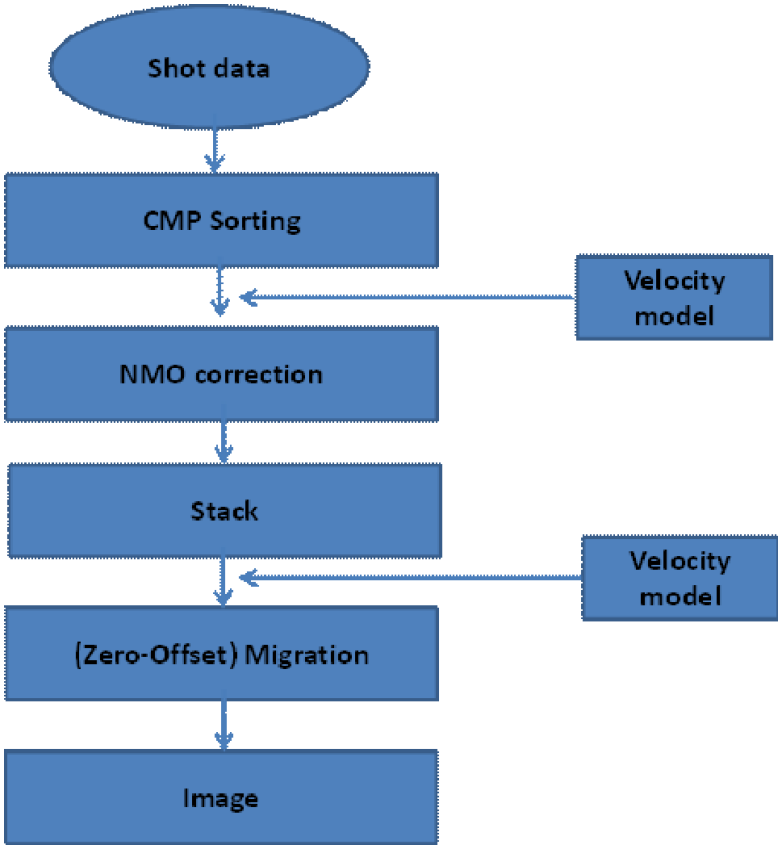

Figure 6.5: *Processing flow of the reflection seismic data.*

The processing steps will include CMP sorting (where velocity model is derived from), analysis of velocities and frequencies, normal moveout (NMO), CMP stacking (improving signal-to-noise ratio), deconvolution, dip moveout (DMO), migration (increasing lateral resolution), migration can be performed before or after stacking.

Sibanye Stillwater Ltd (Kloof) - South Deep (Gold Fields) conducted a 3D reflection seismic survey in the West Rand to map the subsurface structures and the potential ore-bearing horizons Witwatersrand basin. Gibson (1997) and Gibson *et al.* (2000) processed and then interpreted the Sibanye Stillwater 3D reflection seismic data. In 2012 Manzi *et al.* (2012a, b) merged and re-processed the 3D reflection seismic data and produced a continuous, seamless depth converted prestack time migration. The processing of the Kloof-South Deep data was divided into two phases by Manzi *et al*. (2012a):

- Field pre-processing conducted on-site by CGG.
- Full 3D processing undertaken by Velseis Processing Pty Ltd in Brisbane, Australia using ProMAX processing software.

Table 6.1 specifies the summary of the parameters used for processing the 2003 Kloof - South Deep and 1994 Leeudoorn (Kloof 7 Shaft (K7)) 3D reflection seismic data.

Table 6.1: The summary of parameters used for the 2003 Kloof-South Deep and 1994 Leeudoorn 3D Reflection seismic data sets (Manzi *et al*., 2012b)

Processing Step	**Parameters**
Data reformat	From SEGD to Promax internal format
Trace editing	Air-blast attenuation applied
Geometry application	Source, receiver, offsets, etc., assigned to each trace
Gain recovery: spherical divergence correction	$(\frac{1}{TV^2})$, where V=5500 m/s
Surface consistent spiking deconvolution	Operator design window at 0 m offset; 100-2500 ms, operator length:120 ms white noise stabilization: 1%
Zero-phase spectral whitening	Eight frequency window, 500-ms sliding window
3D refraction statics correction	Surface layer V_0= 1200 m/s (contant), seismic datum
Statics application	Smooth processing datum
First-pass interactive velocity analysis	Every 600m in crossline and inline direction
First-pass surface consistent residual statics	Maximum power autostatics, 300-ms time gate around flattened horizons
Interim stack: Leeudoorn and Kloof-South Deep	Data sets stacked separately, 35% stretch mute and 500-ms AGC applied
Prestack phase rotation and time-shift to match Leeudoorn data set and Kloof data sets	Leeudoorn data: time shift of - 8 ms and 90 degrees phase shift
Prestack merge of Kloof-South Deep and Leeudoorn data sets	
Second-pass interactive velocity analysis	Refraction statics calculated on the merged data and tied to upholes
Second-pass surface consistent residual statics application	Every 600m in crossline and inline direction
CDP trim statics	Maximum power autostatics, 300-ms time gate around flattened horizons
DMO velocity analysis	Non-surface consistent CDP statics
Pre-stack time migration (PSTM) flow	Full 3D KIRCHOFF using DMO using 50-m inline and crossline distance
First-pass PSTM velocity analysis	DMO velocity removed and PSTM velocities picked
PSTM	Full 3D KIRCHOFF migration using velocity model from smoothed first pass PSTM velocities
Second-pass PSTM velocity analysis	Second pass PSTM velocities picked
NMO correction Stack	Second pass PSTM velocities picked
Band-pass frequency filter	Time variant Ormsby zero-phase filter, 0-1400 ms: 15/20 - 80/90 Hz
Depth conversion	Using interval velocities derived from borehole data and BR and VCR time horizons

Field seismic pre-processing aimed to produce a brute stack with a simple elevation correction within a day of completing each swath (Manzi *et al*., 2012a). After the field data were loaded into the processing

software, a single velocity function is applied to correct for the normal moveout (NMO) in the gather and then common depth point (CDP) stacking is applied. This allows a user to get the brute stack. The procedure was followed to assess the acquired data's quality, estimate the signal-noise ratio, detect bad and noisy traces, etc.

6.2.3 Seismic data interpretation

Seismic data interpretation involves the extraction of information regarding the subsurface geology from the 3D reflection seismic cube. This can aid in identifying subsurface structures and geological properties of the 4500 m deep seismic cube. This survey was a 4 seconds two-way-time (TWT) which equates to ~13 000 m in depth when using the average seismic velocity of 6500 km/s. Derivation of reflection seismic models could be achieved as well. Interpretation is achieved by combining surface and underground sources of geological information like geological contacts or fault traces. The accuracy of the 3D reflection seismic data interpretation depends on the seismic migration technique during processing (Manzi, 2013).

6.3 Seismic attributes

All the information attained from reflection seismic data, either by logical-based reasoning or experience or direct measurements, is called seismic attributes (Taner *et al*., 1979). Sheriff (1992) defined *seismic attributes* as measures derived from seismic data, such as dip azimuth, dip angle, instantaneous phase, instantaneous envelope frequency, polarity. These seismic attributes are derived from the reflected energy's frequency, time, attenuation, and amplitude (Brown, 1996). Strecker *et al.* (2004) stated that attributes *"form an integral part of the qualitative interpretative tool that facilitates structural and stratigraphic interpretation as well as offers clues to lithology type and the fluids content estimation with a potential benefit of the detailed characteristic."*

6.3.1 Horizon based attributes

An attribute that measures the reflected energy within a given window is the amplitude attribute. When the correct amplitudes (peak or trough) are picked, it eliminates the undesirable phase effects observed. According to Marfurt (2006), an amplitude attribute defines the general structural architecture of an area adequately, and the information is derived from the horizon-based attributes, such as dip-magnitude, dip-azimuth, and edge detection, reveals subtle information and structural complexities.

Attribute analysis is applied where a high resolution is required, i.e., most seismic interpretation projects (Manzi, 2013). We used the edge detection attribute, a tool developed by Rock Deformation Research in 2004 and Petrel interpretation software from Schlumberger. The algorithm combines the dip and azimuth variation, taking local noise into account. The detectability differences between the dip and the azimuth are overcome by an algorithm developed by Rijks and Jauffred (1991).

6.3.1.1 Dip and Dip azimuth

Rijks and Jauffred (1991) highlighted both attributes, azimuth and dip could be seen as functions of the variability in the direction of the time gradient and the inclination computed from each sample trace. The attributes have been found helpful in the detection of third-order scale faults. This can be represented mathematically by Equation (6.3) and graphically as in Figure 6.6:

$$Dip\ magnitude = \sqrt{\left(\frac{dt}{dx}\right)^2 + \left(\frac{dt}{dy}\right)^2} \qquad [6.3]$$

$$Dip\ \ Azimuth = arctan\left(\frac{\frac{dt}{dx}}{\frac{dt}{dy}}\right)$$

where dip in the x-direction is $\frac{dt}{dx}$ and y-direction dip is represented as $\frac{dt}{dy}$.

The dip and dip azimuth attributes define the signal-to-noise ratio of the seismic data.

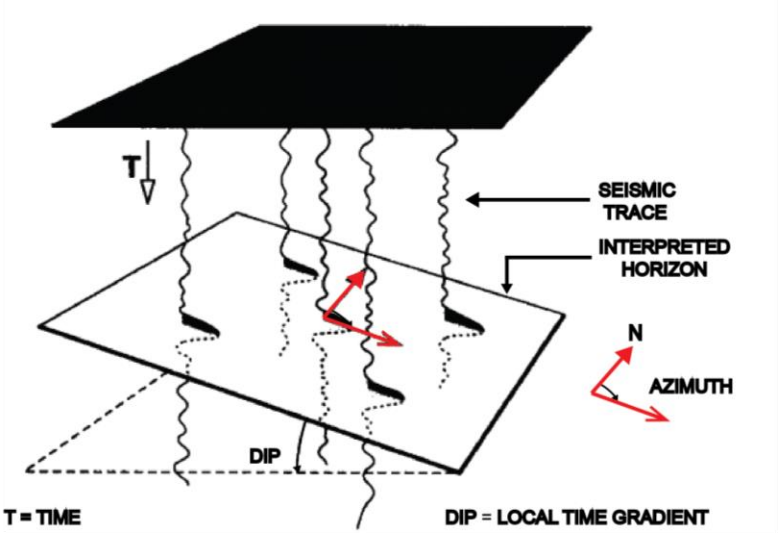

Figure 6.6: *A graphic representation of how the dip azimuth (direction) and dip are extracted from a seismic interpreted horizon. Calculation of both the dip azimuth and dip variations along a horizon (after Rijks and Jauffred, 1991).*

Dalley *et al*. (1989) made two recommendations to the application of the dip and dip-azimuth attributes. Firstly, the use of automatic picking when a chosen reflector is interpreted to ensure that surfaces are picked along the same phase. The noise is reduced and enhanced by the local dip estimates of the reflective surfaces. Secondly, when a fault characterized by the disturbance is encountered along with a reflector,

the fault should be picked as part of the horizon. An irregular azimuth characterizes the picked fault, and a high dip will appear as a feature along the surface. According to Manzi *et al*. (2013), these seismic attributes have limitations in their mapping, which includes:

- Only a noticeable dip angle fault different from the dip of the horizon can be detected by the dip attributes.
- Only a fault with clear dip direction and opposite to that of the layer can be detected by the dip-azimuth.

6.3.1.2 Edge detection

The edge detection attribute is used to overcome the dip-azimuth and dip differences in detectability. This combines both the dip-azimuth and dip variation that is picked and is normalized to the local noise on the horizon grid. According to Manzi *et al*. (2013), this attribute, *"when displayed in suitable colour bars, can highlight subtle faults and complex fault architectures such as fault connectivity, fault continuity, multiple fault bifurcations and the crosscutting relationship between fault systems"* (Figure 6.7). In the studies, the author found that the edge detection attributes resolve faults with throws as small as 10 m, as well as intersections of cross-cutting faults that are difficult to detect using conventional techniques. The edge-detection techniques eliminate errors *"resulting from false complex geometries created by conventional picking around faults, and thus minimize unrealistic fault-horizon geometries"* (Manzi *et al*., 2012b). The edge-detection attribute is a very effective fault-mapping tool, especially for faults with small throws and in structurally-complex regions.

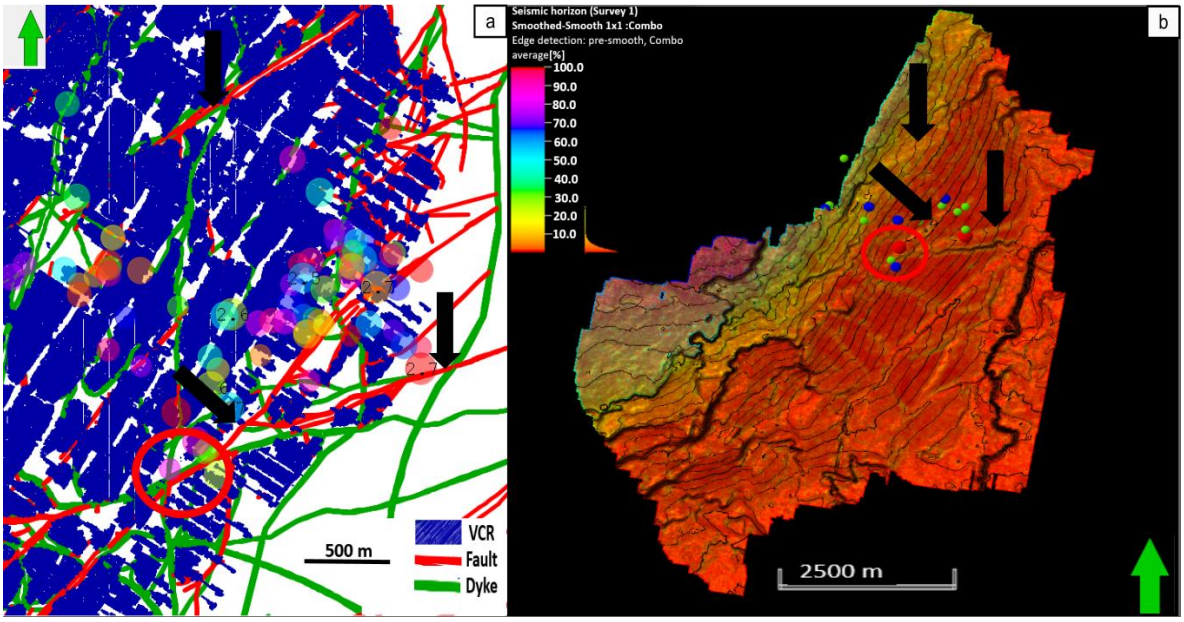

Figure 6.7: *(a) In-stope mapped geological structures indicating a good correlation with mining-induced seismicity data, (b) Edge attribute map of the VCR overlain with mining-induced seismic events ($M_L \geq 1.5$) in Kloof Gold Mine are indicated.*

6.3.2 Volumetric seismic attributes

6.3.2.1 Edge enhancement

The edge enhancement attribute is used to emphasize the spatial continuity of horizons and faults in the seismic data by computing the changes in the signal amplitude. This attribute decreases the noise in the data by using local dip estimates of the reflection layers (Randen et al., 2001). The edge enhancement attribute smooths the data without adding artifacts while reducing the noise and thus permits the detection of minor amplitude changes (Randen and Sønneland, 2005). The edge enhancement technique is applied to the seismic volume to smooth the data and reduce the noise before the ant-tracking attribute is applied.

6.3.2.2 Ant-tracking

Ant-tracking is a very powerful fault detection technique that uses a series of seismic attributes in a workflow to detect and map faults and fracture networks throughout a 3D seismic volume (Cox and Seitz, 2007). The method uses the principles of "swarm intelligence," which explains how ants find the shortest path between their nest and the food by communicating with each other using a chemical substance known as pheromone (Ngeri *et al.* 2015). In the Petrel software coded package, electronic ants called "ant agents" follow discontinuities to detect and enhance fault and fracture networks. This attribute aids the user/interpreter with more accurate and unbiased mapping of fault networks and horizons (Cox and Seitz, 2007).

6.4 Results

Presented in this section are the results obtained by the author using different processing workflows. It contrasts interpretations that resulted from the conventional seismic interpretations and those possible with seismic attributes. The processing workflow started with importing the processed 3D reflection seismic data into Petrel data interpretation software packages (Figure 6.8). The reflectors in the interest area were picked throughout the 3D seismic reflection seismic volume to inspect first-order features. Structural smoothing was used first to condition the data to reduce noise and increase the signal-to-noise ratio before seismic attribute application, as these are sensitive to noise. The analyses showed that the Bank and the West Rand faults, the two first-order scale structures, and various second and third-order faults crosscut Kloof operations in the section where the VCR is mined (Figure 6.8). The VCR cross-section (Figure 6.9b) shows the ore-body, mining-induced seismicity plotted along the reef, as well as second- and third-order faults. The seismic attribute analysis was carried out to investigate and indicate if there are subtle features that fall below the conventional resolution limits.

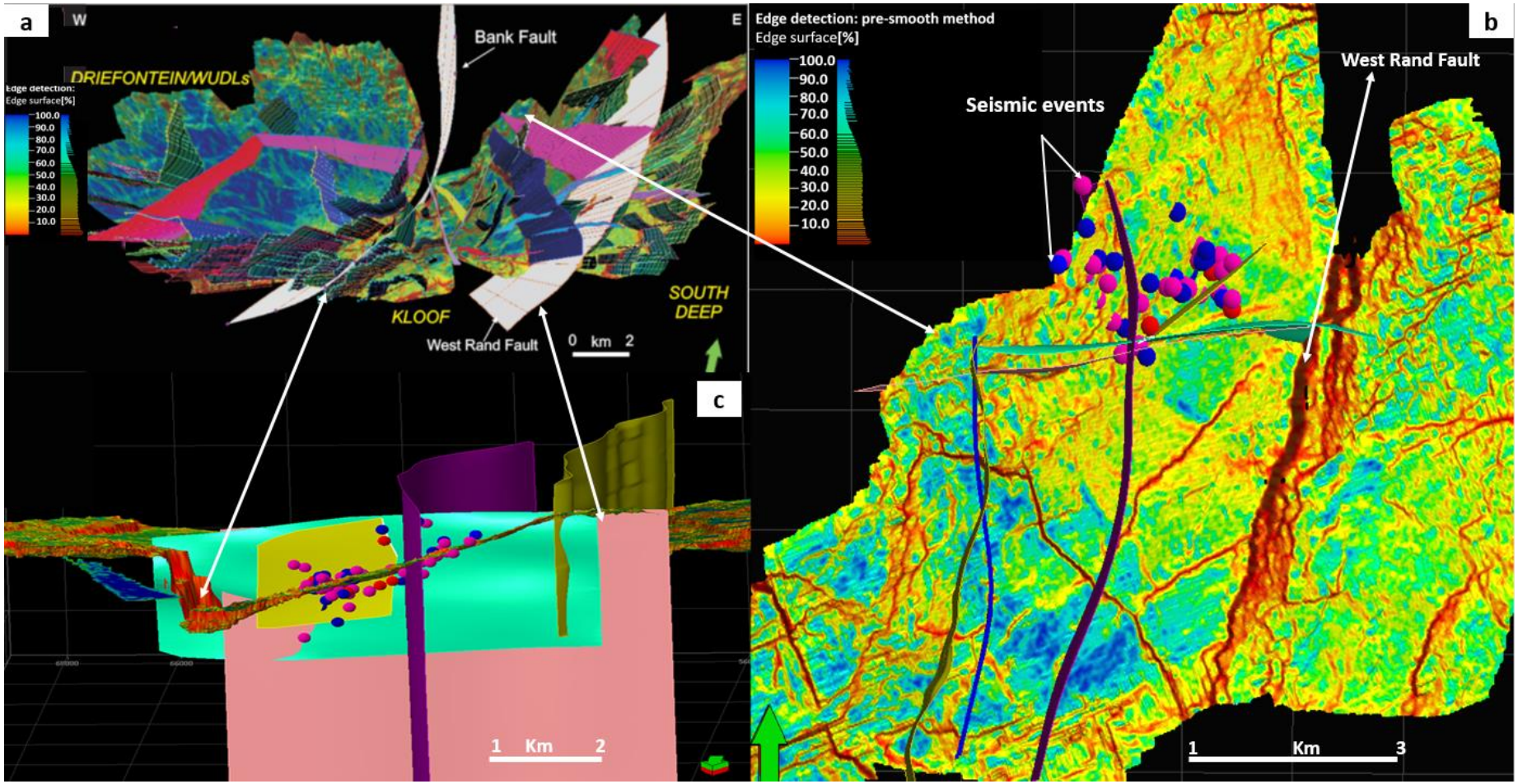

Figure 6.8: *(a) The 3D regional model defined from edge detection attribute analysis constructed from regional VCR pick. (b) Edge detection on section view incorporates the major West Rand Fault and Bank Fault (c) Edge detection model indicating the subtle structures and location of mining-induced seismicity (M_L≥1.5).*

The amplitude display seismic section indicates the rock mass crosscut by several second-order faults, Northeast-trending normal faults dipping to the East at an average of 63° (Figure 6.9). The faults' strike ranges from 90° - 167°, with the largest vertical throws ranging from ~10 to 30 m observed to the East and depths between 1.5 and 3.0 km below the surface. By further examining the crossline and inline sections, some sections display high-amplitude anomalies. However, their origin has not yet been determined by in-mine mapping (Figure 6.9).

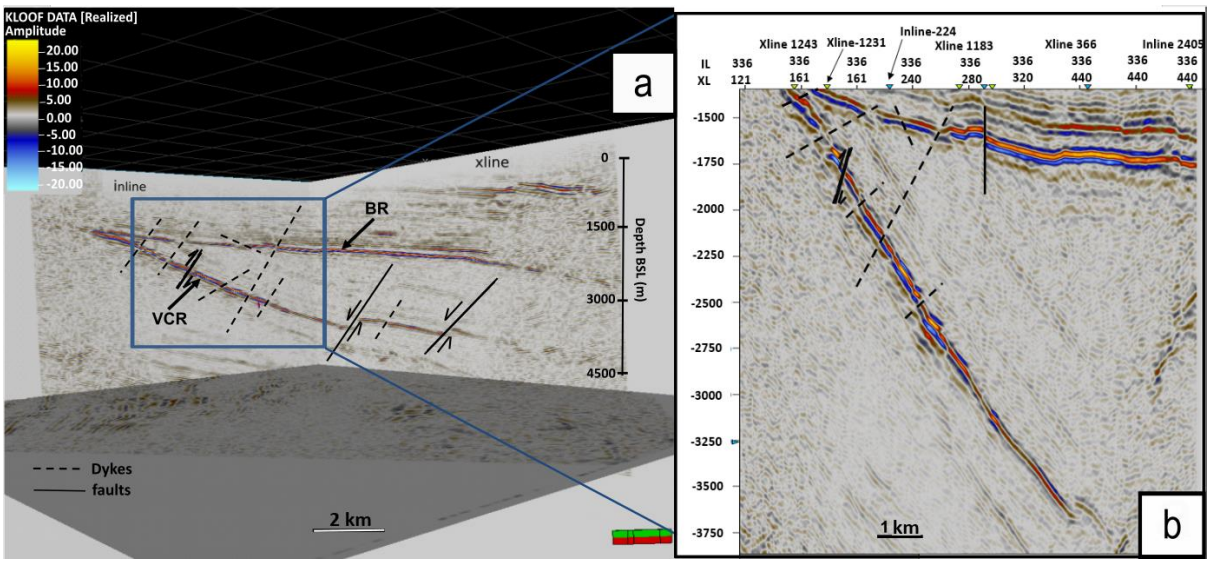

Figure 6.9: *(a) Amplitude display seismic section of the reflection seismic data (Kloof Operations) in the Petrel interpretation package, (b) zoomed-in cross-section for Inline 336 on the top right corner showing the westerly dipping faults and dykes cross-cutting the rock mass with the vertical exaggeration (VE) of 4:1. Owing to the low signal-to-noise of the amplitude display, it is difficult to track faults and dykes up stratigraphy to the Ventersdorp Contact Reef (VCR) and the Black Reef (BR) levels.*

The structural interpretation of the VCR depth map (Figure 6.10) represents the gridded Kloof operation VCR horizon produced from conventional interpretations, dipping to the North-East direction. The seismic section (in amplitude display) indicates an agreement between the borehole data and the VCR depth in Figure 6.10b (Manzi *et al*., 2013). The depth has improved the structural interpretation of the converted seismic data between Kloof 3 shaft (K3) and Kloof 4 shaft (K4). Manzi *et al.* (2013) indicated a minor 12 m depth discrepancy with the borehole control on the VCR horizon pick, as shown in Figure 6.10b.

The VCR was visible and mapped in the data's inline, crossline, and time scale. Some areas within the VCR horizon were picked out by extrapolating from the areas that were confidently mapped. Picking of geological structures (e.g., faults) was complex, as faulting displacement was not evident. All structures (both minor and major) need to be observed, interpreted and understood as they could be the possible

plane of weakness during mining operations and can cause either rockburst or fall of ground. This might delay production or even cause fatalities within the producing shaft.

.

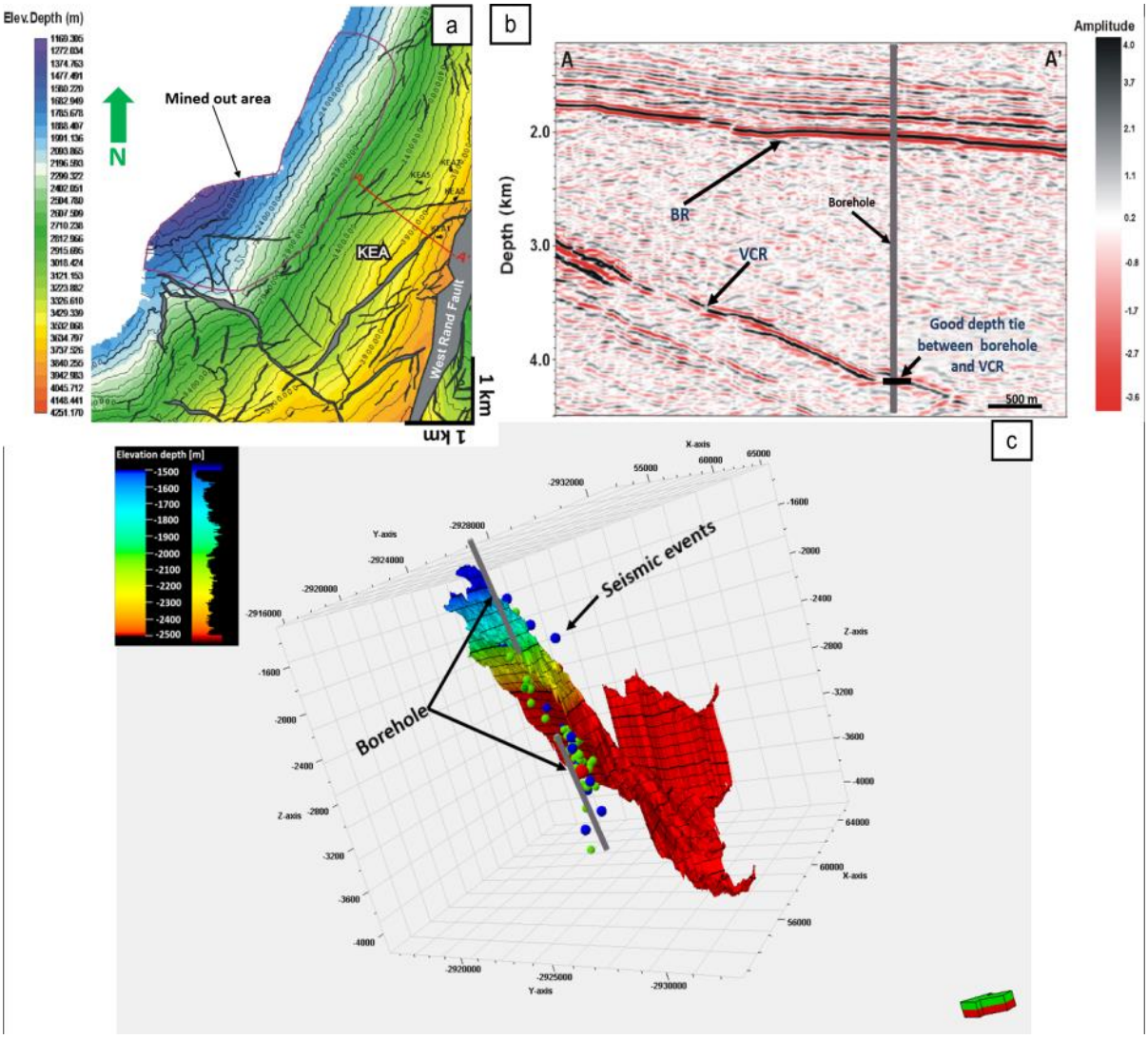

Figure 6.10: *(a) The VCR depth structure map view, with the colour bar showing depth from 1100 ms to 4200 ms with ±100 ms contour interval (b) Seismic section in amplitude display indicating good depth tie between VCR and a borehole and indicating faults (c) Cross sectional view of the VCR elevation map overlain by mining-induced seismicity data and a borehole (modified from Manzi et al., 2013).*

6.4.1 Seismic attributes analysis

From the conventional interpretation, several seismic attributes (dip-azimuth, edge detection, and ant-tracking) were applied to reveal further subtle details that may not have been clear on conventional interpretation techniques. The picked horizon was conditioned in noise reduction and signal-to-noise ratio enhancement. This yield better seismic attribute results.

6.4.1.1. Horizon-based attributes

The dip-azimuth attribute applied to the VCR picked horizon gives information about the general strike of the surface (Figure 6.11). The horizon has, in general, the strike varying between 90º and 175º, with a few areas outside this range that are possibly indicating another form of local geological features. The dip azimuth highlights slightly more details of the surface, adding more linear structures where continuity is visible due to their sharp contrasting azimuth compared to the broad horizon. The dip azimuth map displays some major scale lineaments throughout the surface that trend in the NW-SE and NE-SW directions, highlighting some dip direction lineaments.

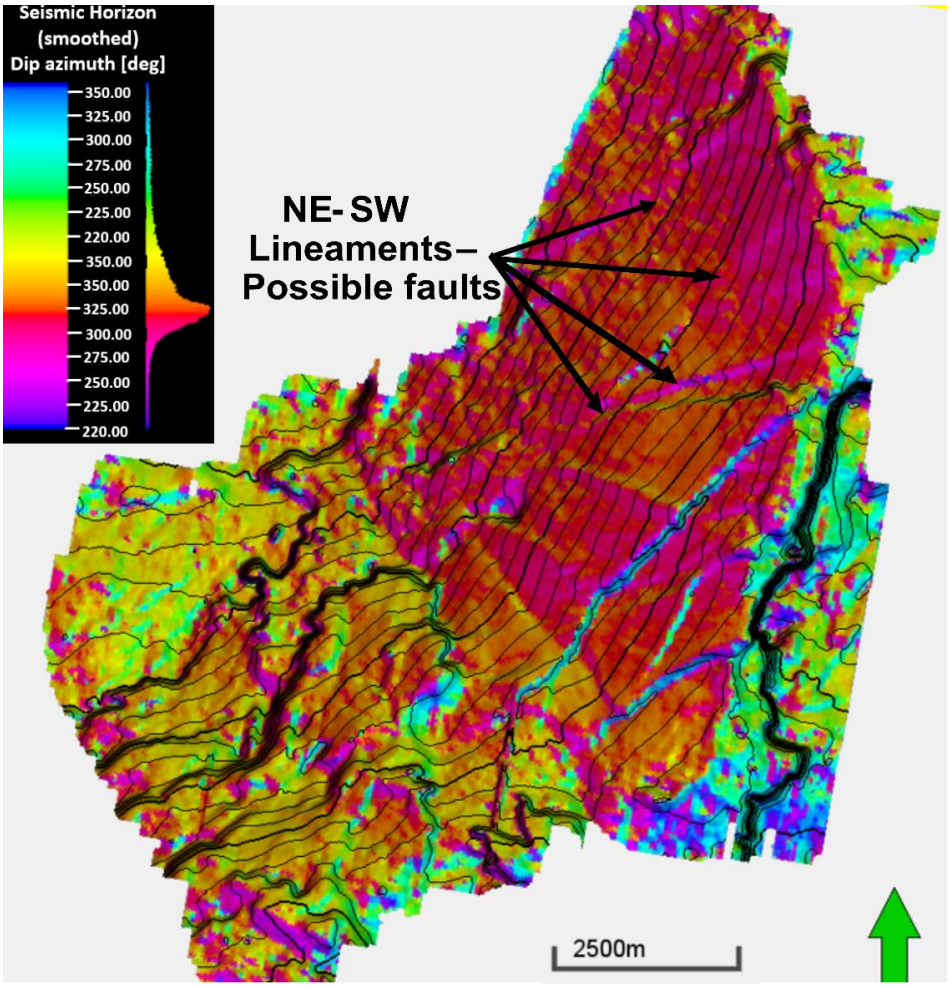

Figure 6.11: *The dip-azimuth map, with the colour bar, restricted to 350º, illuminating the general orientation of structures observed on the horizon.*

Superimposing mining-induced seismicity on the dip azimuth map indicates a positive correlation with identified structures in the study area's vicinity. More large seismic events are located at the intersection of these geological structures (Figure 6.12). The edge detection map (Figure 6.8b and Figure 6.13) illuminates and enhances the subtle features seen from the zoomed-out dip-azimuth maps. The map displays the

edge-like linear structures present in some data areas like those delineated by the dip-azimuth attribute maps (Figure 6.12) correlated with mining-induced seismicity, which plots on the NE-SW lineaments. The edge detection attribute adds more resolution to the areas than the azimuth attributes (compare Figures 6.11 and Figure 6.12).

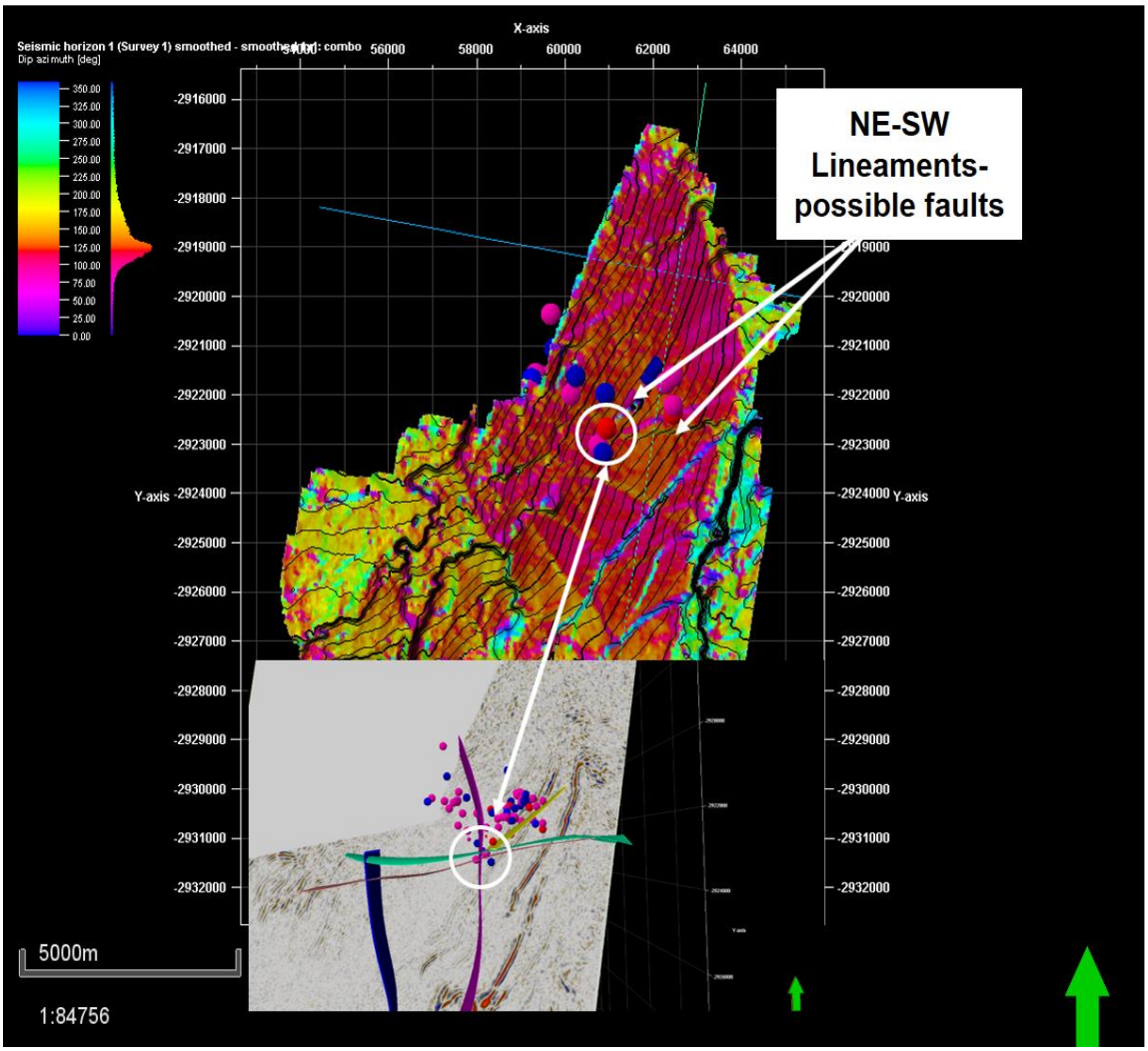

Figure 6.12: *The dip-azimuth map, with the colour bar, restricted to 350º, illuminating the general orientation of structures observed on the horizon and the 3D-seismic structure***.**

The surfaces were gridded, and edge-detection attributes were computed to detect further subtle faults that crosscut the VCR. Figure 6.13 shows the edge-detection attributes indicating a sequence of N-S and the W-E trending faults with small throws that the azimuth maps could not map (Figures 6.11 and Figure 6.12). As indicated on the maps of edge-detection attribute, the inter-connection nature of these faults suggests that they were active after the deposition of the VCR horizon.

Some areas are classified by the low signal-to-noise ratio (SNR) (Figure 6.13). Structural complexity results in deterioration of the horizon in the Northern part of the Kloof region. These might be due to the VCR structural complexity and low fold of coverage in these areas. In the northern part of the Kloof region, the dolomitic compartment that hindered the seismic data acquisition could have caused the low SNR in this region. The black colour (Figure 6.13) represents the area where data is not available, or the area was out of the seismic volume boundaries.

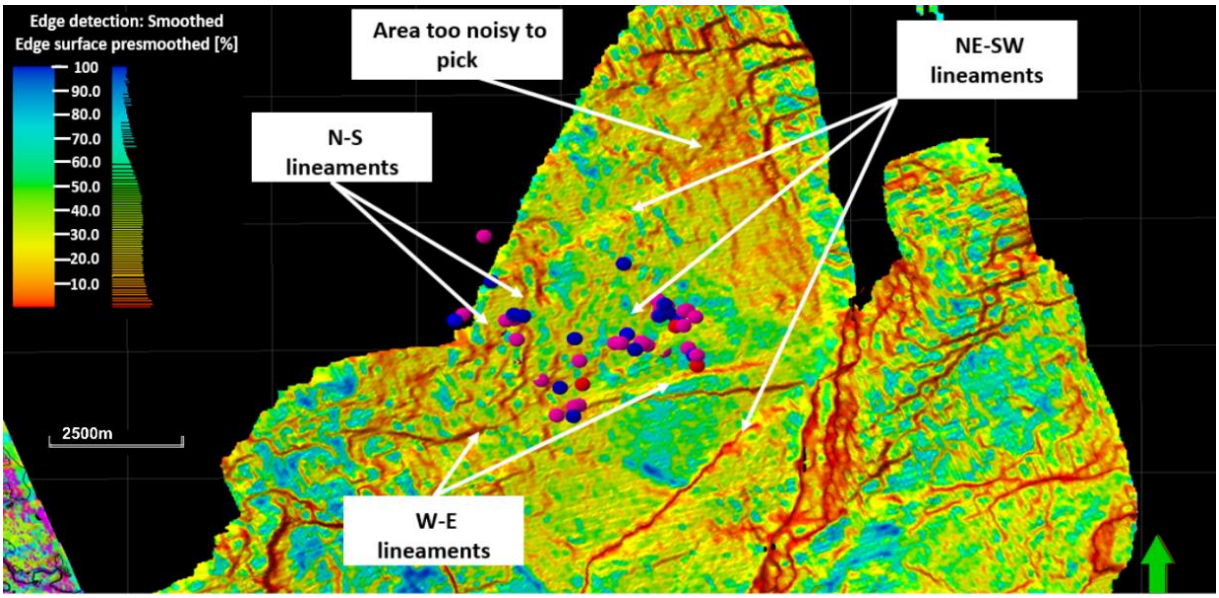

Figure 6.13: *Edge detection map enlightening an array of lineaments that were below the seismic limit and were seismically 'invisible' to conventional seismic interpretations.*

Edge-detection maps (Figure 6.14) overlain with mining-induced seismic events of different magnitude display a series of different direction faults unmapped by the azimuth maps due to significantly low throws (Figures 6.11 and Figure 6.12).

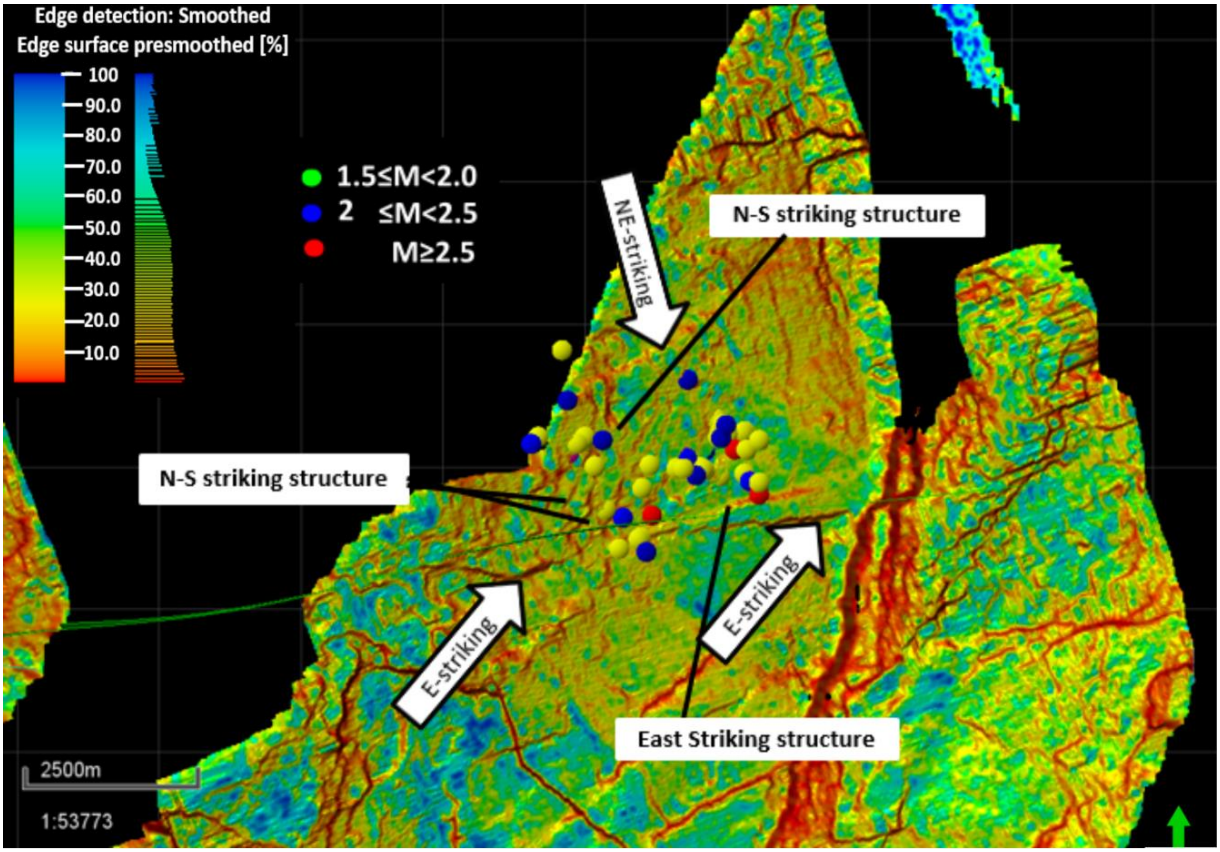

Figure 6.14: *VCR edge attribute map overlain with mining-induced seismicity data in Kloof Gold Mine. Structures show good correlation with seismicity data with different magnitude (blue, green and red).*

The surface stability map, shown in Figure 6.15, illuminates the pick confidence of the VCR horizon, which is essential information as it ties directly with the confidence of the results from other seismic attributes applied on the same surface (Figures 6.11, 6.12, and 6.13). A confidence index above 50% is displayed in the attribute map. It indicates relatively good picking in the vicinity of the area, and thus other different attribute information in the vicinity can be considered dependable. A confidence index below 50% will indicate areas with low SNR and possible linear features due to poor resolution resulting from the vertical displacement of the reflector. In Figure 6.15, areas assigned a low confidence index were also identified as possible geological features by the dip-azimuth and edge detection attributes (Figures 6.11 and 6.13).

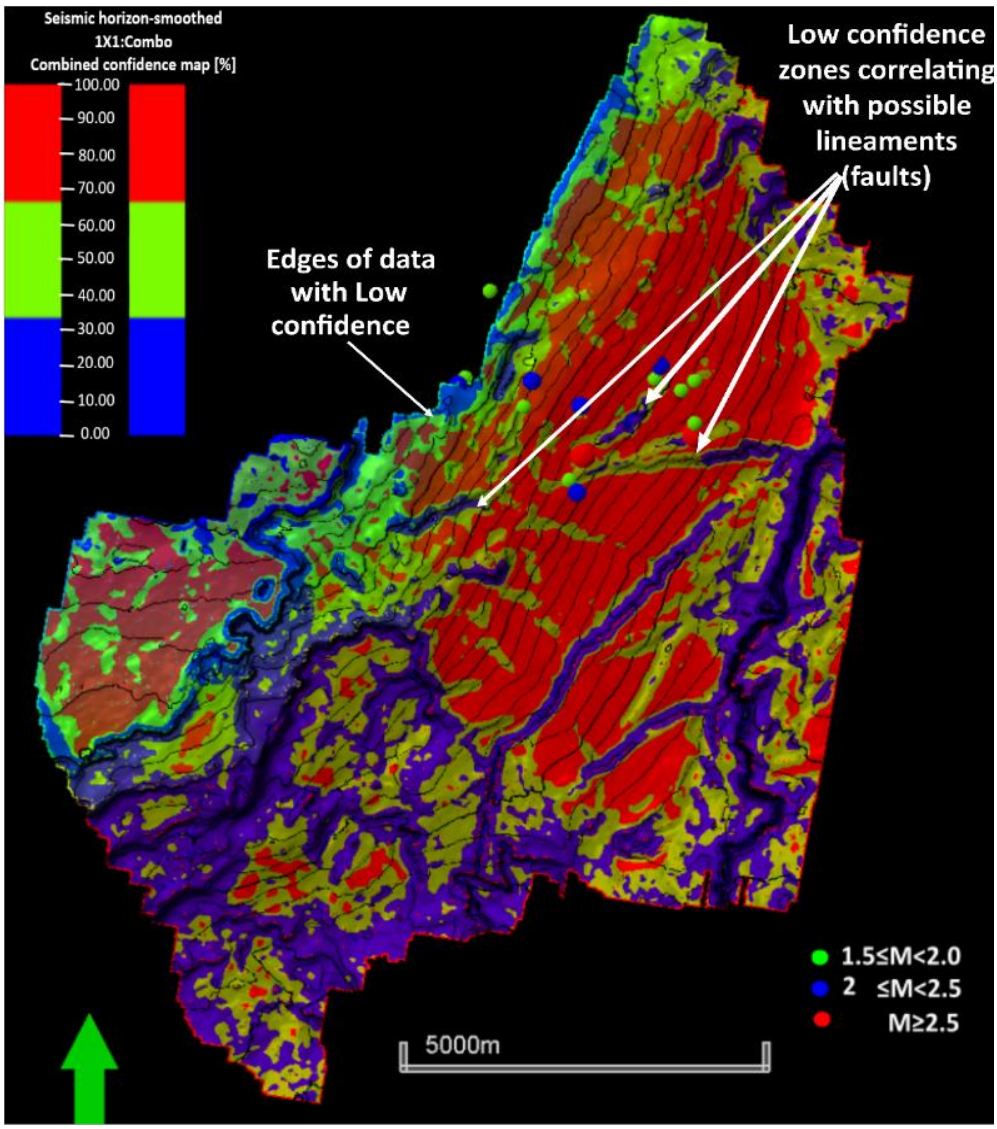

Figure 6.15: *Surface stability map with the confidence index of the picked surface. Areas in red and green have a higher confidence index than those in blue. Mining-induced seismic events are indicated with circles that are green, blue and red.*

6.4.1.2. Volumetric seismic attributes

The data was conditioned before applying the volumetric attributes to improve the signal-to-noise ratio and reduce noise for better attribute results—the structural smoothing and dominant frequency preserved features of interest. The ant-tracking attribute maps were produced from the different edge detection outcomes of the two processing workflows. The ant-tracking attribute application has been known to give a better definition and continuity of subtle lineaments.

Ant-tracking techniques successfully highlighted minor faults with approximately 20 m throw. The ant-tracking technique is in Figure 6.16. Figure 6.17, compared with the conventional amplitude display, shows

a better continuity of the horizons. The technique has proven to be an excellent tool compared to the edge enhancement and the amplitude techniques in mapping the continuity of horizons and faults. Figures 6.16 and Figure 6.17 compare the results obtained from running the ant-tracking algorithm in passive mode from the structural smoothed and graphic equalizer filtered data, respectively, specifically from the variance edge detection attribute. The outcome from the structurally-smoothed data (Figure 6.16) has highlighted more structural detail than seen on the conventional seismic interpretation. Some of the gently dipping structures visible can be attributed to the layering also seen on the amplitude data. Some vertical and steeply-dipping structures that were not apparent on the amplitude data are now visible and can be attributed to joints, fractures, or faults. The ant-tracking scale indicates no opening (-1.0) and opening (1.0). Bluish colour represents tunnels in the underground workings. Dark grey lines represent abnormalities; faults reflected and vague; the broken overlapping relationship is unclear.

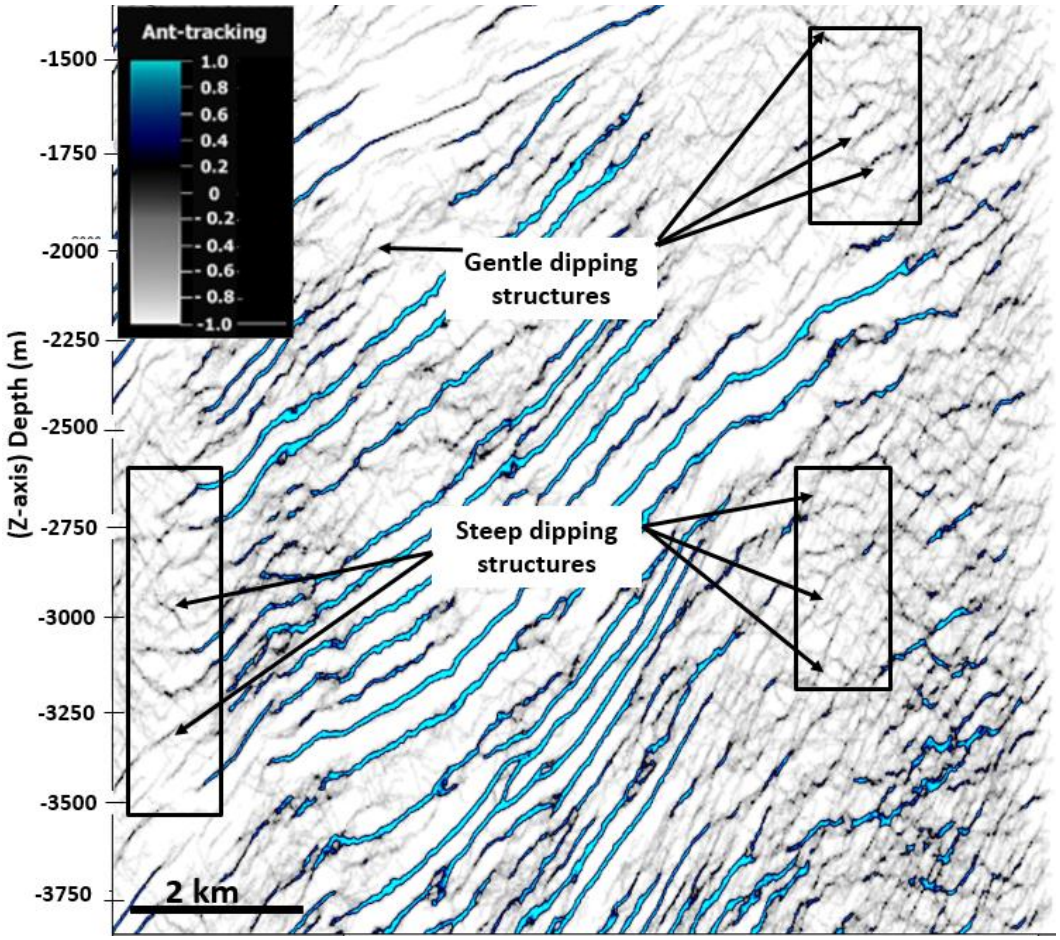

Figure 6.16: *Crossline view of the ant-tracking results, run in passive mode, from the structurally – smoothed data with variance attribute applied. The visibility and continuity of structures are considerably enhanced compared to the conventional amplitude display. Steep and gently dipping structures can be clearly seen, and their extent is better resolved. The vertical exaggeration (VE) of the section is 4:1.*

Areas of steep, gentle, and a combination of steep and gently dipping structures can now be seen, such as in Figure 6.16, but more enhanced. Figure 6.17 shows results from the ant-tracking algorithm run twice on the smoothed and graphic-equalizer-filtered variance data, respectively. The results are still in agreement with those in Figure 6.16, but slightly enhanced, which reaffirms the confidence in the results concerning noise and artefacts.

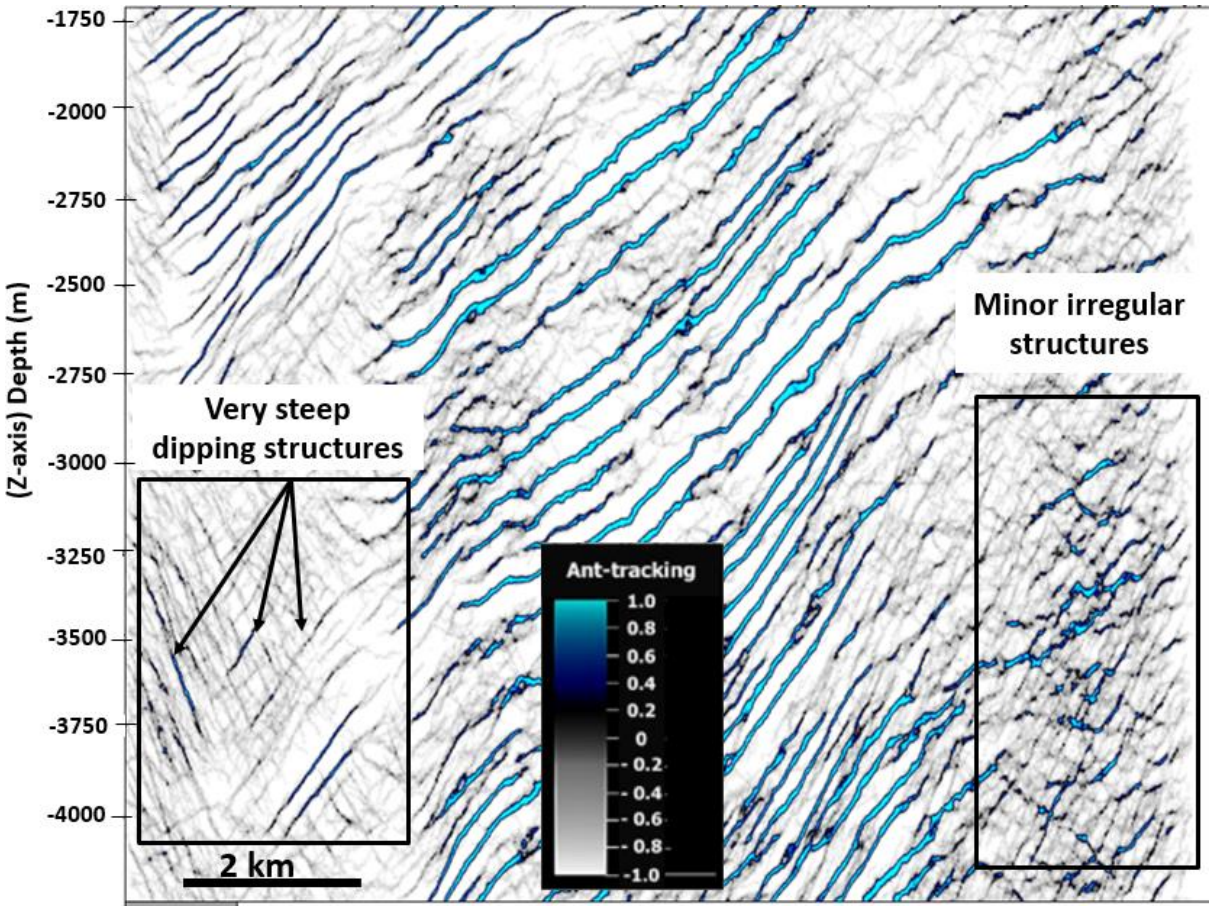

Figure 6.17: *Crossline view of the ant-tracking results, run twice in passive mode, from the structurally – smoothed data with variance attribute applied. The visibility and continuity of structures are considerably enhanced compared to the conventional amplitude display. Steep and gently dipping structures can be clearly seen, and their extents better resolved. Care should always be taken as such detail can also contain artefacts. The vertical exaggeration (VE) of the section is 4:1*

6.5 Discussion

The purpose of this research was to integrate and interpret the mining-induced seismicity data and 3D reflection seismic data collected within the Kloof Operations in the Witwatersrand Basin, where the current mining is operational. The integration was carried out in order to understand the economic VCR marker horizon's local geology better and thereby elucidate the rock mass mechanical behaviour. The integration of mining-induced seismicity, 3D reflection seismic, underground in-stope data mapping has enhanced

knowledge of the structural complexity of the Kloof Operation region. The correlation of all the data sets proved a good check of the 3D reflection seismic data lateral accuracy. The interpretation and the integration carried out in this study utilised the conventional seismic interpretation method and seismic attribute analysis incorporating mining-induced seismic data.

The 3D reflection seismic data is under-sampling a series of minor structures (e.g., small faults with a throw less than 5 m and mainly the dykes) that have been identified by the in-stope underground geological mapping. It indicates that the fault determined by the underground mapping correlates with the one mapped in the 3D reflection seismic data using different techniques. Some mining-induced seismic events plot close to the in-stope identified mapped structures. Some of the in-mine identified structures were not identified by the 3D reflection seismic data. Several seismic events of magnitude ($M_L \geq 1.5$) have occurred close to these structures and have confirmed they are seismically active.

Numerous faults not detected or visible on the VCR depth structural map and seismic sections were successfully imaged using horizon-based seismic attributes, including the edge detection and dip-azimuth on the data. The dip azimuth attribute provides a better delineation of faults. The edge detection attribute has several advantages over the dip-azimuth maps, including the ability to map mapping faults with vertical throws and variable orientations. It can show far more geological structures than the dip-azimuth by increasing structure definition in more orientations. It has proven to enhance details that are invisible within the conventional interpretation method.

CHAPTER 7 – MITIGATING THE RISK OF ROCKBURSTING BY INTEGRATED INTERPRETATION OF 3D REFLECTION SEISMICS AND SOURCE PARAMETERS OF MINING- INDUCED EARTHQUAKES: A CASE STUDY FROM KLOOF GOLD MINE, SOUTH AFRICA.

7.1 Authorship Statement

This chapter presents a summary of the paper which constitutes the main focus of the thesis study. A summary of this paper is provided, highlighting its main objectives, methods, results and conclusions. A description of the candidate's contribution and the contribution of each author is summarized below.

7.2 Manuscript 1

Masethe R.T., Durrheim R.J. and Manzi M.D. 2020. Mitigating the risk of rockbursting by integrated interpretation of 3D reflection seismics and source parameters of mining-induced earthquakes: a case study from Kloof Gold Mine, South Africa,

It is intended to submit this paper to *Geophysics* as it is a sequel to a paper that received the 2012 "Best paper in *Geophysics"* Award that was authored by the supervisors of this thesis.

Manzi, M.S., Durrheim, R.J., Hein, K.A. and King, N., 2012. 3D edge detection seismic attributes used to map potential conduits for water and methane in deep gold mines in the Witwatersrand Basin, South Africa. *Geophysics*, 77(5), pp. WC133-WC147.

The candidate was responsible for the following:

- Importing Kloof 3D reflection seismic data into PETREL software for manual picking of the seismic horizons.
- Mapping of all dykes and faults within the Kloof seismic volume. Prof Musa Manzi guided the structural interpretation.
- Applying the horizon-based attributes (e.g., edge detection, dip, and dip-azimuth) to the picked horizon to enhance sub-seismic faults and volumetric attributes (e.g., ant-tracking) to the seismic volume.
- The 3D structural model Kloof 3D reflection seismic data incorporating fault surfaces were created with the help of Prof. Musa Manzi.
- In-mine mapped geological structures were imported and compared to the structures imaged by the 3D reflection seismic data.
- 75 analyzed large mining seismic events data ($M_L \geq 1.5$) were selected from the seismic volume, reprocessed, converted into LO 27 coordinates system, and imported into PETREL software.
- Seismic events source parameters were determined, correlated, and interpreted.
- Moment tensor inversion and fault plane solution were calculated and overlaid to the Mine Plan.
- The candidate made all graphs and figures in the manuscript, and the comments from Prof. Ray Durrheim and Prof. Musa Manzi helped improve the quality.
- The writing of the manuscript was done by the candidate. Prof. Ray Durrheim and Prof. Musa Manzi improved the quality of the paper.

7.3 Summary of publication

The goal of the present study was to obtain a high-resolution 3D reflection seismic image of the deep (down to 4200 m depth) geological structures, VCR orebody, and its offsets of the Kloof operation, which is the part of Witwatersrand basin using PETREL software and integrated seismicity ($M_L \geq 1.5$). In this study, we have analyzed seventy-five large seismic events with local magnitude from 1.5 to 2.7 that caused damages to the surrounding stopes in the deep underground mine, possibly driven by geological structures. The analyzed data were collected during Jan 2017- Dec 2018, particularly in 57.6 km^2 covered by the 3D reflection seismic survey (Fig. 6 (a)). The following selection criteria were used, including:

- At least 20 sites (geophones) triggered around the seismic event.
- Seismic events with location falling within the central part of the in-mine seismic network and the 3D reflection seismic volume.

A final seismic event selection was made after sorting the seismic events by recording stations with verified sensor orientations (misfit angle $<20^0$) in descending order. The hypocentral locations (error ~ 90 m) and the origin times for selected seismic events are recorded in Table E3.

The energy radiated from the analyzed seismic events ranged between 2.29×10^6 and 3.45×10^8 J, source size between 59 and 237 m, log apparent volume varied between 5.93 and 7.75 m^3, the corner frequencies ranged from 13 Hz to 27 Hz and *Es/Ep* energy ratio from 1.1 to 19.9. The hanging wall seismic events accounted for 52% of the total seismic events, close to the VCR ore body. The analyzed seismic events were categorized into two groups based on their energy ratios as Fault slip (FS) and non-shear (NS). FS seismic events were classified as *Es/Ep* >10 and the NS as *Es/Ep* <10. From the 75 analyzed seismic events, 64 events were classified as Non-Shear, located between 1756 and 3919 m depths. The 11 shear/fault slip events were concentrated from1625 to 4174 m below and above the ore body.

The focal mechanism and moment tensor solutions were related to the mapped and interpreted seismically active geological structures within the 3D seismic reflection volume. Moment tensor inversion results of events ranging in size from $2.1 \leq M_L \geq 2.7$ were superimposed on the mine map (Fig.15) along with mapped geological structures in Region A, B, and C. For some seismic events, the nodal planes had some similarities, not only with one but a few different geological structures in the vicinity. In other seismic events, the nodal planes could not be related to any of the structures. Considering the location error for the seismic events themselves, the structures to which the largest number of seismic events can occur was in Region C as compared to Region A and B.

7.4 Energy Ratio (*Es/Ep*) comparison and the Moment Tensor Inversion

During this study within the 3D reflection, seismic volume seismic events of $M_L \geq 1.5$ were investigated. The analyzed seismic events were categorized into two groups based on their energy ratios as Fault slip (FS) and non-shear (NS). According to Gibowicz *et al*. (1991) and Gibowicz and Kijko (1994), when Es/Ep <10, the source mechanism will involve a tensile failure component, and it was suggested that when Es/Ep >10, the source mechanism corresponds to pure shear (Boatwright and Fletcher, 1984). Hudyma and Potvin (2010) suggest that seismic events with $Es/Ep < 3$ involve a tensile failure component. Others regard seismic events with $Es/Ep < 20$ as involving a pure shear. The distribution of the energy ratios (Es/Ep) that are based on different mine failure case studies have been documented by numerous authors, including Cai *et al*., (1998); Sweby *et al*., (2006), Kwiatek and Ben-Zion (2013), Rebuli and Kohler (2014), Morkel *et al*., (2019) and Liu *et al*., (2020). The confidence of using the parameter Es/Ep ratio for seismic events characterization needs further investigation since it is inconsistent. There is a sensor effect (location and number of the tri-axial geophones), path effect (attenuation), and source effect (seismic energy radiation pattern) that, when events is poorly monitored, can influence the calculation of both the P- and S-wave energy. Each of the three factors adds an element of uncertainty and the potential error to the Es/Ep ratio calculations.

The Es/Ep ratio is compared to the Moment Tensor Inversion results, in particular the isotropic (ISO) and double couple (DC) components. The Es/Ep < 10 can be related to the ISO component and the Es/Ep > 10 to the DC component. Only 38% of the events classified as shear according to the Es/Ep ratio, have a high DC component, while only 3% of the calculated non-shear seismic events (Es/Ep < 10) had a dominant ISO component.

7.5 Manuscript 1

MITIGATING THE RISK OF ROCKBURSTING BY INTEGRATED INTERPRETATION OF 3D REFLECTION SEISMICS AND SOURCE PARAMETERS OF MINING-INDUCED EARTHQUAKES: A CASE STUDY FROM KLOOF GOLD MINE, SOUTH AFRICA

Richard T. Masethe[1,2]*, Raymond J. Durrheim[1] and Musa D. Manzi[1]

[1]School of Geosciences, University of the Witwatersrand, PBag 3, 1 Empire Street, WITS 2050, Gauteng, Johannesburg, South Africa
[2]Seismology Department, Sibanye-Stillwater Limited, Libanon Business Park 1 Hospital Street, Libanon 1780, Westonaria, South Africa

Abstract

Rockbursts pose a significant risk in deep gold mines in the Witwatersrand Basin of South Africa as they may damage the excavation, injure workers and delay production. We analyzed the source mechanisms of 75 large mining-related seismic events (M_L1.5 - 2.7) that caused damage to stopes in Kloof Gold Mine, and reprocessed and interpreted a 3D reflection seismic cube that images the orebody and larger geological structures. We augmented the geological model derived from the 3D seismics with smaller structures (below the seismic resolution limit) that were mapped in tunnels and stopes.

The 75 seismic events took place at depths of 1600–4200 m below surface. Most events located close to stopes mining the Ventersdorp Contact Reef (VCR) ore body. The energy radiated from the analyzed seismic events ranged between 2.29×10^6 and 3.45×10^8 J, corner frequencies from 13 to 27 Hz, source size from 60 to 240 m, log apparent volume from 5.93 and 7.75 m^3, and the S- to P-wave energy ratio (Es/Ep) from 1.1 to 19.9. The source mechanisms of mining-induced seismic events aid in understanding the dominant modes of failure. Planes of weakness may be the result of mining-induced stresses or pre-existing geological structures. The Es/Ep ratio, focal mechanism and moment tensor solutions were related to the mapped geological structures. About 44% of the events were located near known geological structures (faults, dykes), while 56% of the events were related to elements of the mining geometry (dip pillars, abutments and remnants). The focal planes and the mapped strike of structures were generally poorly aligned. Conventionally, the energy ratio is used to define two classes of events, *viz.* Fault Slip (Es/Ep >10, 11 events) and Non-Shear (Es/Ep <10, 64 events). We investigated whether this distinction is valid. The classification of events in crush- and shear-type based on the Es/Ep ratio and the moment tensor components was poorly correlated, and we conclude that the Es/Ep

is not a very reliable classifier. Nonetheless, some seismogenic structures were identified, enabling mining layouts to be modified to minimize the risk of rockbursting.

INTRODUCTION

The deep level gold mines of South Africa are characterized by high stress levels that deform the rock mass and cause intensive mining-induced fracturing. The strain energy may be released in seismic events, which are termed 'rockbursts' if the shaking is strong enough to cause damage to excavations. Because of the large extent of mining and the great mining depth, large seismic events pose a constant risk during mining. Over the past decades, many studies have been conducted to gain understanding and develop technologies to mitigate the risk posed by rockbursts, for example, by mapping geological structures and measuring mining-induced stresses and seismicity, and by designing appropriate layouts, stoping sequences and support systems (Vieira et al., 2001; Ogasawara et al., 2009; Durrheim, 2010; Riemer and Durrheim, 2012; Feng et al., 2017; Simser, 2019).

The seismic reflection method and earthquake seismology are often used independently to gain a better understanding of the Earth's subsurface structure and dynamics. The two methods share the same fundamental physical principles (e.g., seismic wave propagation), but have very different methodologies. We present a study that seeks to mitigate the risk of rockbursting at Kloof Gold Mine, South Africa (Fig. 1) by gaining a better understanding of the factors that control seismicity. Source parameters of mining-induced seismic events were integrated with the geological interpretation of a reprocessed high-resolution 3D reflection seismic cube (originally acquired to explore the extensions of the ore body) and underground mapping of minor faults and dykes that are below the seismic resolution limit, but are still capable of hosting large seismic events.

An understanding the geological complexity of the area and the relationship between mining-induced seismicity and geological structures is critical for the quantitative modeling of the orebody and mine safety. Geological structures are mapped directly on the surface, in underground workings, or in boreholes. Surface mapping is of limited value at Kloof Mine as the ore body is concealed by younger strata. However, reflection seismics data has proven to be very useful because it allows confident interpolation between direct observations in boreholes and mine workings. We applied various advanced seismic horizon-mapping attributes (e.g., edge detection)

to the 3D seismic data, and correlated the interpretation with the mine seismic events to identify the geological structures that are most seismogenic.

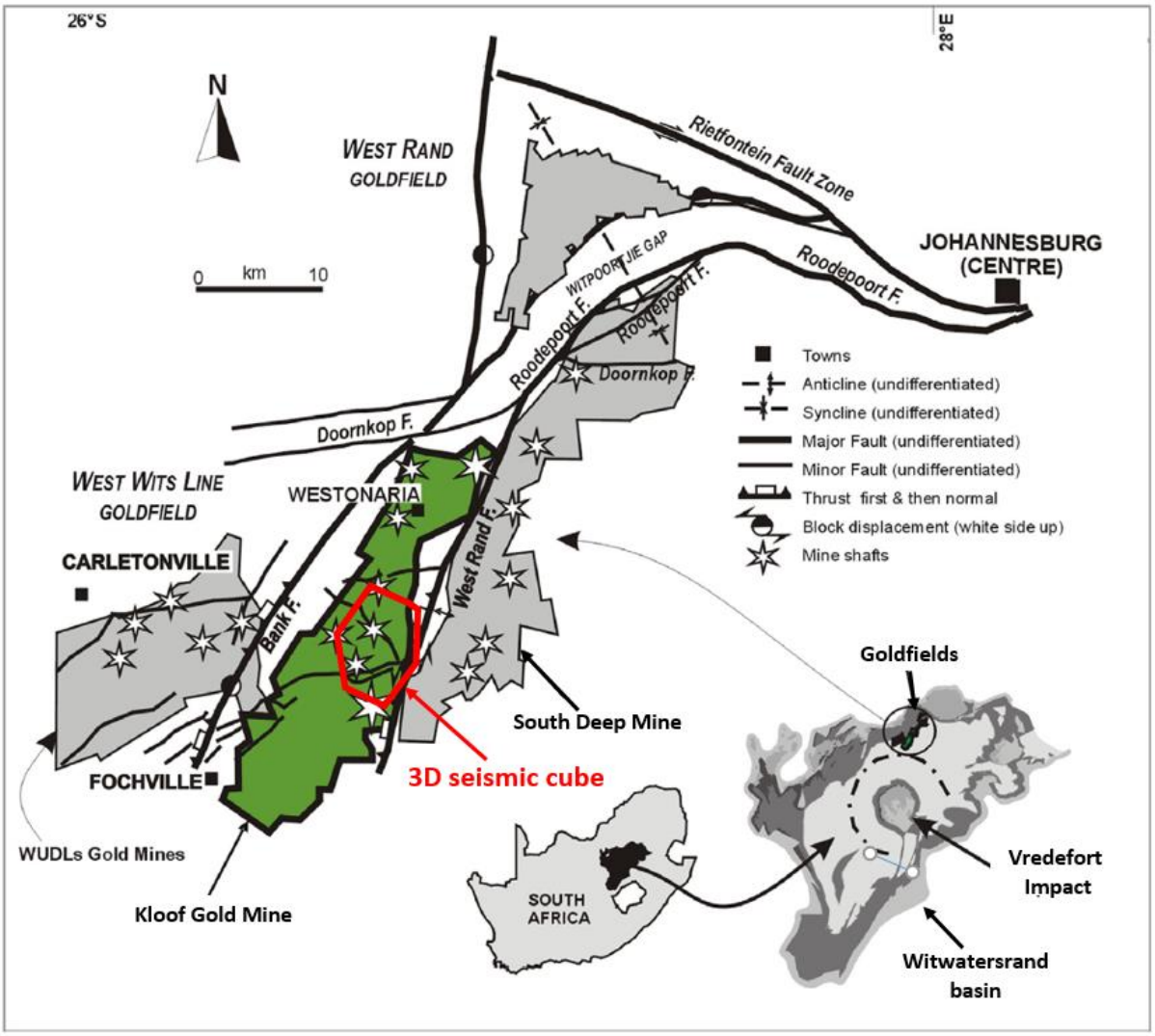

Fig. 1 *Location of Kloof Gold Mine (Modified after Dankert and Hein, 2010). The Red polygon represent the 3D seismic cube location.*

GEOLOGICAL SETTING AND MINING METHOD

The geology of the Witwatersrand Basin has been documented by many authors, including Beach and Smith (2007), Fletcher (2009), Viljoen (2009) and Dankert and Hein (2010). A succession of basins formed when the Zimbabwean Craton collided with the Archaean Kaapvaal Craton between 3.07 and 2.71 Ga (Armstrong *et al*., 1991; Robb and Meyer, 1995). The volcano-sedimentary strata of the Dominion Group were the first to be deposited on the granite-greenstone

basement terrane. The Witwatersrand Supergroup, which overlies the Dominion Group, is divided into the (lower) West Rand Group, mostly quartzite and ferruginous shale, and the (upper) Central Rand Group, mostly quartzite with gold-bearing conglomerate beds (McCarthy, 2006; Dankert and Hein, 2010). The Ventersdorp Supergroup, largely composed of basalt, lies unconformably above the Witwatersrand Supergroup. The Venterspost Formation, which lies at the base of the Ventersdorp Supergoup, is composed of the erosional products of the Witwatersrand Supergroup, and includes an extensive gold-bearing quartz pebble conglomerate bed known as the Ventersdorp Contact Reef (VCR). The Ventersdorp Supergroup is, in turn, unconformably overlain by the Black Reef Formation (BR), which lies at the base of the Transvaal Supergroup. The geology in the vicinity of Kloof Gold Mine and an ideal seismic image is shown in Fig. 2.

The Witwatersrand Basin is structurally complex. Geological structures, such as faults and dykes, are known to be the sources of some largest seismic events experienced in deep South African gold mines, as both static and dynamic stresses can be transferred along and through them. Thus, a knowledge of their location and properties (e.g. strength, cohesion) is critically important when designing the mining layout and extracting the ore.

Kloof Gold Mine, in the West Wits Line (Carletonville) goldfield, is located between two major faults: the West Rand Fault in the east and the Bank Fault in the west (Fig. 1). The mine complex comprises five producing shaft systems and two metallurgical plants. The Kloof lease area is characterized by steep- (~65°) and moderately- (~30°) dipping dykes and faults that influence the rock mass behavior and complicate mining, as the displacements may produce zones of ore loss or duplication and may be seismogenic (Dankert and Hein, 2010; Ogasawara *et al*., 2009; Durrheim *et al.,* 2012). Major geological structures derived from drilling and underground mapping are shown in Fig. 3. These include several large faults and two sets of dykes, *viz.* a north-south striking set of greenish-grey epidotised diabase dykes, and an east-west striking set of highly-altered diabase dykes that contain abundant calcite veins. The larger dykes have local names, e.g., Baby, Running, Black, Henry's.

The primary economic gold-bearing horizon (locally termed a 'reef') is the Archean Ventersdorp Contact Reef (VCR), which is cut by numerous faults and dykes. It constitutes about 97% of the Kloof's ore reserves and is one of South Africa's most important gold-bearing ore bodies. The secondary reefs include the Kloof Reef (KR), Libanon Reef (LR) and the Middelvlei Reef (MR). Mining at Kloof takes place at depths of 1500 m to 3500 m below the surface with an average

channel width of 1.34 m and mining height of 1.8 m. The strata generally dip towards the south-east at ~30°. According to Manzi *et al*. (2013), the faults within the geologically-complex Witwatersrand Basin include: (a) multi-fault segments that bound discrete VCR blocks; (b) multiple bifurcations from a single plane that form branched fault arrays, and (c) faults that cut and displace older faults or fault systems.

The reef is excavated by drilling a series of short (0.90 m) blast holes spaced 0.60 m apart into the face of a panel that is 15-30 m long and 1.2-1.9 m high. Each hole is charged with 0.60 kg of explosive, which is detonated by a centralized electronically-controlled system at a designated time once all workers have returned to surface. Each shot causes a seismic event with $M_L \approx -1.5$. These 'blast events' are easily identified on the basis of their origin time, magnitude and character. Most mining-induced seismic events occur immediately ahead of the stope and are related to the formation of new fractures in intact rock as a result of the redistribution of stress following the production blast. This process can take several hours. Other events, due to slip on pre-existing weaknesses in the rock mass, can occur tens or even hundreds of meters from the blast, and are not as strongly correlated to blasting in time and space.

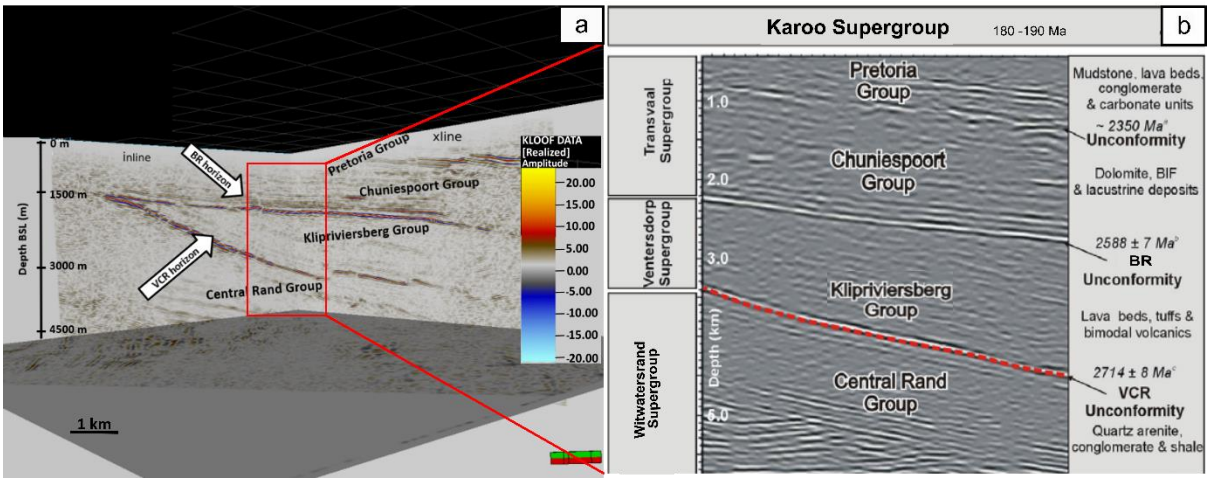

Fig. 2 *(a) Seismic cube showing the geological structure at Kloof Mine. The Ventersdorp Contact Reef (VCR) and Black Reef Formation (BR) give rise to prominent reflections. (b) Generalized stratigraphic column of the Witwatersrand Basin, after Krapež (1985), Myers et al. (1989), Armstrong et al. (1991), Kositcin and Krapež (2004) and Dankert and Hein (2010).*

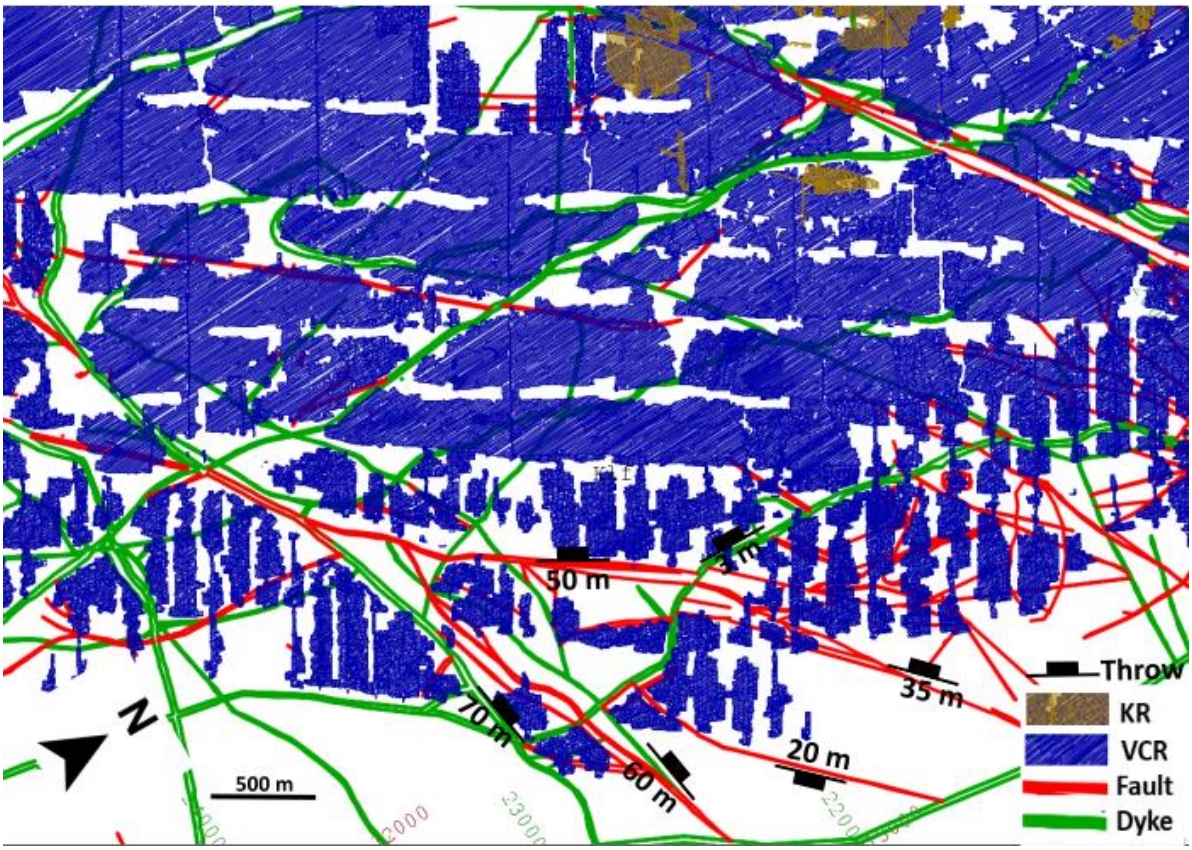

Fig. 3 *Kloof Reef (KR) and Ventersdorp Contact Reef (VCR) stopes and dykes and faults within the 3D reflection seismic cube acquired to map the eastern down-dip extension of Kloof Gold Mine ore body.*

3D REFLECTION SEISMICS

3D reflection seismic surveys were first shot in the early 1970s to explore for hydrocarbons, and, since the 1980s, for minerals (Davies *et al*., 2004; Milkereit *et al*., 1996; Salisbury *et al*., 2003; Salisbury and Snyder, 2007; Malehmir *et al*., 2012, 2013). 3D seismics generally maps the depth, dip and strike of horizons and structures more accurately than other geophysical methods (e.g., 2D reflection seismic, gravity, magnetics). The method has been widely used to image the structurally-complex gold-bearing Witwatersrand Basin and platinum-bearing Bushveld Complex, providing high-resolution images of the ore body prior to the sinking of shafts and the development of tunnels (Pretorius *et al*., 1994; Pretorius *et al*., 2000; Gibson *et al*., 2000; Trickett *et al*., 2005).

A high-resolution 3D seismic reflection survey covering the Kloof, and South Deep mines was conducted in 2003 by Compagnie Générale de Géophysique (CGG). The objective was to target the down-dip portion of the Kloof Gold Mine and provide optimum imaging of the deeper parts

(3.5 km – 4.5 km) of the VCR ore body. Fig. 1 shows the location of Kloof Mine to the west of the West Rand Fault. The survey overlapped a 3D reflection seismic survey undertaken at Kloof Seven Shaft area (K7) in 1994. The 1994 dataset was re-processed and merged with the Kloof - South Deep 2003 data to produce a single pre-stack time migrated seismic volume (Manzi *et al*., 2012a). The details of the acquisition and processing of these datasets are reported in Manzi *et al.* (2014). The dominant frequency of the reflection from the VCR is about 65 Hz. A stacking velocity of 6000 m/s – 6500 m/s was observed during processing (Manzi *et al.,* 2012a), suggesting a dominant seismic wavelength on the order of 100 m, yielding a similar horizontal resolution (for migrated data) and a vertical resolution of approximately 25 m (using the λ/4 rule-of-thumb). However, smaller structures can still be detected using seismic attribute analysis (Manzi *et al.,* 2012a), although their detection depends on the combination of diffractions and geometric attributes (e.g., strike, dip, and azimuth), not solely on the seismic amplitude (Malehmir *et al*., 2018).

The VCR and BR marker horizon were mapped using 3D automatic and manual horizon picking techniques (Fig. 4). The appropriate velocity was chosen to match the borehole VCR contact with the highly characteristic VCR signature. Then the automatic picking algorithm was used to map the horizon throughout the area covered by the survey. The auto-picking algorithm yielded low quality results in structurally complex areas and areas with a low signal-to-noise ratio, such as the edges of the survey area where the fold of the stack was low. Manual picking was then carried out, initially on a 10 m x 10 m inline by crossline spacing, and then on every inline and crossline (Fig. 4a). The three reef horizons, geophone stations and seismic events are shown in Fig. 4(b-d). The seismicity mostly occurs close to the reef as it is driven by the mining geometry (especially the stope face, pillars and the abutments), although some events associated with geological structures occur in the hanging- and footwall.

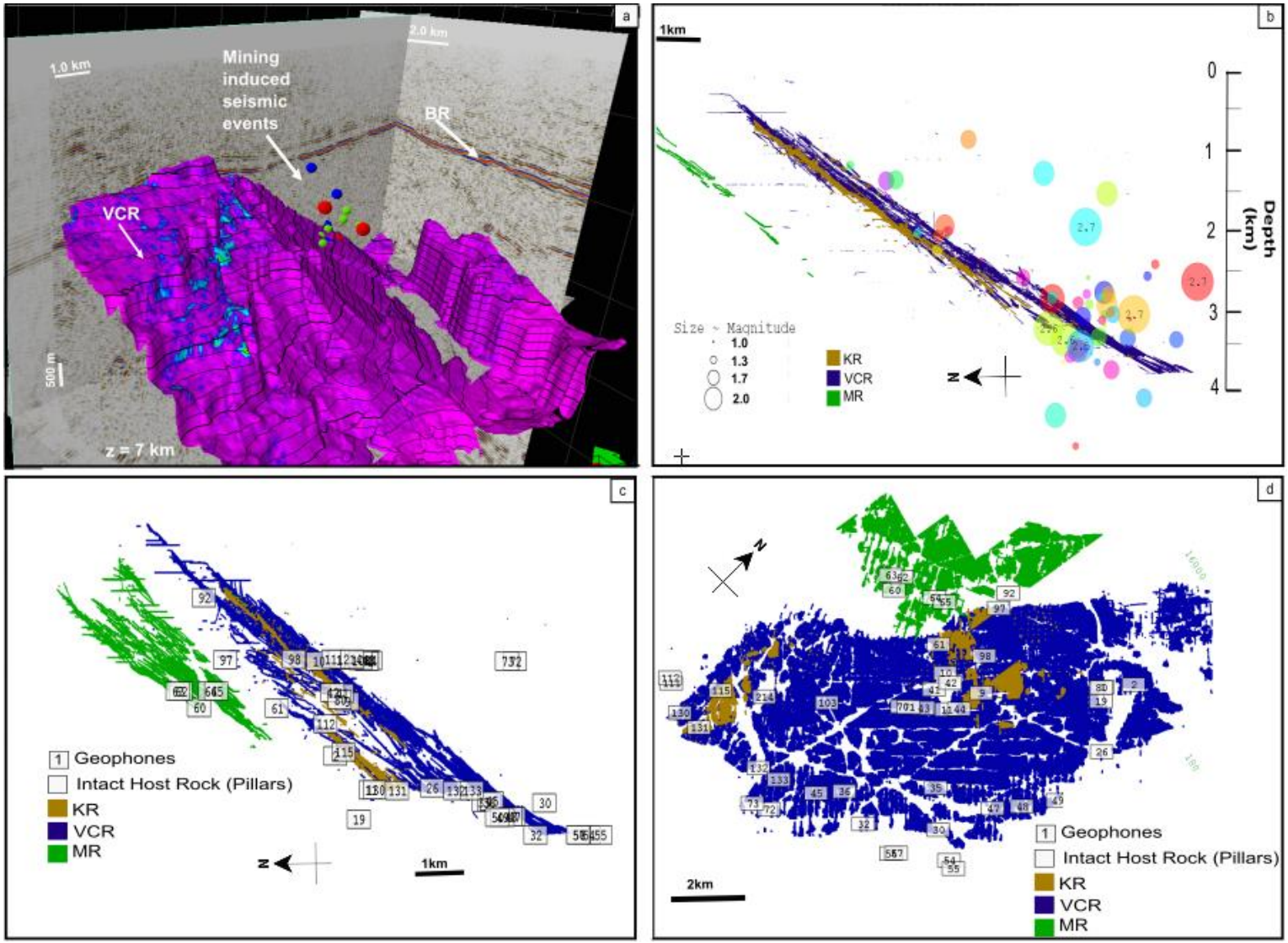

Fig. 4 *(a) 3D visualization of the migrated reflection seismic volume covering Kloof Gold Mine, (b) Depth-section showing seismicity, (c) Depth section showing reefs and seismic system, and (d) Plan view indicating geophone locations and different reef horizons.*

MINING-INDUCED SEISMICITY

Data acquisition and processing

Mining-induced changes in the stress level influence the stability of the rock mass as new ruptures may be created and the cohesion and friction on existing geological structures be exceeded. Stored elastic energy is released, which may cause strong shaking and the ejection of rock that endangers mine workers and damages infrastructure, delays production and may be costly to repair. The region within the 3D reflection seismic volume contains remnants, abutments, and geological structures (faults and dykes) that can contribute to a high level of seismicity. The primary aim of this study was to distinguish seismic events that are related to mining-related stress concentrations, such as abutments and remnants, from those that are related to geological structures so that appropriate mining strategies can be implemented.

The seismic event data for this study was captured by the mine-wide seismic system operating at Kloof Gold Mine. This system comprises 45 4.5 Hz tri-axial geophones sampling at 6 kHz installed at locations that surround the VCR, MR and KR reef planes (Fig. 4d). The seismograms are used to pick P- and S-wave arrival times and calculate the relevant source parameters, *viz.* origin time, location, energy, moment, magnitude, stress drop, etc. A set of 103,753 mining-related seismic events ($-3 \leq M_L \leq 3$) was initially selected for this study (Fig. 5(a-d)) from January 2017 to December 2018. The depth of these seismic events ranges from 1700 – 4000m (Fig. 5a). The Energy - Moment relationship is determined using the Quantile-Quantile method that ranks events by increasing energy, and separately ranks them by increasing moment, and then plots them against one another by rank (Fig. 5b). Then linear regression is used to find the best fit line. This method is much better than using least squares (LS) on the data directly, since least squares tend to underestimate the slope and overestimate the intercept. The corner frequency could not be well defined because of the correction for the attenuation. Hence, the corner frequency appears to be close to 10 Hz (Fig. 5c).

The main criteria used to select a subset of events for detailed analysis were the number of stations that recorded the event and the azimuthal distribution of the sensors. The study focused on 75 large ($1.5 \leq M_L \leq 2.7$) seismic events recorded at 20 or more sites and located within the central part of the in-mine seismic network and the 3D reflection seismic volume. A final selection was made after sorting the seismic events by the number of recording stations with verified sensor orientations (misfit angle $<20^{\circ}$) in descending order. The locations were determined manually by the IMS Trace software using the body wave arrival times (Mendecki, 1993, 1997). The source

parameters for 75 selected events were calculated by IMS Trace software using the spectral method developed by Andrews (1986), and later adapted by Richardson and Jordan (2002). The source parameters of the selected seismic events are listed
inTable1A.

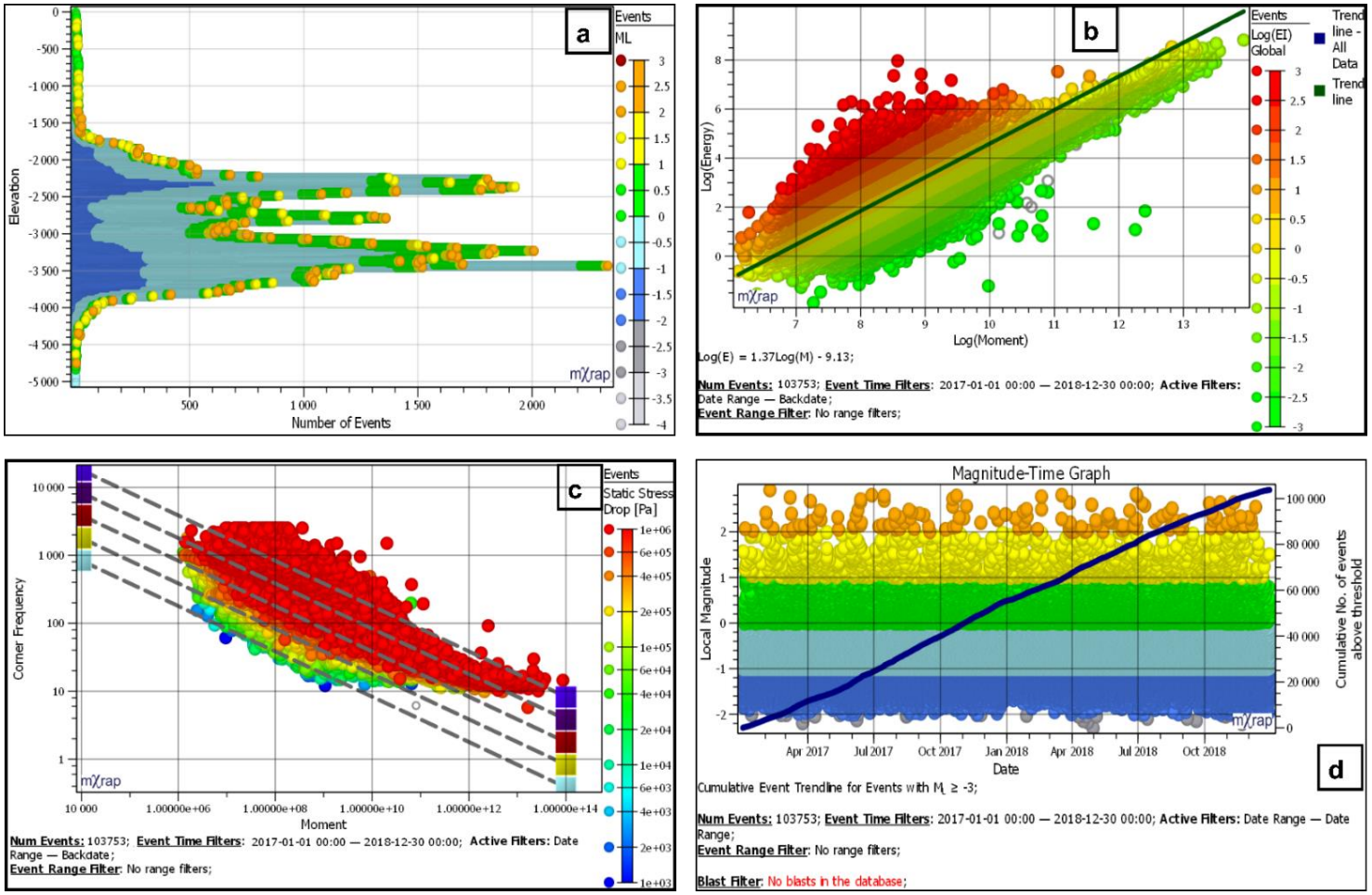

Fig. 5 *Seismicity at Kloof Gold Mine, 103,753 events recorded between 1 January 2017 and 30 December 2018 from mXrap* (Harris and Wesseloo, 2015) *(a) Depth of the recorded seismic events, colour representing local magnitude, (b) Energy-Moment relationship and Energy Index (EI), colour representing EI, (c) Static stress drop for different corner frequencies, colour representing static stress drop, and (d) Magnitude-Time distribution and graph showing the cumulative number of events, colour representing local magnitude*.

The locations of the selected large events that occurred within the 3D reflection seismic volume are shown in Fig. 6. We observed a predominance of selected events in the hanging wall of the VCR (Fig. 6b). Like most SA gold mine seismic systems, the Kloof seismic system has a planar configuration since the tunnels that are accessible for sensor installation lie on a plane parallel to the orebody being mined. This causes the uncertainty in the hypocentre location to be larger in the direction normal to the planar configuration. In terms of elastic theory, at a depth of ~2600 m below surface, the stress concentrations (and thus the seismic events) should be symmetrically distributed around the mining stope abutments if the properties of the rock in the hanging- and footwall are identical. However, there is a significant difference in the properties of the basalt rocks above the VCR, and the quartzite rocks below, causing an asymmetry of the stress field (Roberts and Schweitzer, 1999). Thus, the predominance of events in the hanging wall could be the result of pre-selection of events ($M_L \geq 1.5$), differences in the stress field and the strength of the rock mass, although location errors caused by the planar geometry of the seismic network cannot be excluded.

The three largest seismic events (all with $M_L 2.7$) were located close to known geological structures: in one case 58 m from the intersection of dykes, in the second case 32 m from a different dyke, and lastly 63 m away from the fault. It should be noted that the accuracy of hypocentre location was 20-60 m in the vicinity of these seismic events, while there was also some uncertainty in the exact position of the structures as the contacts mapped in boreholes and mine workings are interpolated in 3D space.

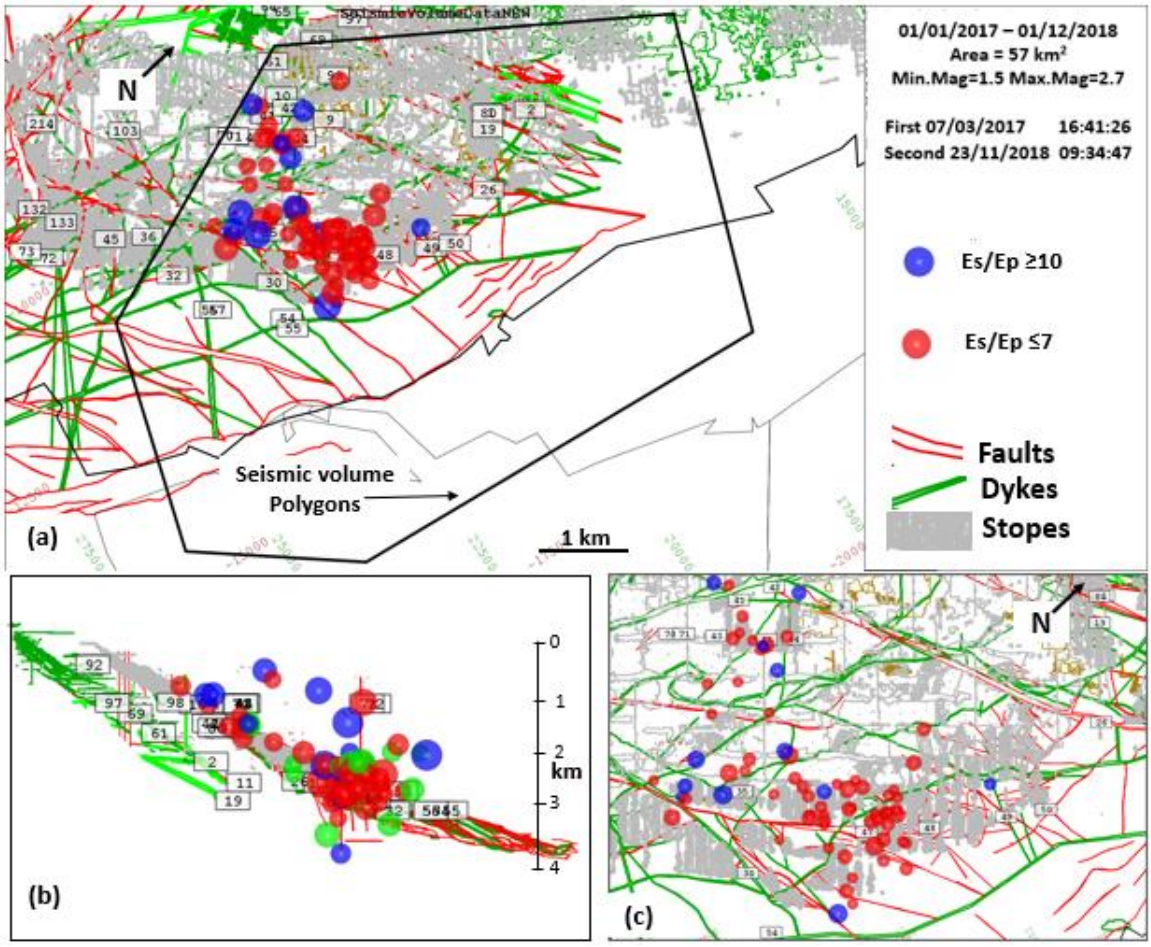

Fig. 6 *Analysis of 75 events with 1.5 ≤ M_L≤ 2.7 at Kloof Gold Mine (a) Plan view showing the location of geophone stations (rectangles) and seismic events (colored circles). Black polygon indicates the location for the analyzed 3D reflection seismic volume, (b) Cross-section view, and (c) Zoomed-in view showing the source mechanisms of the seismic events, mining layout and the geology in the closer range.*

Source parameters

The source mechanism describes how failure occurs within the rock mass at the hypocenter of a seismic event. It was based on the moment tensor inversion process that uses the polarities and amplitudes of seismic waves recorded at many sites distributed around the focus to determine the seismic radiation patterns and hence the direction of the slip vector. Sites with misfit angles between the P-wave polarization direction and the source location exceeding 20° were not used for the calculation of the moment tensor (IMS, 2015).

The calculation and interpretation of moment tensors has been described in numerous papers (e.g. Aki and Richards, 2002; Ben-Menahem Singh, 1981; Jost and Herrmann, 1989; McGarr, 1992a,b; Andersen, 2001). Backus and Mulcahy (1976) state that the moment tensor represents

the part of the internal stress drop dissipated in an inelastic deformation at the point source; while Gibowicz (1993) described it as a general framework to calculate the equivalent forces acting on a point that would best approximate a given seismic event, and considered it to be very useful to elucidate the source mechanism of mining-induced events.

In this study, moment tensor inversions were performed for events that were selected to provide a catalog of “typical” large mining-induced events covering a wide range of magnitudes, depths, and locations. The moment tensor inversion procedure employed here assumes the propagating medium is a homogeneous isotropic whole space with a constant wave speed. This is a practical assumption since the waves from the selected seismic events are anticipated to spread through the quartzite rock mass (density of the medium ρ = 2750 kg/m^3) with uniform wave velocities for the body wave phases (V_p = 5.9 km/s and V_s = 3.6 km/s).

RESULTS

Reflection seismic

Large seismic events may nucleate on geological structures such as faults and dykes, which are common on Kloof Gold Mine (Fig.7a), especially near their intersections, as the structures can transfer stress statically and dynamically. The edge detection seismic attribute (Fig.7b) was used to map the geological structures within the 3D seismic reflection volume. High values of the edge detection parameter indicate the presence of a discontinuity in the mapped horizon, most likely due to a fault or dyke. The edge detection map, which mapped structures with throws greater than 20 m, was correlated with the in-mine geological mapping. Just less than half the events (33/75 or 44%) of the $M_L \geq 1.5$ events occurred within 100 m of geological structures mapped either by in mine geological mapping or by the edge detection attribute. The majority of events (42/75 or 56%) were spatially related to the mining configuration: pillars accounted for 28% (21/75), abutments for 13% (10/75, or 13%), while the remainder (11/75 or 15%) occurred in back areas and remnants.

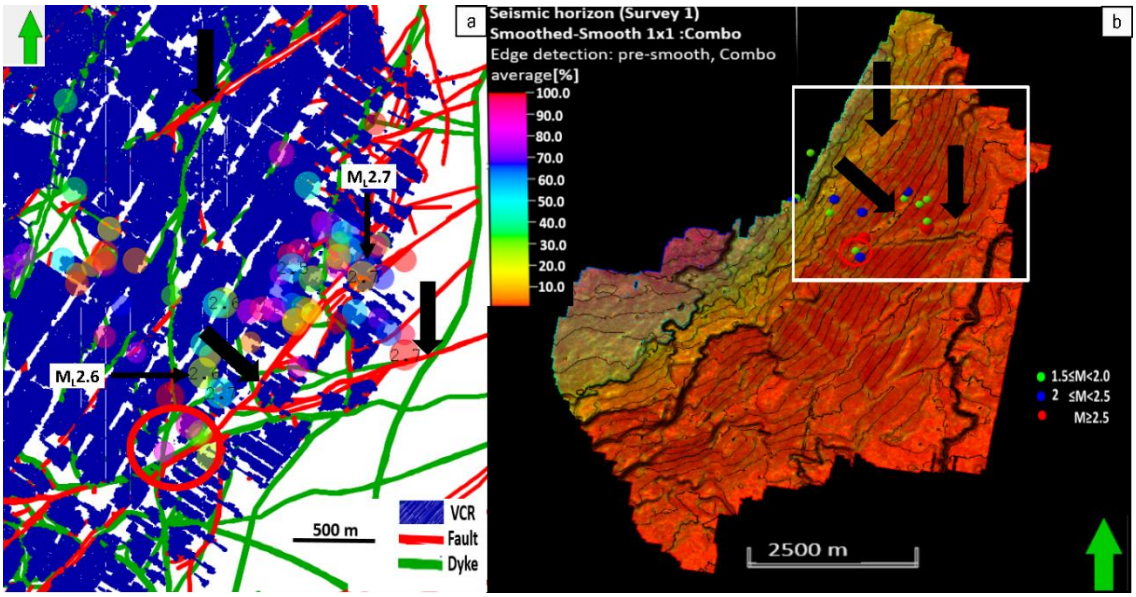

Fig. 7 *(a) Area mapped underground indicating mining, geological structures and seismicity within the 3D reflection seismic volume (b) VCR edge attribute map overlain with mining-induced seismicity data in Kloof Gold Mine. A white rectangle shows the location of Fig 7(a), intersecting structures by a red circle, and faults by black arrows pointing towards them. Large seismic events correlate with the geological structures.*

Moment Tensor

All moment tensors calculated in this study were determined using three-component recordings of ground motion at stations located with within a radius of approximately 1000 m of the source, and a hypocenter that lies within the 3D reflection seismic cube. To ensure accurate picks of arrival times, only seismograms with a good signal-to-noise ratio of both P- and S-wave arrivals were used. The P- and S-wave arrival times were manually picked (Fig. 8). Three component seismograms were rotated into the P-SV-SH local co-ordinate system to help pick the S-wave accurately. The location of the seismic event was then calculated, and the theoretical arrival time at each location determined and compared with the initial pick. The picks were checked and refined until the location residual was less than 100 m or 3% of the average distance between the event and the sites. Moment tensors of the Kloof Gold Mine seismic events were verified by calculating synthetic seismograms. The moment tensor solutions for two large seismic events (M_L 2.6 on 15 July 2017; M_L on 28 June 2018) are discussed below. The source and moment tensor solution for the entire data set are listed in Tables 1-4.

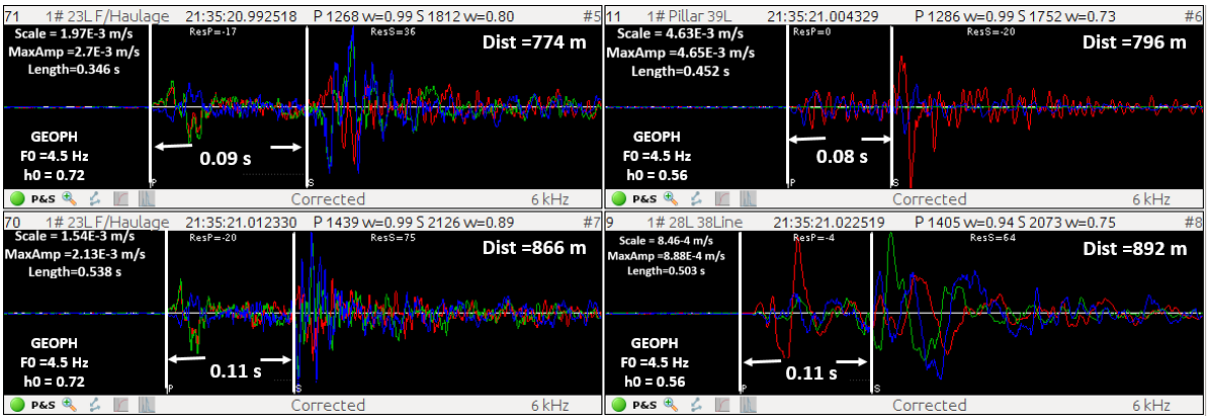

Fig. 8 *Examples of tri-axial waveforms of P, SV, SH in local co-ordinates system of magnitude 2.1 event recorded on 07.10.2018 at distances of 774, 796, 866 and 982 m. The velocity amplitude of the seismograms is displayed in the left upper corner of each seismogram. 'Length' represents the size of the seismogram display window; 'MaxAmp' is the maximum amplitude of the wave.*

The seismic waveforms recorded by the sites with reliable characteristics were used for the estimation of seismic moment tensors. The seismic waveforms recorded at Kloof Gold Mine allow for the use of a relatively simple and quick moment tensor inversion technique based on the amplitudes and polarities of P- and S-wave signals. The amplitudes were calculated in the frequency domain, from the low-frequency plateau of displacement spectra. The moment tensor inversion method procedures consist of the following (Malovichko and Lotter, 2016):

- Input parameters for the inversion include the
    - Seismograms
    - P- and S- waves arrival times (P- and S- picks)
    - Sensor parameters (co-ordinates, sensor type, natural frequency, sensitivity, spectral response, and orientation)
    - Rock mass parameters (density (ρ), velocities of P- (α) and S-wave (β))
    - Seismic source parameters (origin time, location)
- The seismic data from pre-processing, automatic used by Trace software.
    - Estimation of the dominant period of every trace
    - P- and S-wave signal-to-noise ratio estimation
    - P-wave polarization estimation (direction of P-wave)
    - Waveform transformation into a P-SV-SH wave co-ordinate system.
    - Selection of events with very good and clear P- and S- wave arrivals with good signal-to-ratio.
    - P- and S-wave polarity estimation

    - Manual re-location of selected seismic events with accurately picked arrival times.
    - P- and S-waves normalised spectra calculation
    - P- and S-waves normalised spectra fitting with Brune model
    - Calculation of the normalized noise spectrum
    - Spectral model fitting of normalized P, SV, and SH spectra
- Calculation of moment tensor parameters

Event 2017.07.15.16.23.57 (M_L 2.6)

Fig. 9 displays the moment tensor inversion results for the large seismic event, indicating the focal sphere coverage, using the standard “beach ball” representation. Spectral amplitudes for this event were measured for P, SV, and SH arrivals recorded by 25 in-mine seismic stations, and the polarities were assigned by the IMS algorithm for each of them. The focal sphere coverage was typical of mining environments, reflecting the absence of seismic stations covering the area ahead of the advancing mine stopes and in other older (or ‘back’) areas of the mine. The IMS software implemented an algorithm published by Vavrycuk and Kuhn (2012) to invert the seismic moment tensor based on the polarities and amplitudes information recorded at the sensor sites, instead of the traditional method that only uses the amplitudes and polarities of waveforms (Malovichko, 2012). This allows moment tensor solutions to be obtained when the traditional method is unstable. Moment tensor decomposition, shown here in Fig.9, was achieved through polarity of P-wave first motion where the negative and positive signs indicate compression and tension, respectively. The result of the moment tensor solution obtained for this seismic event is: M_{xx} = -0.12 x 10^{11} Nm; M_{xy} = -0.01 x 10^{11} Nm; M_{xz} = -0.55 x 10^{11} Nm; M_{yy} = +0.21 x10^{11} Nm; M_{yz} = +0.19 x 10^{11} Nm; and M_{zz} = -0.63 x 10^{11} Nm. The inversion misfit is 0.31, while the misfit between the observed and synthetic data is 0.259 (this indicates 26% disagreement between observed and synthetic data of the seismic waves and 74% agreement).

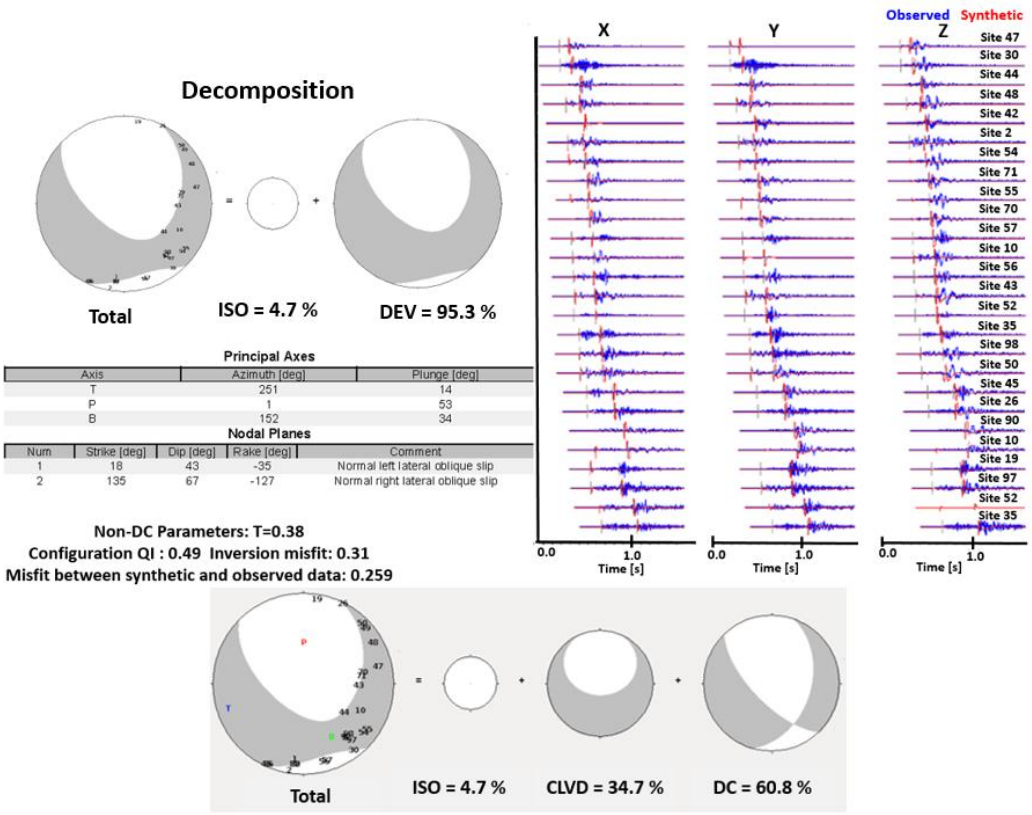

Fig. 9 *Moment tensor inversion results and sites on the focal sphere for the seismic event 2017.07.15.16.23.57. The upper left-hand diagram shows the isotropic and deviatoric moment tensors for the P-wave radiation pattern. The lower left-hand indicates the principal axes and the possible nodal planes. The waveforms corresponding to the observed (blue curves) and the synthetic (red curves) are compared. Moment Tensor decomposition for the event is given at the bottom of the diagram.*

The mechanism obtained (Fig. 9) indicates a very high deviatoric component (DEV=95.3%) and small volume change (isotropic component) within the source of the seismic event (ISO=4.7%). The deviatoric component may be further decomposed into two components: double couple (DC=60.8%) and compensated linear vector dipole (CLVD=34.7%). The moderate compensated linear vector dipole (CLVD) component (34.7%) indicates that uniaxial deformation formed part of the event mechanism. The mechanism is typically associated with dynamic pillar failure and stope closure. This is consistent with the underground observation of dynamic closure on the support units. The small volumetric closure component ISO (4.7%) shows that the non-shearing (NS) motion is small. The moment tensor solution agrees with the expectation that fault- and dyke-controlled seismic events exhibit strong double couple focal mechanisms. The moment tensor solution implies an insignificant implosive isotropic component, and the nodal planes align with the NW-SE striking dyke (Fig. 7 (a) and Fig. 15). The seismic event locates about 10 m from the

dyke and close to mined-out areas. The relatively low energy ratio Es/Ep (=4.7) suggests that the seismic event has a burst-dominated component, while the moment tensor suggests significant slip on the NW-SE trending dyke. This contradiction is discussed below. However, it should be noted that the CLVD solutions might be affected by the focal depth, velocity model uncertainty and the possible complexity of the heterogeneous rock mass.

Event 2018.06.28.18.10.56 (M_L 2.7)

More generally, however, we obtain moment tensors that do have such a dominant burst component. Fig. 10 displays the moment tensor inversion results for one such seismic event locating less than 10 m away from the NW-SE trending fault, with the 55% volumetric and 31% double couple component. The moment tensor solution for this seismic event is: M_{xx} = -0.40 × 10^{12} Nm; M_{xy} = 0.13 × 10^{12} Nm; M_{yy} = 0.16 × 10^{12} Nm; M_{xz} = 0.35 × 10^{12} Nm; M_{yz} = 0.10 × 10^{12} Nm; and M_{zz} = 0.89 × 10^{12} Nm. The nodal plane aligns - with the NW-SE striking feature Fig. 7 (a) and Fig. 15. The analysis has a misfit of ~0.256 and a correlation coefficient of 0.74, which, once more, offers a satisfactory visual match between observations and predictions. The energy ratio Es/Ep (= 5.7) indicated a burst dominated component in its mechanism, which is in accord with the volume change (ISO = 54.7) of the moment tensor.

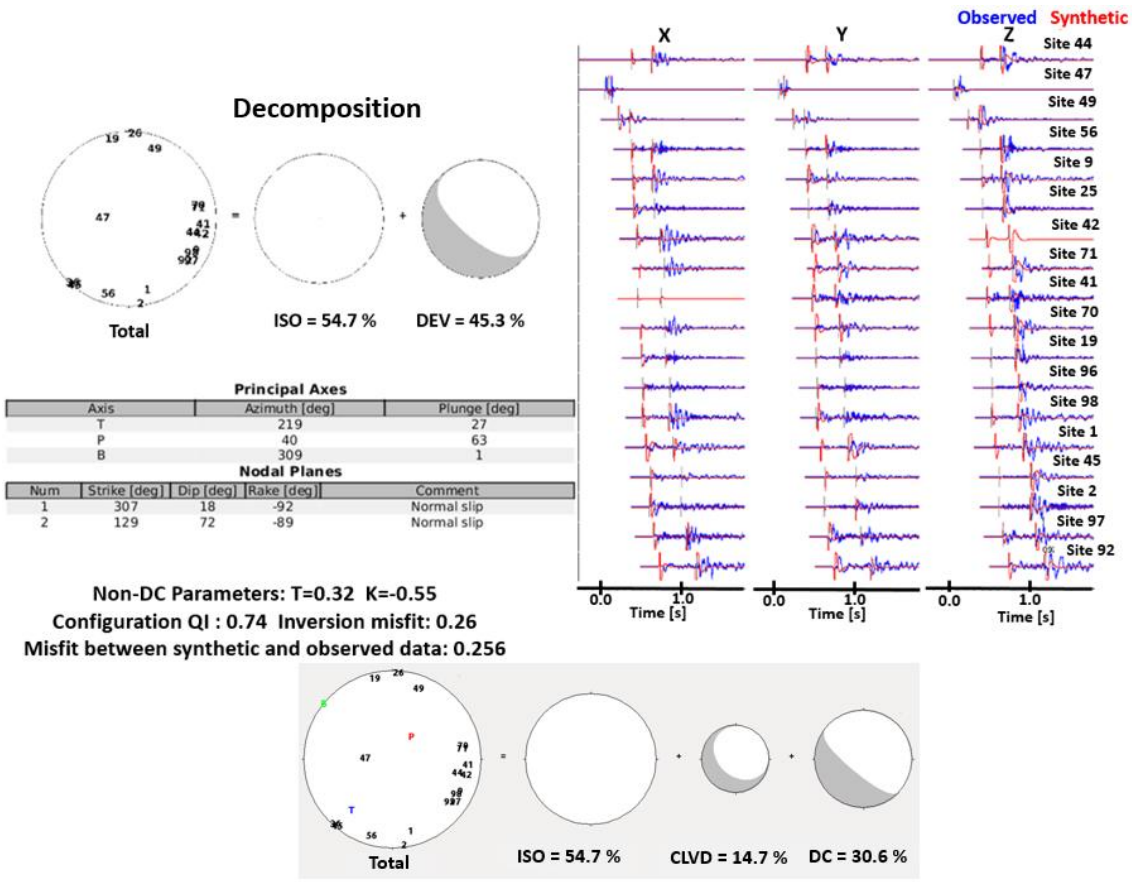

Fig. 10 *Same caption as in Fig. 9, but for event 2018.06.28.18.10.56. The misfit between synthetic and observed data is 0.256.*

Summary

The current analysis concentrates on a set of 75 events with $M_L \geq 1.5$ that occurred between 1 January 2017 and 30 Dec 2018, and which were all located within the 3D reflection seismic volume polygon (Fig. 5 and Fig.6). Manual processing led to a combined set of source mechanism solutions of variable quality. The quality of each moment tensor solution has been quantified using the misfit between observed and synthetic waveforms and the 2D coverage of sensors. The moment tensor inversions results indicating both the deviatoric and isotropic components are listed in Table 2A, while Table 3A and Table 4A provide the fault plane solutions information of the analyzed seismic events from the study data.

To investigate the source mechanism of these events, the data from 3D reflection seismic cube were plotted on a Hudson source-type diagram. The Hudson diagram is a graphical representation of the seismic source based on two plotted parameters, T and k, which represent

the relative proportion of constant volume deformation of the source (i.e., shear) and volume change (i.e., dilation/contraction) of the source, respectively (Hudson et al., 1989). The diagram takes the form of a rhombic-shaped two-dimensional grid, with T and k plotting on the horizontal and vertical axes, respectively. The ISO term represents the isotropic volumetric change in the earthquake source. Positive values indicate an explosive-type source (tensile opening), while negative values indicate an implosive-type source (crack closures). The DC term represents the pure shear motion from two perpendicular vector pairs of opposite signs but equal magnitude. The CLVD represents motion toward (if negative) or motion away (if positive) from the hypocentre with no net volume change; it has a complex physical interpretation (Frohlich, 1994; Julian et al., 1998)

The Hudson chart illustrates source mechanism types including pure implosion and explosion, crack dilation and closure, ± linear dipoles and ±compensated linear vector dipoles. Purely explosive sources plot where k =1 and T =0. Purely implosive sources plot where k = -1 and T = 0 (Fig. 12a). Constant volume shear source mechanisms plot along the line k =0. For example, a simple double couple source plots in the centre of the diagram where T = k = 0 (i.e., unidirectional displacement along a single joint plane with no dilation).

The Hudson diagram for the source mechanisms of the large analysed seismic events is plotted in Fig.12a. The Hudson diagram has been divided into three sections, each separated by the green dotted lines on the diagram. Events plotting within the upper region predominantly demonstrated explosive characteristics. Events in the central region had a high deviatoric nature, indicative of shear failure. Seismic events plotting in the lowest of the three regions had implosive source characteristics typical of compressive overstressing failure and fractures' closure (Fig. 12). The minority of event mechanisms plotted within the explosive region of the Hudson diagram, and all therein were located very close to the deviatoric boundary. The majority of the mechanisms within the 3D reflection seismic volume were plotted within the implosive region of the Hudson diagram. This indicated that closure of openings (which include metre-wide stopes and millimeter-wide mining-induced fractures) was the dominant failure mode in the area of interest. This indicated that the seismic source mechanisms were more clearly indicative of stress-driven fracture closure, although stope closure may also play an important role.

85% of the full moment tensor solutions had a dominant double couple (>60%) component (*DC*); in some cases, the compensated linear vector dipole component (*CLVD*) and isotropic component

(*ISO*) accounts for 15% of the selected events. Out of these seismic events, 21% exhibit positive ISO and CLVD indicating tensile crack dilation ('explosions') while 57% of them show negative ISO and CLVD representing tensile crack closure ('implosions'). The interpretations of either the explosive or implosive point source model (isotropic component) links to the volume change process within the rock mass affected (Fig. 12d). These results correspond to previous studies showing that many large mining events have significant implosive volumetric components (McGarr, 1992a). The solutions computed using the IMS moment tensor inversions indicate that the dominating source mechanisms in all the regions appear to be of a shear-type and shows near-vertical and near-horizontal nodal-planes given the stress field. The large compensated linear vector dipole (CLVD) component indicates that uniaxial deformation formed part of the event mechanism. This mechanism was typically associated with dynamic pillar failure and stope closure (Fig.11).

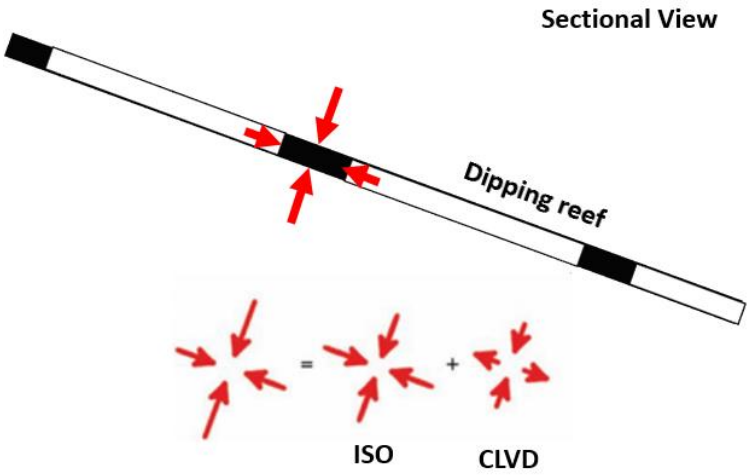

Fig. 11 *The dynamic pillar failure and stope closure example.*

This research indicated that the 75 large, selected events show a range of focal mechanism types, namely: implosive components, explosive components, and no volume change. Fig. 12 (a-e) shows a Hudson diagram plot contributing to the total moment tensor inversion solution of the seismic events. Deviatoric solutions and the high double-couple solutions of the moment tensor are more likely to represent mechanisms of these seismic events.

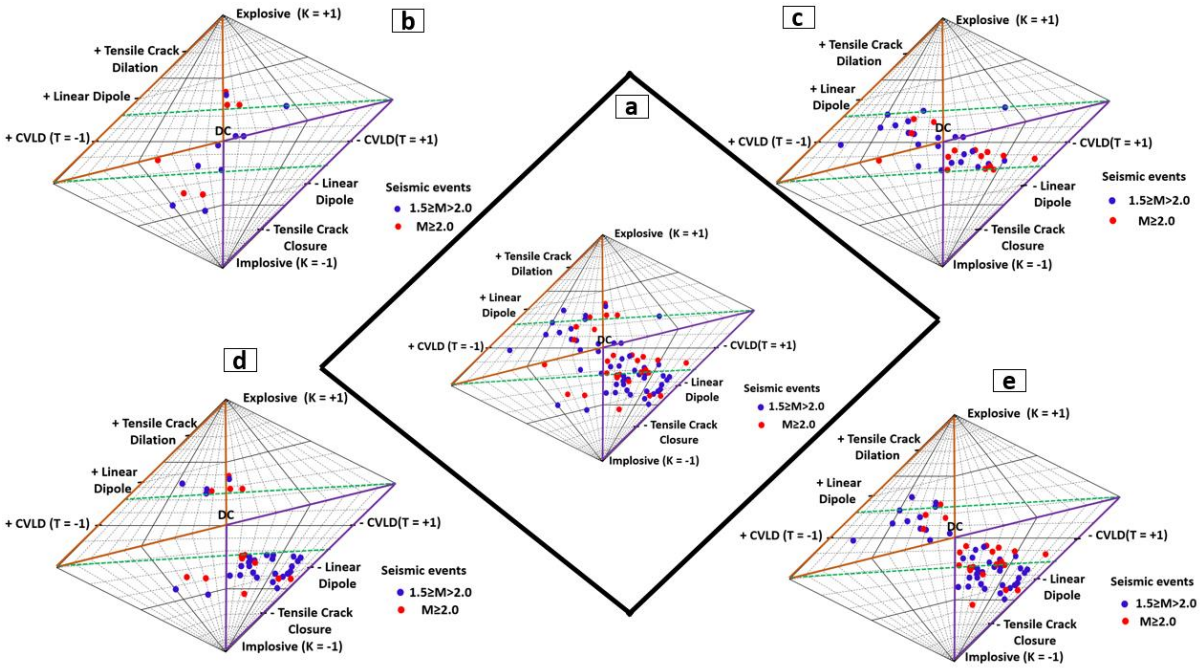

Fig. 12 *(a) Hudson Diagrams plot with all source mechanisms, (b) Explosive positive CVLD and Implosive negative CVLD seismic events, (c) Double couple (DC) plots, (d) Isotropic component (ISO) excluding the DC events, (e) Events with dominant linear vector dipole component (CLVD).*
Black lines are contours of constant T (measure of deviatoric moment release, running from right to left) and k (measure of the change in volume, running from top to bottom). Green dotted line separates the Hudson diagram into 3 regions: Upper region (Explosive), Central region (High DC) and Lower region (implosive). Brown line: Negative CVLD. Purple line: Positive CVLD.

Fig. 12e indicates a dominant (69%) linear compression value of the CLVD. Both the isotropic (implosive and explosive components) and the compensated linear vector dipole component relate to compressive stresses close to the mining excavation (see Fig. 12(d-e)). A high value for the double couple component in the moment tensor may indicate a substantial shear motion on a preexisting fracture (Fig. 12c). The types of seismic events are large and usually occur any time of day and expose mining personnel to a seismic hazard and risk to mining infrastructures.

In the moment tensor solution, small DC components may indicate that nodal planes experienced little shearing motion (Fig. 12d). The high isotropic component value of the moment tensor indicates more of a volume change within the rock mass (Fig. 12d). Fig. 12c indicates moment

tensor solution characterized by the highest DC component and much higher energy and could indicate the rock mass experiencing the elastic rebound.

The source mechanisms of mining-induced seismic events aid in understanding the various modes of failure. The planes of failure may be caused by stresses generated by mining or geological structures. However, less than 20% of the analyzed seismic events have nodal planes that are aligned with nearby mining and geological structures (e.g., seismic event's location accuracy of 70m and its strike-orientation to be parallel or less than 20° deviation to either the mining geometry or geological structure). This indicates that the moment tensor solution cannot be used alone since it is not always reliable and is sensitive to many different errors. The tool can help aid with other methods (e.g., numerical modelling) to understand failure modes in depth.

P- and S-wave energy ratio analysis

Mendecki (2013) suggested that S- and P-wave energy ratios can give an indication of the focal mechanism of mining-induced seismic events. According to Gibowicz et al. (1991) and Gibowicz and Kijko (1994), when Es/Ep <10, the source mechanism will involve a tensile failure component, while Boatwright and Fletcher (1984) suggested that Es/Ep >10 corresponds to pure shear mechanism. The 75 analyzed large events were divided into two categories of failure mode as used in the mining industry depending on their energy ratios (Es/Ep): non-shear type events (**NS**, Es/Ep <10, 62 events) and shear-type events (**FS**, Es/Ep >10, 13 events). The fault slip events occur in all mining levels (1600 to 4000 m), whereas most non-shear events occurred between 2800 to 3200 m (Fig. 13). Calculations were based on the different assumptions based on the IMS software algorithms (e.g., source effect, ray path effect, and the number and location of an array of sensors).

Surprisingly, about 97% of the 62 non-shear events (classified according to the energy ratio criterion) had a dominant deviatoric (DEV) component. The fault plane solution of some events aligned to the structures in the vicinity (Fig. 16). Only 3% of the 62 non-shear indicated a high volume change. Out of the 13 shear-type events, only 38% indicated the dominant DC component with low CLVD. Most of these seismic events were plotted at a shallower depth than those with a dominant CLVD, which mostly occurred between 2800 - 3200 m, close to the reef horizon.

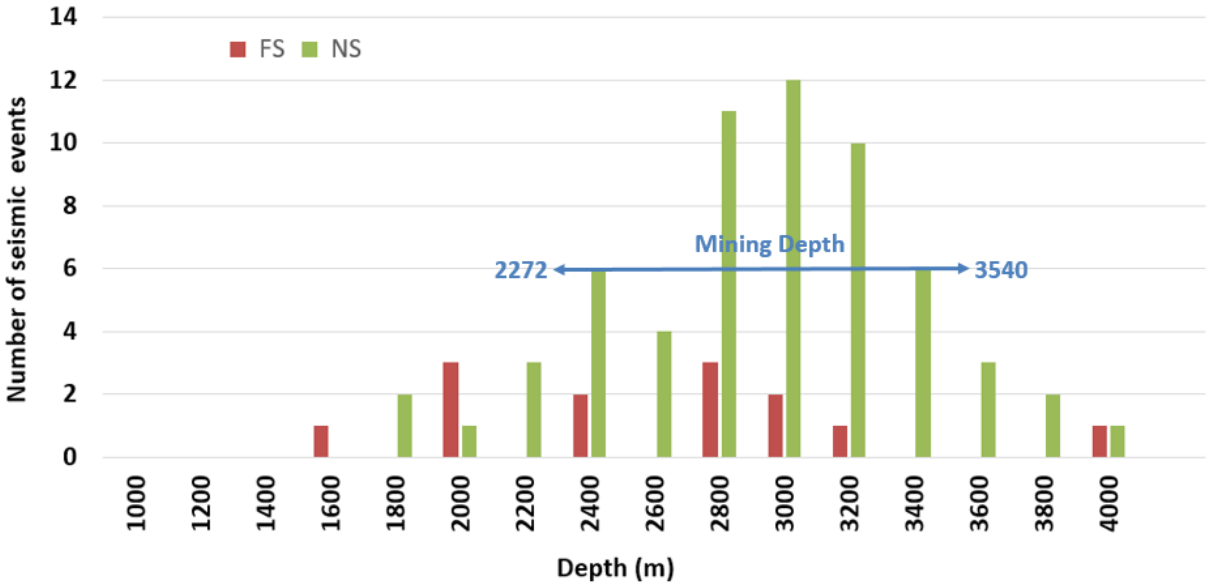

Fig. 13 *The distribution of seismic events source mechanisms in different mining levels within the VCR orebody. Brown represents the Fault Slip (FS), and Green represents the Non-Shear (NS).*

There is a direct proportionality between the apparent volume and the local magnitude (Fig. 14a). The correlation of coefficient between the apparent volume and local magnitude is strong (0.64) for FS compared to NS, which only has a 0.20 correlation. The released energy indicated a good, very strong correlation with the local magnitude for both the NS and FS seismic events (Fig.14b). Higher energy for a similar local magnitude was evident in FS seismic events than NS seismic events, though there is an insignificant statistical difference between the two types. This suggests greater damage, depending, of course, on the proximity of the seismic event to the mine-working place. The source radius and local magnitude have a positive correlation for both the FS and NS events (Fig. 14c). The source radius increases with a local magnitude between FS and NS events with no significant difference. With the value of 10 used to separate NS and FS events, it was found that the log energy ratio (Es/Ep) for NS seismic events fluctuated from 1.1 to 9.4, and for FS events from 10.0 to 19.9 (Fig.14d). For the 13 FS seismic events, the energy ratio (Es/Ep) indicated a negative trend to the local magnitudes. This indicates that the log energy ratio of FS seismic events decreases with the increase in local magnitude, and there is an insignificant statistical difference due to the poor correlation coefficient.

The corner frequencies for these seismic sources varied, ranging from 13 to 27 Hz; the increasing corner frequency with decreasing local magnitude was observed, as would be expected (Table 1A).

.

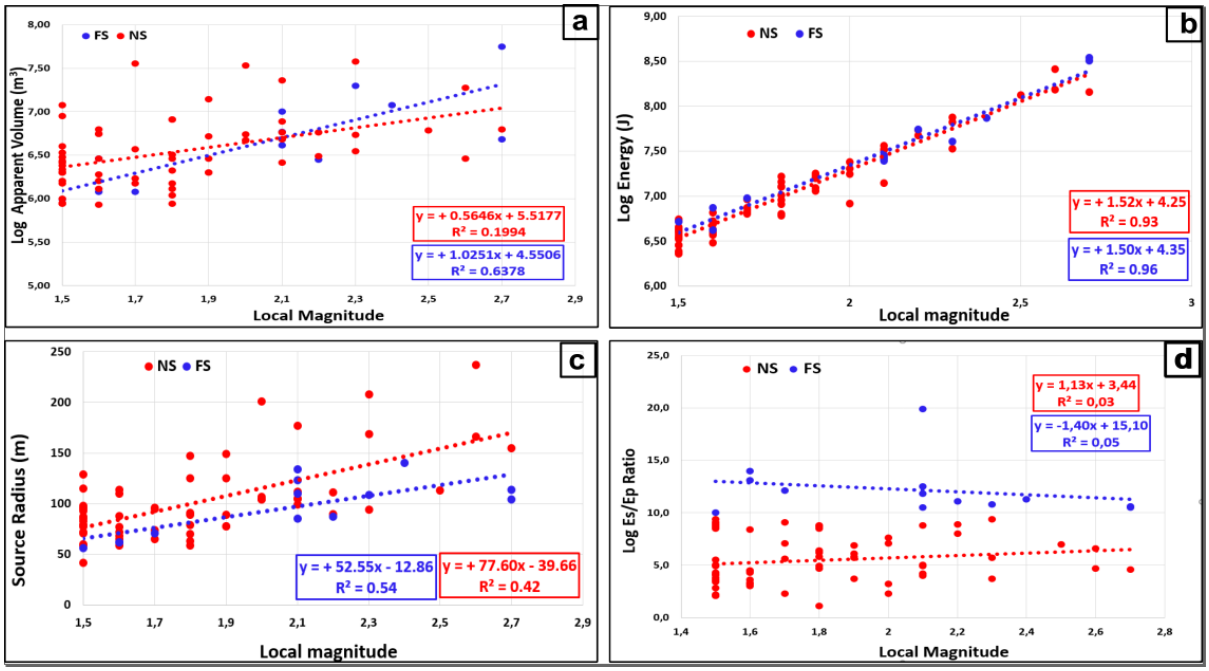

Fig. 14 *Seismic source parameter correlated with the local magnitude (a) Log Apparent volume versus Local magnitude, (b) Energy versus Local magnitude (c) Source radius versus Local magnitude,e and (d) Log* Es/Ep *versus Local magnitude.*

In summary, the energy ratio classification does not correlate well with the Moment Tensor Inversion results. This might be due to the source effect (seismic energy radiation pattern), path effect (attenuation), and sensor effect (location and number of geophones installed) since each of these factors adds the element of potential error and uncertainty to the calculations of the energy ratios (Es/Ep).

About 48% of the 75 seismic events occurred in the footwall of the VCR within the quartzite rock mass (Fig. 6b). The location and mechanisms of the seismic events could be due to high-stress concentration, geological structures, mining methods, remnant or/and abutment, or other factors within the rock mass. However, no definitive conclusion could be derived from these seismic events during the study. An explanation cannot be made of either the random distribution of the FS events are mostly due to the stress redistribution or geological structures or arbitrary distribution of the NS events are due to other unknown factors. Nominated source parameters and local magnitude were compared and investigated to find a difference in the NS and FS seismic events parameter trend. Observation after the comparison of the selected source parameters includes:

- The number of NS events was four times greater than the number of FS events (Fig. 14d).
- On average, for the same magnitude, the shear events (FS) release more seismic energy as compared to the non-shear events (NS).

Factors controlling seismicity

The focal mechanism and moment tensor solutions can be related to the mapped and interpreted seismically-active geological structures within the 3D seismic reflection volume. One of the challenges of moment tensor inversion is to determine whether the results provide a precise reflection of the underground reality. Appropriate ways in which this verification can be undertaken in the detailed mapping of fractures within the study area and then comparing both the orientations and locations of the fault plane solutions with those mapped (Fig. 15). 3D reflection seismic shows high resolution of faults that are not mapped by the mine maps (Fig.7 and Fig15 (b)).

Comparing the orientation of the seismically active structures with the possible nodal planes of the focal mechanisms for each of the four seismic events in Fig. 15 (a) provides some insight into possible modes of failure. All the selected large seismic events ($M_L \geq 2.6$) originated at 2351 m to 3290 m depth, which appears to coincide with the orientation of the faults and dykes in the vicinity. The seismic events were aligning to mapped structures with a north-northeast trend (M_L=2.7, 2017/10/23 and 2018/03/17), north-northwest trend (M_L=2.6, 2017/03/07), and northwest trend (M_L=2.6, 2018/06/28). The Fault Plane Solution of these events corresponded to normal slip (M_L=2.7, 2018/03/17), strike-slip reverse faulting (M_L=2.6, 2018/06/28), and normal strike-slip (M_L=2.7, 2017/10/23). The position, focal mechanisms, and magnitudes of these large seismic events are superimposed on a structural model of the study area (Fig. 15). The fault plane solutions of some seismic events displayed in Fig. 16 align with not only geological structures but with mining geometries (dip pillars, abutment, etc.). These large seismic events are associated with faults and dykes. The source mechanism does, however, also suggest stope closure (Table 4).

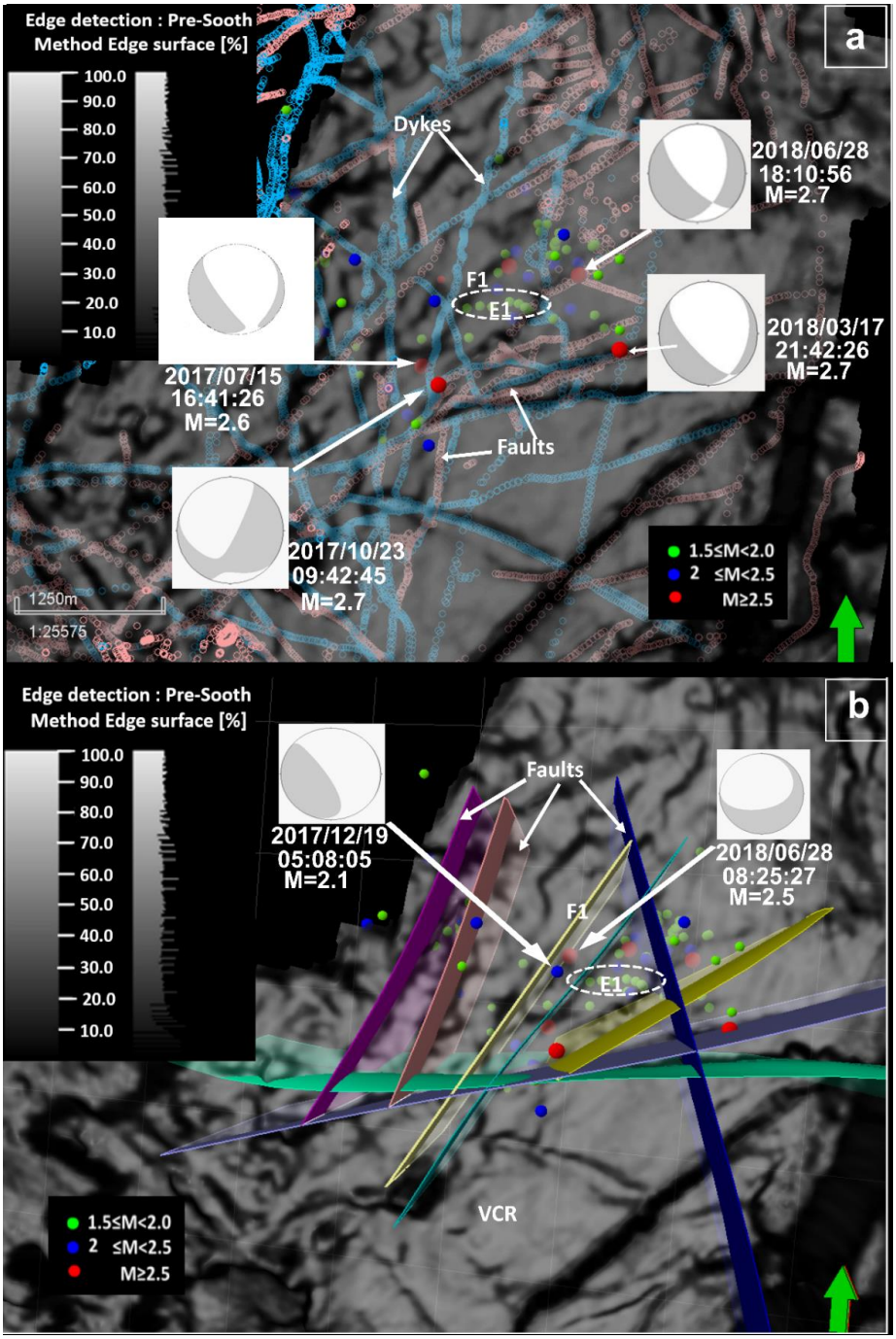

Fig. 15 *(a) The position, focal mechanisms, and magnitudes of selected large seismic events superimposed on geological structures that were mapped using the 3D seismic volume, or projected from underground mapping and drill core logs. Faults and dykes are indicated by pink and blue circles, respectively; (b) 3-D reflection seismic mapped faults and associated seismic events. Only very large seismic events aligned with structures are displayed. F1: structure detected by the edge detection method. E1 (white dashed oval): seismic events following a pattern from West to East.*

Moment tensor inversion results of events ranging in size from $2.1 \leq M_L \geq 2.7$ were superimposed on the mine map (Fig.16) along with mapped geological structures in Region A, B, and C. Due to small stress changes from mining activities, seismic faults can be activated in volumes proportionally much larger than the mining area itself (McKinnon, 2006). Comparing the orientation of the seismically-active structures with the possible nodal planes of the focal mechanisms for each of the twenty-three seismic events in Fig. 16 provides some insight into possible modes of failure. The nodal planes of some seismic events are closely aligned to a nearby structure, others could be aligned to more than one structure, given the uncertainties in the location of the event and the orientation of the nodal planes, while others do not have any obvious correlation. Region C seems to be the part of the mine where there is the largest proportion of events that are aligned with structures, *viz.* 3 out of 11 events (see Figs. 15 and 16).

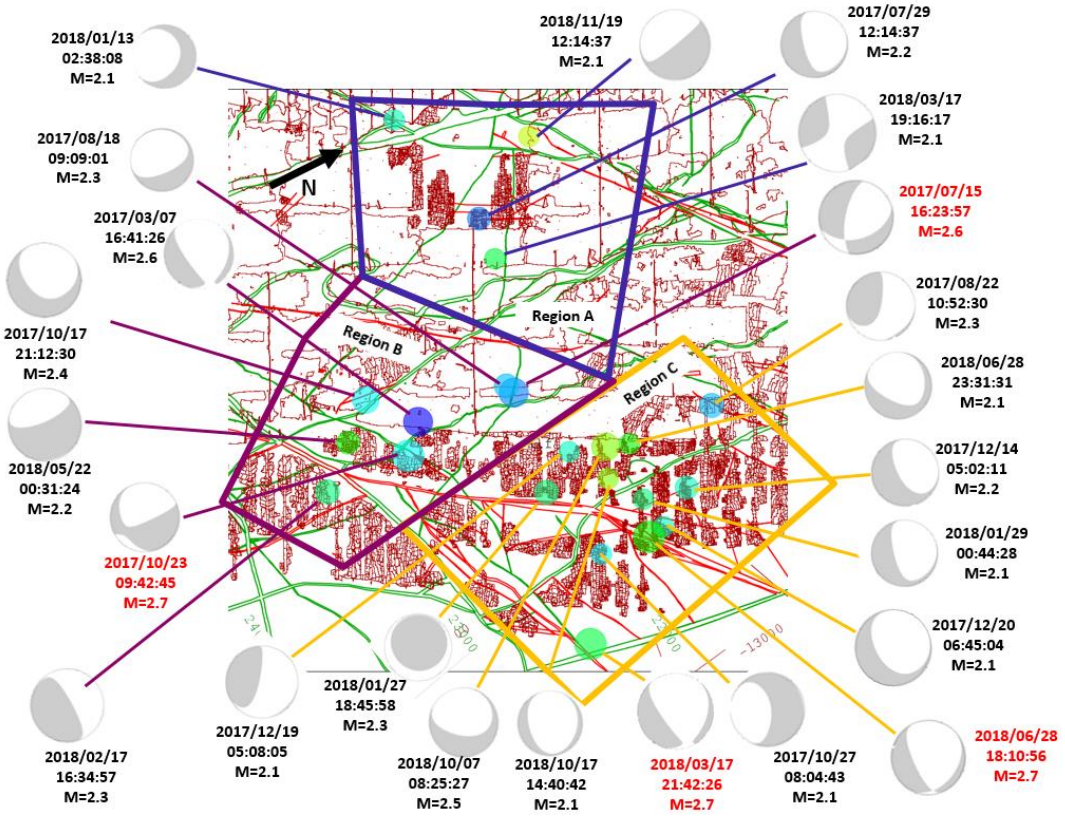

Fig. 16 *Locations and DC component of the focal mechanisms of $M_L \geq 2.1$ seismic events within the 3D seismic volume at Kloof Gold Mine. Moment Tensor were rotated into the plane of the reef. Region A: Blue, Purple and Yellow polygons indicate Regions A, B and C, respectively: Red highlighted seismic events are events in Fig.14.*

Discussion

During the research, hypocenter locations were improved by reprocessing waveforms for back analysis related to the large seismic events. Obtaining a good quality location was vital for the study. The second goal was to determine whether the large seismic events (M_L ≥1.5) in the Kloof Mine seismic system are associated with either the geological structures or the mining geometry (pillars or the abutments).

The day-to-day seismic monitoring includes 43 sensors to determine the hypocenter location. The distance residuals is calculated per site per pick basis, where the residuals for both P- and S-wave are calculated based on the difference in travel times and the velocities. The average "error" was a small percentage (3-5%) of the average distance between the event and the sites. Fig. 5 indicated that most of the observed large seismic events are located in the hanging wall of the VCR. Geological structures (i.e., faults, dykes) were either mapped in mine workings and boreholes, or by the interpretation of a 3D reflection seismic cube. The resolution of the seismic interpretation was maximized by applying the edge detection seismic attribute.

Moment tensors of 75 events were calculated using a polarity of P-wave first motion technique, producing a wide range of solutions. Some events have a dominant deviatoric components typical of slip along a fault plane, while other events had a dominant isotropic component, diagnostic of significant volume change probably related to closure of the mining voids (Fig. 9 and Fig.10).

The large magnitude events show implosive sources, as was observed in previous studies of larger (M_w ≥1) mining-induced seismicity (McGarr, 1992a, b 1984; Fletcher and McGarr, 2005; Julià *et al*., 2009). Overall, the full moment tensor solutions show significant DC components for all events (Fig.12, Fig.16; Table 4). Fig. 12 shows that events recorded in the Kloof Gold Mine indicate that both deviatoric and implosive sources are found throughout the different orders of magnitude, 1.5 ≤M_L ≤ 2.7. Observations show that most of the seismic events from Kloof Gold Mine located within mining depth of 2272 m and 3540 m (Fig. 13) indicate implosion and tensile components with varying magnitudes. Based on the suggestion by Vavryčuk (2011), the events with small components of the CLVD could be a real shear-tensile source mechanism. Data for the 75 seismic events displayed higher seismic energy for shear/fault slip (FS) events than for non-shear (NS) events with an implosive component.

From the analysis comparing the source parameters of Non-Shear (NS) and Fault-Slip (FS) events, several observations were made, including

(1) Higher energy for a similar local magnitude was evident in FS seismic events than NS seismic events (Fig. 14b).
(2) Log apparent volume varied from 5.93 – 7.75 m^3.
(3) The source radius and local magnitude have a positive correlation for both the FS and NS events.
(4) The source size increases with a local magnitude between FS and NS events with no significant difference (Fig. 14c).
(5) The energy ratio (Es/Ep) indicated a negative trend to the local magnitudes for FS, and a steady positive increase of the Es/Ep ratio with the local magnitude is evident for the NS events. However, the Es/Ep ratio, as a method of classifying seismic events, was not consistent with the expected source mechanisms some seismic events when compared to the moment tensor components. It indicated that the parameter is not stable for being used as the only classification method.

Large seismic events plotting in the ore body's hanging wall tend to be more DC type than those on the reef horizon or in the footwall, showing more CLVD (more closure within the stope). Most of the large seismic events recorded at Kloof Gold Mine have considerable deviatoric components in the moment tensor. The geometry of the orientation of nodal planes and principal axes (components) makes it possible to associate the seismic events with either the slip/burst on the geological structure or shear fracture on the intact rock mass ahead of the mine out panels.

The fault plane solutions of some seismic events (M_L=2.5, 2018/10/07 and M_L=2.1, 2017/12/19) displayed in Fig. 14b align with not only geological structures but with mining geometries (abutment and the dip pillar). A NE-SW trending structure was observed (F1), which was not mapped on the in-mine plan but detected using the edge detection method. However, none of the plotted large seismic events aligns with the structure. Seismic events (E1) following an E-W trend might indicate the presence of the structure trending in the same direction that might not be mapped by either the in-mine map or edge detection method. On the other hand, this could imply the dip pillars in the vicinity are failing.

The focal mechanism and moment tensor solutions were related to the mapped and interpreted seismically active geological structures within the 3D seismic reflection volume. Moment tensor inversion results of events ranging in size from $2.1 \leq M_L \geq 2.7$ were superimposed on the mine map (Fig.16) along with mapped geological structures in Region A, B, and C.

For some seismic events, the nodal planes had some similarities, not only with one but with several different geological structures in the vicinity. In other seismic events, the nodal planes could not be related to any of the structures. Taking the location error for the seismic events into account, we found that a greater proportion of events were aligned with geological structures in Region C, compared to Regions A and B.

Conclusions

Seventy-five seismic events have been described from the Kloof operations. All these seismic events are spatially related to either mining geometry or geological features in the vicinity. The analysis of the moment tensor inversion indicates that only 3 out of 11 events give fault-plane solutions in which one of the two derived planes was parallel to a known geological structure in the vicinity. The analysis indicates that mining activities lead to a burst or a slip taking place on pre-existing geological planar structures and these large seismic events in the 3D reflection seismic volume might not be driven by only major geological structures. The 3D structural model indicates seismic events occurring along to the structures. The fault plane solutions aligned to some structures in the 3D reflection seismic volume and the in-mine structures. The Es/Ep ratio, which was used as a method of classifying seismic events, was not consistent with the expected source mechanisms when compared to the moment tensor components. This study indicated that the parameter was not stable for being used as the classification method.

The moment tensor results might have been affected by noise contamination (ambient and instrumentation noise), poorly distributed network (denser network should surround the source), the improper model of the media (poor knowledge of the seismic velocity in the area), and source location (hypocenter mislocated). Under certain specific ranges of these outlined factors, the moment tensor inversion is capable to yield reliable solutions that will align with the mining geometry and geological structures.

Acknowledgement

Sibanye Stillwater and the seismology department are thanked for allowing the proprietary data for Kloof mine to be used in this study. I am also indebted to my supervisors Prof Ray Durrheim and Prof Musa Manzi, for their role in providing guidelines and motivations in writing and analyzing the data in this study.

References

Aki, K.U. and Richards, P.G., 2002. Quantitative Seismology second edition. *Univ. Science Books, Sansalito, CA*, pp.218-235.

Andersen, L.M., 2001. A relative moment tensor inversion technique applied to seismicity induced by mining. PhD Thesis. University of the Witwatersrand, Johannesburg.

Armstrong, R.A., Compston, W., Retief, E.A., Williams, I.T. and Welke, H.J., 1991. Zircon ion microprobe studies bearing on the age and evolution of the Witwatersrand triad. *Precambrian Research*, *53*(3-4), pp.243-266.

Backus, G. and Mulcahy, M., 1976. Moment tensors and other phenomenological descriptions of seismic sources—II. Discontinuous displacements. *Geophysical Journal International*, *47*(2), pp.301-329.

Ben-Menahem, A. and Singh, S.J., 1981. *Seismic Waves and Sources*. Springer Science & Business Media, New York.

Beach, A. and Smith, R., 2007. Structural geometry and development of the Witwatersrand Basin, South Africa. *Geological Society, London, Special Publications*, *272*(1), pp.533-542.

Boatwright, J. and Fletcher, J.B., 1984. The partition of radiated energy between P and S waves. *Bulletin of the Seismological Society of America*, *74*(2), pp.361-376.

Coward, M.P., Spencer, R.M. and Spencer, C.E., 1995. Development of the Witwatersrand Basin, South Africa. *Geological Society, London, Special Publications*, *95*(1), pp.243-269.

Dankert, B.T. and Hein, K.A., 2010. Evaluating the structural character and tectonic history of the Witwatersrand Basin. *Precambrian Research*, *177*(1-2), pp.1-22.

Davies, R.J., Stewart, S.A., Cartwright, J.A., Lappin, M., Johnston, R., Fraser, S.I. and Brown, A.R., 2004. 3D seismic technology: are we realising its full potential. *Geological Society, London, Memoirs*, *29*(1), pp.1-10.

Durrheim, R.J., 2010. Mitigating the risk of rockbursts in the deep hard rock mines of South Africa: 100 years of research. Extracting the Science: a century of mining research, Brune J (eds), Society for Mining, Metallurgy, and Exploration. *J. Brune (editor), Society for Mining, Metallurgy, and Explorations, Inc*, pp.156-171.

Durrheim, R.J., Ogasawara, H., Nawakata, M., Yabe, Y., Naoi, M., Ward, A.K., Murphy, S.K., Wienand, J., Lenegan, P., Milev, A.M., Murakami, O., Yoshimitsu, N., Kgarume, T., Chichowicz, A. and the SATREPS research group, 2012. A Japanese - South African collaboration to mitigate seismic risks in mines: The establishment of experimental sites, In: *Proceedings of the Sixth International Seminar on Deep and High-Stress Mining,* Australia (ed. Yves Potvin), Australian Centre for Geomechanics, Perth, Australia, pp.173-187.

Feng, X.T., Liu, J., Chen, B., Xiao, Y., Feng, G. and Zhang, F., 2017. Monitoring, warning, and control of rockburst in deep metal mines. *Engineering*, *3*(4), pp.538-545.

Fletcher, P., 2009. Carbon Leader Reef West Wits Line internal report, AngloGoldAshanti.

Fletcher, J.B. and McGarr, A., 2005. Moment tensor inversion of ground motion from mining-induced earthquakes, Trail Mountain, Utah. *Bulletin of the Seismological Society of America*, *95*(1), pp.48-57.

Frohlich, C., 1994. Earthquakes with non-double-couple mechanisms. *Science*, *264*(5160), pp.804-809.

Gibowicz, S.J., 1993. Keynote address: Seismic moment tensor and the mechanism of seismic events in mines. *Proceedings of Rockbursts and Seismicity in Mines, Kingston, August 1993*, pp.149-155.

Gibowicz, S.J. and Kijko, A., 1994. *An Introduction to Mining Seismology*. Academic Press, San Diego.

Gibowicz, S.J., Young, R.P., Talebi, S. and Rawlence, D.J., 1991. Source parameters of seismic events at the Underground Research Laboratory in Manitoba, Canada: Scaling relations for events with moment magnitude smaller than −2. *Bulletin of the seismological Society of America*, *81*(4), pp.1157-1182.

Gibson, M.A., Jolley, S.J. and Barnicoat, A.C., 2000. Interpretation of the Western Ultra Deep Levels 3-D seismic survey. *The Leading Edge*, *19*(7), pp.730-735.

Jost, M.U. and Herrmann, R.B., 1989. A student's guide to and review of moment tensors. *Seismological Research Letters*, *60*(2), pp.37-57.

Julià, J., Nyblade, A.A., Durrheim, R., Linzer, L., Gök, R., Dirks, P. and Walter, W., 2009. Source mechanisms of mine-related seismicity, Savuka mine, South Africa. *Bulletin of the Seismological Society of America*, *99*(5), pp.2801-2814.

Julian, B.R., Miller, A.D. and Foulger, G.R., 1998. Non-double-couple earthquakes 1. Theory. *Reviews of Geophysics*, *36*(4), pp.525-549.

Harris, P.C, Wesseloo J., 2015. mXrap software, version 5, Australian Centre for Geomechanics,The University of Western Australia, Perth, Western Australia. http://www.mXrap.com.

Hudson, J.A., Pearce, R.G. and Rogers, R.M., 1989. Source type plot for inversion of the moment tensor. *Journal of Geophysical Research: Solid Earth*, *94*(B1), pp.765-774.

Kositcin, N. and Krapež, B., 2004. Relationship between detrital zircon age-spectra and the tectonic evolution of the Late Archaean Witwatersrand Basin, South Africa. *Precambrian Research*, *129*(1-2), pp.141-168.

Krapež, B., 1985. The Ventersdorp Contact placer: a gold-pyrite placer of stream and debris-flow origins from the Archaean Witwatersrand Basin of South Africa. *Sedimentology*, *32*(2), pp.223-234.

Malehmir, A., Durrheim, R., Bellefleur, G., Urosevic, M., Juhlin, C., White, D.J., Milkereit, B. and Campbell, G., 2012. Seismic methods in mineral exploration and mine planning: A general overview of past and present case histories and a look into the future. *Geophysics*, *77*(5), pp.WC173-WC190.

Malehmir, A., Andersson, M., Lebedev, M., Urosevic, M. and Mikhaltsevitch, V., 2013. Experimental estimation of velocities and anisotropy of a series of Swedish crystalline rocks and ores. *Geophysical prospecting*, *61*(1), pp.153-167.

Malehmir, A., Bergman, B., Andersson, B., Sturk, R. and Johansson, M., 2018. Seismic imaging of dyke swarms within the Sorgenfrei–Tornquist Zone (Sweden) and implications for thermal energy storage. *Solid Earth*, *9*(6), pp.1469-1485.

Malovichko, D., 2012. Discrimination of blasts in mine seismology. In *Proceedings of the sixth International Seminar on Deep and High Stress Mining* (pp. 161-172). Australian Centre for Geomechanics.

Manzi, M.S., Gibson, M.A., Hein, K.A., King, N. and Durrheim, R.J., 2012a. Application of 3D seismic techniques to evaluate ore resources in the West Wits Line goldfield and portions of the West Rand goldfield, South Africa Application of 3D seismic techniques. *Geophysics*, *77*(5), pp.WC163-WC171.

Manzi, M.S., Durrheim, R.J., Hein, K.A. and King, N., 2012b. 3D edge detection seismic attributes used to map potential conduits for water and methane in deep gold mines in the Witwatersrand Basin, South Africa. *Geophysics*, *77*(5), pp.WC133-WC147.

Manzi, M.S., Hein, K.A., King, N. and Durrheim, R.J., 2013. Neoarchaean tectonic history of the Witwatersrand Basin and Ventersdorp Supergroup: New constraints from high-resolution 3D seismic reflection data. *Tectonophysics*, *590*, pp.94-105.

Manzi, M.S., Hein, K.A., Durrheim, R.J. and King, N., 2014. The Ventersdorp Contact Reef model in the Kloof Gold Mine as derived from 3D seismics, geological mapping and exploration borehole datasets. *International Journal of Rock Mechanics and Mining Sciences*, *66*, pp.97-113.

McCarthy, T.S., 2006. The Witwatersrand Supergroup. In Johnson M. R., Anhaeusser C. R. and Thomas R.J. *The geology of South Africa*. *Geol. Soc. S. Afr.,* pp.155-186.

McGarr, A., 1992a. An implosive component in the seismic moment tensor of a mining-induced tremor. *Geophysical Research Letters*, *19*(15), pp.1579-1582.

McGarr, A., 1992b. Moment tensors of ten Witwatersrand mine tremors. *Pure and Applied Geophysics*, *139*(3-4), pp.781-800.

McKinnon, S.D., 2006. Triggering of seismicity remote from active mining excavations. *Rock Mechanics and Rock Engineering*, *39*(3), pp.255-279.

Mendecki, A.J., 1993. Keynote address: Real time quantitative seismology in mines. *Rockbursts and Seismicity in Mines*, pp.287-295.

Mendecki, A.J., 1997. Location of seismic events. In *Seismic Monitoring in Mines* (pp. 87-107). Springer, Dordrecht.

Mendecki, A.J., 2013. Mine Seismology: Glossary of Selected Terms. *Proceedings of Eighth International Symposium on Rockbursts and Seismicity in Mines, RaSiM8*. Malovichko, A. and Malovichko, D., (eds.), Geophysical Survey of Russian Academy of Sciences, Mining Institute of Ural Branch of Russian Academy of Sciences, pp. 527-551.

Myers, R.E., McCarthy, T.S. and Stanistreet, I.G., 1989. A tectono-sedimentary reconstruction of the development of the Witwatersrand Basin, with particular emphasis on the Central Rand Group. *Economic Geology Research Unit Information Circular*, *216*, pp.497-540.

Ogasawara, H., Kawakata, H., Ishii, H., Nakatani, M., Yabe, Y. and Iio, Y., 2009. Semi-controlled earthquake-generation experiments in deep gold mines, South Africa Monitoring at closest proximity to elucidate seismogenic process. *Journal of the Seismological Society of Japan (Zisin)*, *61*, pp.S563-S573.

Ogasawara, H., Durrheim, R.J., Nakatani, M., Yabe, Y., Milev, A., Cichowicz, A., Kawakata, H., Moriya, H. and JST-JICA SA research group, 2009. Japanese-South African collaboration to mitigate seismic risks in deep gold mines, Proceedings of 1st Hard Rock Safe Safety Conference, *South African Institute of Mining and Metallurgy*, pp.115-134

Pretorius, C.C., Steenkamp, W.H. and Smith, R.G., 1994. Developments in data acquisition, processing, and interpretation over ten years of deep vibroseismic surveying in South Africa. In *Proceedings of the 15th CMMI Congress, Journal of the Southern African Institute of Mining and Metallurgy,* **3**, pp.249-258.

Pretorius, C.C., Trewick, W.F., Fourie, A. and Irons, C., 2000. Application of 3-D seismics to mine planning at Vaal Reefs gold mine, number 10 shaft, Republic of South Africa. *Geophysics*, *65*(6), pp.1862-1870.

Richardson, E. and Jordan, T.H., 2002. Seismicity in deep gold mines of South Africa: Implications for tectonic earthquakes. *Bulletin of the Seismological Society of America*, *92*(5), pp.1766-1782.

Riemer, K.L. and Durrheim, R.J., 2012. Mining seismicity in the Witwatersrand Basin: monitoring, mechanisms and mitigation strategies in perspective. *Journal of Rock Mechanics and Geotechnical Engineering*, *4*(3), pp.228-249.

Robb, L.J. and Meyer, F.M., 1995. The Witwatersrand Basin, South Africa: geological framework and mineralization processes. *Ore Geology Reviews*, *10*(2), pp.67-94.

Roberts, M.K. and Schweitzer, J.K., 1999. Geotechnical areas associated with the Ventersdorp Contact Reef, Witwatersrand Basin, South Africa. *Journal of the Southern African Institute of Mining and Metallurgy*, 99(3), pp.157-166.

Salisbury, M. H., and D. Snyder, 2007, Application of seismic methods to mineral exploration, in W. D. Goodfellow, ed., Mineral deposits of Canada: A synthesis of major deposit types, district metallogeny, the evolution of geological provinces, and exploration methods: Geological Association of Canada, Mineral Deposits Division, Special Publication 5, 971–982.

Salisbury, M.H., Milkereit, B., Ascough, G., Adair, R., Matthews, L., Schmitt, D.R., Mwenifumbo, J., Eaton, D.W. and Wu, J., 2000. Physical properties and seismic imaging of massive sulfides. *Geophysics*, *65*(6), pp.1882-1889.

Simser, B.P., 2019. Rockburst management in Canadian hard rock mines. *Journal of Rock Mechanics and Geotechnical Engineering*, *11*(5), pp.1036-1043.

Trickett, J. C., Duweke, W.A. and Kock, S., 2005. Three-dimensional reflection seismics: worth its weight in platinum. *Journal of the Southern African Institute of Mining and Metallurgy*, *105*(5), pp.357-363

Vavryčuk, V., 2011. Tensile earthquakes: Theory, modeling, and inversion. *Journal of Geophysical Research: Solid Earth*, *116*(B12):12320, pp.1-14.

Vavryčuk, V. and Kühn, D., 2012. Moment tensor inversion of waveforms: a two-step time-frequency approach. *Geophysical Journal International*, *190*(3), pp.1761-1776.

Vieira, F.M.C.C., Diering, D.H. and Durrheim, R.J., 2001. Methods to mine the ultra-deep tabular gold-bearing reefs of the Witwatersrand Basin, South Africa. In *Underground Mining Methods: Engineering Fundamentals and International Case Studies.* Society of Mining, Metallurgy and Exploration, Littleton, USA, pp.691-704.

Viljoen, M., 2009. The life, death and revival of the Central Rand goldfield. *Special Publication for the World Gold Conference*, pp.131-138.

CHAPTER 8 – THE SEISMIC RESPONSE TO MINING DURING THE EXTRACTION OF THE THUTHUKANI SHAFT PILLAR, KLOOF OPERATION, SOUTH AFRICA

8.1 Authorship Statement

This chapter presents a summary of the published paper which constitutes one of the main focuses of the thesis study. A summary of this paper is provided, highlighting its main objectives, methods, results and conclusions. A description of the candidate's contribution and the contribution of each author is summarised below.

8.2 Manuscript 2

Masethe, R.T., Durrheim, R.J., and Manzi, M.S.S., 2019. The seismic response to mining during the extraction of the Thuthukani shaft pillar, Kloof operations, South Africa. In *Proceedings of the 9th International Conference on Deep and High-Stress Mining, Southern African Institute of Mining and Metallurgy*, pp 71-87.

The candidate was responsible for the following:

- Loading the Kloof mining-induced seismic data in a suitable format into both the KORHAAN and the EGRET interpretation software using the mining coordinate system.
- Uploading the production data, mine plans, geophones sites and geological structures of the Kloof Gold Operation.
- Modifying and creating a base map that included only the shaft pillar polygon within the Kloof operation which was the area of interest.
- Identifying seismic events of concern
- Data conditioning which entailed the filtering of the unwanted seismic events into the data application.
- Correlating the production data and interpretation of the seismic data.
- Reporting and interpretation of the results were done by the candidate and the supervisor; Prof Ray Durrheim assisted by giving pointers regarding scientific writing.
- Prof Ray Durrheim also assisted in the journal selection process, procedures for uploading the manuscript and gave insight on the journal review process. He also improved the quality of the paper with his suggestions and comments.

8.3 Summary of the publication

The study area is at a South African gold mine known as Thuthukani mine, which is part of the Kloof Operation. The mine is located 70 km west of Johannesburg, which is owned and operated by Sibanye Stillwater. Gold-bearing quartz pebble conglomerate ore bodies (locally known as 'reefs') are mined. The primary ore body is the Ventersdorp Contact Reef (VCR) and secondary ore bodies include the Middelvlei

Reef (MR), Kloof Reef (KR) and the Libanon Reef (LR). The VCR has been extensively mined from Thuthukani shaft at depths between 2000 m and 3500 m over the last forty years. The No. 1 shaft at Thuthukani extends to a depth of 2023 m below surface, while the 1 sub-vertical (SV) and 2 SV shafts extend to depths of 2773 and 3306 m, respectively. Thuthukani shaft is in the final stage of mining, it is extracting the shaft pillar. The extraction of ore in the shaft pillar started in January 2007 to recent. Three major geological structures traverse the shaft pillar (the Venterspost Dyke, Tear Fault and Shaft Fault). Dyke intrusions are associated with both the Tear and the Shaft faults. A 'bottle-shaped' shaft protection pillar was designed to protect the four-shaft system (1, 1SV, 1SV Vent and 2SV) during the initial mining around these 4 shafts. It measures approximately 680 m on strike and 970 m on the dip. All seismic data recorded since the extraction of the Thuthukani shaft pillar commenced in January 2007 are analysed. We compare seismicity in two five-year periods (1 January 2007 to 30 November 2012 and 1 December 2012 to 31 July 2017) and find that there was an increase in the rate of seismicity and the maximum magnitude (M_{max}) from 2.7 to 3.2. Strategies to mitigate the seismic hazard during shaft pillar extraction are discussed.

8.4 Comparison of Seismic Potency release at Kloof, Mponeng and TauTona gold mines

During the Thuthukani shaft pillar extraction, the seismic potency was compared within two different periods (period P1 (1 January 2007- 30 November 2012) to period P2 (1 December 2012- 31 July 2017). The production and potency during these periods are summarised in Table 4 of the manuscript. The total amounts, normalised annual and monthly amounts are presented. In an industry review of mining shaft pillars, it was found that the mining rate within the shaft pillar boundaries should be limited to 2000 m^2/month (Dukes, 2007), which Thuthukani adhered to after few consultation reports with the mining industry experts.

It was interesting to note that the average production was slightly lower in P2 (1 880.2 m^2) than in P1 (~1 970.1 m^2), but the ratio of seismic potency was three times greater. The final period (P2) stands out as being of significantly higher seismic hazard. The reasons for the increases in the seismic hazard are still not fully understood and is the subject of further investigation (e.g. 3D stress modelling). Rakumakoe (2019) investigated the improvements of lead-lags and the effects it has on Potency to production ratio in some stopes in Mponeng Gold mine. The results indicated that good discipline in mining crew correcting the lead-lags decreases the seismic hazard (low ratio of potency to production) within the mine area of interest. The comparison and control of lead-lags was done over the 4 years data sample of which 2018 indicated improvement in lowering the ratio by decreasing the seismic hazard. In Figure 7.1, the ratio of potency to the production graph for 2018 does not fluctuate much compared to the other three graphs. The 2018 potency to production ratio graph is constrained between 0.02 and 0.04, except for May and December exceptional months, when large seismic events ($M_L \geq 3.0$) were recorded along with a geological feature in the back areas.

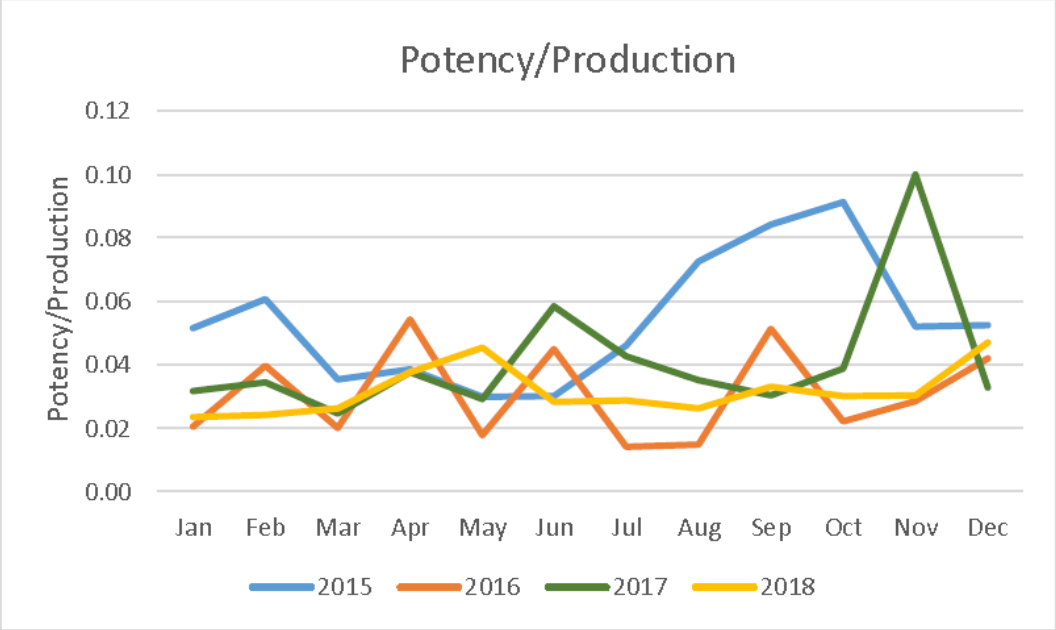

Figure 8.1: *The ratio of potency to production on mining stopes in Mponeng Gold Mine (Rakumakoe, 2019).*

In 2012 a seismic assessment was done in an attempt to determine the effect that mining rate has on seismicity that occurs as a result of mining the Tautona Shaft Pillar. The assessment was analysed by comparing the cumulative production to cumulative seismic displacement for a period of 14 months starting from March 2006 to May 2007 (Figure 8.2). Murphy (2012) highlighted that the production curve was indicating higher mining rate (steeper) and the seismic response was significantly higher in terms of the occurred seismicity and their magnitudes (Figure 8.2). When TauTona shaft pillar production rate exceeds 3500–4000 m^2 per quarter (1333 m^2 per month), the shaft pillar seismic response increased. The seismic analysis at TauTona Mine indicated that the shaft pillar seismic response was higher than in any of the normal longwalls. The high the extraction rate, specifically in the shaft pillars, has either an exponential effect on the seismic response within the shaft pillar boundaries or seismic lockup may occur (Murphy, 2012). Consequently,Thuthukani shaft pillar lowered the monthly production rate though the seismic hazard tripled. In the case of the Thuthukani shaft, production might not be the only driving factor that controlled the increase in seismic hazard within the shaft pillar. As Rakumakoe (2019) indicated, lead-lags might control the ratio of seismic potency to production.

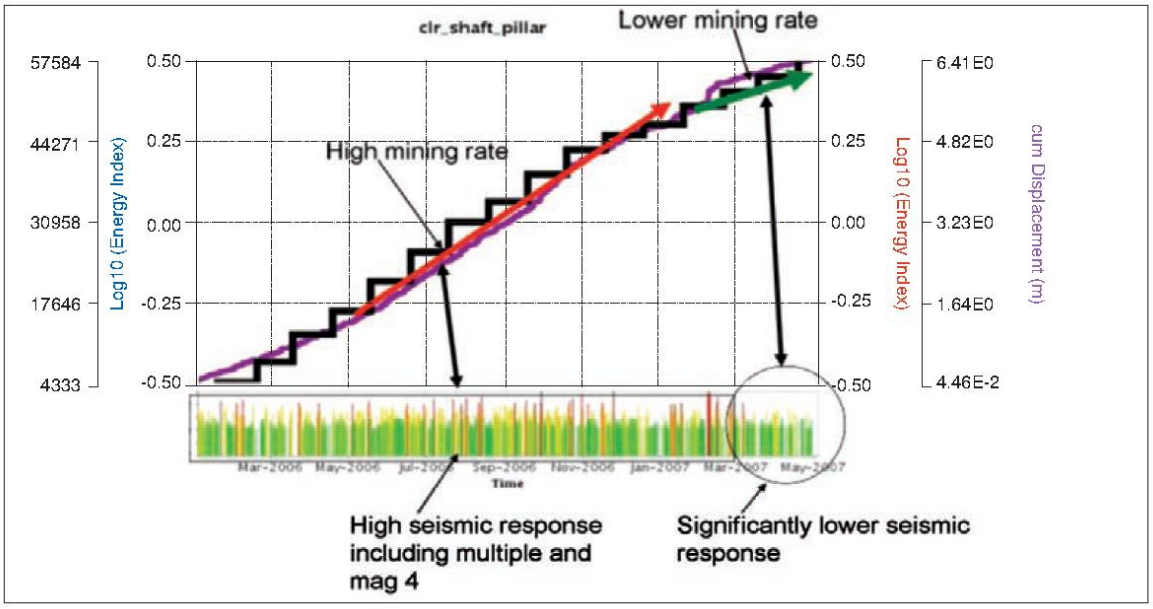

Figure 8.2:*Tautona shaft pillar seismic response compared to the mining rate (Murphy, 2012).*

8.5 Manuscript 2

The Manuscript has been modified and presented according to journal article standards.

THE SEISMIC RESPONSE TO MINING DURING THE EXTRACTION OF THE THUTHUKANI SHAFT PILLAR, KLOOF OPERATIONS, SOUTH AFRICA

R.T. Masethe[1, 2, 3], R. J. Durrheim[1] and M. S. D. Manzi[1]

[1]School of Geosciences, University of the Witwatersrand, Johannesburg, South Africa.
[2]School of Mining Engineering, University of the Witwatersrand, Johannesburg, South Africa.
[3]Seismology Department, Sibanye-Stillwater Limited, Westonaria, South Africa

Abstract

All seismic data recorded since the extraction of the Thuthukani shaft pillar commenced in January 2007, has been analysed. Seismicity was compared in two five-year periods (1 January 2007 to 30 November 2012 and 1 December 2012 to 31 July 2017). It was found that there was an increase in the rate of seismicity and the maximum magnitude (M_{max}) from 2.7 to 3. 2. Strategies to mitigate the seismic risk during shaft extraction are discussed in this paper.

Introduction

The study area is at Thuthukani mine, part of the Kloof Operation, which is owned and operated by Sibanye Stillwater (See Figure 1). Gold-bearing quartz pebble conglomerate ore bodies (locally known as reefs) are mined. The primary ore body is the Ventersdorp Contact Reef (VCR); secondary ore bodies include the Middelvlei Reef (MR), Kloof Reef (KR) and the Libanon Reef (LR). The VCR has been extensively mined from Thuthukani shaft at depths between 2000 m and 3500 m during the last forty years. The No. 1 shaft at Thuthukani extends to a depth of 2023 m below surface, while the 1 sub-vertical (SV) and 2 SV shafts extend to depths of 2773 and 3306 m, respectively.

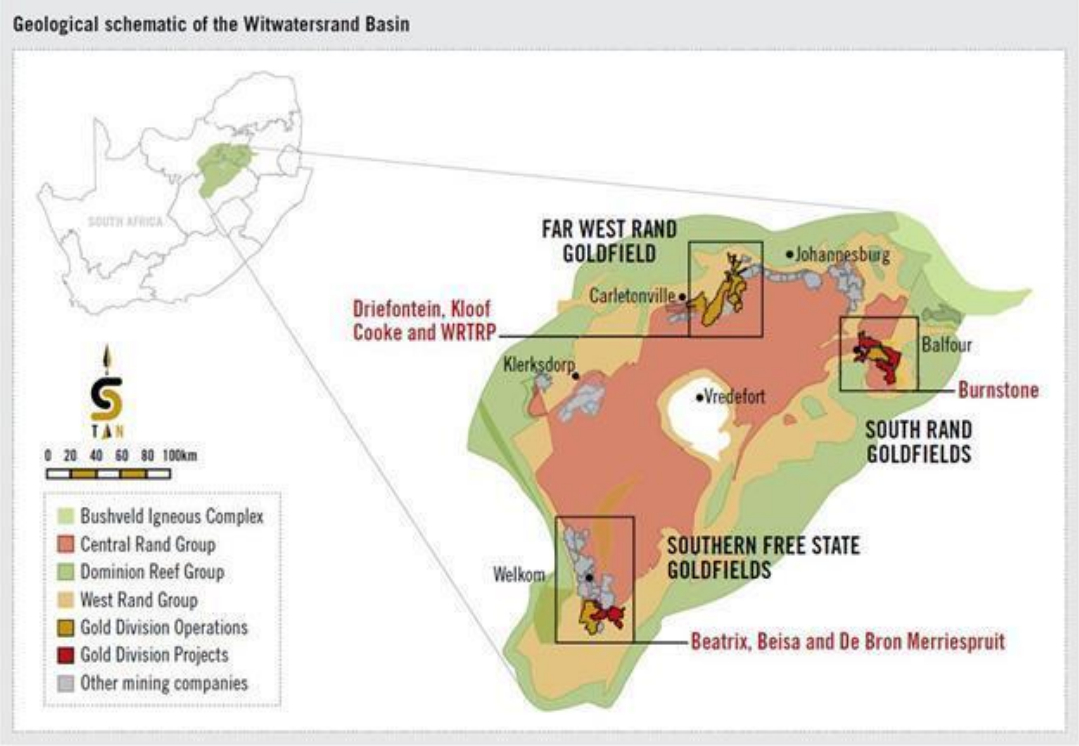

Figure 1: *Geological map of the Witwatersrand Basin indicating the location of Kloof Operations (after Dankert and Hein (2010))*

Shaft pillar extraction strategy

The originally proposed shaft pillar extraction layout was a mini-longwall with overhand mining faces. The layout was designed to have two 30 m dip pillars on each side of the shafts and four 40 m strike stability pillars (Maritz *et al.,* 2007). Pillars were placed so that the span on both the strike and the dip pillars would not exceed 200 m. A 20 m bracket pillar was proposed to protect the major geological structure. In 2008, an analysis from the borehole data was obtained and indicated a weaker rock mass than originally anticipated, suggesting that both sub-vertical shafts would fail (Naicker, 2013). The re-assessment of the Thuthukani shaft pillar extraction project resulted in the proposed extraction sequence shown in Figure 2.

Extraction of ore in the shaft pillar started in January 2007 (See Figure 2). Three major geological structures traverse the shaft pillar: the Venterspost Dyke, the Tear Fault and Shaft Fault. Dyke intrusions are associated with both the Tear and the Shaft faults. A bottle-shaped shaft protection pillar was designed to protect the four-shaft system (1, 1SV, 1SV Vent and 2SV) during the initial mining around these 4 shafts. It measures approximately 680 m on strike and 970 m on the dip. The final block of unmined VCR ground (the final pillar) to remain after the pillar extraction is coloured in pink in Figure 2. Four 30-m-wide dip pillars, together with a block of ground left unmined to clamp the major geological structures, provide regional stability for the mining in the shaft pillar. The sequential grid layout, mining in the strike direction with an

overhand configuration, was designed to keep the average Energy release rate below 30 MJ/m^2, Jager and Ryder (1999). The characteristics and the geology of the Thuthukani shaft are summarised in Table1.

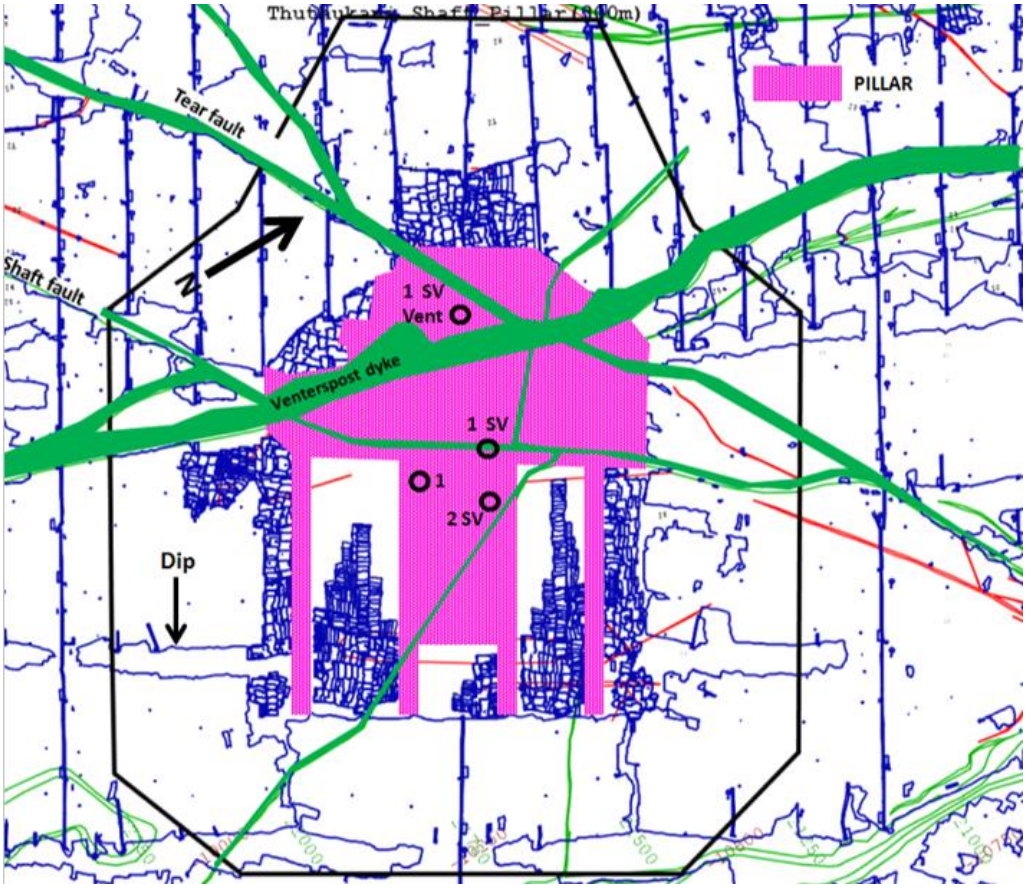

Figure 2: *Plan view of the Thuthukani shaft pillar showing the Permanent Pillar, four dip pillars, and the Venterspost Dyke and the Tear and Shaft faults (both containing dyke material). 1 - Main shaft, 1 SV - 1 Sub- vertical shaft, 1 SV Vent - 1 Sub- vertical ventilation shaft, 2 SV - 2 sub-vertical shaft. A black line defines the polygon of analysis*

Table 1: Characteristics of the Thuthukani shaft pillar (extraction area)

Reef	Ventersdorp Contact Reef (VCR)
Stoping width	1.2m
Foot wall	The quartzite of the Mondeor formation
Hanging wall	Basalt of the Alberton or Westonaria Formations
Area of pillar (m^2)	659 600
Strike	45^0
Dip	~32^0
Max strike span of pillar (m)	680
Max dip span of pillar (m)	970
Depth below the surface (m)	-2453
Mining Method	Sequential grid with dip pillar
Regional support	Dip pillars (30m in width)
Inner pillar (m^2)	No inner pillar, but large unmined block

Geology and geotechnical properties

The geology of the Witwatersrand Supergroup has been described by many authors (e.g. Dankert and Hein (2010); Manzi *et al.* (2013)). A geological cross-section is shown in Figure 3. The VCR is the primary ore body in the study area. It is a member of the Venterspost Formation, which is the basal unit of the Ventersdorp Supergroup. The hanging wall of the VCR consists of basalt. Two types of basalt are found on Kloof Operations: strong and competent basalts of the Alberton Formation, and weaker komatiitic basalts of the Westonaria Formation (WAF). Most of the Thuthukani shaft pillar is in the WAF area; it has a high density of cooling fractures and is very blocky, hence poor hanging wall conditions were expected. The immediate footwall rocks are mostly competent Elsburg quartzites of the Mondeor Formation, Witwatersrand Supergroup. The basalts and quartzites have very different physical properties. The most important property for rock engineering design is the uniaxial compressive strength (UCS). Rock strength tests on 28 samples from Kloof Operations showed that the UCS can vary significantly Chen (2007). The results of the rock strength tests are presented in Table 2.

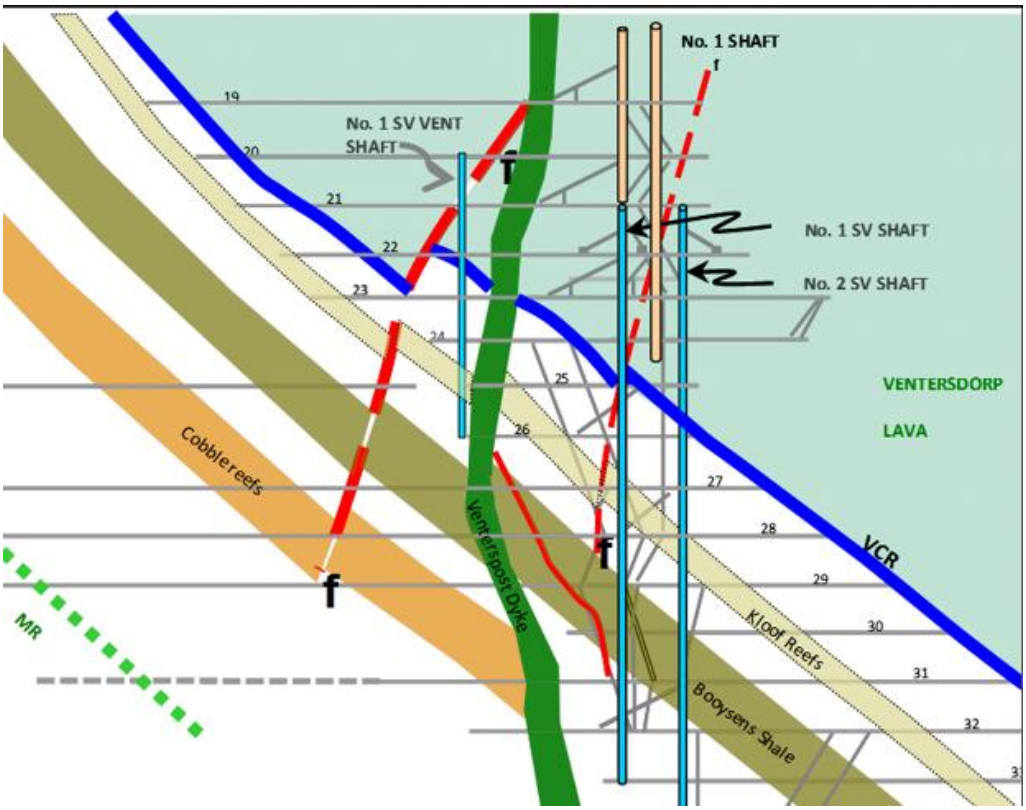

Figure 3: *Schematic section of the Thuthukani shaft pillar highlighting geological structures that might influence mining (after Naicker (2013). VCR: Venterspost Contact Reef, MR: Middelvlei Reef*

Table 2: Rock strength in UCS for Kloof Operations. (Van der Heever and Ryder, 2007)

Formation	Rock Type	Min UCS (MPa)	Mean UCS (MPa)	Max UCS (MPa)
Alberton	Basalt	220	260	300
Westonaria	Komatiitic basalt	56	88	120
Mondeor	Quartzite	220	260	300

Mine design and seismic monitoring strategies

Mine design strategies

As mining progresses, shaft pillars become more and more susceptible to stress-related problems. The pillar's stability is mostly affected by geological structures, depth, the host rock, mining methods, mining geometry and the extraction volumes. Rules of thumb were developed for the current shaft-pillar extraction based on seismic and instrumentation monitoring, stress modelling, underground observation and experience. Naicker (2013) provides a summary of the mining layout and the seismic monitoring measures that have been adopted by Kloof Operations in mining the shaft pillar. These include:

- Design of mining layouts to keep average energy release rate (ERR) values below 30 MJ/m$^{2;}$
- Design of bracket pillars using numerical modelling to reduce excess shear stress (ESS) on the existing geological structures;

- Managing and control of the face shape index (FSI);
- Application of the 70 m rock engineering rule when panels are mined towards each other. For example, when two panels mining towards each other are separated by less than 70 m, one panel should be stopped;
- Limiting the mining rate and avoiding the concentration of mining;
- Introduction of the centralised blasting and the removal of the night shift;
- Preconditioning of all mining panels to reduce the incidence of face bursts; and
- Seismic monitoring and a comprehensive monitoring program using various types of instrumentation.

Seismic monitoring system

The current Institute of Mine Seismology (IMS) seismic network on the Kloof Operations consists of thirty-seven 4.5 Hz three-component geophones with a sample rate at 6 kHz. The mine-wide network covers approximately 202 km^2 of the mine's lease area (See Figure 4 and Figure 5). To optimise the accuracy of hypocentre locations, some geophones were located at sites that are some distance away from the reef planes, as allowed by the mine's shaft and development infrastructure. The Thuthukani shaft pillar covers an area of 0.66 km^2, with eleven geophones in close proximity (See Figure 4). Geophone sites were selected to provide the optimum sensitivity and location accuracy (within metres) in the area of interest. However, the minimum recorded magnitude of events is dependent on the maintenance of the underground sites.

Modelled system sensitivity

The sensitivity of the system in each area is proportional to the number and proximity of installed geophones. The idealised system sensitivity for the Thuthukani shaft pillar is depicted in Figure 4. A maximum sensitivity (magnitude -0.9) is achievable in this block of ground, which according to Jager and Ryder (1999), is adequate for location, prevention and control requirements.

Modelled system location accuracy

The current system location accuracy on the XY plane is shown in Figure 5. Should an additional geophone be installed on 18 levels (to improve accuracy in the Z-direction), the location accuracy would be adequate for location, prevention and control requirements.

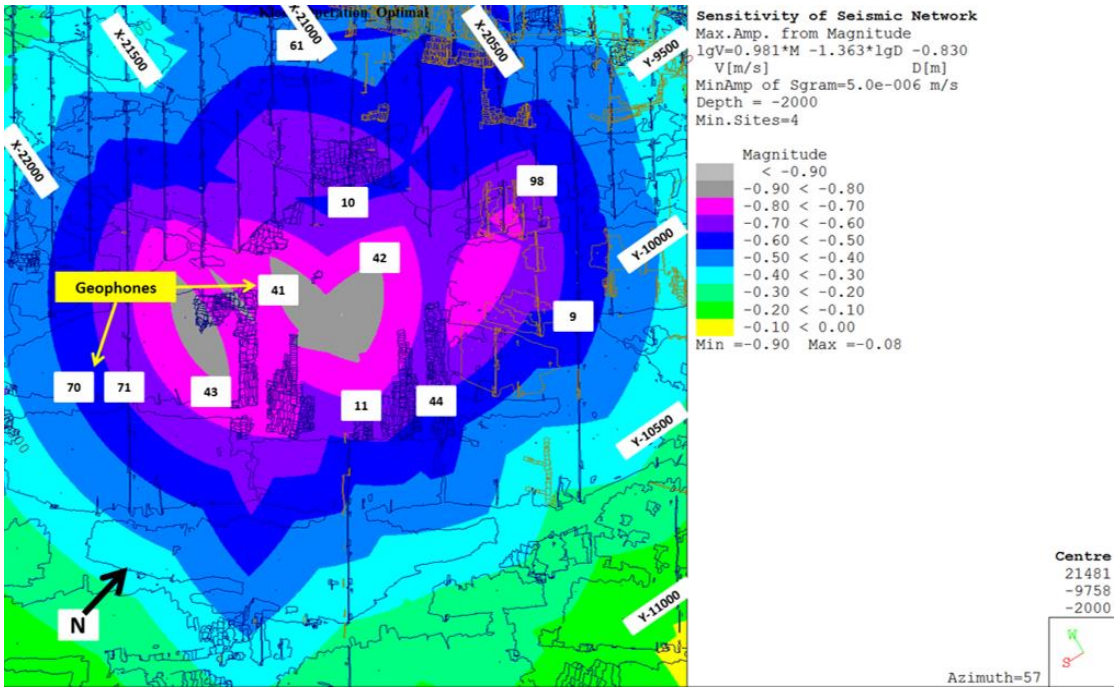

Figure 4: *Seismic system sensitivity (if all geophones are operational), which is deemed adequate for short-term seismic hazard identification and long-term strategic planning. Geophones within a shaft pillar are labelled and named. Sensitivity increases towards the centre of the Thuthukani shaft pillar*.

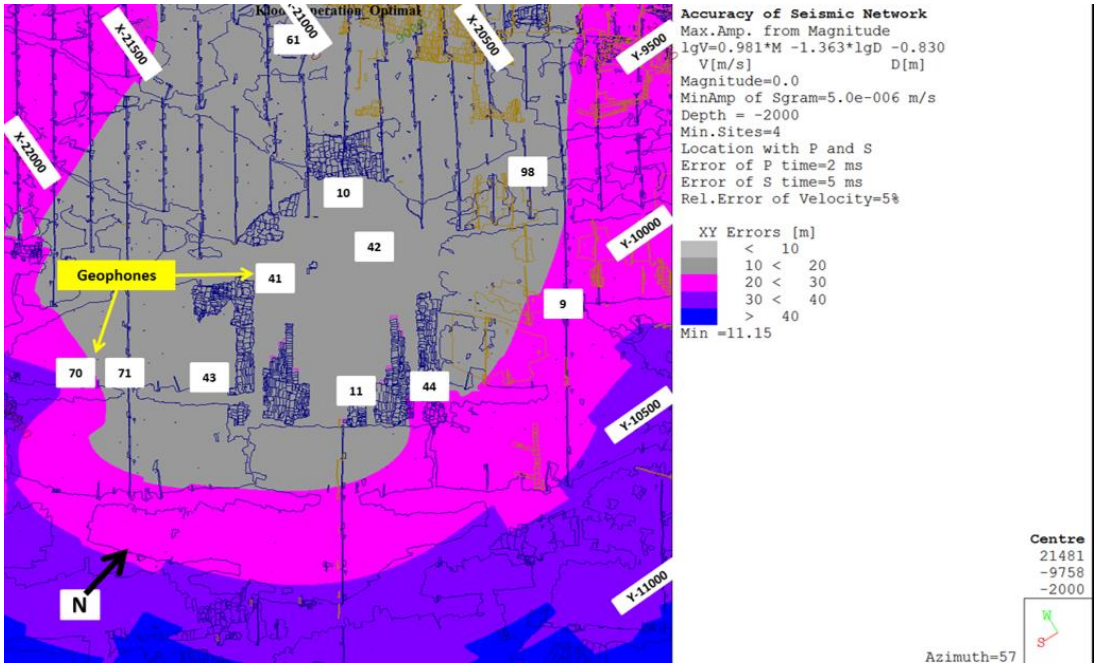

Figure 5*: Seismic system location accuracy (if all geophones are operational), which is deemed adequate for short-term seismic hazard identification and long-term strategic planning. Geophones within a shaft pillar are labelled and named. Sensitivity increases towards the centre of the Thuthukani shaft pillar.*

Results

Seismicity data

The seismic energy release during shaft pillar extraction is governed by factors such as the depth, production volume, mining geometry and the geological structures. The Institute of Mining Seismology (IMS) seismic system recorded 2896 events with $M_L \geq 0.0$ within the Thuthukani shaft pillar section from 1 January 2007 to 31 July 2017. These are presented in both plan and section views in Figure 6; the colours representing the seismic activity in this plot are based on annual intervals as shown in the legend while the size is represented in terms of the apparent volume of each event. Seismic activity migrates in a North-West direction, in accordance with the general trend of the mining. It is evident that most of the seismic events locate close to the active working areas and the stope horizon. Most events occur just ahead of the mining faces. Several large events have been observed in the abutment of the shaft pillar and far from the mining horizon. For example, an $M_L 3$ event in the hanging wall was located 170 m away from the Venterspost dyke (See Figure 6a).

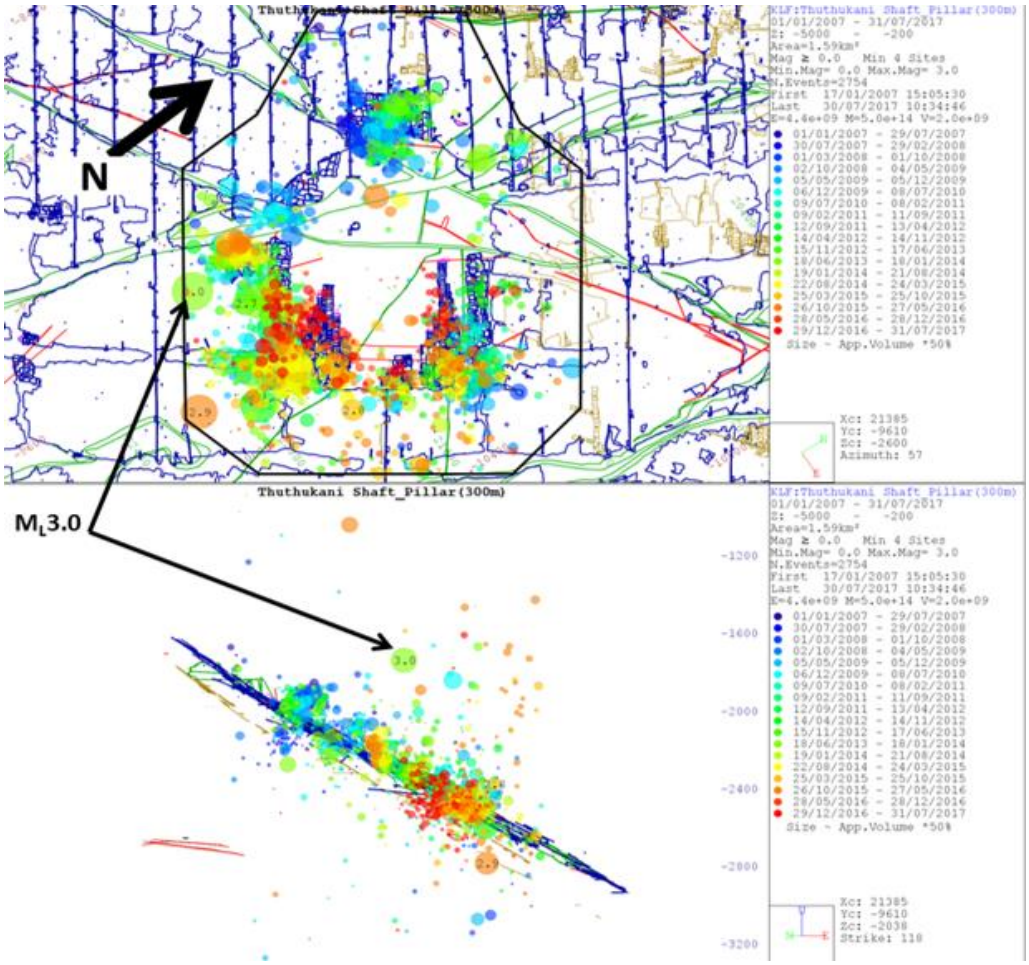

Figure 6*: (a) Plan and (b) Dip section view showing the location of seismic events with $M_L \geq 0$ between 1 January 2007 to 31 July 2017 where production was extracted.*

Table 3 summarises the range of seismic events observed and recorded within the shaft pillar for the duration of the case study. Most seismic events are located on the reef. The depth locations of these seismic events are probably inaccurate, which is common in tabular mines since the seismic networks tend to be planar, rather than fully three dimensional. For this reason, the selection of seismic events for these analyses was carried out in plan-view and the elevation was ignored. Two-thirds of the larger magnitude events ($M_L \geq 2$) locate on the edge of the shaft pillar due to the highly stressed abutments. Only one $M_L \geq 2$ seismic event was located within the shaft pillar and this occurred near the intersection of geological structures.

Table 3: Seismic events categorised according to their magnitudes and cumulative energy, moment and apparent volume in various magnitude bins

Magnitude range	Number of events	Σ Energy (MJ)	Σ Moment (10^{12}Nm)	Σ App. Volume ($10^6 m^3$)
0.0 - 1.0	2489	678.68	92.30	855.06
1.0 - 2.0	372	1 336.18	192.09	817.41
2.0 - 3.0	34	2 305.70	205.22	398.20
> 3.0	1	322.00	38.90	71.20
Total	**2 896**	**4 642.56**	**528.50**	**2 141.87**

Shaft pillar production

Production data for the Thuthukani shaft pillar from 1 January 2007 to 31 July 2017 (The selected period of analysis) is shown in Figure 7. Mining in the area has already contributed more than 204 000 m^2 of ore production with a monthly average of 1 608 m^2. It should be noted that while the monthly production was variable (e.g. production declined steeply from July 2011 to Nov 2012), the cumulative production was roughly linear (See Figure 8). Both the production data and the associated seismicity were analysed for the period to determine any changes in seismic response to production (See Figure 7). Production is measured in square meters (m^2), but the volume (m^3) of the extracted ore can easily be estimated using an average stoping height of 1.2 m. Seismic activity is measured in the number of $M_L \geq 0$ events per month. A 3-sample moving average was used to smooth the graphs and to highlight the trends in the data.

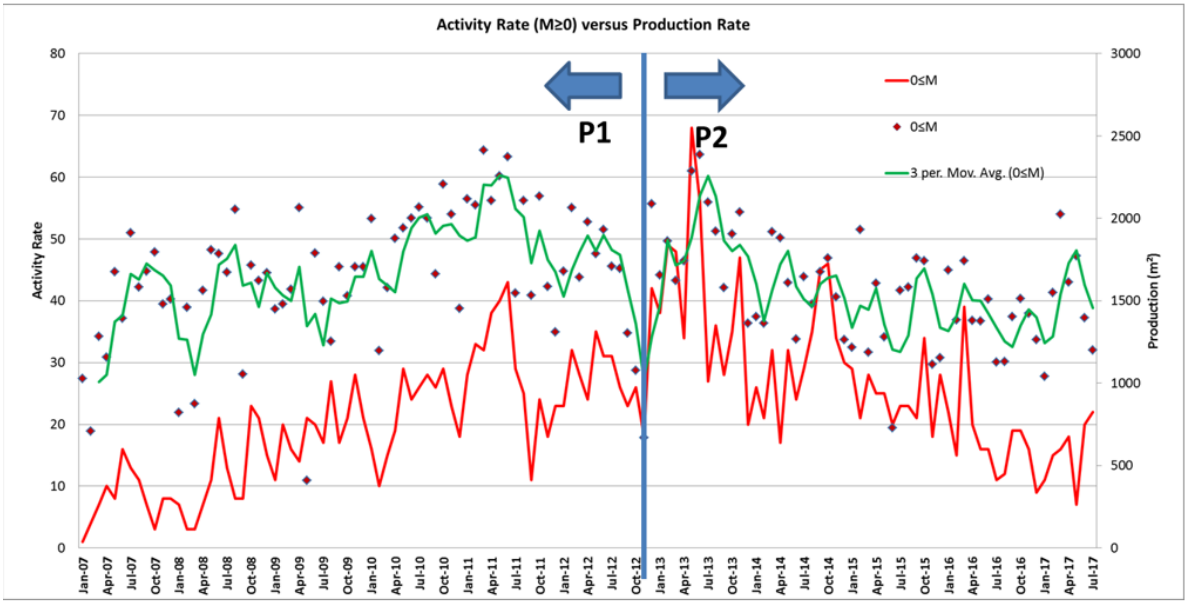

Figure 7*: - Monthly production volume and seismic activity from 1 January 2007 to 31 July 2017. Greenline: smoothed production in m2; Diamonds: Actual production; Redline: seismic activity in a number of ML≥0 events per month*

Seismic response analysis

The seismic response to production is assessed to distinguish changes in the seismic response in the area of interest. Seismic potency (P) is the parameter that is very useful for this purpose. The seismic potency per unit area mined was calculated as defined by Mendecki (2016):

$$P = \frac{M_0}{G} = Ad \qquad [1]$$

where M_0= seismic moment, G = modulus of rigidity (30 GPa), A = area of slip (m^2) and d = slip displacement (m).

Seismic potency (m^3) could be considered as the volume of shear displacement associated with a seismic event. The cumulative seismic potency and production are plotted against time for the entire shaft pillar area (See Figure 8). The cumulative production is fairly linear, while the seismic potency is more variable, showing some significant changes, notably in November 2012 and January 2016. The correlation coefficient (R^2 = 0.481) indicates a moderate positive relationship between seismic activity and production throughout the entire period, indicating that production plays a major role in controlling seismicity.

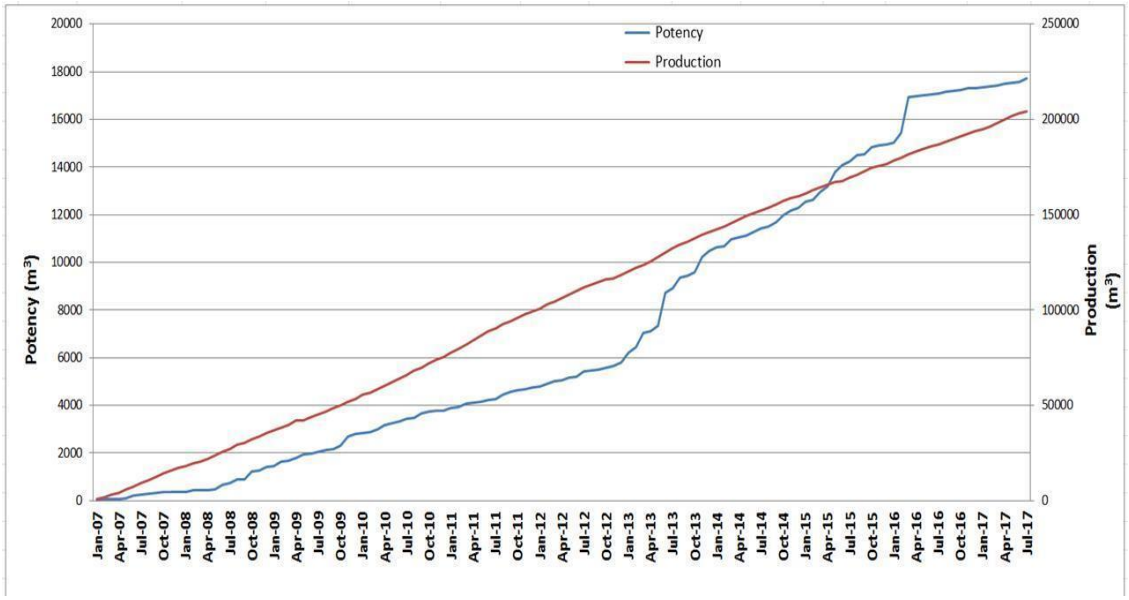

Figure 8: *Seismic Potency and Cumulative Production from 1 January 2007 to 31 July 2017*

Two periods with differing seismic responses were identified and compared, namely Period 1 (1 January 2007 to 30 November 2012) and Period 2 (1 December 2012 to 31 Jul 2017; see Figure 7, Figure 8 and Figure 9). The slope of the line in Figure 9 indicates the seismic response to production during the specific period: the steeper the slope, the more hazardous the seismic response was deemed to be. Period 2 (Blue line in Figure 9) has a steeper slope (0.1435) than Period 1 (0.052, brown line in Figure 9.

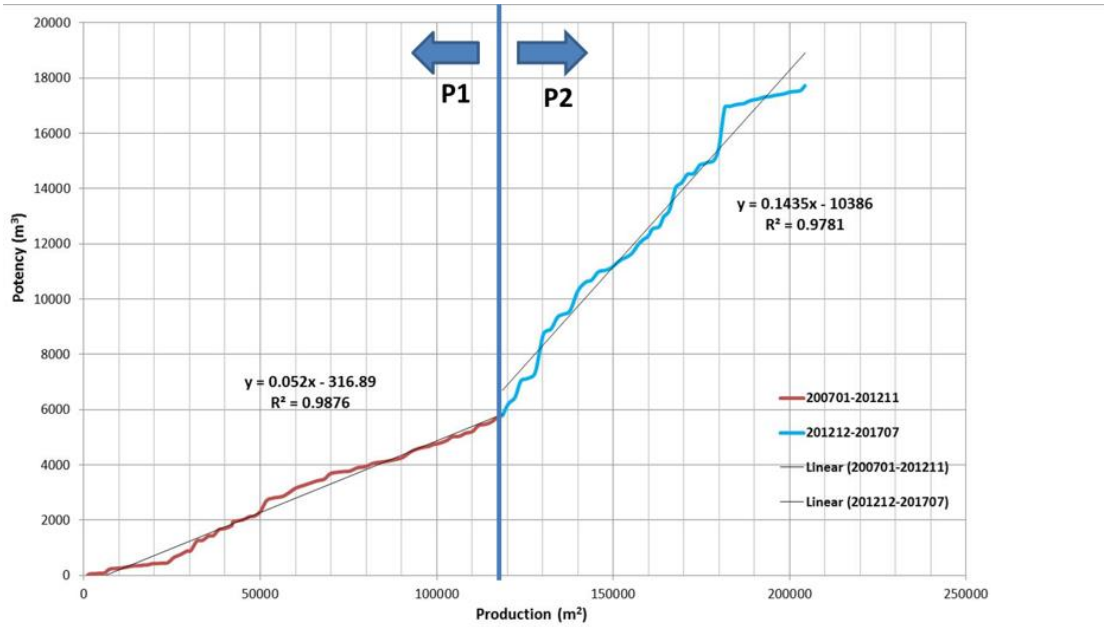

Figure 9*: Seismic Potency versus production indicating the change in the seismic response of the rock mass to mining from period P1 (1 January 2007- 30 November 2012) to period P2 (1 December 2012- 31 July 2017)*

The production (V_m) and seismic potency (P) during Period 1 (P1) and Period 2 (P2) are summarised in Table 4. The seismic hazard is estimated by finding the ratio between V_m and P. It is interesting to note that the average monthly production in P1 is higher than in P2, and the ratio of potency to production is greater in P2. P2 stands out as being of higher seismic hazard when compared to P1. The high level of seismicity within the shaft pillar in P2 is alarming, and the reason for the increase is still not fully understood and is the subject of further investigation.

Table 4: Seismic Potency versus Production

	P1 (1/1/2007 - 30/11/2012 = 71 months)		**P2 (1/12/2012-31/7/2017 = 56 months)**	
	Production V_m (m^3)	**Potency P (m^3)**	**Production V_m (m^3)**	**Potency P (m^3)**
Monthly	1 970.1	79.7	1 880.2	215.5
Annual	23 641.8	956.4	22 562.0	2 586.1
Total	139 880.4	5 658.7	105 289.2	12 068.3
P:V_m	**0.040**		**0.115**	

During the first period (P1), there was a large degree of scattering in the locations of the seismic events, while during the second period (P2) the seismicity was concentrated in the southern portion of the shaft pillar where the mining was taking place (See Figure 9). In both periods, the largest seismic events were located on the geological structures and abutments of the mining areas (Figure 6). The main features of these two mining periods are summarised below:

Period 1: This period spans 2130 days and contains 2 $M_L \geq 2.5$ seismic events, 11 $M_L \geq 2.0$ events, 60 $M_L \geq 1.5$ events, 177 $M_L \geq 1.0$ events, 496 $M_L \geq 0.5$, 1317 $M_L \geq 0.0$ events and 59,778 $M \geq -3.0$ events. The volume-mined is 139.9 x $10^3 m^3$ and the cumulative seismic potency is 5.7 x 10^3 m^3; the ratio of volume-mined to seismic potency is thus $\sum P/V_m = 0.040$. The largest seismic events occurred on 16 June 2008 and 04 November 2009, both with $M_L = 2.5$.

Period 2: This period spans 1680 days and contains 4 $M_L \geq 2.5$ seismic events, 24 $M_L \geq 2.0$ events, 81 $M_L \geq 1.5$ events, 226 $M_L \geq 1.0$ events, 627 $M_L \geq 0.5$, 1531 $M_L \geq 0.0$ events and 49,111 $M \geq -3.0$ events. The volume-mined is 105.3 x 10^3 m^3 and the cumulative seismic potency is 12.1 x 10^3 m^3. The ratio of cumulative seismic potency to volume-mined for Period 2 is $\sum P/V_m = 0.115$, almost three times the ratio in Period 1, indicating an increased seismic hazard in the shaft pillar area. The largest seismic event, $M_L = 3.0$, occurred on 26 June 2013 close to the abutment of the shaft pillar.

Seismic hazard

The data indicate that events of $M_L \geq 0.6$ adversely affected panels within the area of interest. During the first period (P1) 443 seismic events of $M_L \geq 0.6$ were recorded; 22 caused damage. The second period P2 recorded 519 events of $M \geq_L 0.6$; 18 caused damage.

In mine seismology, seismic hazard is defined as the probability of occurrence within time ΔT of a potentially damaging event (e.g. $M_L \geq 0.0$). Hazard assessments in the mining areas are of great assistance in evaluating both the frequency and intensity of seismic events. This allows the adoption and implementation of measures to be taken in reducing both the risks and associated damages to seismicity. The probabilities of occurrence in the shaft pillar are estimated by assuming a stationary Poisson process (Mendecki, 2016):

$$Pr\ Pr\ (\geq P, \Delta T)\ = 1 - exp\left[-\frac{\Delta T}{T} N(\geq P)\right] \qquad [2]$$

where T is the observed time and $N(\geq P)$ is the number of seismic events during the respective period. Table 5 summarises the intermediate- and long-term probabilities of occurrence in the time domain comparing both Period 1 and Period 2, respectively. The probability of occurrence of a seismic event of any given magnitude obviously increases as the period increases.

Table 5: Intermediate-term probabilities of occurrence for Period 1 and Period 2

Probabilities (Period 1/Period 2)					
	M_L= 0.5	**M_L= 1.0**	**M_L= 1.5**	**M_L= 2.0**	**M_L= 2.5**
ΔT = 30 days	0.997/1.000	0.871/0.967	0.495/0.712	0.182/0.354	0.031/0.126
ΔT = 90 days	1.000/1.000	0.998/1.000	0.871/0.976	0.453/0.730	0.009/0.333
ΔT = 180 days	1.000/1.000	1.000/1.000	0.983/0.999	0.701/0.927	0.017/0.555
ΔT= 365 days	1.000/1.000	1.000/1.000	1.000/1.000	0.910/0.995	0.031/0.802
ΔT = 2 years	1.000/1.000	1.000/1.000	1.000/1.000	0.992/1.000	0.053/0.961
ΔT = 5 years	1.000/1.000	1.000/1.000	1.000/1.000	1.000/1.000	0.849/1.000

In Period 1, the probability that a seismic event with $M_L \geq 1.0$ occurs somewhere in the shaft pillar during one month is $Pr\ Pr\ [\geq P, \Delta T]\ = 0.871$; while the corresponding probability for Period 2 is even higher, 0.967. The probability that a seismic event of $M_L \geq 2.0$ occurs within six-months in Period 1 is 0.701; while it is 0.927 in Period 2. The parameters used to reflect the seismic hazard for both Period 1 and Period 2 are summarised in Table 6. Period 2 indicates a slightly higher probability of $M_L \geq 1$ events (hence a shorter recurrence time) with a seismic event of $M_L \geq 1$ expected to occur in the Thuthukani shaft pillar every 9 days, on average. The maximum credible magnitude (M_{max}) is greater in P2 than P1. This indicates an increase in seismic hazard.

Table 6: Comparison of seismic hazard for both Period 1 and Period 2

Seismic Parameter	Period 1 (P1)	Period 2 (P2)
M_{max} (date of occurrence)	2.5 (16/7/2008; 4/11/2009)	3.0 (26/6/2013)
M_{max} expected	2.70	3.20
b-value	1.05	0.92
Recurrence time M ≥ 1 (months)	0.4	0.3
Probability M ≥ 1 (per month)	91.1%	97.8%
No. of events M ≥ 1	178	221
Events occurring off-shift	36%	61%

Hazard is the likelihood of a potentially damaging event occurring, while risk takes the consequences of a damaging event into account. This is governed by the fragility of geological structures as well as the exposure of workers and other assets. The majority of M_L≥0.0 events occur on-shift (Blue lines and green bars in Figure 10) in both periods; the second period indicates a 25% improvement of events occurring off-shift (red bar graph), which limits the exposure of mine workers to injury (See Figure 10).

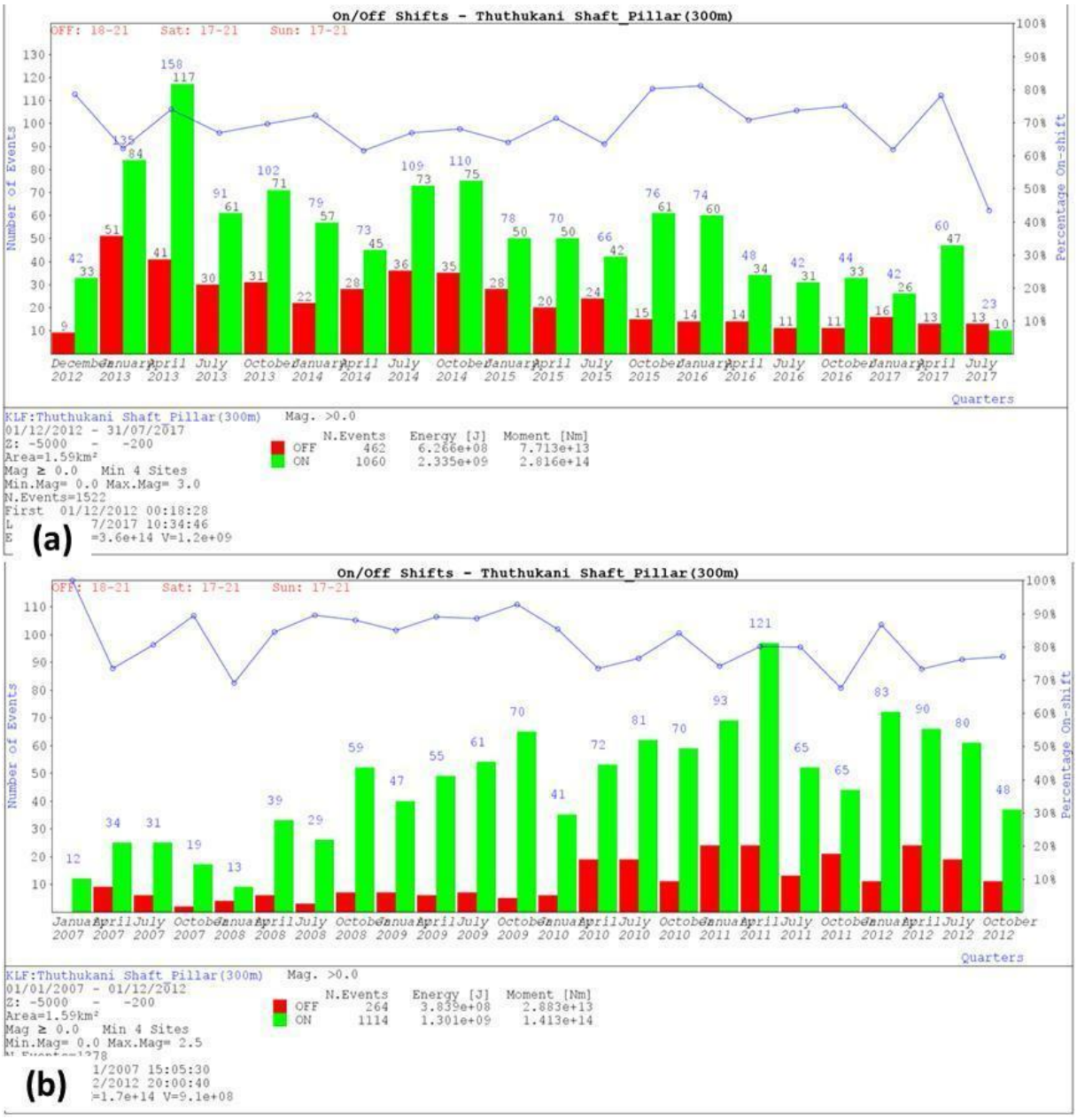

Figure 10: *On-off shift recorded seismic events for (a) Period 1 (a) and (b) Period 2*

Changing seismic response to mining

The seismic response to the mining in any ore body may change as a result of changes in extraction sequences and methods. The changes in the seismic response at the Thuthukani pillar extraction, as manifested by the increase in several larger seismic events, have been evident since October 2010.

Figure 11 shows the magnitude-time history graph for events M_L = 0.0 and incorporates the cumulative number of large seismic events between January 2007 and July 2017. The magnitude-time history analysis (i.e., how magnitude varies with time) of clusters of seismic events in space provides valuable insight into

the seismic hazard. The magnitude-time graph summarises several items of valuable information. It shows the largest event to occur within a given period, which is an indicator of relative seismic hazard. It also graphs the cumulative number of seismic events, revealing changes in the rate of occurrence. A significant change in the number of large events M≥1.5 is noticeable from October 2010 to April 2015 followed by a decrease in their occurrence (See Figure 11).

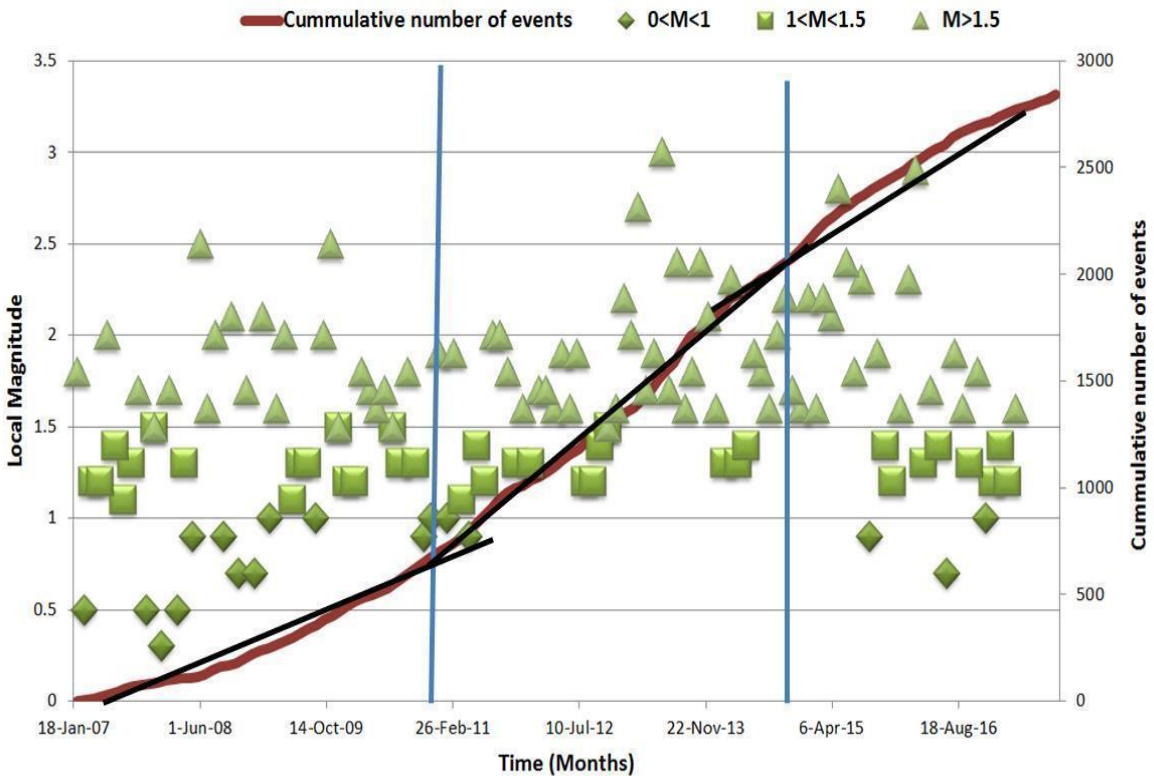

Figure 11: *Event time history and the cumulative number of events M_L≥0.0 for a period 1 January 2007 to 31 July 2017. Green symbols indicate the maximum events magnitude in a given month*

When the extraction started at the top of the shaft pillar the rock-mass responded with large seismic events up to M_L=3. As mining progressed, the number of events with magnitude greater than M_L=2 increased until early 2016. This was followed by an apparent decrease. The reason for this response is not currently known and is the subject of further investigations.

Discussion

During a decade of seismic monitoring, large amounts of information have been recorded within the shaft pillar. The transition from a seismically-quiet shaft pillar to one exhibiting moderate-to-high levels of seismicity has occurred as mining progressed within the pillar. Analysis of the time history graph shows that seismic events are concentrated in time, driven by the concentration of mining activities over a certain

period. The combined effects of mining configuration (such as type of mining, lead-lags), complex geology, rock mass properties, active geological structures, the concentration of mining, the volume of mining, numbers of mining crews and the increase in depth, all lead to changes in the rock mass response. Due to the high seismic activity within the shaft pillar, the volume of mining has been reduced from 1650 m^2 and capped at 1200 m^2 per month. This could be reduced even further, depending on the seismic response.

Analysis of the seismic response revealed two stages, P1 (1 January 2007 to 30 November 2012) and P2 (1 December 2012 to 31 July 2017). P2 seems to be a more hazardous period, as compared to P1. A significant increase in the ratio of seismic potency to production is observed in P2. Cumulative frequency magnitude and cumulative frequency potency distributions were determined for both periods. P2 highlighted the severity of seismic response within the shaft pillar. An assessment of seismic hazard revealed that the probability of occurrences for different ranges magnitudes was higher in P2 compared to P1.

Magnitude time-history analyses can sometimes indicate different stages in the seismic response to mining, it indicates stages in the timeline that are characterised by several factors and is influenced by extraction volume, mining geometry, mining layout and mining practices used within the shaft pillar. These stages include:

1. **Quiet stage**: This is when relatively few seismic events occur, and minimal damage is done to the surrounding rock mass. The few seismic events are generally of low magnitude and triggered by blasting. The seismic hazard at this stage is low.
2. **Transition stage:** During this stage, seismicity increases with stoping activity and the magnitude of these seismic events is expected to increase. This is the stage where large seismic events become more common, resulting in an increase in the seismic hazard from low to medium hazard.
3. **Active stage:** The number of large events increases. Large seismic events are more likely to cause substantial damage to the mining infrastructures. The production in this stage may decrease owing to rockburst damage. The design and sequencing of layouts to manage the seismic hazard are crucial.

Seismicity data indicate that the Thuthukani shaft pillar is transforming from the quiet stage into the transition stage. The layout used to extract the remaining resources within the shaft pillar will be continuously reviewed in an attempted to mitigate or decrease seismic risk in identified hazardous area (hot spots). In-stope support practices are being revised in an attempt to ensure stoping and development ends are being supported adequately to ensure mining safety.

Conclusions

The seismic database collected since 2007 has proved invaluable in understanding the seismic response to mining within the main shaft pillar. The evaluation of this seismic response was carried out using seismic statistical hazard parameters and production. Production positively correlates (R=0.481) with seismicity of M≥0. Though the production rate was essentially constant, on average the seismic hazard within the shaft pillar kept on increasing as mining advanced. Risk mitigation measures were regularly reviewed by Kloof Operations.

The study shows that the seismic hazard has increased during the extraction of the Thuthukani shaft pillar. An assessment of seismic hazard using the intermediate-term probability of occurrence indicates an increase in the rate of occurrence of M≥1.0 seismic events in period 2 as compared to period 1. The M_{max} value of 3.2 is higher for Period 2 as compared to M_{max} of 2.7 during Period 1. In terms of seismic event statistics, 221 events of M ≥ 1 indicated more instability for Period 2. The reasons, however, leading to these changes during the extraction are not yet well known and will form part of further investigation.

Acknowledgements

The Management of Sibanye-Stillwater is gratefully acknowledged for permission to publish this paper. Ricardo Ferreira is thanked for providing valuable comments and suggestions.

References

Chen, J.F. (2007). *Results of rock property tests*. Rocklab Report 2007-OHS- Research-Works-03. *Rocklab*. Pretoria, South Africa.

Dankert, B. T., and Hein, K. A. A. (2010). Evaluating the structural character and tectonic history of the Witwatersrand Basin: Precambrian Research, 177, 1–22.

Jager, A.J. and Ryder, J.A. (1999). *Rock Engineering Practice for Tabular Hard Rock Mines*. The Safety in Mines Research Advisory Committee (SIMRAC), Johannesburg.

Manzi, M. S. D., Hein, K. A. A., King, N. and Durrheim, R. J. (2013). Neoarchaean tectonic history of the Witwatersrand Basin and Ventersdorp Supergroup: new constraints from high-resolution 3D seismic reflection data. *Tectonophysics,* 590, 94-105.

Maritz, A.J., Greyling, P.A., Geyser, D. (2007). Extraction of the shaft pillar on the VCR horizon Kloof Main Shaft Complex. *Challenges in Deep and High-Stress Mining*, Potvin, Y., Hadjigeorgiou, J. and Stacey, D. (eds), Australian Centre for Geomechanics, pp. 105-111.

Mendecki, A. J. (2016). Mine Seismology Reference Book: Seismic Hazard. Institute of Mine Seismology, ISBN 978-0-9942943-0-2, www.imseismology.org/msrb/, 1 edition. http://www.imseismology.org/msrb/.

Naicker, N. (2013). Application of seismic information in the mining design and monitoring of the KDC-East shaft Pillar. *Proceedings of the Eighth International Symposium on Rockbursts and Seismicity in Mines*, Saint Petersburg – Moscow, Russia, 1-7 September 2013, Malovichko, A. and Malovichko, D. (eds), Geophysical Survey of the Russian Academy of Sciences and Mining Institute of Ural Branch of Russian Academy of Sciences, pp. 395-412.

Van der Heever, P and Ryder, J.A. (2007). *Characterisation of the Westonaria Formation at Main Shaft, Kloof Gold Mine.* Consultancy Report. Groundwork. Johannesburg, South Africa.

Table 1A: Source parameters

Seismic event time is local time (subtract two hours to obtain UTC time). Event locations are listed in terms of the mine co-ordinate system specifying their latitude (X), longitude (Y), and depth (Z- meters below datum). The datum reference point on Kloof Gold Mine is about 250 m above the surface and 1800 m above sea level.

Seismic event number	Event Date & Time yyyymmddhhmmss	Location Error (m)	X (m)	Y (m)	Z(m)	Moment (Nm)	Local Magnitude (M_L)	Energy (Joules)	Corner Frequency (Hz)	Log Apparent Volume (M^3)
1	20170307 164126	18	22523.5	-10804.5	-3290.9	1.39E+13	2.6	1.52E+08	13	7.28
2	20170331 175326	29	22387.5	-10862.4	-3477.6	8.99E+11	1.6	4.23E+06	14	6.46
3	20170715 162357	25	21960.1	-10966.9	-3196.6	7.04E+12	2.6	2.58E+08	15	6.46
4	20170729 202255	30	21574.8	-9994.5	-2344.8	3.32E+12	2.2	5.40E+07	16	6.49
5	20170731 022236	28	22361.5	-10253.8	-3082.3	5.86E+11	1.5	5.24E+06	20	6.00
6	20170818 090901	24	21974.3	-10909.4	-1906.4	7.37E+12	2.3	4.06E+07	13	7.30
7	20170822 105230	31	21026.5	-11661.6	-3918.7	3.90E+12	2.3	6.65E+07	16	6.54
8	20171009 141642	29	21904.1	-10538.4	-2940.2	6.04E+11	1.5	5.51E+06	20	6.00
9	20171017 211230	29	22711.5	-10529.5	-2950.3	7.50E+12	2.4	7.41E+07	13	7.08
10	20171019 015107	31	22035.1	-11177.6	-3433	1.98E+12	1.9	1.14E+07	15	6.72
11	20171021 161958	30	22103.7	-11539.1	-3175.7	6.81E+11	1.6	5.26E+06	18	6.11
12	20171023 094245	29	22680.1	-10940.2	-2351.5	1.04E+13	2.7	3.45E+08	15	6.68
13	20171023 103209	29	22293.9	-10799.8	-2943.4	1.54E+12	1.9	1.80E+07	17	6.30
14	20171027 080443	29	22043.1	-12042	-3774.5	3.24E+12	2.1	3.29E+07	17	6.68
15	20171028 215820	30	20537.2	-12214.8	-4174.2	8.56E+11	1.7	9.47E+06	17	6.08
16	20171031 010807	30	23147.4	-10479	-2978	5.07E+11	1.5	4.43E+06	24	5.94
17	20171103 221501	30	21575.4	-11497.7	-3690.7	7.55E+11	1.5	4.12E+06	18	6.33
18	20171110 003754	25	21320.7	-11771	-3363.6	7.43E+11	1.5	2.29E+06	18	6.43
19	20171116 131014	25	21610	-10006.3	-2438	6.04E+11	1.6	6.51E+06	17	5.93
20	20171126 005305	25	20775.3	-11444.2	-2776.2	2.53E+12	2.0	1.75E+07	16	6.74
21	20171211 135853	25	21994.7	-11608.9	-3223.5	5.90E+11	1.5	3.44E+06	16	6.18
22	20171211 142353	28	23015.6	-10751.2	-2777.5	8.97E+11	1.6	4.20E+06	16	6.46
23	20171214 050211	30	21411.6	-11984.9	-2899.7	4.23E+12	2.2	4.70E+07	17	6.76
24	20171219 050805	28	21874.9	-11433.7	-3098.4	2.66E+12	2.1	2.61E+07	13	6.61
25	20171220 064504	27	21651.2	-12104.1	-3280.4	4.62E+12	2.1	1.40E+07	15	7.36
26	20171225 071122	28	21979.2	-11532.8	-3476	1.26E+12	1.7	6.64E+06	15	7.56
27	20180102 122952	28	21586.2	-11869.8	-3077.7	9.08E+11	1.7	7.45E+06	22	6.23
28	20180104 192629	29	22281.4	-11194.4	-3465.5	7.36E+11	1.5	4.07E+06	14	6.30
29	20180113 022616	26	21576.6	-9339	-2100.8	1.17E+12	1.6	3.70E+06	18	6.75
30	20180113 023808	27	21674.9	-9241.9	-1967	3.32E+12	2.1	2.82E+07	15	6.77
31	20180115 002045	24	22472	-11575.3	-3494.8	5.00E+11	1.5	4.25E+06	26	5.95

32	20180116 220402	35	21494.5	-11906	-3129.7	2.36E+12	1.8	6.05E+06	18	6.91
33	20180121 033457	26	22091.2	-12241.4	-3310.2	1.16E+12	1.5	2.30E+06	16	6.95
34	20180125 230457	28	22014.6	-11285.9	-2985	1.45E+12	1.9	1.59E+07	15	6.30
35	20180127 184558	29	22119	-11560.7	-3001.5	9.21E+12	2.3	3.39E+07	14	7.58
36	20180129 004428	31	21661	-11904.6	-3541.5	3.54E+12	2.1	3.25E+07	17	6.76
37	20180212 010742	29	22020.8	-11385.9	-2911.1	1.08E+12	1.8	1.66E+07	16	6.04
38	20180217 163457	30	23193.5	-10860.6	-2074.6	5.16E+12	2.3	7.50E+07	15	6.73
39	20180219 220252	29	22218.5	-12449.6	-2788.7	7.00E+11	1.5	2.84E+06	16	6.41
40	20180223 001911	30	21745.6	-11694.9	-3297.1	7.14E+11	1.5	3.90E+06	18	6.30
41	20180317 191617	36	21624.2	-10245.5	-1625.9	2.92E+12	2.1	2.67E+07	15	6.68
42	20180317 214226	36	22383.1	-12449.3	-2809.5	1.15E+13	2.7	3.19E+08	16	6.80
43	20180322 231627	28	22237	-9994.9	-2628.9	7.79E+11	1.6	4.89E+06	18	6.28
44	20180329 173214	35	21376	-10033.2	-2557.1	1.80E+12	1.9	1.68E+07	14	6.46
45	20180402 055211	30	21755.4	-12271.4	-2765.3	9.17E+11	1.8	1.45E+07	19	5.94
46	20180404 120747	32	20357.7	-9673.9	-1840.7	1.33E+12	1.8	9.11E+06	15	6.46
47	20180406 051333	30	21988	-10133.7	-1756.1	5.55E+11	1.5	5.25E+06	20	5.95
48	20180411 211434	28	21620.6	-12450.2	-2665.9	2.10E+12	1.8	8.11E+06	17	6.91
49	20180420 155924	23	22989.2	-10783.3	-2998.3	1.11E+12	1.8	1.28E+07	17	6.18
50	20180428 000853	40	21516.9	-11912.8	-3115.1	9.35E+11	1.5	3.31E+06	18	6.60
51	20180504 181525	28	21727.8	-9760.7	-2260.6	7.60E+11	1.5	2.43E+06	19	7.08
52	20180504 205920	28	21809.5	-9770.2	-2426.7	2.58E+12	1.9	1.23E+07	18	7.15
53	20180522 003124	32	22933.2	-10682.9	-3382.3	3.18E+12	2.2	5.55E+07	16	6.45
54	20180526 083550	29	21539.2	-12007.5	-3083	4.28E+12	2	8.22E+06	17	7.53
55	20180608 090342	29	21622.1	-9647.5	-2402.1	1.46E+12	1.8	1.02E+07	16	6.51
56	20180626 181730	32	21668.7	-9887.6	-2341.1	6.80E+11	1.5	4.52E+06	27	6.20
57	20180628 181056	27	21754.1	-12108.7	-3080.9	2.30E+13	2.7	1.44E+08	14	7.75
58	20180628 233131	31	21554.6	-11588	-3368.3	2.49E+12	2.1	3.63E+07	14	6.41
59	20180803 134602	32	21472.3	-11915.8	-2973.5	7.02E+11	1.5	3.67E+06	16	6.30
60	20180813 230521	21	21648.2	-9995.7	-2383.5	1.33E+12	1.8	1.28E+07	17	6.32
61	20180816 183153	25	21592.6	-11913.8	-2917.9	2.51E+12	2	2.02E+07	17	6.67
62	20180826 190054	30	22024.1	-11659.2	-3064.1	2.37E+12	1.8	6.39E+06	16	6.11
63	20180831 205912	26	21613.9	-9980.5	-2368.5	7.55E+11	1.6	7.37E+06	18	6.08
64	20180902 061326	31	22203.4	-12321.2	-3290.3	2.73E+12	2	2.40E+07	14	6.67
65	20180910 214921	24	22126.4	-11896.5	-3344	6.70E+11	1.5	2.84E+06	20	6.38
66	20180913 032343	25	21325	-11845.2	-3130.7	7.27E+11	1.6	5.03E+06	15	6.20
67	20180915 035929	23	21385.9	-11787.8	-3362.2	1.24E+12	1.7	6.32E+06	17	6.57
68	20181005 024848	24	21733.1	-11436.5	-3288.4	8.24E+11	1.5	3.44E+06	15	6.48
69	20181007 082527	30	21679.8	-11529.5	-3342.1	7.32E+12	2.5	1.33E+08	14	6.79
70	20181008 174016	27	22044.7	-11688.8	-3250.4	7.34E+11	1.5	2.42E+06	14	6.53
71	20181016 161913	27	21494.6	-12247.3	-3198.5	1.06E+12	1.6	3.03E+06	16	6.75
72	20181017 144042	29	21769.3	-11690.1	-3270.4	3.66E+12	2.1	2.63E+07	14	6.89
73	20181110 233000	37	21509.9	-12221.1	-3118.6	1.28E+12	1.6	3.96E+06	15	6.80

74	20181119 121437	29	21066.1	-9750.9	-1961.3	4.07E+12	2.1	2.47E+07	16	7.00
75	20181123 093447	44	21399.3	-11944	-2933.3	9.53E+11	1.7	9.19E+06	16	6.18

Table 2A: Moment tensor solutions

No.	Event Date & Time	X (m)	Y (m)	Z(m)	Moment (Nm)	Local Magnitude (M_L)	DEV	ISO	Misfit	QI	Es/Ep ratio	M_{xx} (10^{12}) (Nm)	M_{yy} (10^{12}) (Nm)	M_{zz} (10^{12}) (Nm)	M_{xy} (10^{12}) (Nm)	M_{xz} (10^{12}) (Nm)	M_{yz} (10^{12}) (Nm)
1	20 170 307 164 126	22523.5	-10804.5	-3290.9	1.39E+13	2.6	88.5	11.5	0.34	0.56	6.6	-0.36	0.41	-0.66	0.21	-0.45	0.01
2	20 170 331 175 326	22387.5	-10862.4	-3477.6	8.99E+11	1.6	60.1	39.9	0.33	0.52	3.3	-0.35	-0.26	-0.59	0.14	-0.38	0.28
3	20 170 715 162 357	21960.1	-10966.9	-3196.6	7.04E+12	2.6	95.3	4.7	0.32	0.48	4.7	-0.26	0.51	-0.57	0.15	-0.57	-0.14
4	20 170 729 202 255	21574.8	-9994.5	-2344.8	3.32E+12	2.2	74.2	25.8	0.31	0.6	8.9	-0.25	0.13	0.63	0.42	-0.05	0.54
5	20 170 731 022 236	22361.5	-10253.8	-3082.3	5.86E+11	1.5	75.3	24.7	0.24	0.68	10	-0.36	0.34	-0.73	0.08	0.05	0.43
6	20 170 818 090 901	21974.3	-10909.4	-1906.4	7.37E+12	2.3	94.8	5.2	0.39	0.9	10.8	0.29	0.25	-0.69	-0.22	-0.22	0.69
7	20 170 822 105 230	21026.5	-11661.6	-3918.7	3.90E+12	2.3	74.9	25.1	0.29	0.65	9.4	-0.23	0.71	0.27	-0.02	-0.23	-0.45
8	20 171 009 141 642	21904.1	-10538.4	-2940.2	6.04E+11	1.5	93.1	6.9	0.27	0.65	9.4	0.29	0.1	-0.59	0.38	-0.68	0.01
9	20 171 017 211 230	22711.5	-10529.5	-2950.3	7.50E+12	2.4	76.3	23.7	0.35	0.48	11.3	-0.4	0.27	-0.64	-0.14	-0.42	-0.19
10	20 171 019 015 107	22035.1	-11177.6	-3433	1.98E+12	1.9	85	15	0.22	0.6	5.7	-0.33	0.05	0.73	0.42	-0.15	0.44
11	20 171 021 161 958	22103.7	-11539.1	-3175.7	6.81E+11	1.6	89.2	10.8	0.34	0.4	3.2	0.44	0.15	-0.91	0.34	-0.35	0
12	20 171 023 094 245	22680.1	-10940.2	-2351.5	1.04E+13	2.7	71.8	28.2	0.26	0.8	10.6	-0.1	0.77	0.18	0.33	-0.25	0.18
13	20 171 023 103 209	22293.9	-10799.8	-2943.4	1.54E+12	1.9	95	5	0.38	0.5	6.9	-0.1	0.56	-0.61	0.12	-0.57	-0.32
14	20 171 027 080 443	22043.1	-12042	-3774.5	3.24E+12	2.1	72.4	27.6	0.34	0.57	8.8	-0.36	-0.1	-0.37	-0.34	0.37	0.35
15	20 171 028 215 820	20537.2	-12214.8	-4174.2	8.56E+11	1.7	71.3	28.7	0.24	0.53	12.1	0.02	-0.38	-0.5	0.25	-0.42	0.32
16	20 171 031 010 807	23147.4	-10479	-2978	5.07E+11	1.5	69.6	30.4	0.33	0.48	8.5	0.06	0.45	0.4	-0.4	-0.03	-0.49
17	20 171 103 221 501	21575.4	-11497.7	-3690.7	7.55E+11	1.5	71.8	28.2	0.36	0.79	5.5	-0.67	0.12	-0.3	0.31	-0.44	-0.11
18	20 171 110 003 754	21320.7	-11771	-3363.6	7.43E+11	1.5	87.3	12.7	0.25	0.29	2.2	-0.11	0.4	0.09	-0.03	-0.06	-0.74
19	20 171 116 131 014	21610	-10006.3	-2438	6.04E+11	1.6	78.2	21.8	0.27	0.63	8.4	-0.41	0.16	0.89	0.13	0.35	0.1
20	20 171 126 005 305	20775.3	-11444.2	-2776.2	2.53E+12	2	97.4	2.6	0.32	0.46	3.2	-0.08	0.9	-0.9	-0.01	-0.08	-0.9
21	20 171 211 135 853	21994.7	-11608.9	-3223.5	5.90E+11	1.5	99.4	0.6	0.18	0.41	8.9	-0.42	0.37	0.03	-0.02	-0.56	-0.68
22	20 171 211 142 353	23015.6	-10751.2	-2777.5	8.97E+11	1.6	90	10	0.28	0.61	14	-0.6	0.01	0.9	-0.13	0.12	-0.3
23	20 171 214 050 211	21411.6	-11984.9	-2899.7	4.23E+12	2.2	63.6	36.4	0.34	0.72	8	-0.48	-0.06	-0.55	0.02	-0.47	-0.55

24	20 171 219 050 805	21874.9	-11433.7	-3098.4	2.66E+12	2.1	89.2	10.8	0.25	0.43	19.9	-0.23	0.54	0.01	0.14	-0.39	-0.57
25	20 171 220 064 504	21651.2	-12104.1	-3280.4	4.62E+12	2.1	55.2	44.8	0.17	0.43	4	-0.4	-0.15	-0.8	0.04	-0.34	-0.8
26	20 171 225 071 122	21979.2	-11532.8	-3476	1.26E+12	1.7	95.6	4.4	0.16	0.5	9.1	-0.29	0.46	-0.31	0.27	-0.5	-0.51
27	20 180 102 122 952	21586.2	-11869.8	-3077.7	9.08E+11	1.7	61.8	38.2	0.33	0.61	5.6	-0.34	-0.24	-0.72	0.07	-0.43	-0.01
28	20 180 104 192 629	22281.4	-11194.4	-3465.5	7.36E+11	1.5	76.1	23.9	0.25	0.63	5	-0.03	-0.13	-0.61	0.03	-0.56	-0.27
29	20 180 113 022 616	21576.6	-9339	-2100.8	1.17E+12	1.6	85.1	14.9	0.43	0.69	4.5	0.99	0.12	-0.55	0.07	0.1	-0.55
30	20 180 113 023 808	21674.9	-9241.9	-1967	3.32E+12	2.1	79.1	20.9	0.42	0.71	11.8	-0.42	0.21	-0.42	-0.3	0.39	0.39
31	20 180 115 002 045	22472	-11575.3	-3494.8	5.00E+11	1.5	94.3	5.7	0.36	0.57	4.1	0.67	-0.08	-0.68	0.31	0.47	0.18
32	20 180 116 220 402	21494.5	-11906	-3129.7	2.36E+12	1.8	57.9	42.1	0.25	0.56	1.1	-0.31	-0.02	-0.79	0	-0.37	0.13
33	20 180 121 033 457	22091.2	-12241.4	-3310.2	1.16E+12	1.5	79.1	20.9	0.4	0.52	2.1	0.14	0.03	-0.79	0.29	-0.02	0.44
34	20 180 125 230 457	22014.6	-11285.9	-2985	1.45E+12	1.9	61.1	38.9	0.36	0.45	5.8	0.35	0.23	0.59	1	0.17	-0.54
35	20 180 127 184 558	22119	-11560.7	-3001.5	9.21E+12	2.3	82.8	17.2	0.4	0.54	3.7	-0.54	-0.54	0.54	-0.11	0.25	-0.2
36	20 180 129 004 428	21661	-11904.6	-3541.5	3.54E+12	2.1	72.8	27.2	0.27	0.69	4.9	-0.18	-0.19	-0.86	0.07	-0.33	-0.86
37	20 180 212 010 742	22020.8	-11385.9	-2911.1	1.08E+12	1.8	96.3	3.7	0.34	0.46	8.5	0.22	0.01	-0.73	-0.33	0.25	-0.52
38	20 180 217 163 457	23193.5	-10860.6	-2074.6	5.16E+12	2.3	60.7	39.3	0.34	0.91	5.7	-0.41	-0.53	-0.23	-0.01	-0.39	-0.4
39	20 180 219 220 252	22218.5	-12449.6	-2788.7	7.00E+11	1.5	78.3	21.7	0.23	0.79	8.7	0.35	-0.27	0.57	0.1	0.47	0.27
40	20 180 223 001 911	21745.6	-11694.9	-3297.1	7.14E+11	1.5	58.6	41.4	0.34	0.41	4.3	-0.2	-0.22	-0.82	-0.12	0.12	-0.37
41	20 180 317 191 617	21624.2	-10245.5	-1625.9	2.92E+12	2.1	82.4	17.6	0.33	0.95	12.5	-0.34	0.82	0.05	0.49	-0.08	0
42	20 180 317 214 226	22383.1	-12449.3	-2809.5	1.15E+13	2.7	66	34	0.33	0.75	10.5	-0.15	-0.31	-0.56	0.3	-0.49	-0.08
43	20 180 322 231 627	22237	-9994.9	-2628.9	7.79E+11	1.6	82.5	17.5	0.25	0.54	3.6	-0.11	0.28	-0.69	0.38	-0.51	-0.11
44	20 180 329 173 214	21376	-10033.2	-2557.1	1.80E+12	1.9	96.9	3.1	0.28	0.71	6.1	0.39	-0.02	-0.28	0.48	-0.69	0.22
45	20 180 402 055 211	21755.4	-12271.4	-2765.3	9.17E+11	1.8	76.1	23.9	0.32	0.69	8.8	-0.22	0.12	-0.62	-0.15	0.02	-0.5
46	20 180 404 120 747	20357.7	-9673.9	-1840.7	1.33E+12	1.8	84	16	0.42	0.78	6.2	-0.22	0.24	-0.5	-0.07	-0.52	0.48
47	20 180 406 051 333	21988	-10133.7	-1756.1	5.55E+11	1.5	83.1	16.9	0.39	0.94	4.9	0.06	-0.06	-0.5	-0.22	-0.57	-0.29
48	20 180 411 211 434	21620.6	-12450.2	-2665.9	2.10E+12	1.8	49.1	50.9	0.36	0.76	6.4	-0.51	-0.51	-0.51	-0.09	-0.41	0.19
49	20 180 420 155 924	22989.2	-10783.3	-2998.3	1.11E+12	1.8	89.4	10.6	0.29	0.51	4.9	-0.52	-0.12	0.32	0.5	-0.54	-0.06
50	20 180 428 000 853	21516.9	-11912.8	-3115.1	9.35E+11	1.5	60.6	39.4	0.25	0.38	9.1	-0.35	0	-0.83	-0.19	-0.02	-0.39

51	20 180 504 181 525	21727.8	-9760.7	-2260.6	7.60E+11	1.5	75.8	24.2	0.33	0.62	4.1	-0.08	0	-0.65	-0.11	0.53	-0.14
52	20 180 504 205 920	21809.5	-9770.2	-2426.7	2.58E+12	1.9	62.1	37.9	0.27	0.72	3.7	-0.21	-0.18	-0.75	0.29	-0.32	0.17
53	20 180 522 003 124	22933.2	-10682.9	-3382.3	3.18E+12	2.2	60.3	39.7	0.37	0.57	11.1	-0.39	-0.48	-0.32	0.27	-0.27	0.35
54	20 180 526 083 550	21539.2	-12007.5	-3083	4.28E+12	2	57	43	0.39	0.65	2.3	-0.45	-0.1	-0.75	0.06	-0.34	0.16
55	20 180 608 090 342	21622.1	-9647.5	-2402.1	1.46E+12	1.8	72.4	27.6	0.27	0.74	4.7	-0.51	0.25	-0.56	0.04	-0.46	-0.07
56	20 180 626 181 730	21668.7	-9887.6	-2341.1	6.80E+11	1.5	93.5	6.5	0.29	0.67	3.8	-0.41	0.35	0.25	0.49	-0.48	-0.36
57	20 180 628 181 056	21754.1	-12108.7	-3080.9	2.30E+13	2.7	45.3	54.7	0.26	0.74	4.6	-0.39	-0.43	-0.82	0.06	-0.26	-0.22
58	20 180 628 233 131	21554.6	-11588	-3368.3	2.49E+12	2.1	73.2	26.8	0.31	0.51	5	0.27	-0.33	-0.74	0.25	-0.31	-0.74
59	20 180 803 134 602	21472.3	-11915.8	-2973.5	7.02E+11	1.5	70.8	29.2	0.33	0.66	3.4	-0.37	0.18	-0.69	0.08	-0.41	-0.27
60	20 180 813 230 521	21648.2	-9995.7	-2383.5	1.33E+12	1.8	95.2	4.8	0.26	0.67	8.7	0.03	0.03	0.08	0.52	0.01	0.78
61	20 180 816 183 153	21592.6	-11913.8	-2917.9	2.51E+12	2	63.3	30.7	0.37	0.71	7.1	-0.28	0.06	-0.71	0.11	-0.44	-0.25
62	20 180 826 190 054	22024.1	-11659.2	-3064.1	2.37E+12	1.8	53.2	46.8	0.34	0.57	5.8	-0.41	-0.21	-0.78	0.17	-0.29	0.15
63	20 180 831 205 912	21613.9	-9980.5	-2368.5	7.55E+11	1.6	82.1	17.9	0.25	0.68	13.1	-0.21	-0.38	0.06	0.4	0.14	0.62
64	20 180 902 061 326	22203.4	-12321.2	-3290.3	2.73E+12	2	92.9	7.1	0.42	0.53	7.6	-0.04	0.18	0.07	0.57	0.63	0.18
65	20 180 910 214 921	22126.4	-11896.5	-3344	6.70E+11	1.5	59.1	40.9	0.31	0.45	2.1	-0.01	-0.44	-0.78	0.3	-0.19	-0.78
66	20 180 913 032 343	21325	-11845.2	-3130.7	7.27E+11	1.6	82.3	17.7	0.3	0.52	4.5	-0.04	0.27	-0.27	-0.17	-0.2	-0.46
67	20 180 915 035 929	21385.9	-11787.8	-3362.2	1.24E+12	1.7	80.8	19.2	0.33	0.47	2.3	-0.1	0.11	-0.59	0.07	-0.59	0.13
68	20 181 005 024 848	21733.1	-11436.5	-3288.4	8.24E+11	1.5	62.6	37.8	0.29	0.46	2.8	-0.31	-0.09	-0.73	0.05	-0.43	-0.04
69	20 181 007 082 527	21679.8	-11529.5	-3342.1	7.32E+12	2.5	88.6	11.4	0.29	0.48	7	0.19	0.08	-0.61	0.28	-0.56	0.22
70	20 181 008 174 016	22044.7	-11688.8	-3250.4	7.34E+11	1.5	51.5	48.5	0.28	0.45	3.6	-0.46	-0.26	-0.74	0.11	-0.35	0.07
71	20 181 016 161 913	21494.6	-12247.3	-3198.5	1.06E+12	1.6	60.6	39.4	0.37	0.64	3	-0.26	-0.26	-0.67	0.15	-0.5	-0.1
72	20 181 017 144 042	21769.3	-11690.1	-3270.4	3.66E+12	2.1	91.7	8.3	0.38	0.43	4.2	0.27	0.4	-0.92	0.42	-0.31	-0.01
73	20 181 110 233 000	21509.9	-12221.1	-3118.6	1.28E+12	1.6	64	36	0.36	0.66	4.3	-0.19	-0.03	-0.85	-0.19	-0.3	0.24
74	20 181 119 121 437	21066.1	-9750.9	-1961.3	4.07E+12	2.1	74.1	25.9	0.25	0.82	10.5	0.28	0.23	0.26	0.23	-0.07	0.67
75	20 181 123 093 447	21399.3	-11944	-2933.3	9.53E+11	1.7	73.1	26.7	0.36	0.54	7.1	-0.13	0.17	-0.85	-0.17	-0.16	-0.34

Table 3A:Fault Plane Solutions

Event ID	X (m)	Y (m)	Z(m)	Local Magnitude (M_L)	DEV %	ISO %	Fault-Plane Solution 1 (degrees)			Fault-Plane Solution 2 (degrees)		
							Strike	Dip	Rake	Strike	Dip	Rake
20181017 144042	21769.3	-11690.1	-3270.4	2.1	91.7	8.3	126	53	-107	333	40	-68
20171219 050805	21554.6	-11588	-3368.3	2.1	89.2	10.8	139	84	-117	38	27	-12
20180317 191617	21661	-11904.6	-3541.5	2.1	82.4	17.6	115	86	-174	25	84	-4
20180113 023808	22043.1	-12042	-3774.5	2.1	79.1	20.9	10	60	-128	247	47	-44
20181119 121437	21651.2	-12104.1	-3280.4	2.1	74.1	25.9	90	19	177	184	89	71
20180628 233131	21874.9	-11433.7	-3098.4	2.1	73.2	26.8	317	43	-42	81	63	-124
20180129 004428	21624.2	-10245.5	-1625.9	2.1	72.8	27.2	310	25	-74	113	66	-97
20171027 080443	21674.9	-9241.9	-1967	2.1	72.4	27.6	247	47	-16	349	78	-136
20171220 064504	21066.1	-9750.9	-1961.3	2.1	55.2	44.8	133	68	-112	1	30	-46
20170729 202255	21574.8	-9994.5	-2344.8	2.2	74.2	25.8	354	32	-33	114	73	-117
20171214 050211	21411.6	-11984.9	-2899.7	2.2	63.6	36.4	18	26	-19	125	82	-115
20180522 003124	22933.2	-10682.9	-3382.3	2.2	60.3	39.7	66	14	123	213	78	82
20170818 090901	22119	-11560.7	-3001.5	2.3	94.8	5.2	236	23	-64	28	69	-101
20180127 184558	21026.5	-11661.6	-3918.7	2.3	82.8	17.2	116	50	68	327	45	113
20170822 105230	23193.5	-10860.6	-2074.6	2.3	74.9	25.1	318	87	135	51	45	5
20180217 163457	21974.3	-10909.4	-1906.4	2.3	60.7	39.3	317	84	84	180	9	133
20171017 211230	22711.5	-10529.5	-2950.3	2.4	76.3	23.7	157	63	-132	41	48	-37
20181007 082527	21679.8	-11529.5	-3342.1	2.5	88.6	11.4	329	33	-39	93	70	-117
20170715 162357	21960.1	-10966.9	-3196.6	2.6	95.3	4.7	13	26	-41	141	73	-110
20170307 164126	22523.5	-10804.5	-3290.9	2.6	88.5	11.5	354	42	-32	109	69	-127
20171023 094245	21754.1	-12108.7	-3080.9	2.7	71.8	28.2	119	51	-171	23	83	-39
20180317 214226	22680.1	-10940.2	-2351.5	2.7	66.0	34.0	343	27	-29	100	77	-114
20180628 181056	22383.1	-12449.3	-2809.5	2.7	45.3	54.7	307	18	-92	129	72	-89

Table 4A: Moment tensor inversion decomposition (ISO, CLVD and DC)

Seismic event Number	Event Date & Time	Location Error (m)	X (m)	Y (m)	Z(m)	Local Magnitude (M_L)	ISO (%)	CLVD (%) [compression or Extension]	DC (%) [Shear Component]
1	20170307 164126	18	22523.5	-10804.5	-3290.9	2.6	11.5	32.4	58.0
2	20170331 175326	29	22387.5	-10862.4	-3477.6	1.6	39.9	49.4	10.7
3	20170715 162357	25	21960.1	-10966.9	-3196.6	2.6	4.7	34.7	60.8
4	20170729 202255	30	21574.8	-9994.5	-2344.8	2.2	25.8	8.3	70.8
5	20170731 022236	28	22361.5	-10253.8	-3082.3	1.5	3.9	18.5	80.6
6	20170818 090901	24	21974.3	-10909.4	-1906.4	2.3	5.2	70.5	24.3
7	20170822 105230	31	21026.5	-11661.6	-3918.7	2.3	25.1	11.5	63.8
8	20171009 141642	29	21904.1	-10538.4	-2940.2	1.5	6.9	23.4	70.1
9	20171017 211230	29	22711.5	-10529.5	-2950.3	2.4	23.7	39.3	37.0
10	20171019 015107	31	22035.1	-11177.6	-3433	1.9	15.0	49.0	37.3
11	20171021 161958	30	22103.7	-11539.1	-3175.7	1.6	10.8	60.6	27.6
12	20171023 094245	29	22680.1	-10940.2	-2351.5	2.7	28.2	10.4	62.2
13	20171023 103209	29	22293.9	-10799.8	-2943.4	1.9	5.0	37.6	55.2
14	20171027 080443	29	22043.1	-12042	-3774.5	2.1	27.6	57.3	15.1
15	20171028 215820	30	20537.2	-12214.8	-4174.2	1.7	28.7	12.3	59.0
16	20171031 010807	30	23147.4	-10479	-2978	1.5	30.4	16.0	56.5
17	20171103 221501	30	21575.4	-11497.7	-3690.7	1.5	28.2	18.5	53.3
18	20171110 003754	25	21320.7	-11771	-3363.6	1.5	12.7	16.6	70.3
19	20171116 131014	25	21610	-10006.3	-2438	1.6	21.8	76.7	1.7
20	20171126 005305	25	20775.3	-11444.2	-2776.2	2.0	2.6	25.3	67.5
21	20171211 135853	25	21994.7	-11608.9	-3223.5	1.5	1.6	38.5	59.0
22	20171211 142353	28	23015.6	-10751.2	-2777.5	1.6	10.0	49.6	40.7
23	20171214 050211	30	21411.6	-11984.9	-2899.7	2.2	36.4	4.4	70.1
24	20171219 050805	28	21874.9	-11433.7	-3098.4	2.1	10.8	4.7	84.1
25	20171220 064504	27	21651.2	-12104.1	-3280.4	2.1	44.8	50.5	5.6
26	20171225 071122	28	21979.2	-11532.8	-3476	1.7	4.4	19.4	78.2
27	20180102 122952	28	21586.2	-11869.8	-3077.7	1.7	38.2	41.5	20.4
28	20180104 192629	29	22281.4	-11194.4	-3465.5	1.5	23.9	36.2	39.9
29	20180113 022616	26	21576.6	-9339	-2100.8	1.6	14.9	29.4	55.7
30	20180113 023808	27	21674.9	-9241.9	-1967	2.1	20.9	34.2	45.0
31	20180115 002045	24	22472	-11575.3	-3494.8	1.5	5.7	28.8	65.5

32	20180116 220402	35	21494.5	-11906	-3129.7	1.8	42.1	45.1	12.8
33	20180121 033457	26	22091.2	-12241.4	-3310.2	1.5	20.9	27.5	51.6
34	20180125 230457	28	22014.6	-11285.9	-2985	1.9	38.9	1.9	59.1
35	20180127 184558	29	22119	-11560.7	-3001.5	2.3	17.2	40.4	41.2
36	20180129 004428	31	21661	-11904.6	-3541.5	2.1	27.2	13.3	59.5
37	20180212 010742	29	22020.8	-11385.9	-2911.1	1.8	3.7	8.6	87.7
38	20180217 163457	30	23193.5	-10860.6	-2074.6	2.3	39.3	14.3	46.5
39	20180219 220252	29	22218.5	-12449.6	-2788.7	1.5	21.7	43.6	34.7
40	20180223 001911	30	21745.6	-11694.9	-3297.1	1.5	41.4	23.4	35.2
41	20180317 191617	36	21624.2	-10245.5	-1625.9	2.1	17.6	22.9	59.5
42	20180317 214226	36	22383.1	-12449.3	-2809.5	2.7	34.0	27.0	38
43	20180322 231627	28	22237	-9994.9	-2628.9	1.6	17.5	5.8	76.7
44	20180329 173214	35	21376	-10033.2	-2557.1	1.9	3.1	15.1	81.8
45	20180402 055211	30	21755.4	-12271.4	-2765.3	1.8	23.9	1.1	75.2
46	20180404 120747	32	20357.7	-9673.9	-1840.7	1.8	16.0	14.4	69.6
47	20180406 051333	30	21988	-10133.7	-1756.1	1.5	16.9	49.3	34.5
48	20180411 211434	28	21620.6	-12450.2	-2665.9	1.8	50.9	12.4	36.6
49	20180420 155924	23	22989.2	-10783.3	-2998.3	1.8	10.6	19.0	70.5
50	20180428 000853	40	21516.9	-11912.8	-3115.1	1.5	39.4	2.0	58.6
51	20180504 181525	28	21727.8	-9760.7	-2260.6	1.5	24.2	54.3	21.5
52	20180504 205920	28	21809.5	-9770.2	-2426.7	1.9	37.9	23.0	37.8
53	20180522 003124	32	22933.2	-10682.9	-3382.3	2.2	39.7	47.5	12.8
54	20180526 083550	29	21539.2	-12007.5	-3083	2	10.9	65.2	22.9
55	20180608 090342	29	21622.1	-9647.5	-2402.1	1.8	27.6	35.6	36.9
56	20180626 181730	32	21668.7	-9887.6	-2341.1	1.5	6.5	25.8	67.7
57	20180628 181056	27	21754.1	-12108.7	-3080.9	2.7	54.7	14.7	30.6
58	20180628 233131	31	21554.6	-11588	-3368.3	2.1	26.8	11.9	61.3
59	20180803 134602	32	21472.3	-11915.8	-2973.5	1.5	29.2	19.8	51
60	20180813 230521	21	21648.2	-9995.7	-2383.5	1.8	4.8	3.0	92.2
61	20180816 183153	25	21592.6	-11913.8	-2917.9	2	30.7	24.1	45.4
62	20180826 190054	30	22024.1	-11659.2	-3064.1	1.8	46.8	36.0	17.2
63	20180831 205912	26	21613.9	-9980.5	-2368.5	1.6	17.9	17.2	64.9
64	20180902 061326	31	22203.4	-12321.2	-3290.3	2	7.1	24.4	68.5
65	20180910 214921	24	22126.4	-11896.5	-3344	1.5	40.9	34.0	25.1
66	20180913 032343	25	21325	-11845.2	-3130.7	1.6	17.7	36.9	45.4
67	20180915 035929	23	21385.9	-11787.8	-3362.2	1.7	19.2	64.6	16.2

68	20181005 024848	24	21733.1	-11436.5	-3288.4	1.5	37.8	43.1	13.1
69	20181007 082527	30	21679.8	-11529.5	-3342.1	2.5	11.4	47.3	41.2
70	20181008 174016	27	22044.7	-11688.8	-3250.4	1.5	48.5	40.5	11
71	20181016 161913	27	21494.6	-12247.3	-3198.5	1.6	39.4	11.2	49.4
72	20181017 144042	29	21769.3	-11690.1	-3270.4	2.1	8.3	9.4	82.2
73	20181110 233000	37	21509.9	-12221.1	-3118.6	1.6	36.0	12.0	51.9
74	20181119 121437	29	21066.1	-9750.9	-1961.3	2.1	25.9	12.3	61.9
75	20181123 093447	44	21399.3	-11944	-2933.3	1.7	26.7	30.0	43.1

CHAPTER 9 – SUMMARY AND CONCLUSIONS

9.1 Summary and Conclusions

The occurrence of mining-induced seismicity is widespread in the hard rock mines within the Witwatersrand Basin. As mines mature and extend to greater depths and higher stress geotechnical environments, the challenges and risks associated with mining-induced seismicity and rockburst are likely to increase. Seismic monitoring is being used as an integral component in managing ground related hazards in seismically active mines.

In seismically active mines, thousands of seismic events are recorded yearly by the seismic system. The data can be used to understand the rock mass response to mining and can be correlated with mining production or the emission sources. The broad objective of this thesis was to integrate the mining-induced seismic events, the 3D seismic reflection data and the structural complexity to understand the rock mass behaviour within the Witwatersrand Basin. Rock mass failures found in the mines were identified, including loading and failures on the abutments, loading and failures of the mine pillars, and failure along with the geological structure. These were correlated with the processed 3D seismic reflection data and the in-mine structural plan.

3D reflection seismic has been widely used to map ore bodies in the deep level gold mines of the Witwatersrand basin. Here, we have used 3D reflection seismic to mitigate the risks to mining personnel posed by mining-induced seismicity (being able to classify and relate seismic mechanisms that can be correlated to the known structure within the seismic cube). The horizons and faults were manually picked using PETREL and edge detection attributes applied to enhance the seismic data resolution. Geological structures (i.e.faults, dykes) were identified that displace both the Ventersdorp Contact Reef (VCR) and Black Reef (BR) horizons. These structures are either mapped in mine workings and boreholes or by interpreting a 3D reflection seismic cube. The resolution of the seismic interpretation was maximized by applying the edge detection seismic attribute. The author correlated the geologic- and seismic-mapped faults with the occurrence of the mining-induced seismicity and lastly characterized strikes and dips of these structures and their continuity and connectivity. The study highlighted the outcomes of conventional seismic data interpretation techniques and how the application of horizon-based and volumetric seismic attributes is essential to mine planning. The edge detection attribute has shown its superiority over the dip and azimuth by enhancing the detection of intersecting, cross-cutting faults, which are not possible to be visualized in seismic sections using traditional interpretation.

The ant-tracked volume yielded enhanced visibility of gently dipping structures, initially seen in the data but not well resolved, as well as steeply dipping structures that were not previously visible to the interpreter. In conclusion, the research found that definitive results cannot be acquired from using a single seismic attribute, but more confidence was acquired using a combination of attributes. However, care should be taken when applying seismic attribute interpretation techniques.

The analysis of mining-induced seismic data indicated that mining activities lead to a burst or slip on pre-existing geological planar structures. Only major geological structures might not drive these large seismic events in the 3D reflection seismic volume. Other mining elements might be loading stress on these geological structures over time, resulting in large seismic events occurring. This information could be used to assess and mitigate the risks posed by these structures, abutment, pillars, mining geometry as mining advances to greater depths. The new technique provides a better understanding of seismicity since it might image structures ahead of the mining face or in the new block of ground to be mined.

The Es/Ep ratios, tested to classify seismic events, were not consistent as source mechanisms classification compared to the moment tensor dominating components. For some analyzed seismic events, the nodal planes had some similarities, not only with one but a few different geological structures in the vicinity. In other seismic events, the nodal planes could not be related to any of the structures. Considering the location error for the seismic events themselves, the structures to which the most significant number of seismic events can occur was in Region C compared to the other two regions analyzed.

The use of moment tensor results in this thesis might have been affected by the denser network not surrounding the source, ambient and instrumentation noise, poor knowledge of the seismic velocity in the KEA area, and probably the hypocenter mislocated. The moment tensor inversion can yield reliable solutions that will align with the mining geometry and geological structures within the area of interest under certain specific ranges listed above.

Although 3D reflection seismic data and mining-induced seismic data may offer a good overview, numerical modelling analysis and the damage mechanisms may provide valuable further information. This was to refine better source parameters associated with different emission sources and provide a comprehensive understanding of the stratigraphy, structures and deformation mechanisms. The 3D reflection seismic cube consists of numerous dykes that were

more active than the faults in the area and might include several dip pillars being loaded and failing as the mining span increases.

The seismic database collected from Jan 2007 to July 2017 has proved invaluable in understanding the seismic response to mining within the main shaft pillar. The correlation coefficient (R^2 = 0.481) indicated a moderate positive relationship between seismic activity and production throughout the entire period, indicating that production plays a major role in controlling seismicity. The cumulative production was fairly linear while the seismic potency was more variable, showing some significant changes, notably in November 2012 and January 2016.

The seismic risk within the shaft pillar increased as mining progressed, despite the fact that the production rate remained essentially constant. Risk mitigation measures are regularly reviewed by Kloof Operations. An assessment of seismic hazard using the intermediate-term probability of occurrence indicates an increase in the rate of occurrence of M≥1.0 seismic events in period 2 as compared to period 1. The M_{max} value of 3.2 was higher for Period 2 as compared to the M_{max} of 2.7 during Period 1. In terms of seismic event statistics, 221 events of M ≥ 1 indicated more instability for Period 2. The reasons, however, for the changes during the extraction are not yet well known and will form part of further investigation. Mining layout (strive to limit ERR to 30 MJ/m^2), reduction of ESS on existing geological structure, limiting mining rate, avoiding concentration of mining, implementation of centralised blasting, preconditioning, and other strategies are used to mitigate seismic risk during shaft pillar extraction.

REFERENCES

Abolfazlzadeh, Y., Smith-Bougher, L., Anderson, Z., Jalbout, A. and Mataseje, A. (2019). Calibration of a Seismic Hazard Assessment Tool Using Velocity Fields and Geotechnical Data. *Proceedings of Proceedings of the First International Conference on Mining Geomechanical Risk*. Wesseloo, J., (ed.), Perth, Australian Centre for Geomechanics, pp. 233-244.

Aki, K.U. and Richards, P.G., 1980. *Quantitative Seismology,* Freeman, San Francisco.

Aki, K.U. and Richards, P.G., 2002. Quantitative Seismology second edition. *University Science Books, Sansalito, CA*, pp.218-235.

Andersen, L.M., 2001. A relative moment tensor inversion technique applied to seismicity induced by mining. PhD Thesis. University of the Witswatersrand, Johannesburg.

Andrews, D.J., 1986. Objective determination of source parameters and similarity of earthquakes of different size. *Earthquake source mechanics*, *37*, pp.259-267.

Ansell, A., 2004. In situ testing of young shotcrete subjected to vibrations from blasting. *Tunnelling and Underground Space Technology*, *19*(6), pp.587-596.

Armstrong, R.A., Compston, W., Retief, E.A., Williams, I.T. and Welke, H.J., 1991. Zircon ion microprobe studies bearing on the age and evolution of the Witwatersrand triad. *Precambrian Research*, *53*(3-4), pp.243-266.

Asch, G., 2009. Seismic recording systems. In *New Manual of Seismological Observatory Practice (NMSOP)*, Deutsches GeoForschungsZentrum GFZ, pp. 1-20.

Bacon, M., Simm, R. and Redshaw, T., 2007. *3D seismic interpretation*. Cambridge University Press, 84, pp.102-117.

Backus, G. and Mulcahy, M., 1976. Moment tensors and other phenomenological descriptions of seismic sources—II. Discontinuous displacements. *Geophysical Journal International*, *47*(2), pp.301-329.

Balmer, G., 1952. A general analysis solution for Mohr's envelope. In *Proc. American Society for Testing and Materials*, 52, pp.1260-1271.

Beach, A. and Smith, R., 2007. Structural geometry and development of the Witwatersrand Basin, South Africa. *Geological Society, London, Special Publications*, *272*(1), pp.533-542.

Ben-Menahem, A. and Singh, S.J., 1981. *Seismic waves and sources*. Springer Science and Business Media.

Bieniawski, Z.T., 1974. Geomechanics classification of rock masses and its application in tunnelling. In *Proceedings of the 3rd International Congress on Rock Mechanics, Denver,* pp. 27-32.

Boatwright, J. and Fletcher, J.B., 1984. The partition of radiated energy between P and S waves. *Bulletin of the Seismological Society of America*, *74*(2), pp.361-376.

Bodonyi, J., 1970. Laboratory tests of certain rocks under axially symmetrical loading conditions. In *2nd International Society for Rock Mechanics and Rock Engineering., Belgrade,* , pp.2-17.

Brady, B.G.H. and Brown, E.T., 1985. Rock Mechanics for Underground Mining, Allen & Unwin, Boston, Mass, USA.

Brady, B.H. and Brown, E.T., 1993. *Rock Mechanics: for Underground Mining*. Springer.

Brandt, M.B., 2000. A review of the reservoir induced seismicity at the Katse Dam, Kingdom of Lesotho, November 1995 to March 1999. *Cant. Scient. diss., University of Bergen, Norway*.

Brandt, M.B., Bejaichund, B., Kgaswane, E.M., Hattingh, E. and Roblin, D.L., 2005. Seismic history of southern Africa. *Seismological series of the Council for Geoscience*.

Brink, A.V.Z. and Mountfort, P.I., 1985. December. Feasibility studies on the prediction of rockbursts at Western deep levels: Proc 1st international congress on rockbursts and seismicity in mines, Johannesburg, Sept 1982 P317–325. Publ Johannesburg: SAIMM, 1984. In *International Journal of Rock Mechanics and Mining Sciences & Geomechanics Abstracts*, Pergamon, 22(6), pp.187.

Brown, A.R., 1996. Seismic attributes and their classification. *The Leading Edge*, *15*(10), pp.1090-1090.

Brummer, R.K., 1999. Simple truths about rockbursts. *In proceedings of SARES99,2nd south African Rock Engineering Symposium, Johannesburg, 13-15 September 1999*, T.O Hagan (editor),pp.6-11.

Brune, J.N., 1970. Tectonic stress and the spectra of seismic shear waves from earthquakes. *Journal of Geophysical Research* 75, pp.4997–5009.

Buland, R., 1976. The mechanics of locating earthquakes, *Bulletin of the Seismological Society of America,* 66, pp. 173-187.

Burridge, R. and Knopoff, L., 1964. Body Force Equivalents for Seismic Dislocations. *Seismological Research Letters, 54(6A),* pp.1875–1888.

Butler, A.G. and Van Aswegen, G., 1993. Ground velocity relationships based on a large sample of underground measurements in two South African mining regions. *Rockbursts and Seismicity in Mines, Kingston, Canada*, pp.41-51.

Cai, M., Kaiser, P.K. and Martin, C.D., 1998. A tensile model for the interpretation of microseismic events near underground openings. In *Seismicity caused by mines, fluid injections, reservoirs, and oil extraction*. Birkhäuser, Basel, pp. 67-92.

Campbell, G. and Crotty, J. H., 1988. The application of 3D seismic surveys to mine planning: *South African Chamber of Mines MINTEK Seminar*, 4th March.

Chen, J.F., 2007. Results of rock property tests. Rocklab Report 2007-OHS- Research-Works-03. Rocklab. Pretoria, South Africa.

Chopra, S., Castagna, J. and Portniaguine, O., 2006. Seismic resolution and thin-bed reflectivity inversion. *CSEG recorder*, *31*(1), pp.19-25.

Cichowicz, A. and Durrheim, R.G., 1997. The site response of the tunnel sidewall in a deep gold mine, analysis in the time domain, In *Proceedings of the 1st Southern African Rock Engineering Symposium*, Gurtunca and Hagan (eds.), SANGORM, pp. 56-61.

Cichowicz, A., Birch, D., Kgaswane, E., Kijko, A., Mangongolo, A., Ngobeni, D., Midzi, V., Rathod, G.W. Smit A., 2016. Fluid-Induced Seismicity in the Central Basin Area: Ground Motion

Prediction and the Development of an Early Warning System for Risk Reduction, Council for Geoscience, Project number SIM 14-02-05.

Crow, C. and Condie, K.C., 1987. Geochemistry and origin of late Archean volcanic rocks from the Rhenosterhoek Formation, Dominion Group, South Africa. *Precambrian Research*, *37*(3), pp.217-229.

Coward, M.P., Spencer, R.M. and Spencer, C.E., 1995. Development of the Witwatersrand Basin, South Africa. *Geological Society, London, Special Publications*, *95*(1), pp.243-269.

Cox, T. and Seitz, K., 2007. Ant tracking seismic volumes for automated fault interpretation. Calgary: CSPG CSEG Convention.

Dahm, T. and Krüger, F., 2014. Moment tensor inversion and moment tensor interpretation. In *New Manual of Seismological Observatory Practice 2 (NMSOP-2)*. Deutsches GeoForschungsZentrum GFZ, pp.1-37

Dalley, R.M., Gevers, E.A., Stampfli, G.B., Davies, D.J. and Gastaldi, C.N., 1989. Dip and azimuth displays for 3D seismic interpretation. *First Break (Print)*, *7*(3), pp.86-95.

Dankert, B.T. and Hein, K.A., 2010. Evaluating the structural character and tectonic history of the Witwatersrand Basin. *Precambrian Research*, *177*(1-2), pp.1-22.

Davies, R.J., Stewart, S.A., Cartwright, J.A., Lappin, M., Johnston, R., Fraser, S.I. and Brown, A.R., 2004. 3D seismic technology: are we realising its full potential. *Geological Society, London, Memoirs*, *29*(1), pp.1-10.

Davis, G.H. and Reynolds, S.J., 1996. Structural geology of rocks and regions, John Wiley & Sons. *Inc, New Jersey*, pp.*212*.

De Wit, M.J., Armstrong, R.A., de Ronde, C.E., Green, R.W., Hart, R.A., Hart, R.J., Peberdy, E., Roering, C. and Tredoux, M., 1992. Formation of an Archaean continent. *Nature*, *357*(6379), pp.553-562.

Disley, N.V. (2014). Seismic Risk and Hazard Management at Kidd Mine. *Proceedings of Proceedings of the Seventh International Conference on Deep and High Stress Mining*. Hudyma, M. and Potvin, Y., (eds.), Perth, Australian Centre for Geomechanics, pp. 107-121.

Dubiński, J. and Mutke, G., 1996. Characteristics of mining tremors within the near-wave field zone: *Induced Seismic Events*. Birkhäuser Basel, pp. 249-261.

Dukes, G., , 2007. Shaft pillar extraction survey. AngloGold Ashanti. *Unpublished internal report* .

Durrheim, R.J., Spottiswoode, S.M., Roberts, M.K.C. and Brink, A.V.Z., 2005. Comparative seismology of the Witwatersrand Basin and Bushveld Complex and emerging technologies to manage the risk of rockbursting. *Journal of the Southern African Institute of Mining and Metallurgy*, *105*(6), pp.409-416.

Durrheim, R.J., Anderson, R.L., Cichowicz, A., Ebrahim-Trolloped, R., Hubert, G., Kijko, A., McGarr, A., Ortlepp, W.D. and Van der Merwe, N., 2006. The risks to miners, mines, and the public posed by large seismic events in the gold mining districts of South Africa. In *Proceedings of the 3rd International Seminar on Deep and High Stress Mining*, Quebec City, Canada, J Hadjigeorgiou and M Grenon (editors), Universitè Laval, Canada, pp.1-14.

Durrheim, R.J., Cichowicz, A., Ebrahim-Trollope, R., Essrich, F., Goldbach, O., Linzer, L.M., Spottiswoode, S.M. and Stankiewicz, T., 2007,. Guidelines, standards and best practice for seismic hazard assessment and rockburst risk management in South African mines. In *Proceedings of the 4th International Seminar on Deep and High-Stress Mining,* Australian Centre for Geomechanics*,* pp.249-261.

Durrheim, R.J., Ogasawara, H., Nawakata, M., Yabe, Y., Naoi, M., Ward, A.K., Murphy, S.K., Wienand, J., Lenegan, P., Milev, A.M., Murakami, O., Yoshimitsu, N., Kgarume, T., Chichowicz, A. and the SATREPS research group., 2012. A Japanese - South African collaboration to mitigate seismic risks in mines: The establishment of experimental sites, In *Proceedings of the 6th International Seminar on Deep and High-Stress Mining, Australia (ed. Yves Potvin)*, Australian Centre for Geomechanics, Perth, Australia, pp.173-187.

Durrheim, R.J., 2014. September. Has research and development contributed to improvements in safety and profitability of deep South African mines?. In *Proceedings of the Seventh*

International Conference on Deep and High Stress Mining. Australian Centre for Geomechanics, pp. 23-40.

Ebrahim-Trollope, R. and Jooste, Y., 2005. Seismic hazard quantification. In *Controlling Seismic Risk, Proc. of the 6th International Symposium on Rockburst and Seismicity in Mines. Nedlands:* Australian Centre for Geomechanics, pp.157-164.

Edelbro, C., 2004. *Evaluation of rock mass strength criteria.* MSc thesis, Univ, Luleå tekniska universitet).

Els, B.G., Van den Berg, W.A. and Mayer, J.J., 1995. The Black Reef Quartzite Formation in the western Transvaal: sedimentological and economic aspects, and significance for basin evolution. *Mineralium Deposita*, *30*(2), pp.112-123.

Eriksson, P.G. and Altermann, W., 1998. An overview of the geology of the Transvaal Supergroup dolomites (South Africa). *Environmental Geology*, *36*(1-2), pp.179-188.

Fairhurst, C., 1964,. On the validity of the 'Brazilian'test for brittle materials. *International Journal of Rock Mechanics an-d Mining Sciences and Geomechanics Abstracts,* 1(4), pp.535-546.

Fairhurst, C. and Cook, N.G.W., 1966. The phenomenon of rock splitting parallel to the direction of maximum compression in the neighbourhood of a surface. In *Proceedings of the 1st congress on the international society of rock mechanics*, 1, pp.687-692.

Fernández, L.M., 1973. Program to evaluate epicentral distance, origin time and local magnitude of regional tremors. *Report No. Gh 1968, Geological Survey of South Africa*, pp.11.

Fernández, L. M., and. Guzman, J. A 1979. In *Seismic History of Southern Africa*. Geological Survey of South Africa Seismologic Series 9.Pretoria: *Geological Survey of South Africa*, pp.1–38.

Fletcher, P., 2009. Carbon Leader Reef West Wits Line internal report. Anglogold Ashanti.

Fletcher, J.B. and McGarr, A., 2005. Moment tensor inversion of ground motion from mining-induced earthquakes, Trail Mountain, Utah. *Bulletin of the Seismological Society of America*, *95*(1), pp.48-57.

Franklin, J.A., 1971. Triaxial strength of rock materials. *Rock Mechanics*, *3*(2), pp.86-98.

Frimmel, H.E. and Gartz, V.H., 1997. Witwatersrand gold particle chemistry matches model of metamorphosed, hydrothermally altered placer deposits. *Mineralium Deposita*, *32*(6), pp.523-530.

Gay, N. C., Durrheim, R. J., Spottiswoode, S. M. and Van der Merwe, A. J. 1995. Effect of geology, in-situ stress and mining methods on seismicity in Southern African gold and platinum mines. In *Proceedings of the International Congress of Rock Mechanics, Tokyo, Japan. Fujii, T. (ed.). International Society for Rock Mechanics*, vol. 3, pp. 1321-1325.

Gibowicz, S.J., 1990. Seismicity induced by mining. In *Advances in Geophysics* Vol. 32, pp. 1-74

Gibowicz, S.J., Young, R.P., Talebi, S. and Rawlence, D.J., 1991. Source parameters of seismic events at the Underground Research Laboratory in Manitoba, Canada: Scaling relations for events with moment magnitude smaller than− 2. *Bulletin of the Seismological Society of America*, *81*(4), pp.1157-1182.

Gibowicz, S.J., 1992. Seismic moment tensor and its application in mining seismicity studies: A review. *Acta Montana*, *88*, pp.37-69.

Gibowicz, S.J., 1993. Keynote address: Seismic moment tensor and the mechanism of seismic events in mines. In *Proceedings of Rockbursts and Seismicity in Mines, Kingston, August 1993*, pp.149-155.

Gibowicz, S.J. and Kijko, A., 1994. *An Introduction to Mining Seismology*. Academic Press, San Diego.

Gibson, M. A. S. 1997. The structural interpretation and seismic characterization of a 3-D seismic survey, Western Deep Levels Gold Mine, South Africa. M.Sc. Thesis, University of Leeds, U.K.

Gibson, M. A., 2004. Goldfields KEA 3D Seismic Project, Final Report. Unpublished internal report to Gold Fields Mining, pp.52.

Gibson, M.A., 2005. Interpretation of the 2003 South Deep 3D seismic survey.Unpublished internal report to Gold Fields Mining, pp.62.

Gibson, M.A., Jolley, S.J. and Barnicoat, A.C., 2000. Interpretation of the Western Ultra Deep Levels 3D seismic survey. *The Leading Edge*, *19*(7), pp.730-735.

Gilbert, F., 1970. Research Note: Excitation of the normal modes of the earth by earthquake sources. *Geophysical Journal of the Royal Astronomical Society*, *22*, pp.223-226.

Green, R.W.E. and Bloch, S., 1971. The Ceres, South Africa, earthquake of September 29, 1969: I. Report on some aftershocks. *Bulletin of the Seismological Society of America*, *61*(4), pp.851-859.

Gross, S.J. and Kisslinger, C., 1994. Tests of models of aftershock rate decay. *Bulletin of the Seismological Society of America*, *84*(5), pp.1571-1579.

Gutenberg, B. and Richter, C.F., 1944. Frequency of earthquakes in California. *Bulletin of the Seismological Society of America*, *34*(4), pp.185-188.

Hadjigeorgiou, J. and Potvin, Y., 2007. Overview of dynamic testing of ground support. In *Proceedings of the 4th International Seminar on Deep and High-Stress Mining*, Australian Centre for Geomechanics, pp.349-371.

Hagan, T.O., Milev, A.M., Spottiswoode, S.M., Hildyard, M.W., Grodner, M., Rorke, A.J., Finnie, G.J., Reddy, N., Haile, A.T., Le Bron, K.B. and Grave, D.M., 2001. Simulated rockburst experiment-an overview. *Journal of the Southern African Institute of Mining and Metallurgy*, *101*(5), pp.217-222.

Hanks, T.C. and Kanamori, H., 1979. A moment magnitude scale. *Journal of Geophysical Research: Solid Earth*, *84*(B5), pp.2348-2350.

Hardebeck, J.L. and Shearer, P.M., 2002. A new method for determining first-motion focal mechanisms. *Bulletin of the Seismological Society of America*, *92*(6), pp.2264-2276.

Harris P.C., Wesseloo J., 2015. mXrap software, version 5, Australian Centre for Geomechanics, The University of Western Australia, Perth, Western Australia. http://www.mXrap.com

Haskell, N.A., 1964. Total energy and energy spectral density of elastic wave radiation from propagating faults. *Bulletin of the Seismological Society of America*, *54*(6A), pp.1811-1841.

Havskov, J. and Ottemoller, L., 2010. *Routine data processing in earthquake seismology: With sample data, exercises and software*. Springer Science and Business Media.

Handley, J.R., 2004. *Historic overview of the Witwatersrand goldfields: a review of the discovery, geology, geophysics, development, mining, production and future of the Witwatersrand goldfields as seen through a geological and financial association spanning 50 years*. JRF Handley.

Heal, D., 2010. Observation and analysis of incidences of rockburst damage in underground mines, PhD Thesis, University of Western Australia, School of Civil and Resource Engineering.

Heyman, J., 1972. Coulomb's Memoir on Statics. Cambridge University Press, London

Hills, P.B., Rebuli, D.B., and Lynch, R.A., 2013. Micro-seismic monitoring at the Tasmania Mine, Beaconsfield, Tasmania. *In: Malovichko A, Malovichko D (eds) Eighth international symposium on rockbursts and seismicity in mines, RaSiM8, 1–7 September 2013*, Saint-Petersburg-Moscow, Geophysical Survey of Russian Academy of Sciences, Mining Institute of Ural Branch of Russian Academy of Sciences, Russia, pp. 485-494

Hobbs, D.W., 1964. The strength and the stress-strain characteristics of coal in triaxial compression. *The Journal of Geology*, *72*(2), pp.214-231.

Hoek, E.T., 1968. Brittle failure of rock*: Stagg KG, Zienkiewicz OC (eds) Rock Mechanics in Engineering Practice. Wiley, New york*, pp 99–124.

Hoek, E. and Brown, E.T., 1980. Underground excavations in rock. Institute of *Mining and Metallurgy, London*, pp.*156*.

Hoek, E., Carranza-Torres, C. and Corkum, B., 2002. Hoek-Brown failure criterion-2002 edition. In *Proceedings of the 5th North American Rock Mechamics Symposium*, Toronto *1*(1), pp.267-273.

Hoek, E., Wood, D. and Shah, S., 1992. A modified Hoek–Brown failure criterion for jointed rock masses. In *Rock Characterization: International Society for Rock Mechanics and Rock Engineering*. *Symposium, Eurock'92, Chester, UK, 14–17 September 1992*, Thomas Telford Publishing, pp.209-214.

Hudyma, M.R., Milne, D. and Grant, D.R., 1995. Geomechanics of sill pillar mining in rockburst prone conditions. *Final report: sill pillar monitoring using conventional methods. Mining Research Directorate*, pp.*104*.

Hudyma, M.R., 2005. Seismic hazard mapping in mines. *Seminar on advanced Geomechanics in Mines*. Australian Centre for Geomechanics, 3 August 2005, Perth, Australia, pp.24.

Hudyma, M.R. and Brummer, R.K., 2007. Seismic monitoring in mines-design, operation, tricks and traps, [w:] In *1st Canada-US Rock Mechanics Symposium*.Conference Paper American Rock Mechanics Association.

Hudyma, M. and Potvin, Y., 2008. Characterizing caving induced seismicity at Ridgeway gold mine. In *Proceedings of the 5th International Conference and Exhibition on Mass Mining*, Luleá, Sweden, 9-11 June 2008. Schunnesson, H. and Nordlund, E. (eds.). Luleá University of Technology. pp. 931-942.

Hudyma, M.R., 2008. *Analysis and interpretation of clusters of seismic events in mines*. PhD thesis. University of Western Australia.

Hudyma, M. and Potvin, Y.H., 2010. An engineering approach to seismic risk management in hardrock mines. *Rock mechanics and rock engineering*, *43*(6), pp.891-906.

Hutton, L.K. and Boore, D.M., 1987. The ML scale in southern California. *Bulletin of the Seismological Society of America*, *77*(6), pp.2074-2094.

IMS (Institute of Mine Seismology). 2015. User Manual. Retrieved from http://www.imseismology.org/

Jackson, M.C., 1992. A review of the late Archean volcano-sedimentary Dominion Group and implications for the tectonic setting of the Witwatersrand Supergroup, South Africa. *Journal of African Earth Sciences (and the Middle East)*, *15*(2), pp.169-186.

Jaeger, J.C. and Cook, N.G.W., 1979. Fundamentals of Rock Mechanics, Chapman and Hall.

Jager, A.J. and Ryder, J.A., 1999. A handbook on rock engineering practice for tabular hard rock mines. *Safety in Mines Research Advisory Committee, Johannesburg*, pp.46.

Jarufe, J.A. and Vasquez, P., 2014. Numerical modelling of rock-burst loading for use in rock support design at Codelco's New Mine Level Project. *Mining Technology*, *123*(3), pp.120-127.

James, D.E., Niu, F. and Rokosky, J., 2003. Crustal structure of the Kaapvaal craton and its significance for early crustal evolution. *Lithos*, *71*(2-4), pp.413-429.

Johnston, I.W., 1985. Strength of intact geomechanical materials. *Journal of Geotechnical Engineering*, *111*(6), pp.730-749.

Jost, M.U. and Herrmann, R.B., 1989. A student's guide to and review of moment tensors. *Seismological Research Letters*, *60*(2), pp.37-57.

Joubert, A., Beukes, G.J., VISSER, J.J. and De Bruiyn, H., 1991. A note on fluorite in Late Pleistocene thermal spring deposits at Florisbad, Orange Free State. *South African Journal of Geology*, *94*(2-3), pp.174-177.

Julià, J., Nyblade, A.A., Durrheim, R., Linzer, L., Gök, R., Dirks, P. and Walter, W., 2009. Source mechanisms of mine-related seismicity, Savuka mine, South Africa. *Bulletin of the Seismological Society of America*, *99*(5), pp.2801-2814.

Kaiser, P.K. and Cai, M., 2013. Rockburst damage mechanisms and support design principles. *In: Malovichko A, Malovichko D (eds) Eighth international symposium on rockbursts and seismicity in mines, RaSiM8, 1–7 September 2013*, Saint-Petersburg-Moscow, Geophysical Survey of Russian Academy of Sciences, Mining Institute of Ural Branch of Russian Academy of Sciences, Russia, pp.349-370.

Kaiser, P.K., Vasak, P., Suorineni, F.T. and Thibodeau, D., 2005. New dimensions in seismic data interpretation with 3D virtual reality visualization for burst-prone mines. *Controlling seismic risk*, pp.*33*.

Kanamori, H. and Given, J.W., 1981. Use of long-period surface waves for rapid determination of earthquake source parameters. *Physics of the Earth and Planetary Interiors*, *27*(1), pp.8-31.

Kearey, P. and Brooks, M., 1991. An Introduction to Geophysical Exploration 2nd ed. Oxford: Scientific Publications, pp.254.

Kearey, P., Brooks, M. and Hill, I., 2002. *An introduction to geophysical exploration* 3rd ed. Hong Kong: Blackwell, pp.72.

Kearney, P., Brooks, M. and Hill, I., 2013. *An introduction to geophysical exploration*. John Wiley and Sons.

Kidybiński, A., 1986. Design criteria for roadway support to resist dynamic loads. *International Journal of Mining and Geological Engineering*, *4*(2), pp.91-109.

Kijko, A., Stankiewicz, T. and Krol, M., 1986. Relative location of mining events. *Przegl. Gorn*.10, pp219-223 (in polish; English abstract).

Kgarume, T.E., 2010. *Mine Aftershocks and Implications for Seismic Hazard Assessment, MSc thesis*, University of the Witwatersrand.

Kgarume, T.E., Spottiswoode, S.M. and Durrheim, R.J., 2010. Statistical properties of mine tremor aftershocks. *Pure and Applied geophysics*, *167*(1), pp.107-117.

Knopoff, L. and Randall, M.J., 1970. The compensated linear-vector dipole: A possible mechanism for deep earthquakes. *Journal of Geophysical Research*, *75*(26), pp.4957-4963.

Kositcin, N. and Krapež, B., 2004. Relationship between detrital zircon age-spectra and the tectonic evolution of the Late Archaean Witwatersrand Basin, South Africa. *Precambrian Research*, *129*(1-2), pp.141-168.

Krapež, B., 1985. The Ventersdorp Contact placer: a gold-pyrite placer of stream and debris-flow origins from the Archaean Witwatersrand Basin of South Africa. *Sedimentology*, *32*(2), pp.223-234.

Kwiatek, G. and Ben-Zion, Y., 2013. Assessment of P and S wave energy radiated from very small shear-tensile seismic events in a deep South African mine. *Journal of Geophysical Research: Solid Earth*, *118*(7), pp.3630-3641.

Liu, J.P., Si, Y.T., Zhang, C.Y. and Wang, R., 2020. Estimation of fracturing mechanisms by the ratio of radiated energy between S and P waves of microseismic events during mining in metal mines. *Applied Geophysics*, *17*(3), pp.465-474.

Malehmir, A., Durrheim, R., Bellefleur, G., Urosevic, M., Juhlin, C., White, D.J., Milkereit, B. and Campbell, G., 2012. Seismic methods in mineral exploration and mine planning: A general overview of past and present case histories and a look into the future. *Geophysics*, *77*(5), pp.173-190.

Malehmir, A., Andersson, M., Lebedev, M., Urosevic, M. and Mikhaltsevitch, V., 2013. Experimental estimation of velocities and anisotropy of a series of Swedish crystalline rocks and ores. *Geophysical prospecting*, *61*(1), pp.153-167.

Malmgren, L. and Nordlund, E., 2006. The behaviour of shotcrete supported rock wedges subjected to blast-induced vibrations. *International Journal of Rock Mechanics and Mining Sciences*, *43*(4), pp.593-615.

Malovichko, D., 2012. Discrimination of blasts in mine seismology. In *Proceedings of the 6th international seminar on deep and high-stress mining*. Australian Centre for Geomechanics, pp.162-172.

Malovichko, D. and Lotter E., 2016. Course notes: IMS Moment Tensor User's guide,

Manzi, M.S., Gibson, M.A., Hein, K.A., King, N. and Durrheim, R.J., 2012a. Application of 3D seismic techniques to evaluate ore resources in the West Wits Line goldfield and portions of the West Rand goldfield, South Africa Application of 3D seismic techniques. *Geophysics*, *77*(5), pp.163-171.

Manzi, M.S., Durrheim, R.J., Hein, K.A. and King, N., 2012b. 3D edge detection seismic attributes used to map potential conduits for water and methane in deep gold mines in the Witwatersrand Basin, South Africa. *Geophysics*, *77*(5), pp.133-147.

Manzi, M.S., Hein, K.A., King, N. and Durrheim, R.J., 2013. Neoarchaean tectonic history of the Witwatersrand Basin and Ventersdorp Supergroup: New constraints from high-resolution 3D seismic reflection data. *Tectonophysics*, *590*, pp.94-105.

Manzi, M.S.D., 2013. *Application of 3D seismic analysis techniques to evaluate ore resources on Kloof, South deep and Driefontein gold Mines*, *Witwatersrand Basin, South Africa*. PhD Thesis, University of the Witwatersrand.

Manzi, M.S., Hein, K.A., Durrheim, R.J. and King, N., 2014. The Ventersdorp Contact Reef model in the Kloof Gold Mine as derived from 3D seismics, geological mapping and exploration borehole datasets. *International Journal of Rock Mechanics and Mining Sciences*, *66*, pp.97-113.

Manzunzu, B., Midzi, V., Mulabisana, T.F., Zulu, B., Pule, T., Myendeki, S. and Rathod, G.W., 2019. Seismotectonics of South Africa. *Journal of African Earth Sciences*, *149*, pp.271-279.

Marfurt, K.J., 2006. Robust estimates of 3D reflector dip and azimuth. *Geophysics*, *71*(4), pp.29-40.

Marsh, J. S., 2006. The Dominion Group. In: M. R. Johnson, C. R. Anhaeusser and R. J. Thomas, eds. *The Geology of South Africa*. 1st ed. Johannesburg, Pretoria: Geological Society of South Africa, Council of Geosciences, pp.691.

Masethe, R., 2012. Seismology and the Short-term Seismic Hazard Assessment method, Sibanyestillwater Gold and Platinum Operations, Unpublished Sibanyestillwater Internal report.

Masny, W., 2006. Practical application of the sensors for measuring static and dynamic loadings. XXIX. Winter School of Rock Mechanics and Geoengineering. Krynica 12-17 March, pp.237–245.

Masny, W. and Prusek, S., 2012. The underground tests of peak particle velocities (PPV) and loads of mixed support. In: The safety of mixed support under the dynamic load conditions, Ed. M. Turek, GIG.

McCarthy, T.S., 2006. The Witwatersrand Supergroup. In: M. R. Johnson, C. R. Anhaeusser and R. J. Thomas, eds. *The Geology of South Africa*. 1st ed. Johannesburg, Pretoria: Geological Society of South Africa, Council of Geosciences, pp.155-186.

McGarr, A., Green, R.W.E. and Spottiswoode, S.M., 1981. Strong ground motion of mine tremors: some implications for near-source ground motion parameters. *Bulletin of the Seismological Society of America*, *71*(1), pp.295-319.

McGarr, A., 1991. Observations constraining near-source ground motion estimated from locally recorded seismograms. *Journal of Geophysical Research: Solid Earth*, *96*(B10), pp.16495-16508.

McGarr, A., 1984. Some applications of seismic source mechanism studies to assessing underground hazard, in *Rockbursts and Seismicity in Mines*, edited by N. C. Gay, and E. H. Wainwright, *Journal of the Southern African Institute of Mining and Metallurgy*, Johannesburg, pp.199-208.

McGarr, A., 1992a. An implosive component in the seismic moment tensor of a mining-induced tremor. *Geophysical research letters*, *19*(15), pp.1579-1582.

McGarr, A., 1992b. Moment tensors of ten Witwatersrand mine tremors. *Pure and Applied Geophysics*, *139*(3-4), pp.781-800.

McGarr, A., 1999. On relating apparent stress to the stress-causing earthquake fault slip. *Journal of Geophysical Research: Solid Earth*, *104*(B2), pp.3003-3011.

McGarr, A. 2001 Control of strong ground motion of mining-induced earthquakes by the strength of the seismogenic rock Proc. RASiM 5, G. van Aswegen, R.J. Durrhem and W.D. Ortlepp (Editors), *Journal of the Southern African Institute of Mining and Metallurgy*, pp.69-74.

McKinnon, S.D., 2006. Triggering of seismicity remote from active mining excavations. *Rock Mechanics and Rock Engineering*, *39*(3), pp.255-279.

Melkoumian, N., Priest, S.D. and Hunt, S.P., 2009. Further development of the three-dimensional Hoek–Brown yield criterion. *Rock Mechanics and Rock Engineering* , *42*(6), pp.835-847.

Mendecki, A.J., 1993. Keynote address: Real-time quantitative seismology in mines. *Rockbursts and Seismicity in Mines*, pp.287-295.

Mendecki, A.J., 1995. SIMRAC Project GAP 017 Seismology for rockburst prevention, control and prediction. *SIMRAC website: http://www. simrac.co.za*.

Mendecki, A.J., 1997. *Seismic monitoring in mines*. Springer Science and Business Media.

Mendecki, A.J., 2016. Mine seismology reference book: seismic hazard. *Institute of Mine Seismology*, pp.88.

Mendecki, A.J., Van Aswegen, G. and Mountfort, P., 1999. A guide to routine seismic monitoring in mines. In *A Handbook on Rock Engineering Practice for Tabular Hard Rock Mines, A.J. Jager and J.A. Ryder (eds),* SIMRAC, Johannesburg, pp.3 -35.

Mendecki, A.J. and Van Aswegen, G., 2001. Seismic monitoring in mines: selected terms and definitions. *Rockbursts and Seismicity in Mines-RaSiM5*, *5*(563-570), p.2.

Milev, A.M., Spottiswoode, S.M., and Stewart, R.D., 1999. Dynamic response of the rock surrounding deep level mining excavations. In *Proceedings of the 9th International Society for Rock Mechanics and Rock Engineering*, Vonille and Berset (eds.), Paris,pp.1109–1114.

Milev, AM and Spottiswoode, S.M., 2005. Strong ground motion and site response in deep South African mines. *Journal of the Southern African Institute of Mining and Metallurgy*, *105*(7), pp.515-524.

Milkereit, B., Eaton, D., Wu, J., Perron, G., Salisbury, M.H., Berrer, E.K. and Morrison, G., 1996. Seismic imaging of massive sulfide deposits; Part II, Reflection seismic profiling. *Economic Geology*, *91*(5), pp.829-834.

Morkel, I.G., Wesseloo, J. and Potvin, Y., 2019. The validity of Es/Ep as a source parameter in mining seismology. In *Proceedings of the 9th International Conference on Deep and High-Stress Mining, Southern African Institute of Mining and Metallurgy,* pp.385-397

Morrison, D.M., Swan, G. and Scholz, C.H., 1993. Chaotic behaviour and mining-induced seismicity. *In Procedings of Rockbursts and seismicity in mines*, *Kingston August 1993,* (Editor: R.P. Young) Rotterdam, A.A. Balkema, pp.233-238.

Mulabisana, T. F.,2016. *Compiling a homogeneous earthquake catalogue for Southern Africa*, MSc dissertation, University of the Witwatersrand.

Murrell, S.A.F., 1963. A criterion for brittle fracture of rocks and concrete under triaxial stress and the effect of pore pressure on the criterion. *Rock Mechanics*, pp.563-577.

Murphy, S.K., 2012. Linear elastic numerical modelling for failure prediction-an assessment. *Journal of the Southern African Institute of Mining and Metallurgy*, *112*(8), pp.737-748.

Mussett, A.E. and Khan, M.A., 2000. *Looking into the earth: an introduction to geological geophysics*. Cambridge University Press.

Mutke, G., 2002. Ground motion associated with coal mine tremors close to the underground openings. *Seismogenic process monitoring, AA Balkema Publishers*, pp.91-102.

Mutke, G., 2008. Stability of the underground mine workings in the near-field zone of seismic events. In *21st World Mining Congress,* pp.89-97.

Mutke, G., Masny, W. and Prusek, S., 2016. Peak particle velocity as an indicator of the dynamic load exerted on the support of underground workings. *Acta Geodynamica et Geomaterialia*, *13*(4), pp.367-378.

Myers, R.E., McCarthy, T.S. and Stanistreet, I.G., 1989. A tectonic-sedimentary reconstruction of the development of the Witwatersrand Basin, with particular emphasis on the Central Rand Group. *Economic Geology Research Unit Information Circular*, *216*, pp.497-540.

Nanjo, K., Nagahama, H. and Satomura, M., 1998. Rates of aftershock decay and the fractal structure of active fault systems. *Tectonophysics*, *287*(1-4), pp.173-186.

Ngcobo, T.A., 2006. The risk associated with mines in dolomitic compartments. *Journal of the South African Institute of Mining and Metallurgy*, *106*(4), pp.251-264.

Nkosi, T.Z., 2016. *Seismological and mineralogical studies of the world's deepest gold-bearing horizon, the Carbon Leader Reef, West Wits Line goldfields (South Africa): Implications for its poor seismic reflective character*, MSc thesis, University of the Witwatersrand.

Ngeri, A., Tamunobereton-ari, I., and Amakiri, A., 2015. Ant-tracker attributes: an effective approach to enhancing fault identification and interpretation. Journal of VLSI and Signal Processing, **5**, pp.67-73.

Nguuri, T.K., Gore, J., James, D.E., Webb, S.J., Wright, C., Zengeni, T.G., Gwavava, O., Snoke, J.A. and Kaapvaal Seismic Group, 2001. Crustal structure beneath southern Africa and its implications for the formation and evolution of the Kaapvaal and Zimbabwe cratons. *Geophysical Research Letters*, *28*(13), pp.2501-2504.

Nordström, E., Dineva, S., & Nordlund, E., 2017. Source parameters of seismic events potentially associated with damage in block 33/34 of the Kiirunavaara mine(Sweden). Acta Geophysica, 65(6), pp.1229-1242

Ogasawara, H., Kawakata, H., Ishii, H., Nakatani, M., Yabe, Y. and Iio, Y., 2009a. Semi-controlled earthquake-generation experiments in deep gold mines, South Africa Monitoring at closest proximity to elucidate seismogenic process. *Journal of the Seismological Society of Japan (Zisin)*, *61*, pp.563-573.

Ogasawara, H., Durrheim, R.J., Nakatani, M., Yabe, Y., Milev, A., Cichowicz, A., Kawakata, H., Moriya, H. and JST-JICA SA research group, 2009b. Japanese-South African collaboration to mitigate seismic risks in deep gold mines. In Proceedings of 1st Hard Rock Safe Safety Conference, *South African Institute of Mining and Metallurgy*, pp.115-134.

Ortlepp, W.D., 1997. Rock fracture and rockbursts-an illustrative study. *Journal of the South African Institute of Mining and Metallurgy*, Johannesburg, pp.100.

Ortlepp, W.D., 2000. Observation of mining-induced faults in an intact rock mass at depth. *International Journal of Rock Mechanics and Mining Sciences*, *37*(1-2), pp.423-436.

Ortlepp, W.D., 2001. The behaviour of tunnels at great depth under large static and dynamic pressures. *Tunnelling and Underground Space Technology*, *16*(1), pp.41-48.

Ortlepp, W.D. and Stacey, T.R., 1994. Rockburst mechanisms in tunnels and shafts. *Tunnelling and Underground Space Technology*, *9*(1), pp.59-65.

Ozbay, M.U., Spottiswoode, S. and Ryder, J.A., 1993. A quantitative analysis of pillar associated large seismic events in deep mines. *In Procedings of Rockbursts and seismicity in mines*, *Kingston August 1993,* (Editor: R.P. Young) Rotterdam, A.A. Balkema, pp.107-110.

Peters, T., 2005. The successful integration of 3D seismic into the mining process: Practical examples from Bowen Basin underground coal mines. In *Proceedings of the Bowen Basin Symposium*, pp.165-169.

Pretorius, C.C., Steenkamp, W.H. and Smith, R.G., 1994. Developments in data acquisition, processing, and interpretation over ten years of deep vibroseismic surveying in South Africa. In *Proceedings of the 15th Congress of the Council for Mining and Metallugical Institutions., Southern African Institute of Mining and Metallurgy,* pp.249-258.

Pretorius, C.C., Trewick, W.F., Fourie, A. and Irons, C., 2000. Application of 3D seismics to mine planning at Vaal Reefs gold mine, number 10 shaft, Republic of South Africa. *Geophysics*, *65*(6), pp.1862-1870.

Prieto, G.A., 2007. *Improving earthquake source spectrum estimation using multitaper techniques*, PhD Thesis, UC San Diego.

Pujol, J. and Herrmann, R.B., 1990. A student's guide to point sources inhomogeneous media, *Seismological Research. Letter.* 61, pp 209-220.

Rakumakoe, O., 2019. Ideal stope profile to manage seismicity in deep tabular narrow reef mines. In *Proceedings of the 9th International Conference on Deep and High-Stress Mining, Southern African Institute of Mining and Metallurgy,* pp.293-306.

Ramamurthy, T., 1995. Bearing capacity of rock foundations. In Conference *Rock Foundation*, Balkema Rotterdam, pp.311-316.

Randen, T. Pedersen, S., and Sonneland, L., 2001. Automatic extraction of fault surfaces from three-dimensional seismic data. San Antonio: SEG International Exposition and Annual Meeting.

Randen, T. and Sønneland, L., 2005. Atlas of 3D seismic attributes. In Mathematical Methods and Modelling in Hydrocarbon Exploration and Production. Heidelberg: Springer. Pp. 23-46.

Rebuli, D.B. and Van Aswegen, G., 2013, September. Short term Seismic hazard assessment in SA Gold Mines. *In: Malovichko A, Malovichko D (eds) Eighth international symposium on rockbursts and seismicity in mines, RaSiM8, 1–7 September 2013*, Saint-Petersburg-Moscow, Geophysical Survey of Russian Academy of Sciences, Mining Institute of Ural Branch of Russian Academy of Sciences, Russia, pp 323-331

Rebuli, D.B. and Kohler, S.J., 2014. Using clustering algorithms to assist short-term seismic hazard analysis in deep South African mines. In *Proceedings of the Seventh International Conference on Deep and High-Stress Mining,* Australian Centre for Geomechanics*,* pp.699-708.

Riemer, K.L. and Durrheim, R.J., 2012. Mining seismicity in the Witwatersrand Basin: monitoring, mechanisms and mitigation strategies in perspective. *Journal of Rock Mechanics and Geotechnical Engineering*, *4*(3), pp.228-249.

Richter, C.F.,1935. An instrumental earthquake magnitude scale. *Bulletin of the Seismological Society of America*, *25*(1), pp.1-32.

Richardson, E. and Jordan, T.H., 2002. Seismicity in deep gold mines of South Africa: Implications for tectonic earthquakes. *Bulletin of the Seismological Society of America*, *92*(5), pp.1766-1782.

Rijks, E.J.H. and Jauffred, J.C.E.M., 1991. Attribute extraction: An important application in any detailed 3D interpretation study. *The Leading Edge*, *10*(9), pp.11-19.

Robb, L.J. and Meyer, F.M., 1995. The Witwatersrand Basin, South Africa: Geological framework and mineralization processes. *Ore Geology Reviews*, *10*(2), pp.67-94.

Robb, L.J., Brandl, G., Anhaeusser, C.R. and Poujol, M., 2006. Archaean granitoid intrusions. In: M. R. Johnson, C. R. Anhaeusser and R. J. Thomas, eds. *The Geology of South Africa*. 1st ed. Johannesburg, Pretoria: Geological Society of South Africa, Council of Geosciences, pp.57-94.

Ryder, J.A., Jager, A.J., 2002. A textbook on rock mechanics for tabular hard rock mines. *The Safety in Mines Research Advisory Committee (SIMRAC), Johannesburg*.

SACS (South African Committee for Stratigraphy), 1980. Stratigraphy of South Africa. Part 1 (Comp. L.E. Kent). *Lithostratigraphy of the Republic of South Africa, South West Africa/Namibia, and the Republics of Bophuthatswana, Transkei and Venda*, Handb. Geol. Surv. S Afr., 8, pp.690.

Salisbury, M.H., Milkereit, B., Ascough, G., Adair, R., Matthews, L., Schmitt, D.R., Mwenifumbo, J., Eaton, D.W. and Wu, J., 2000. Physical properties and seismic imaging of massive sulfides. *Geophysics*, *65*(6), pp.1882-1889.

Salisbury, M.H., Harvey, C.W. and Matthews, L., 2003. The Acoustic Properties of Ores and Host Rocks in Hardrock Terranes, in D. W. Eaton, B. Milkereit, and M. H. Salisbury, eds., *Hardrock Seismic Exploration, Society of Exploration Geophysicists*, pp.9-19.

Salisbury, M. H., and D. Snyder, 2007, Application of seismic methods to mineral exploration, *in W. D. Goodfellow, ed., Mineral deposits of Canada: A synthesis of major deposit types, district metallogeny, the evolution of geological provinces, and exploration methods*: Geological Association of Canada, Mineral Deposits Division, Special Publication 5, 971–982.

Saunders, I., Ottemöller, L., Brandt, M.B. and Fourie, C.J., 2013. Calibration of an ML scale for South Africa using tectonic earthquake data recorded by the South African National Seismograph Network: 2006 to 2009. *Journal of seismology*, *17*(2), pp.437-451.

Shapiro, S.A., Rothert, E., Rindschwentner, J. and Rath V., 2002. Characterization of fluid transport properties of reservoirs using induced microseismicity.*Geophysics*, *67*, pp. 212–220.

Shapiro, S.A., Rentsch, S. and Rothert, E., 2005. Fluid-induced seismicity: Theory, modeling and applications.*Journal of Engineering Mechanics*, *131*, pp. 947–952.

Sheriff, R.E., 1992. Reservoir Geophysics; Society of Exploration Geophysicists: Tulsa, OK, USA.

Sheriff, R.E., 2002. *Encyclopedic dictionary of applied geophysics*. Society of exploration geophysicists.

Sheorey, P.R., Biswas, A. and Choubey, V.D., 1989. An empirical failure criterion for rocks and jointed rock masses. *Engineering Geology*, *26*(2), pp.141-159.

Sibanye-Stillwater Gold division., 2016 Kloof Gold Mine. Intenal geological Report. Johannesburg: Sibanyestillwater Gold.

Sibanye-Stillwater Gold division., 2018 Kloof Gold Mine. Internal daily seismic Report. Johannesburg: Sibanyestillwater Gold.

Sibson, R. H., 1986. Rupture interaction with fault jogs, in Earthquake Source Mechanics, S. Das, J. Boatwright, and C. H. Scholz (Editors), *Geophysical Monograph*, American Geophysical Union, Washington,D.C.,37, pp.157–167.

Singh, M. and Pule, T., 2007. Maximum possible earthquakes in the Witwatersrand Basin. In *Proceedings of Conference: Seismology Workshop 2007: Neotectonics and Mining Seismology—is a Relationship Possible*.Council for Geoscience, Pretoria.

Singh, M., Kijko, A. and Durrheim, R., 2009. Seismotectonic models for South Africa: Synthesis of geoscientific information, problems, and the way forward. *Seismological Research Letters*, *80*(1), pp.71-80.

Stanistreet, I.G. and McCarthy, T.S., 1991. Changing tectono-sedimentary scenarios relevant to the development of the Late Archaean Witwatersrand Basin. *Journal of African Earth Sciences (and the Middle East)*, *13*(1), pp.65-81.

Stankiewicz, T., 2006. Program KORHAAN Seismic hazard in mines, User's Guide, ver. 5.0, HAMERKOP SUITES Scientific Services.

Stein, S. and Wysession, M., 2003. *An Introduction to Seismology, Earthquakes, and Earth*, *7*(9), pp.10.

Stevenson, F., Higgs, R.M. and Durrheim, R.J., 2003. Seismic imaging of precious and base-metal deposits in Southern Africa. *Hardrock seismic exploration. Edited by DW Eaton, B. Milkereit, and MH Salisbury. Society of Exploration Geophysicists, Tulsa, Okla*, pp.141-156.

Stjern, G. and Myrvang, A., 1998. The influence of blasting on grouted rock bolts. *Tunnelling and Underground Space Technology*, *13*(1), pp.65-70.

Strecker, M.R., Carrapa, B., Hulley, G.E., Scoenbohm, L. and Sobel, E.R., 2004. Erosional control of plateau evolution in the Central Andes. *Geological Society of America*, *36*(5), pp. 7–10.

Sweby, G., Trifu, C., Goodchild, D. and Morris, L., 2006. High resolution seismic monitoring at Mt Keith Open Pit Mine. In *Proceedings of Golden Rocks 2006, The 41st U.S. Symposium on Rock Mechanics (USRMS)*. American Rock Mechanics Association, pp.6.

Szweda, S., 2003. Dynamic action of rock mass on the powered support legs. *Journal of Mining Science*, *39*(2), pp.154-161.

Taner, M.T., Koehler, F. and Sheriff, R.E., 1979. Complex seismic trace analysis. *Geophysics*, *44*(6), pp.1041-1063.

Tannant, D.D., Kaiser, P.K. and McDowell, G.M., 1992. Dynamic support monitoring. In *International symposium on rock support*, pp.657-664.

Trickett, J. C., Duweke, W.A and Kock, S., 2004. Three-dimensional reflection seismic: Worth its weight in platinum: International Platinum Conference, *South African Institute of Mining and Metallurgy*, pp.257–264.

Trickett, J. C., Duweke, W.A. and Kock, S., 2005. Three-dimensional reflection seismics: worth its weight in platinum. *Journal of the Southern African Institute of Mining and Metallurgy*, *105*(5), pp.357-363.

Ulusay, R. and Hudson, J.A., 2007. The complete ISRM suggested methods for rock characterization, testing and monitoring. *International Society for Rock Mechanics and Rock Engineering*.*Turkish National Group, Ankara, Turkey*, pp. 971-1010.

Utsu, T., 1961. A statistical study on the occurrence of aftershocks. *Geophysical Magazine*, *30*, pp.521-605.

Vallejos, J.A. and McKinnon, S.D., 2010. Omori's law applied to mining-induced seismicity and re-entry protocol development. *Pure and Applied Geophysics*, *167*(1-2), pp.91-106.

Van Aswegen, G., 2005. Routine seismic hazard assessment in some South African mines. In *Proceedings of the 6th International Symposium on Rockbursts and Seismicity in Mines, Y. Potvin and M. Hudyma (eds),* Australian Centre for Geomechanics*,* pp.437-444.

Van Aswegen, G., 2008. Ortlepp shears—dynamic brittle shears of South African gold mines. In *Proceedings of the first southern hemisphere international rock mechanics symposium,* Y. Potvin, J.Caster, A. Dyskin and R. Jeffrey (eds). Australian Centre for Geomechanics, pp.111-119.

Van der Heever, P and Ryder, J.A., 2007. Characterisation of the Westonaria Formation at Main Shaft, Kloof Gold Mine. Consultancy Report. Groundwork. Johannesburg, South Africa.

Van der Westhuizen, W.A., De Bruiyn, H. and Meintjes, P.G., 1991. The Ventersdorp supergroup: an overview. *Journal of African Earth Sciences (and the Middle East)*, *13*(1), pp.83-105.

Vavryčuk, V., 2011. Tensile earthquakes: Theory, modeling, and inversion. *Journal of Geophysical Research: Solid Earth*, *116*(B12):12320, pp.1-14.

Vavryčuk, V. and Kühn, D., 2012. Moment tensor inversion of waveforms: a two-step time-frequency approach. *Geophysical Journal International*, *190*(3), pp.1761-1776.

Vavryčuk, V. (2014). Moment tensors: Decomposition and visualization. In M. Beer, I. A. Kougioumtzoglou, E. Patelli, & I. S.-K. Au (Eds.), *Encyclopedia of earthquake engineering* (pp. 1– 16). Berlin, Heidelberg: Springer Berlin Heidelberg.

Vavryčuk, V., 2015. Moment tensor decompositions revisited. *Journal of Seismology*, *19*(1), pp.231-252.

Viljoen, M., 2009. The life, death and revival of the Central Rand goldfield. *Special Publication for the World Gold Conference*, pp.131-138.

Visser, J.N.J. and Joubert, A., 1990. Possible earthquake-induced sediment liquefaction in thermal spring deposits at Florisbad, Orange Free State. *South African Journal of Geology*, *93*(3), pp.525-530.

Wallace, T.C., 1985. A re-examination of the moment tensor solutions of the 1980 Mammoth Lakes earthquakes. *Journal of Geophysical Research: Solid Earth*, *90*(B13), pp.11171-11176.

Warner, M., 1990. Absolute reflection coefficients from deep seismic reflections. *Tectonophysics*, *173*(1-4), pp.15-23.

Wesseloo, J. and Sweby, G.J. (2008). Microseismic Monitoring of Hard Rock Mine Slopes. *Proceedings of First Southern Hemisphere International Rock Mechanics Symposium, SHIRMS 2008*. Potvin, Y., Carter, J., Dyskin, A. and Jeffrey, R., (eds.), Perth, Western Australia, Australian Centre for Geomechanics, pp. 433–450.

Wesseloo, J., Woodward, K. and Pereira, J., 2014. Grid-based analysis of seismic data. *In Proceedings of the 6th South African Rock Engineering Symposium, SARES 2014,* South Africa, Southern African Institute of Mining and Metallurgy, Johannesburg, pp. 815-822.

Wiles, T.D., 2006. Course notes: MAP3D User's Manual, Mine Numerical Modelling.

Yilmaz, H., 2016. Course notes: Advanced mechanics of solids. University of the Witwatersrand, Johannesburg.

Yilmaz, Ö., 2001. *Seismic data analysis: Processing, inversion, and interpretation of seismic data*. Society of exploration geophysicists.

Yoshida, N., Morgenstern, N.R. and Chan, D.H., 1990. A failure criterion for stiff soils and rocks exhibiting softening. *Canadian Geotechnical Journal*, *27*(2), pp.195-202.

Yudhbir, Y., Lemanza, W. and Prinzl, F., 1983. An empirical failure criterion for rock masses. *In Proceedings of 5th Congress of International Society for Rock Mechanics and Rock Engineering*. Melbourne, pp.10-18.

APPENDICES

Appendix A: *South African National Seismograph Network (SANSN) stations* with their installation date and type of instrumentation.Lastly the brief explanation of seismic parameters

Table A: South African National Seismograph Network stations with their installation date and type of instrumentation (extracted from CGS, 2012). SANSN – South African National Seismograph Network, SWMP – Strategic Water Management Project Broadband – B, Extended Short Period – ESP, Short Period – SP, Strong Motion – SM, Vertical – V, East-West – EW, North-South – NS, Klerksdorp Orkney Stillfontein Haartebesfontein – KOSH, Water Ingress – WI.

Station Location	Operation Date	Instrumentation	Classification
Grahamstown	Oct 1967 to Nov 2013	B: V, EW and NS	SANSN, part of AfricaArray
Ceres	May 1971 to Present	B: V, EW and NS	SANSN, part of AfricaArray
Gariep Dam	Jun 1971 to Present	ESP: V, EW and NS	SANSN, part of AfricaArray
Koster	Jun 1972 to Present	ESP: V, EW and NS	SANSN
Silverton	Jul 1981 to Present	B: V, EW and NS	SANSN
Senekal	Sep1982 to 2011	ESP: V, EW and NS	SANSN
Belfast	Mar 1986 to 2009	ESP: V, EW and NS	Not operating (vandalized)
Upington	Sep1991 to Present	B: V, EW and NS	SANSN, part of AfricaArray
Calvinia	Feb 1992 to Present	B: V, EW and NS	SANSN, part of AfricaArray
Prieska	Jul 1992 to Present	ESP: V, EW and NS	SANSN, part of AfricaArray
Schweizer-Reneke	Aug 1992 to Present	ESP: V, EW and NS	SANSN
Newcastle	Nov 1992 to 2004	SP: V	SANSN

Musina	Sep 1993 to Present	B: V, EW and NS	SANSN, part of AfricaArray
Kokstad	Apr 1995 to Present	B: V, EW and NS	SANSN
Elim	Oct 1996 to Present	SP: V, EW and NS	SANSN
Komaggas	May 1997 to Present	ESP: V, EW and NS	SANSN
Buffelsbos	Dec 1997 to Present	SP: V, EW and NS	SANSN
Mopani	Apr 2004 to Present	SP: V, EW and NS	SANSN, part of AfricaArray
Lephalale	Nov 2004 to 2005	ESP: V, EW and NS	SANSN
Parys	Nov 2004 to Present	ESP: V, EW and NS	SANSN
Pongola	Mar 2005 to Present	B: V, EW and NS	SANSN, part of AfricaArray
Somerset East	Mar 2005 to Present	ESP: V, EW and NS	SANSN, part of AfricaArray
East Rand Propriety Mines	May 2006 to Present	SP: V, EW and NS	SANSN
Kloof	Aug 2006 to Present	SP: V, EW and NS	SANSN
Buffelsfontein	Apr 2008 to 2012	SM: V, EW and NS	KOSH
Tau Lekoa	Apr 2008 to 2012	SM: V, EW and NS	KOSH
Moab Khotsong	May 2008 to 2012	SM: V, EW and NS	KOSH
Western Deep Levels Mine	Dec 2009 to Present	B: V, EW and NS	SANSN
Crown Mines	Feb-10	SP: V, EW and NS	SWMP
Keimoes	Nov 2010 to Present	SP: V, EW and NS	SANSN
Observatory	2010 to 2012	SP: V, EW and NS	WI
Augrabies	Apr 2011 to Present	ESP	SANSN
Kromhout	Sep 2011 to Present	SP: V, EW and NS	SANSN
Rosenhof	Sep 2011 to Present	SP: V, EW and NS	SANSN
Grantham	Nov 2012 to Present	ESP: V, EW and NS	SANSN

Brief explanation of seismic parameters : Measuring the size of an earthquake

Tectonic earthquakes

Generally different scales have been defined some commonly used are :

- M_L = Log (A_{max}) +B log (R) – C (Fernández ,1968)
- M_w = 2⁄3 log M_o – 6 (Hanks and Kanamori, 1979)
- Others (M_S, M_d, M_b,M_c etc.)

where

M_L- Local magnitude ,

A_{max}- Maximum amplitude (nm),

R- Hypocental distance in km ,

B and C are regional scaling factor,

M_w - Moment magnitude,

M_0 – Seismic Moment (N.m),

M_s - Surface wave magnitude,

M_d - Duration magnitude,

M_b - Body wave magnitude, and

M_c – Coda magnitude.

Mining-induced seismic events (earthquakes)

Local magnitude (M_L) definition was based on the equation :

$$\mathbf{M_L = A\ Log\ (E) + B\ Log\ (M_o) – C}$$

where A, B and C are magnitude calibration constants that differs from different region and mines. Typical common used values are as follow (Ebrahim-Trollope and Jooste, 2005) :

- Carletonville: A - 0.272, B - 0.393, C - 4.630
- Klerksdorp: A - 0.263, B - 0.333, C - 3.612 and
- Welkom: A - 0.275, B - 0.433 and C -5.124.

Sibanye-Stillwater Group currently uses:

$$\mathbf{M_L = 0.344\ log\ (E) + 0.516\ log\ (M_o) - 6.572}$$

where **E** and $\mathbf{M_o}$ represents Seismic Energy (J) and Seismic Moment (N.m), respectively.

Appendix B: Geophones used in the seismic monitoring

Table B : Triaxial Geophone in the seismic system

4.5 Hz Geophones are usually the sensor of choice in most mining applications, because of the low cost, large bandwidth and excellent reliability. The 4.5 Hz geophone has a usable frequency bandwidth of between 3 Hz (natural frequency for very large seismic events above Magnitude 3), and 2000 Hz (high-frequency small events of below magnitude -1.0).

The 4.5Hz geophones are the primary geophone used to record seismic events for all large Gold and Platinum Mining Companies in South Africa, and worldwide.

Small events of magnitude below -1.0 have been recorded by a 4.5Hz geophone located more than 2 km from the source of an event. This obviously depends on the quality of the signal that the seismic geophone can record. On the Sibanyestillwater Mines using GS technology, we have been able to record events smaller than -1.0 from distances of more than 2 km.

4.5Hz geophones are installed and grouted into a vertical down borehole. The borehole was drilled 10 meters down from the footwall of a suitable excavation. The diameter of the borehole must be NX (76mm). 4.5Hz is the geophone of choice for Kloof Operation for the following reasons –

- These geophones are most suited for the recording of events generated on mine-wide systems in South Africa.
- Kloof Operation offers limited access for the positioning of geophones. These geophones are suitable for installing a distance away from mining.
- These geophones offer good regional seismic coverage for seismic events smaller than magnitude -1.0

Appendix C : Software used for the peak particle velocity, location accuracy and seinsitivity analysis.

Table C: Peak Particle Velocity (PPV), Sensitivity and Location accuracy

The “Egret” software module is a Windows-based computer program that has been developed by Hamerkop Scientific Services (Dr Ted Stankiewicz). It allows for the optimisation and planning of seismic network layouts, more especially those applicable to underground mines. Two parameters are important in this respect namely, location accuracy and system sensitivity.

The sensitivity of any network can be calculated using an empirical relationship between peak particle velocity (PPV), magnitude (or energy) and the hypocentral distance of any event i.e.

Log (PPV) = A*Magnitude – B*Log (Distance) + C

So, if a site can be used for location, and if the amplitude of the waveform exceeds some threshold level (e.g. signal/noise ratio 10 as used in the STA/LTA trigger criterion), then sensitivity can be estimated. Given the occurrence of an event in any assumed position (X, Y, Z), if the PPV from this event location exceeds this level using the above relationship for a given minimum number of sites, then the event can be detected and located. The minimum magnitude of such an event is the sensitivity of the network in the assumed X, Y, Z location.

Location accuracy is dependent on the condition that an event can be detected and located as outlined above. The equations for the arrival times as used in the location process can be utilised to generate an estimate of the errors associated with the solution of the least-squares method used in the location algorithm. Inputs for this estimate include the minimum number of sites required in the triggering process, as well as the expected errors in the wave velocities and the arrival picks used during the location.

Based on the above methodology, the program then generates the expected magnitude and sensitivity using a spatial layout of grid points on a two-dimensional plane. The depth of this plane must also be specified during the input process. Some versions of the Hamerkop software include the option of an inclined plane. Otherwise, the variation in accuracy and sensitivity for various depths above and below any reef plane can then be investigated by means of repeated runs of the software using various depth values. The variation in the expected location accuracy and system sensitivity is then summarized using various contour plots of the results.

Appendix D : Procedure for the large seismic event.

Table D1. Procedures to be implemented when a seismic event of M≥0.9 occurs in a working stope within an area of interest (Sibanyestillwater Seismological Department, 2018).

Seismic Event Magnitude	Affected Radius (from Centroid)	Required Procedure
$0.9 \leq M_L \leq 1.5$	50m	Phone all crews within a radius of 50m and inform of the seismic event. Crews to assess the workplace and to complete the seismic checklist. The crew has the right to withdrawal. Crew to report to the Shaft Control Room regarding the situation.
$1.6 \leq M_L \leq 2.0$	100m	Phone all crews within a radius of 100m and inform of the seismic event. Crews to assess the workplace and to complete the seismic checklist. The crew has the right to withdrawal. Crew to report to the Shaft Control Room regarding the situation.
$2.1 \leq M_L \leq 2.5$	200m	Phone all crews within a radius of 200m and inform of the seismic event. Crews to withdraw to the waiting place or Refuge Bay further than 200m away from the hypocentre and wait for instruction from the line supervisor. Crew to report to the Shaft Control Room regarding the situation.
$2.6 \leq M_L \leq 3.0$	400m	Phone all crews within a radius of 400m and inform of the seismic event. Crews to withdraw to the waiting place or Refuge Bay further than 400m away from the hypocentre and wait for instruction from the line supervisor. Crew to report to the Shaft Control Room regarding the situation.
$3.1 \leq M_L \leq 3.5$	1000m	Phone all crews within a radius of 1000m and inform of the seismic event. Crews to withdraw to the waiting place or Refuge Bay further than 1000m away from the hypocentre and wait for instruction from the line supervision. Crew to report to the Shaft Control Room regarding the situation.
$M_L \geq 3.6$	Total Shaft evacuation	Phone all crews on the shaft and inform of the seismic event. All crews to withdraw to the station and wait for instructions from the line supervision.

(N.B) - The above applies immediately to the affected working place for the shift underground. The following shift must be advised by means of the revised Seismic Rating (SR) which should be run and updated after large magnitude events.

Appendix E : Seismic event locations, Moment Tensor, Fault plane solution and Source Parameters.

Table E1 : Seismic event time is local time (subtract two hours to obtain UTC time). Event locations are listed in terms of the mine co-ordinate system specifying their latitude (X), longitude (Y), and depth (Z- meters below datum). The datum reference point on Kloof Gold Mine is about 250 m above the surface and 1800 m above sea level.

Seismic event Number	Event Date and Time	Location Error (m)	X (m)	Y (m)	Z(m)	Moment (Nm)	Local Magnitude (M_L)	Energy (Joules)	Corner Frequency (Hz)	Static Stress Drop (MPa)
1	20170307 164126	18	22523.5	-10804.5	-3290.9	1.39E+13	2.6	1.52E+08	13	1.63E+06
2	20170331 175326	29	22387.5	-10862.4	-3477.6	8.99E+11	1.6	4.23E+06	14	4.27E+05
3	20170715 162357	25	21960.1	-10966.9	-3196.6	7.04E+12	2.6	2.58E+08	15	6.75E+06
4	20170729 202255	30	21574.8	-9994.5	-2344.8	3.32E+12	2.2	5.40E+07	16	1.99E+06
5	20170731 022236	28	22361.5	-10253.8	-3082.3	5.86E+11	1.5	5.24E+06	20	1.22E+06
6	20170818 090901	24	21974.3	-10909.4	-1906.4	7.37E+12	2.3	4.06E+07	13	7.83E+05
7	20170822 105230	31	21026.5	-11661.6	-3918.7	3.90E+12	2.3	6.65E+07	16	4.10E+06
8	20171009 141642	29	21904.1	-10538.4	-2940.2	6.04E+11	1.5	5.51E+06	20	1.49E+06
9	20171017 211230	29	22711.5	-10529.5	-2950.3	7.50E+12	2.4	7.41E+07	13	1.20E+06
10	20171019 015107	31	22035.1	-11177.6	-3433	1.98E+12	1.9	1.14E+07	15	5.92E+05
11	20171021 161958	30	22103.7	-11539.1	-3175.7	6.81E+11	1.6	5.26E+06	18	5.93E+05
12	20171023 094245	29	22680.1	-10940.2	-2351.5	1.04E+13	2.7	3.45E+08	15	4.99E+06
13	20171023 103209	29	22293.9	-10799.8	-2943.4	1.54E+12	1.9	1.80E+07	17	1.02E+06

14	20171027 080443	29	22043.1	-12042	-3774.5	3.24E+12	2.1	3.29E+07	17	2.68E+06
15	20171028 215820	30	20537.2	-12214.8	-4174.2	8.56E+11	1.7	9.47E+06	17	1.56E+06
16	20171031 010807	30	23147.4	-10479	-2978	5.07E+11	1.5	4.43E+06	24	1.45E+06
17	20171103 221501	30	21575.4	-11497.7	-3690.7	7.55E+11	1.5	4.12E+06	18	5.59E+05
18	20171110 003754	25	21320.7	-11771	-3363.6	7.43E+11	1.5	2.29E+06	18	8.61E+05
19	20171116 131014	25	21610	-10006.3	-2438	6.04E+11	1.6	6.51E+06	17	2.00E+06
20	20171126 005305	25	20775.3	-11444.2	-2776.2	2.53E+12	2.0	1.75E+07	16	1.35E+06
21	20171211 135853	25	21994.7	-11608.9	-3223.5	5.90E+11	1.5	3.44E+06	16	4.62E+05
22	20171211 142353	28	23015.6	-10751.2	-2777.5	8.97E+11	1.6	4.20E+06	16	7.76E+05
23	20171214 050211	30	21411.6	-11984.9	-2899.7	4.23E+12	2.2	4.70E+07	17	1.30E+06
24	20171219 050805	28	21874.9	-11433.7	-3098.4	2.66E+12	2.1	2.61E+07	13	5.07E+05
25	20171220 064504	27	21651.2	-12104.1	-3280.4	4.62E+12	2.1	1.40E+07	15	5.73E+05
26	20171225 071122	28	21979.2	-11532.8	-3476	1.26E+12	1.7	6.64E+06	15	1.02E+06
27	20180102 122952	28	21586.2	-11869.8	-3077.7	9.08E+11	1.7	7.45E+06	22	8.03E+05
28	20180104 192629	29	22281.4	-11194.4	-3465.5	7.36E+11	1.5	4.07E+06	14	8.07E+05
29	20180113 022616	26	21576.6	-9339	-2100.8	1.17E+12	1.6	3.70E+06	18	5.30E+05
30	20180113 023808	27	21674.9	-9241.9	-1967	3.32E+12	2.1	2.82E+07	15	1.03E+06
31	20180115 002045	24	22472	-11575.3	-3494.8	5.00E+11	1.5	4.25E+06	26	1.74E+06
32	20180116 220402	35	21494.5	-11906	-3129.7	2.36E+12	1.8	6.05E+06	18	1.14E+06
33	20180121 033457	26	22091.2	-12241.4	-3310.2	1.16E+12	1.5	2.30E+06	16	4.13E+05
34	20180125 230457	28	22014.6	-11285.9	-2985	1.45E+12	1.9	1.59E+07	15	1.40E+06
35	20180127 184558	29	22119	-11560.7	-3001.5	9.21E+12	2.3	3.39E+07	14	7.01E+05

36	20180129 004428	31	21661	-11904.6	-3541.5	3.54E+12	2.1	3.25E+07	17	1.17E+06
37	20180212 010742	29	22020.8	-11385.9	-2911.1	1.08E+12	1.8	1.66E+07	16	1.60E+06
38	20180217 163457	30	23193.5	-10860.6	-2074.6	5.16E+12	2.3	7.50E+07	15	3.02E+06
39	20180219 220252	29	22218.5	-12449.6	-2788.7	7.00E+11	1.5	2.84E+06	16	7.80E+05
40	20180223 001911	30	21745.6	-11694.9	-3297.1	7.14E+11	1.5	3.90E+06	18	1.12E+06
41	20180317 191617	36	21624.2	-10245.5	-1625.9	2.92E+12	2.1	2.67E+07	15	1.99E+06
42	20180317 214226	36	22383.1	-12449.3	-2809.5	1.15E+13	2.7	3.19E+08	16	5.72E+06
43	20180322 231627	28	22237	-9994.9	-2628.9	7.79E+11	1.6	4.89E+06	18	1.58E+06
44	20180329 173214	35	21376	-10033.2	-2557.1	1.80E+12	1.9	1.68E+07	14	1.87E+06
45	20180402 055211	30	21755.4	-12271.4	-2765.3	9.17E+11	1.8	1.45E+07	19	1.82E+06
46	20180404 120747	32	20357.7	-9673.9	-1840.7	1.33E+12	1.8	9.11E+06	15	2.13E+06
47	20180406 051333	30	21988	-10133.7	-1756.1	5.55E+11	1.5	5.25E+06	20	2.55E+06
48	20180411 211434	28	21620.6	-12450.2	-2665.9	2.10E+12	1.8	8.11E+06	17	1.08E+06
49	20180420 155924	23	22989.2	-10783.3	-2998.3	1.11E+12	1.8	1.28E+07	17	1.61E+06
50	20180428 000853	40	21516.9	-11912.8	-3115.1	9.35E+11	1.5	3.31E+06	18	9.03E+05
51	20180504 181525	28	21727.8	-9760.7	-2260.6	7.60E+11	1.5	2.43E+06	19	9.97E+05
52	20180504 205920	28	21809.5	-9770.2	-2426.7	2.58E+12	1.9	1.23E+07	18	1.56E+06
53	20180522 003124	32	22933.2	-10682.9	-3382.3	3.18E+12	2.2	5.55E+07	16	2.52E+06
54	20180526 083550	29	21539.2	-12007.5	-3083	4.28E+12	2	8.22E+06	17	1.21E+06
55	20180608 090342	29	21622.1	-9647.5	-2402.1	1.46E+12	1.8	1.02E+07	16	1.93E+06
56	20180626 181730	32	21668.7	-9887.6	-2341.1	6.80E+11	1.5	4.52E+06	27	2.13E+06
57	20180628 181056	27	21754.1	-12108.7	-3080.9	2.30E+13	2.7	1.44E+08	14	3.31E+06

58	20180628 233131	31	21554.6	-11588	-3368.3	2.49E+12	2.1	3.63E+07	14	2.62E+06
59	20180803 134602	32	21472.3	-11915.8	-2973.5	7.02E+11	1.5	3.67E+06	16	1.03E+06
60	20180813 230521	21	21648.2	-9995.7	-2383.5	1.33E+12	1.8	1.28E+07	17	1.71E+06
61	20180816 183153	25	21592.6	-11913.8	-2917.9	2.51E+12	2	2.02E+07	17	2.08E+06
62	20180826 190054	30	22024.1	-11659.2	-3064.1	2.37E+12	1.8	6.39E+06	16	1.01E+06
63	20180831 205912	26	21613.9	-9980.5	-2368.5	7.55E+11	1.6	7.37E+06	18	1.96E+06
64	20180902 061326	31	22203.4	-12321.2	-3290.3	2.73E+12	2	2.40E+07	14	1.79E+06
65	20180910 214921	24	22126.4	-11896.5	-3344	6.70E+11	1.5	2.84E+06	20	1.35E+06
66	20180913 032343	25	21325	-11845.2	-3130.7	7.27E+11	1.6	5.03E+06	15	1.27E+06
67	20180915 035929	23	21385.9	-11787.8	-3362.2	1.24E+12	1.7	6.32E+06	17	1.36E+06
68	20181005 024848	24	21733.1	-11436.5	-3288.4	8.24E+11	1.5	3.44E+06	15	7.50E+05
69	20181007 082527	30	21679.8	-11529.5	-3342.1	7.32E+12	2.5	1.33E+08	14	3.23E+06
70	20181008 174016	27	22044.7	-11688.8	-3250.4	7.34E+11	1.5	2.42E+06	14	7.99E+05
71	20181016 161913	27	21494.6	-12247.3	-3198.5	1.06E+12	1.6	3.03E+06	16	9.83E+05
72	20181017 144042	29	21769.3	-11690.1	-3270.4	3.66E+12	2.1	2.63E+07	14	1.72E+06
73	20181110 233000	37	21509.9	-12221.1	-3118.6	1.28E+12	1.6	3.96E+06	15	1.00E+06
74	20181119 121437	29	21066.1	-9750.9	-1961.3	4.07E+12	2.1	2.47E+07	16	1.83E+06
75	20181123 093447	44	21399.3	-11944	-2933.3	9.53E+11	1.7	9.19E+06	16	1.17E+06

Table E2 : Moment tensor solutions

No.	Event Date and Time	X (m)	Y (m)	Z(m)	Moment (Nm)	Local Magnitude (M_L)	DEV	ISO	Misfit	QI	Es/Ep ratio	M_{xx} (10^{12}) Nm	M_{yy} (10^{12}) Nm	M_{zz} (10^{12}) Nm	M_{xy} (10^{12}) Nm	M_{xz} (10^{12}) Nm	M_{yz} (10^{12}) Nm
1	20 170 307 164 126	22523.5	-10804.5	-3290.9	1.39E+13	2.6	88.5	11.5	0.34	0.56	6.6	-0.36	0.41	-0.66	0.21	-0.45	0.01
2	20 170 331 175 326	22387.5	-10862.4	-3477.6	8.99E+11	1.6	60.1	39.9	0.33	0.52	3.3	-0.35	-0.26	-0.59	0.14	-0.38	0.28
3	20 170 715 162 357	21960.1	-10966.9	-3196.6	7.04E+12	2.6	95.3	4.7	0.32	0.48	4.7	-0.26	0.51	-0.57	0.15	-0.57	-0.14
4	20 170 729 202 255	21574.8	-9994.5	-2344.8	3.32E+12	2.2	74.2	25.8	0.31	0.6	8.9	-0.25	0.13	0.63	0.42	-0.05	0.54
5	20 170 731 022 236	22361.5	-10253.8	-3082.3	5.86E+11	1.5	75.3	24.7	0.24	0.68	10	-0.36	0.34	-0.73	0.08	0.05	0.43
6	20 170 818 090 901	21974.3	-10909.4	-1906.4	7.37E+12	2.3	94.8	5.2	0.39	0.9	10.8	0.29	0.25	-0.69	-0.22	-0.22	0.69
7	20 170 822 105 230	21026.5	-11661.6	-3918.7	3.90E+12	2.3	74.9	25.1	0.29	0.65	9.4	-0.23	0.71	0.27	-0.02	-0.23	-0.45
8	20 171 009 141 642	21904.1	-10538.4	-2940.2	6.04E+11	1.5	93.1	6.9	0.27	0.65	9.4	0.29	0.1	-0.59	0.38	-0.68	0.01
9	20 171 017 211 230	22711.5	-10529.5	-2950.3	7.50E+12	2.4	76.3	23.7	0.35	0.48	11.3	-0.4	0.27	-0.64	-0.14	-0.42	-0.19
10	20 171 019 015 107	22035.1	-11177.6	-3433	1.98E+12	1.9	85	15	0.22	0.6	5.7	-0.33	0.05	0.73	0.42	-0.15	0.44
11	20 171 021 161 958	22103.7	-11539.1	-3175.7	6.81E+11	1.6	89.2	10.8	0.34	0.4	3.2	0.44	0.15	-0.91	0.34	-0.35	0

12	20 171 023 094 245	22680.1	-10940.2	-2351.5	1.04E+13	2.7	71.8	28.2	0.26	0.8	10.6	-0.1	0.77	0.18	0.33	-0.25	0.18
13	20 171 023 103 209	22293.9	-10799.8	-2943.4	1.54E+12	1.9	95	5	0.38	0.5	6.9	-0.1	0.56	-0.61	0.12	-0.57	-0.32
14	20 171 027 080 443	22043.1	-12042	-3774.5	3.24E+12	2.1	72.4	27.6	0.34	0.57	8.8	-0.36	-0.1	-0.37	-0.34	0.37	0.35
15	20 171 028 215 820	20537.2	-12214.8	-4174.2	8.56E+11	1.7	71.3	28.7	0.24	0.53	12.1	0.02	-0.38	-0.5	0.25	-0.42	0.32
16	20 171 031 010 807	23147.4	-10479	-2978	5.07E+11	1.5	69.6	30.4	0.33	0.48	8.5	0.06	0.45	0.4	-0.4	-0.03	-0.49
17	20 171 103 221 501	21575.4	-11497.7	-3690.7	7.55E+11	1.5	71.8	28.2	0.36	0.79	5.5	-0.67	0.12	-0.3	0.31	-0.44	-0.11
18	20 171 110 003 754	21320.7	-11771	-3363.6	7.43E+11	1.5	87.3	12.7	0.25	0.29	2.2	-0.11	0.4	0.09	-0.03	-0.06	-0.74
19	20 171 116 131 014	21610	-10006.3	-2438	6.04E+11	1.6	78.2	21.8	0.27	0.63	8.4	-0.41	0.16	0.89	0.13	0.35	0.1
20	20 171 126 005 305	20775.3	-11444.2	-2776.2	2.53E+12	2	97.4	2.6	0.32	0.46	3.2	-0.08	0.9	-0.9	-0.01	-0.08	-0.9
21	20 171 211 135 853	21994.7	-11608.9	-3223.5	5.90E+11	1.5	99.4	0.6	0.18	0.41	8.9	-0.42	0.37	0.03	-0.02	-0.56	-0.68
22	20 171 211 142 353	23015.6	-10751.2	-2777.5	8.97E+11	1.6	90	10	0.28	0.61	14	-0.6	0.01	0.9	-0.13	0.12	-0.3
23	20 171 214 050 211	21411.6	-11984.9	-2899.7	4.23E+12	2.2	63.6	36.4	0.34	0.72	8	-0.48	-0.06	-0.55	0.02	-0.47	-0.55
24	20 171 219 050 805	21874.9	-11433.7	-3098.4	2.66E+12	2.1	89.2	10.8	0.25	0.43	19.9	-0.23	0.54	0.01	0.14	-0.39	-0.57

25	20 171 220 064 504	21651.2	-12104.1	-3280.4	4.62E+12	2.1	55.2	44.8	0.17	0.43	4	-0.4	-0.15	-0.8	0.04	-0.34	-0.8
26	20 171 225 071 122	21979.2	-11532.8	-3476	1.26E+12	1.7	95.6	4.4	0.16	0.5	9.1	-0.29	0.46	-0.31	0.27	-0.5	-0.51
27	20 180 102 122 952	21586.2	-11869.8	-3077.7	9.08E+11	1.7	61.8	38.2	0.33	0.61	5.6	-0.34	-0.24	-0.72	0.07	-0.43	-0.01
28	20 180 104 192 629	22281.4	-11194.4	-3465.5	7.36E+11	1.5	76.1	23.9	0.25	0.63	5	-0.03	-0.13	-0.61	0.03	-0.56	-0.27
29	20 180 113 022 616	21576.6	-9339	-2100.8	1.17E+12	1.6	85.1	14.9	0.43	0.69	4.5	0.99	0.12	-0.55	0.07	0.1	-0.55
30	20 180 113 023 808	21674.9	-9241.9	-1967	3.32E+12	2.1	79.1	20.9	0.42	0.71	11.8	-0.42	0.21	-0.42	-0.3	0.39	0.39
31	20 180 115 002 045	22472	-11575.3	-3494.8	5.00E+11	1.5	94.3	5.7	0.36	0.57	4.1	0.67	-0.08	-0.68	0.31	0.47	0.18
32	20 180 116 220 402	21494.5	-11906	-3129.7	2.36E+12	1.8	57.9	42.1	0.25	0.56	1.1	-0.31	-0.02	-0.79	0	-0.37	0.13
33	20 180 121 033 457	22091.2	-12241.4	-3310.2	1.16E+12	1.5	79.1	20.9	0.4	0.52	2.1	0.14	0.03	-0.79	0.29	-0.02	0.44
34	20 180 125 230 457	22014.6	-11285.9	-2985	1.45E+12	1.9	61.1	38.9	0.36	0.45	5.8	0.35	0.23	0.59	1	0.17	-0.54
35	20 180 127 184 558	22119	-11560.7	-3001.5	9.21E+12	2.3	82.8	17.2	0.4	0.54	3.7	-0.54	-0.54	0.54	-0.11	0.25	-0.2
36	20 180 129 004 428	21661	-11904.6	-3541.5	3.54E+12	2.1	72.8	27.2	0.27	0.69	4.9	-0.18	-0.19	-0.86	0.07	-0.33	-0.86
37	20 180 212 010 742	22020.8	-11385.9	-2911.1	1.08E+12	1.8	96.3	3.7	0.34	0.46	8.5	0.22	0.01	-0.73	-0.33	0.25	-0.52

38	20 180 217 163 457	23193.5	-10860.6	-2074.6	5.16E+12	2.3	60.7	39.3	0.34	0.91	5.7	-0.41	-0.53	-0.23	-0.01	-0.39	-0.4
39	20 180 219 220 252	22218.5	-12449.6	-2788.7	7.00E+11	1.5	78.3	21.7	0.23	0.79	8.7	0.35	-0.27	0.57	0.1	0.47	0.27
40	20 180 223 001 911	21745.6	-11694.9	-3297.1	7.14E+11	1.5	58.6	41.4	0.34	0.41	4.3	-0.2	-0.22	-0.82	-0.12	0.12	-0.37
41	20 180 317 191 617	21624.2	-10245.5	-1625.9	2.92E+12	2.1	82.4	17.6	0.33	0.95	12.5	-0.34	0.82	0.05	0.49	-0.08	0
42	20 180 317 214 226	22383.1	-12449.3	-2809.5	1.15E+13	2.7	66	34	0.33	0.75	10.5	-0.15	-0.31	-0.56	0.3	-0.49	-0.08
43	20 180 322 231 627	22237	-9994.9	-2628.9	7.79E+11	1.6	82.5	17.5	0.25	0.54	3.6	-0.11	0.28	-0.69	0.38	-0.51	-0.11
44	20 180 329 173 214	21376	-10033.2	-2557.1	1.80E+12	1.9	96.9	3.1	0.28	0.71	6.1	0.39	-0.02	-0.28	0.48	-0.69	0.22
45	20 180 402 055 211	21755.4	-12271.4	-2765.3	9.17E+11	1.8	76.1	23.9	0.32	0.69	8.8	-0.22	0.12	-0.62	-0.15	0.02	-0.5
46	20 180 404 120 747	20357.7	-9673.9	-1840.7	1.33E+12	1.8	84	16	0.42	0.78	6.2	-0.22	0.24	-0.5	-0.07	-0.52	0.48
47	20 180 406 051 333	21988	-10133.7	-1756.1	5.55E+11	1.5	83.1	16.9	0.39	0.94	4.9	0.06	-0.06	-0.5	-0.22	-0.57	-0.29
48	20 180 411 211 434	21620.6	-12450.2	-2665.9	2.10E+12	1.8	49.1	50.9	0.36	0.76	6.4	-0.51	-0.51	-0.51	-0.09	-0.41	0.19
49	20 180 420 155 924	22989.2	-10783.3	-2998.3	1.11E+12	1.8	89.4	10.6	0.29	0.51	4.9	-0.52	-0.12	0.32	0.5	-0.54	-0.06
50	20 180 428 000 853	21516.9	-11912.8	-3115.1	9.35E+11	1.5	60.6	39.4	0.25	0.38	9.1	-0.35	0	-0.83	-0.19	-0.02	-0.39

51	20 180 504 181 525	21727.8	-9760.7	-2260.6	7.60E+11	1.5	75.8	24.2	0.33	0.62	4.1	-0.08	0	-0.65	-0.11	0.53	-0.14
52	20 180 504 205 920	21809.5	-9770.2	-2426.7	2.58E+12	1.9	62.1	37.9	0.27	0.72	3.7	-0.21	-0.18	-0.75	0.29	-0.32	0.17
53	20 180 522 003 124	22933.2	-10682.9	-3382.3	3.18E+12	2.2	60.3	39.7	0.37	0.57	11.1	-0.39	-0.48	-0.32	0.27	-0.27	0.35
54	20 180 526 083 550	21539.2	-12007.5	-3083	4.28E+12	2	57	43	0.39	0.65	2.3	-0.45	-0.1	-0.75	0.06	-0.34	0.16
55	20 180 608 090 342	21622.1	-9647.5	-2402.1	1.46E+12	1.8	72.4	27.6	0.27	0.74	4.7	-0.51	0.25	-0.56	0.04	-0.46	-0.07
56	20 180 626 181 730	21668.7	-9887.6	-2341.1	6.80E+11	1.5	93.5	6.5	0.29	0.67	3.8	-0.41	0.35	0.25	0.49	-0.48	-0.36
57	20 180 628 181 056	21754.1	-12108.7	-3080.9	2.30E+13	2.7	45.3	54.7	0.26	0.74	4.6	-0.39	-0.43	-0.82	0.06	-0.26	-0.22
58	20 180 628 233 131	21554.6	-11588	-3368.3	2.49E+12	2.1	73.2	26.8	0.31	0.51	5	0.27	-0.33	-0.74	0.25	-0.31	-0.74
59	20 180 803 134 602	21472.3	-11915.8	-2973.5	7.02E+11	1.5	70.8	29.2	0.33	0.66	3.4	-0.37	0.18	-0.69	0.08	-0.41	-0.27
60	20 180 813 230 521	21648.2	-9995.7	-2383.5	1.33E+12	1.8	95.2	4.8	0.26	0.67	8.7	0.03	0.03	0.08	0.52	0.01	0.78
61	20 180 816 183 153	21592.6	-11913.8	-2917.9	2.51E+12	2	63.3	30.7	0.37	0.71	7.1	-0.28	0.06	-0.71	0.11	-0.44	-0.25
62	20 180 826 190 054	22024.1	-11659.2	-3064.1	2.37E+12	1.8	53.2	46.8	0.34	0.57	5.8	-0.41	-0.21	-0.78	0.17	-0.29	0.15
63	20 180 831 205 912	21613.9	-9980.5	-2368.5	7.55E+11	1.6	82.1	17.9	0.25	0.68	13.1	-0.21	-0.38	0.06	0.4	0.14	0.62

64	20 180 902 061 326	22203.4	-12321.2	-3290.3	2.73E+12	2	92.9	7.1	0.42	0.53	7.6	-0.04	0.18	0.07	0.57	0.63	0.18
65	20 180 910 214 921	22126.4	-11896.5	-3344	6.70E+11	1.5	59.1	40.9	0.31	0.45	2.1	-0.01	-0.44	-0.78	0.3	-0.19	-0.78
66	20 180 913 032 343	21325	-11845.2	-3130.7	7.27E+11	1.6	82.3	17.7	0.3	0.52	4.5	-0.04	0.27	-0.27	-0.17	-0.2	-0.46
67	20 180 915 035 929	21385.9	-11787.8	-3362.2	1.24E+12	1.7	80.8	19.2	0.33	0.47	2.3	-0.1	0.11	-0.59	0.07	-0.59	0.13
68	20 181 005 024 848	21733.1	-11436.5	-3288.4	8.24E+11	1.5	62.6	37.8	0.29	0.46	2.8	-0.31	-0.09	-0.73	0.05	-0.43	-0.04
69	20 181 007 082 527	21679.8	-11529.5	-3342.1	7.32E+12	2.5	88.6	11.4	0.29	0.48	7	0.19	0.08	-0.61	0.28	-0.56	0.22
70	20 181 008 174 016	22044.7	-11688.8	-3250.4	7.34E+11	1.5	51.5	48.5	0.28	0.45	3.6	-0.46	-0.26	-0.74	0.11	-0.35	0.07
71	20 181 016 161 913	21494.6	-12247.3	-3198.5	1.06E+12	1.6	60.6	39.4	0.37	0.64	3	-0.26	-0.26	-0.67	0.15	-0.5	-0.1
72	20 181 017 144 042	21769.3	-11690.1	-3270.4	3.66E+12	2.1	91.7	8.3	0.38	0.43	4.2	0.27	0.4	-0.92	0.42	-0.31	-0.01
73	20 181 110 233 000	21509.9	-12221.1	-3118.6	1.28E+12	1.6	64	36	0.36	0.66	4.3	-0.19	-0.03	-0.85	-0.19	-0.3	0.24
74	20 181 119 121 437	21066.1	-9750.9	-1961.3	4.07E+12	2.1	74.1	25.9	0.25	0.82	10.5	0.28	0.23	0.26	0.23	-0.07	0.67
75	20 181 123 093 447	21399.3	-11944	-2933.3	9.53E+11	1.7	73.1	26.7	0.36	0.54	7.1	-0.13	0.17	-0.85	-0.17	-0.16	-0.34

Table E3 : Location of seismic events, local magnitude, deviatoric and isotropic components including their fault plane solutions

Event ID	X (m)	Y (m)	Z(m)	Local Magnitude (M_L)	DEV %	ISO %	Fault-Plane Solution 1 (degrees)			Fault-Plane Solution 2 (degrees)		
							Strike	Dip	Rake	Strike	Dip	Rake
20181017 144042	21769.3	-11690.1	-3270.4	2.1	91.7	8.3	126	53	-107	333	40	-68
20171219 050805	21554.6	-11588	-3368.3	2.1	89.2	10.8	139	84	-117	38	27	-12
20180317 191617	21661	-11904.6	-3541.5	2.1	82.4	17.6	115	86	-174	25	84	-4
20180113 023808	22043.1	-12042	-3774.5	2.1	79.1	20.9	10	60	-128	247	47	-44
20181119 121437	21651.2	-12104.1	-3280.4	2.1	74.1	25.9	90	19	177	184	89	71
20180628 233131	21874.9	-11433.7	-3098.4	2.1	73.2	26.8	317	43	-42	81	63	-124
20180129 004428	21624.2	-10245.5	-1625.9	2.1	72.8	27.2	310	25	-74	113	66	-97
20171027 080443	21674.9	-9241.9	-1967	2.1	72.4	27.6	247	47	-16	349	78	-136
20171220 064504	21066.1	-9750.9	-1961.3	2.1	55.2	44.8	133	68	-112	1	30	-46
20170729 202255	21574.8	-9994.5	-2344.8	2.2	74.2	25.8	354	32	-33	114	73	-117
20171214 050211	21411.6	-11984.9	-2899.7	2.2	63.6	36.4	18	26	-19	125	82	-115

20180522 003124	22933.2	-10682.9	-3382.3	2.2	60.3	39.7	66	14	123	213	78	82
20170818 090901	22119	-11560.7	-3001.5	2.3	94.8	5.2	236	23	-64	28	69	-101
20180127 184558	21026.5	-11661.6	-3918.7	2.3	82.8	17.2	116	50	68	327	45	113
20170822 105230	23193.5	-10860.6	-2074.6	2.3	74.9	25.1	318	87	135	51	45	5
20180217 163457	21974.3	-10909.4	-1906.4	2.3	60.7	39.3	317	84	84	180	9	133
20171017 211230	22711.5	-10529.5	-2950.3	2.4	76.3	23.7	157	63	-132	41	48	-37
20181007 082527	21679.8	-11529.5	-3342.1	2.5	88.6	11.4	329	33	-39	93	70	-117
20170715 162357	21960.1	-10966.9	-3196.6	2.6	95.3	4.7	13	26	-41	141	73	-110
20170307 164126	22523.5	-10804.5	-3290.9	2.6	88.5	11.5	354	42	-32	109	69	-127
20171023 094245	21754.1	-12108.7	-3080.9	2.7	71.8	28.2	119	51	-171	23	83	-39
20180317 214226	22680.1	-10940.2	-2351.5	2.7	66.0	34.0	343	27	-29	100	77	-114
20180628 181056	22383.1	-12449.3	-2809.5	2.7	45.3	54.7	307	18	-92	129	72	-89

Table E4 : Source Parameters

Seismic event time is local time (subtract two hours to obtain UTC time). Event locations are listed in terms of the mine co-ordinate system specifying their latitude (X), longitude (Y), and depth (Z- meters below datum). The datum reference point on Kloof Gold Mine is about 250 m above the surface and 1800 m above sea level.

Seismic event number	Event Date and Time yyyymmddhhmmss	Location Error (m)	X (m)	Y (m)	Z(m)	Moment (Nm)	Local Magnitude (M_L)	Energy (Joules)	Corner Frequency (Hz)	Log Apparent Volume (M^3)
1	20170307 164126	18	22523.5	-10804.5	-3290.9	1.39E+13	2.6	1.52E+08	13	7.28
2	20170331 175326	29	22387.5	-10862.4	-3477.6	8.99E+11	1.6	4.23E+06	14	6.46
3	20170715 162357	25	21960.1	-10966.9	-3196.6	7.04E+12	2.6	2.58E+08	15	6.46
4	20170729 202255	30	21574.8	-9994.5	-2344.8	3.32E+12	2.2	5.40E+07	16	6.49
5	20170731 022236	28	22361.5	-10253.8	-3082.3	5.86E+11	1.5	5.24E+06	20	6.00
6	20170818 090901	24	21974.3	-10909.4	-1906.4	7.37E+12	2.3	4.06E+07	13	7.30
7	20170822 105230	31	21026.5	-11661.6	-3918.7	3.90E+12	2.3	6.65E+07	16	6.54
8	20171009 141642	29	21904.1	-10538.4	-2940.2	6.04E+11	1.5	5.51E+06	20	6.00
9	20171017 211230	29	22711.5	-10529.5	-2950.3	7.50E+12	2.4	7.41E+07	13	7.08
10	20171019 015107	31	22035.1	-11177.6	-3433	1.98E+12	1.9	1.14E+07	15	6.72
11	20171021 161958	30	22103.7	-11539.1	-3175.7	6.81E+11	1.6	5.26E+06	18	6.11
12	20171023 094245	29	22680.1	-10940.2	-2351.5	1.04E+13	2.7	3.45E+08	15	6.68
13	20171023 103209	29	22293.9	-10799.8	-2943.4	1.54E+12	1.9	1.80E+07	17	6.30
14	20171027 080443	29	22043.1	-12042	-3774.5	3.24E+12	2.1	3.29E+07	17	6.68
15	20171028 215820	30	20537.2	-12214.8	-4174.2	8.56E+11	1.7	9.47E+06	17	6.08
16	20171031 010807	30	23147.4	-10479	-2978	5.07E+11	1.5	4.43E+06	24	5.94
17	20171103 221501	30	21575.4	-11497.7	-3690.7	7.55E+11	1.5	4.12E+06	18	6.33
18	20171110 003754	25	21320.7	-11771	-3363.6	7.43E+11	1.5	2.29E+06	18	6.43
19	20171116 131014	25	21610	-10006.3	-2438	6.04E+11	1.6	6.51E+06	17	5.93
20	20171126 005305	25	20775.3	-11444.2	-2776.2	2.53E+12	2.0	1.75E+07	16	6.74
21	20171211 135853	25	21994.7	-11608.9	-3223.5	5.90E+11	1.5	3.44E+06	16	6.18
22	20171211 142353	28	23015.6	-10751.2	-2777.5	8.97E+11	1.6	4.20E+06	16	6.46
23	20171214 050211	30	21411.6	-11984.9	-2899.7	4.23E+12	2.2	4.70E+07	17	6.76
24	20171219 050805	28	21874.9	-11433.7	-3098.4	2.66E+12	2.1	2.61E+07	13	6.61
25	20171220 064504	27	21651.2	-12104.1	-3280.4	4.62E+12	2.1	1.40E+07	15	7.36
26	20171225 071122	28	21979.2	-11532.8	-3476	1.26E+12	1.7	6.64E+06	15	7.56
27	20180102 122952	28	21586.2	-11869.8	-3077.7	9.08E+11	1.7	7.45E+06	22	6.23
28	20180104 192629	29	22281.4	-11194.4	-3465.5	7.36E+11	1.5	4.07E+06	14	6.30
29	20180113 022616	26	21576.6	-9339	-2100.8	1.17E+12	1.6	3.70E+06	18	6.75
30	20180113 023808	27	21674.9	-9241.9	-1967	3.32E+12	2.1	2.82E+07	15	6.77
31	20180115 002045	24	22472	-11575.3	-3494.8	5.00E+11	1.5	4.25E+06	26	5.95
32	20180116 220402	35	21494.5	-11906	-3129.7	2.36E+12	1.8	6.05E+06	18	6.91
33	20180121 033457	26	22091.2	-12241.4	-3310.2	1.16E+12	1.5	2.30E+06	16	6.95
34	20180125 230457	28	22014.6	-11285.9	-2985	1.45E+12	1.9	1.59E+07	15	6.30

35	20180127 184558	29	22119	-11560.7	-3001.5	9.21E+12	2.3	3.39E+07	14	7.58
36	20180129 004428	31	21661	-11904.6	-3541.5	3.54E+12	2.1	3.25E+07	17	6.76
37	20180212 010742	29	22020.8	-11385.9	-2911.1	1.08E+12	1.8	1.66E+07	16	6.04
38	20180217 163457	30	23193.5	-10860.6	-2074.6	5.16E+12	2.3	7.50E+07	15	6.73
39	20180219 220252	29	22218.5	-12449.6	-2788.7	7.00E+11	1.5	2.84E+06	16	6.41
40	20180223 001911	30	21745.6	-11694.9	-3297.1	7.14E+11	1.5	3.90E+06	18	6.30
41	20180317 191617	36	21624.2	-10245.5	-1625.9	2.92E+12	2.1	2.67E+07	15	6.68
42	20180317 214226	36	22383.1	-12449.3	-2809.5	1.15E+13	2.7	3.19E+08	16	6.80
43	20180322 231627	28	22237	-9994.9	-2628.9	7.79E+11	1.6	4.89E+06	18	6.28
44	20180329 173214	35	21376	-10033.2	-2557.1	1.80E+12	1.9	1.68E+07	14	6.46
45	20180402 055211	30	21755.4	-12271.4	-2765.3	9.17E+11	1.8	1.45E+07	19	5.94
46	20180404 120747	32	20357.7	-9673.9	-1840.7	1.33E+12	1.8	9.11E+06	15	6.46
47	20180406 051333	30	21988	-10133.7	-1756.1	5.55E+11	1.5	5.25E+06	20	5.95
48	20180411 211434	28	21620.6	-12450.2	-2665.9	2.10E+12	1.8	8.11E+06	17	6.91
49	20180420 155924	23	22989.2	-10783.3	-2998.3	1.11E+12	1.8	1.28E+07	17	6.18
50	20180428 000853	40	21516.9	-11912.8	-3115.1	9.35E+11	1.5	3.31E+06	18	6.60
51	20180504 181525	28	21727.8	-9760.7	-2260.6	7.60E+11	1.5	2.43E+06	19	7.08
52	20180504 205920	28	21809.5	-9770.2	-2426.7	2.58E+12	1.9	1.23E+07	18	7.15
53	20180522 003124	32	22933.2	-10682.9	-3382.3	3.18E+12	2.2	5.55E+07	16	6.45
54	20180526 083550	29	21539.2	-12007.5	-3083	4.28E+12	2	8.22E+06	17	7.53
55	20180608 090342	29	21622.1	-9647.5	-2402.1	1.46E+12	1.8	1.02E+07	16	6.51
56	20180626 181730	32	21668.7	-9887.6	-2341.1	6.80E+11	1.5	4.52E+06	27	6.20
57	20180628 181056	27	21754.1	-12108.7	-3080.9	2.30E+13	2.7	1.44E+08	14	7.75
58	20180628 233131	31	21554.6	-11588	-3368.3	2.49E+12	2.1	3.63E+07	14	6.41
59	20180803 134602	32	21472.3	-11915.8	-2973.5	7.02E+11	1.5	3.67E+06	16	6.30
60	20180813 230521	21	21648.2	-9995.7	-2383.5	1.33E+12	1.8	1.28E+07	17	6.32
61	20180816 183153	25	21592.6	-11913.8	-2917.9	2.51E+12	2	2.02E+07	17	6.67
62	20180826 190054	30	22024.1	-11659.2	-3064.1	2.37E+12	1.8	6.39E+06	16	6.11
63	20180831 205912	26	21613.9	-9980.5	-2368.5	7.55E+11	1.6	7.37E+06	18	6.08
64	20180902 061326	31	22203.4	-12321.2	-3290.3	2.73E+12	2	2.40E+07	14	6.67
65	20180910 214921	24	22126.4	-11896.5	-3344	6.70E+11	1.5	2.84E+06	20	6.38
66	20180913 032343	25	21325	-11845.2	-3130.7	7.27E+11	1.6	5.03E+06	15	6.20
67	20180915 035929	23	21385.9	-11787.8	-3362.2	1.24E+12	1.7	6.32E+06	17	6.57
68	20181005 024848	24	21733.1	-11436.5	-3288.4	8.24E+11	1.5	3.44E+06	15	6.48
69	20181007 082527	30	21679.8	-11529.5	-3342.1	7.32E+12	2.5	1.33E+08	14	6.79
70	20181008 174016	27	22044.7	-11688.8	-3250.4	7.34E+11	1.5	2.42E+06	14	6.53
71	20181016 161913	27	21494.6	-12247.3	-3198.5	1.06E+12	1.6	3.03E+06	16	6.75
72	20181017 144042	29	21769.3	-11690.1	-3270.4	3.66E+12	2.1	2.63E+07	14	6.89
73	20181110 233000	37	21509.9	-12221.1	-3118.6	1.28E+12	1.6	3.96E+06	15	6.80
74	20181119 121437	29	21066.1	-9750.9	-1961.3	4.07E+12	2.1	2.47E+07	16	7.00
75	20181123 093447	44	21399.3	-11944	-2933.3	9.53E+11	1.7	9.19E+06	16	6.18